論文 / 著書情報
Article / Book Information

題目(和文)	III-V族混晶半導体の物理的諸性質に関する研究
Title(English)	Investigations of the physical properties relating to III-V compound semiconductor alloys
著者(和文)	益一哉
Author(English)	Kazuya Masu
出典(和文)	学位:工学博士, 学位授与機関:東京工業大学, 報告番号:甲第1372号, 授与年月日:1982年3月26日, 学位の種別:課程博士, 審査員:
Citation(English)	Degree:Doctor of Engineering, Conferring organization: , Report number:甲第1372号, Conferred date:1982/3/26, Degree Type:Course doctor, Examiner:
学位種別(和文)	博士論文
Type(English)	Doctoral Thesis

DOCTORAL THESIS

INVESTIGATIONS OF THE PHYSICAL PROPERTIES RELATING TO III-V COMPOUND SEMICONDUCTOR ALLOYS

A THESIS SUBMITTED IN PARTIAL FULFILLMENT
OF THE REQUIREMENTS FOR THE DEGREE OF
DOCTOR OF ENGINEERING
December, 1981

Directed by Professor Kiyoshi TAKAHASHI

Presented by
Kazuya MASU
Department of Electronics
Graduate School of Science
and Engineering
Tokyo Institute of Technology

PREFACE

It is no exaggeration to say that the semiconductor industries which serve the communication systems and, in fact, whole industries, have been supported by silicon technology. One might say, " Silicon is the Superman " of the various semiconducting materials. However, silicon has not been the only material supporting the semiconductor industries. Since silicon has an indirect energy band gap of 1.1eV, it can not be used for laser diodes, nor is it always a suitable material for microwave and opto-electronic devices.

The III-V compound semiconductors, which were called 'magic crystals' in the 1960's, have been produced for use in various electronic devices resulting in higher performances than those obtained from devices using silicon. High quality single crystals have been made and epitaxial techniques established. The electronic devices that have been fabricated using III-V compound semiconductors are; (1) microwave devices such as the IMPATT and Gunn diode (GaAs, InP, InGaSb, etc.), (2) opto-electronic devices such as the laser diode, LED, APD, and the solar cell (GaAs, InP, GaP, GaAlAs, InGaAs, GaAsP, InGaAsP, etc.), and (3) high-speed FETs such as the MESFET and HEMT (GaAs, InP, GaAlAs, InGaAs, etc.). These electronic devices, which either could not be prepared from silicon, or the performance of which is better than those using silicon, have been playing important parts in the semiconductor industries. The high performance of these devices originated from the inherent properties of III-V compound semiconductors, i.e., various direct energy band gaps, the small electron effective masses, etc. Most of the opto-electronic devices and the high-speed FET such as HEMT consist of multi-layers of III-V compound semiconductors and of their alloys, in which each layer has a different energy band gap and the same lattice parameter. One must not overlook the heteroepitaxy technology, which has produced heterostructure multi-layers on suitable substrates. Heteroepitaxy technologies, for instance, LPE, MBE, and CVD, were established in the 1970's.

R&D of III-V compound semiconductor devices will continue in the 1980's, since III-V materials can be used for high performance opto-electronic devices, which are essential for optical communication systems. For example, the optimum design of silicon devices is relatively easy, because the physical properties and parameters have been thoroughly investigated. In other words, without a knowledge of the physical properties and parameters, the optimum design of the electronic devices would have been difficult, if not, impossible. Most of the III-V compound semiconductor devices mentioned above usually consist of III-V binary, ternary, and quaternary solid solutions such as GaAs, InP, GaAlAs, InGaAs, and InGaAsP. The physical properties and parameters of the III-V binary solid solutions have been relatively well investigated. However, those of the ternary and quaternary solid solutions, especially the electrical properties, have not been sufficiently investigated. In order to obtain a higher performance from III-V compound semiconductor devices, it is necessary to investigate the physical properties of III-V compound semiconductor alloys.

GaAlAs, InGaAs, and InGaAsP have hitheto been the most commonly used device materials, and these will be used in the 1980's. However, other optoelectronic alloy materials should also be investigated as there exists wavelength regions which the above materials can not cover. III-V materials with energy band gap wavelength region in the visible and infra-red wavelength regions are required.

In the 1980's, further R&D of III-V compound semiconductors will be required, and it must be recognized that this will involve investigations of their physical properties and development of new materials.

This thesis describes the theoretical and experimental achievements which have been obtained from a systematic study of p-type $Ga_{1-x}Al_xAs$ ternary alloys, with particular cosideration to the new III-V quaternary alloys needed for the opto-electronic devices in the 1980's, the development of $(Al_xGa_{1-x})_yIn_{1-y}As$ which is one of the Ⅲ-Ⅲ-Ⅲ-V quaternary alloys, and the development of high performance GaAs based solar cells as an application field.

This thesis consists of five PARTs. In PART I, an overview of this work is described. The theoretical and experimental achievements are described in PART Ⅱ, PART Ⅲ, and PART Ⅳ. The general conclusions are described in PART V.

TABLE OF CONTENTS

PART I

INTRODUCTION

CHAPTER 1. OVERVIEW AND OBJECTIVES OF THIS RESEARCH.

III-V compound semiconductor alloys have been utilized in the preparation of various electronic devices, and they yield higher performances than those of silicon devices. Although it is self-evident that physical properties, such as electrical properties, of III-V compound semiconductor alloys must be investigated in order to obtain an optimum-design and hence high performance devices, little attention has been paid to this requirement. Consequently, research was initiated based on this point of view, and aims of this research work were to investigate the behaviour of II-column impurities in $Ga_{1-x}Al_xAs$ ternary alloys, to develop new III-V quaternary alloys, and to develop high performance GaAs based solar cells on the basis of the above achievements.

This thesis is separated into five PARTs and consists of twelve chapters. Table 1-1 shows an overview of this research. The theoretical and experimental achievements are described in PART II, PART III, PART IV. In PART V, the general conclusions are stated.

The general features of the research are described in PART I. Fundamentals of the physical properties of III-V compound semiconductors and the epitaxial growth techniques are briefly described in Chap. 2.

$Ga_{1-x}Al_xAs$ is one of the most commonly used III-V ternary alloys. However, only a few systematic studies of the physical properties of p-type $Ga_{1-x}Al_xAs$ have been reported. A detailed systematic study of the physical properties such as transport properties of p-type $Ga_{1-x}Al_xAs$ is described in PART II.

The $Ga_{1-x}Al_xAs$ ternary alloys in this work were prepared on GaAs substrates. The fundamentals of LPE technique are described in Chap. 3.

II-column impurity diffusion during the LPE growth process is described in Chap. 4. It is shown that the diffusion process in GaAs can be represented by simple diffusion in a semi-infinite medium, if the surface free-carrier concentration is less than about $6x10^{18}cm^{-3}$.

In the previous analyses of hole mobility, an important problem has been neglected, i.e., the analytical expression for the Hall mobility. Hitherto only the calculated drift mobility and the experimentally observed values for the Hall mobility were presented. An analytic model for hole mobility, termed the Modified Two-Band Transport model, in which the drift and the Hall mobilities can be separately calculated, is derived in Chap. 5. The numerical calculations show clearly that the existence of alloy scattering in $Ga_{1-x}Al_xAs$ influences the room temperature mobility.

The acceptor energy level in $Ga_{1-x}Al_xAs$, which is produced by Zn or Be, affects the transport and optical properties. The acceptor energy level in $Ga_{1-x}Al_xAs$ increases with increasing Al composition x, and this is demonstrated theoretically and experimentally. The alloy scattering potential, which influences the hole mobility in ternary alloys, is experimentally determined for p-$Ga_{1-x}Al_xAs$. A value of about 0.7eV for this potential in p-$Ga_{1-x}Al_xAs$ was obtained by fitting the theoretical values to the experimental values. These results are described in Chap. 6.

The new III-V quaternary alloys are required for the preparation of opto-electronic devices operating in the infra-red and the visible wavelength regions. The development of new quaternary alloys is described in PART III.

The III-III-III-V quaternary solid solutions such as (AlGaIn)As and (AlGaIn)P are suitable materials for opto-electronic devices operating in these wavelength regions. It is shown that the molecular beam epitaxy technique is the most suitable epitaxial growth technique for these materials. These alloys and the growth techniques are discussed in Chap. 7.

In Chap. 8, the MBE preparation of $(Al_xGa_{1-x})_yIn_{1-y}As$, which is one of the III-III-III-V quaternary sloid solutions and is suitable for opto-electronic devices operating in the infra-red wavelength region, is discussed. This is the first reported preparation of this quaternary solid solution (on an InP substrate) in the world. It is shown that (AlGaIn)As lattice matched to InP has the predicted energy band gap and that it is possible to prepare both n-type and p-type films.

The development of GaAs based solar cell, which possesses the highest energy conversion efficiency among the various solar cells, is carried out on the basis of the results given in PART II. The GaAs solar cell development is described in PART IV.

The necessity for further solar cell R&D and the current status of GaAs based solar cells are discussed in Chap. 9.

From a systematic study of p-type $Ga_{1-x}Al_xAs$ described in Chap. 6, it is shown that beryllium is a more suitable p-type dopant for (GaAl)As/GaAs heterostructure solar cells. The development of (GaAl)As/GaAs p-p-n solar cells is described in Chap. 10. Finally, the development of the monolithic series-connected multi-junction solar cell arrays is described in Chap. 11.

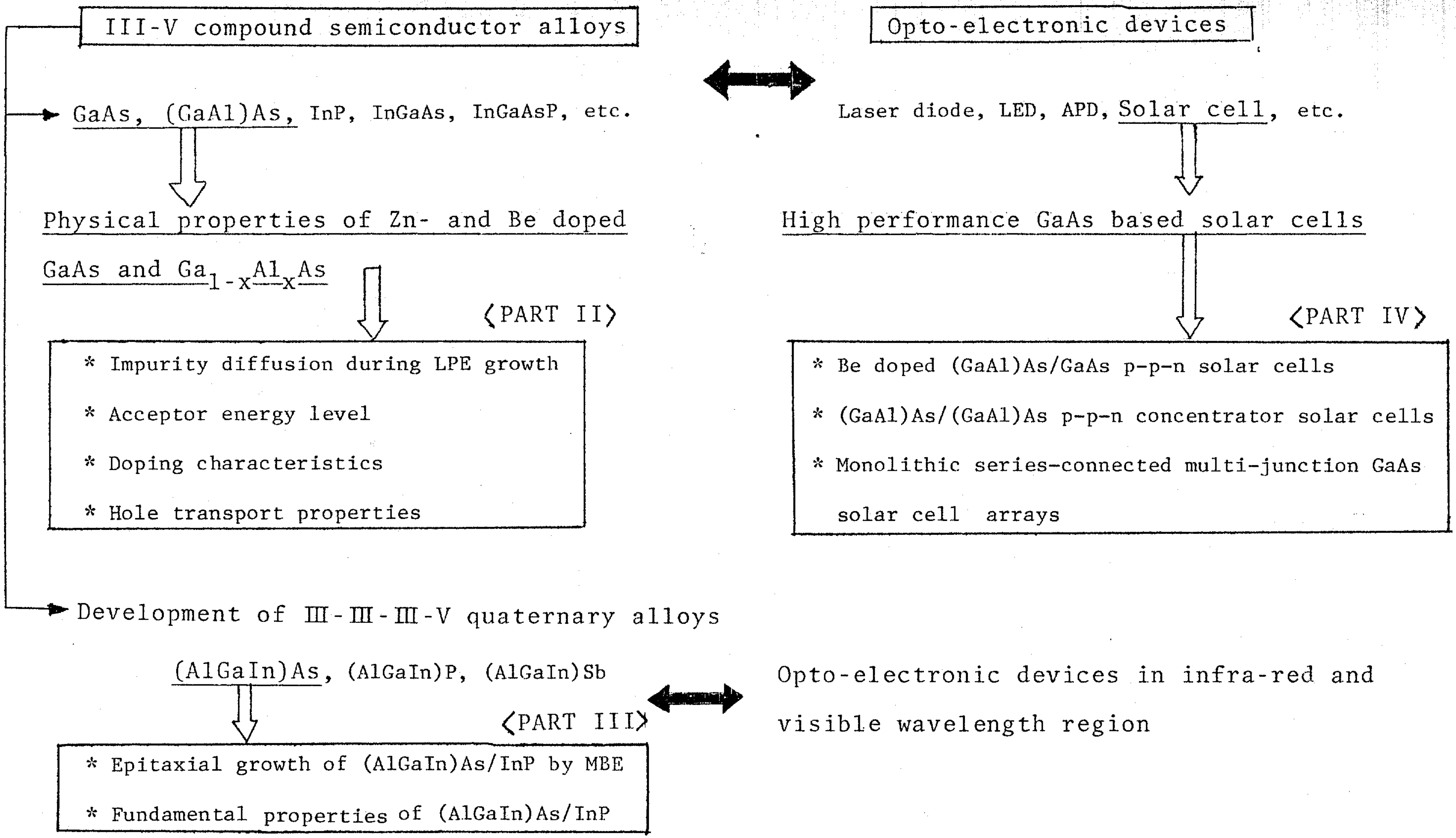

Table 1-1. Overview of this work.

CHAPTER 2.

FUMDAMENTAL FEATURES OF III-V COMPOUND SEMICONDUCTORS.

In this chapter, the fundamental physical properties of III-V compound semiconductors are described.

2-1. Fundamental physical properties of III-V compound semiconductors —— with particular emphasis on the $Ga_{1-x}Al_xAs$ ternary system.

2-1-2. Crystal structure.

The III-V compounds of interest in this work are those between Al, Ga, and In (group-III), and P, As, and Sb (group-V). All of the III-V binary compounds crystallized in the zinc-blende lattice structure. A unit cell structure is shown in Fig. 2-1. The zinc-blende lattice for a binary compound $A^{III}B^{V}$ consists of two interpenetrating FCC sublattices (each sublattice containing only A or B atoms) displaced along<111> direction by a distance of one A-B bond length. If all atoms of the B sublattice were replaced by A atoms, one would obtain a lattice of slightly higher symmetry : the diamond structure of group-IV semiconductors. The additional symmetry gain in going from zinc blende to diamond is known as an inversion symmetry (the symmetry operation in which $\vec{r}$ is replaced by-$\vec{r}$).

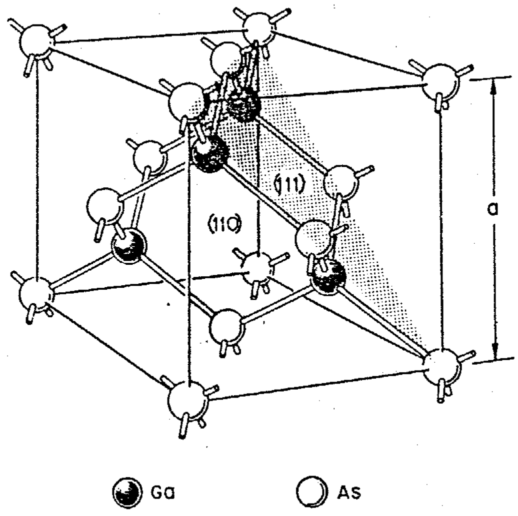

Fig. 2-1.

The unit cell in GaAs for the zinc-blende structure. The lattice constant is 'a'. The six faces of the cube are the six equivalent (100) planes.

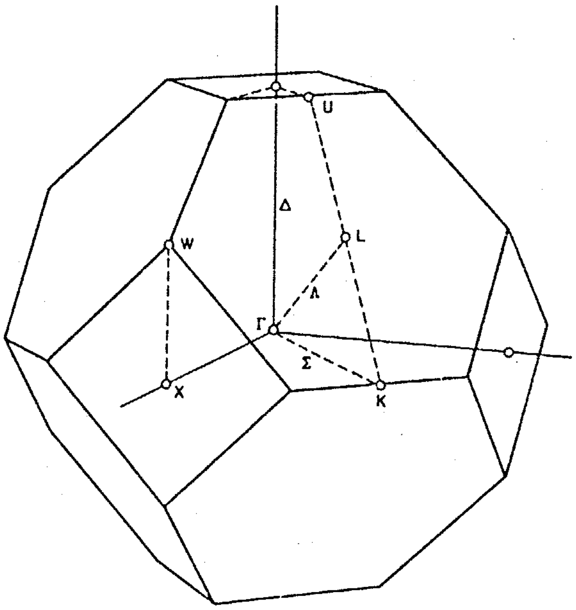

Fig. 2-2.

The first Brillouin zones for the zinc-blende and diamond lattices, showing the principal symmetry points and lines labeled in the conventional notation.

In ternary III-V solid solutions, the lattice parameter of the crystal tal generally scales linearly with composition (Vegard's law). It must be noted that linear variation with composition does not, in general, occur for the other properties. However, when detailed data are unavailable, it is often necessary to use linear interpolation.

2-1-2. Energy band structure.

The first Brillouin zone for the zinc-blende lattice is shown in Fig. 2-2 with high-symmetry points and lines labeled according to standard notation.

Figure 2-3 shows the major feature of the energy band structure of GaAs. The band structure depends on the crystal direction. This figure serves to illustrate the major features of the band structures of all III-V compound semiconductors. The band structure of other III-V compound and group IV semiconductors differ from GaAs only in quantitative detail.
In GaAs, a direct energy band gap material, the minimum energy in the conduction band and the maximum energy in the valence band both occur at the same value of $\vec{k}$ (k=0). For an indirect energy band gap material, the minimum of the conduction band does not occur at k = 0. In the 9 binary III-V solid solutions (see Table 2-1.), there are four indirect materials.
The minimum of the conduction band of these indirect material occur at point X. The energy band gaps of Γ, X, and L points of the binary compound semiconductors at room temperature are listed in Table 2-1. It is better to note here; when one

mention 'the energy band gap of a semiconductor', it generally means the lowest energy band gap. The temperature dependence of the energy band gap is generally written as

$$E_g(T) = E_g(0) - \alpha T^2/(T + \Theta), \qquad (2\text{-}1)$$

where $E_g(T)$ is the energy band gap at 0°K, α an empirical parameter of $\sim 5\times10^{-4}\mathrm{eV}\cdot\mathrm{K}^{-1}$, and Θ an empirical parameter often near the Debye temperature. For GaAs, $E_g(0)=1.519\mathrm{eV}$, $\alpha=5.405\times10^{-4}\mathrm{eV}\cdot\mathrm{K}^{-1}$, and $\Theta=204\mathrm{K}$.

For the ternary and quaternary solid solutions, it is the most important to determine the compositional variation of the energy band gap. The energy band gap of the ternary alloy $A_xB_{1-x}C$ can be generally written as

$$E_g^i = a + bx + cx^2 \quad (i = \Gamma,\ X,\ \text{and } L). \qquad (2\text{-}2)$$

Figure 2-4 shows the compositional variation of the energy band gaps of $Ga_{1-x}Al_xAs$. Since GaAs has a direct energy gap whereas AlAs has an indirect energy gap, the direct-indirect conduction band crossover occurs. The compositions of this crossover from x=0.37 to x=0.45 have been assigned. This region of $0.4 \lesssim x \lesssim 0.5$ where the bands cross is relatively uncertain at present time. Table 2-2 listed the energy band gaps and the density-of-states effective masses of GaAs, AlAs, and $Ga_{1-x}Al_xAs$, which were summarized by Casey (1978). Although there may remained the uncertainty of each value in Tabel 2-2, they are some of the most reliable values available at the present time.

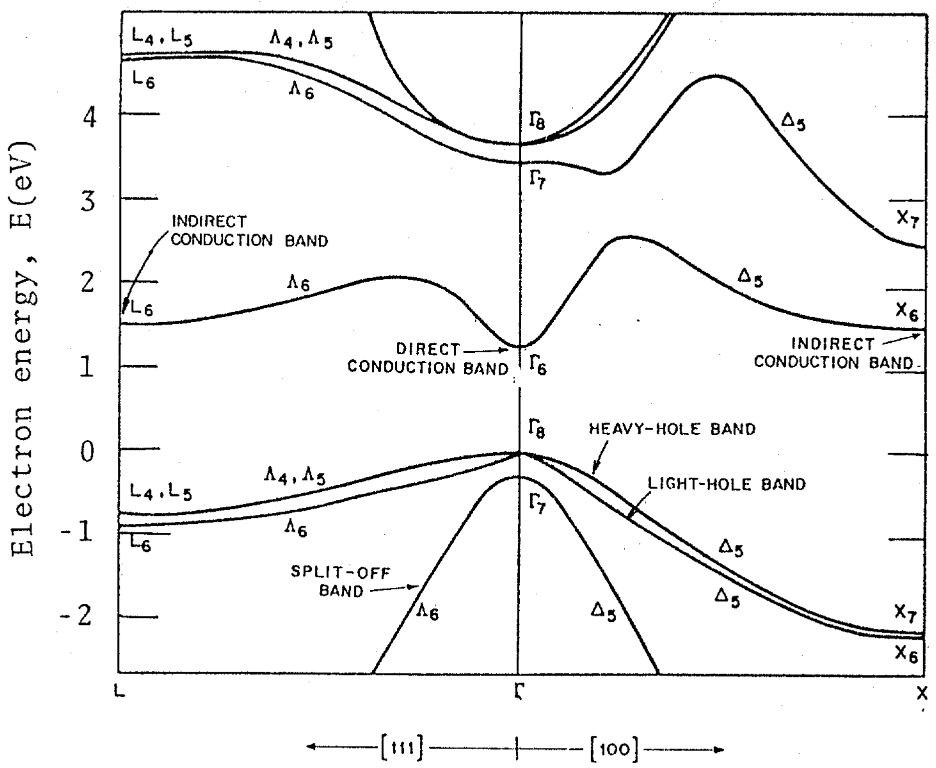

Fig. 2-3.

The band structure of GaAs with energy 'E' plotted as a function of momentum wave vector $\vec{k}$ along with <100> and<111> directions.

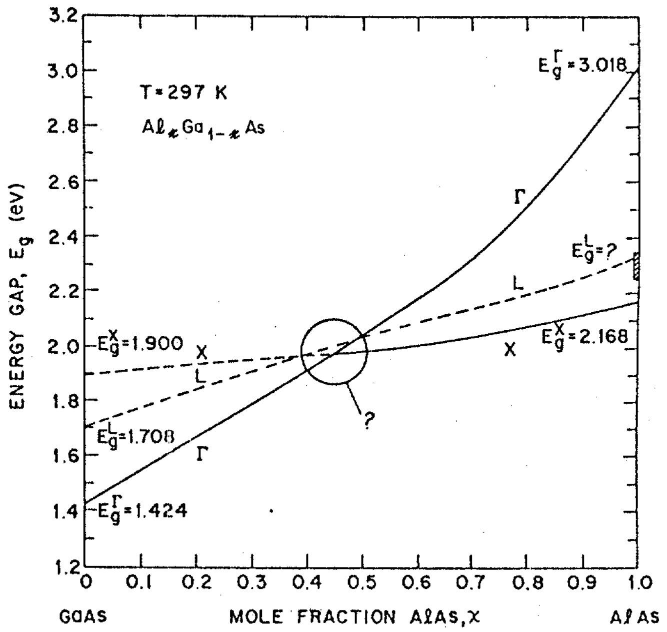

Fig. 2-4.

The compositional dependence of the direct $\Gamma_8 \rightarrow \Gamma_6$ and the indirect $\Gamma_8 \rightarrow X_6$ and $\Gamma_8 \rightarrow L_6$ energy gaps for $Ga_{1-x}Al_xAs$.

	Lattice parameter		Energy band gap (R.T.)				Effective mass	
	a (Å)	T(°C)	D or I	Γ (eV)	X (eV)	L (eV)	Conduction band m_n/m_o	Valence band m_p/m_o
AlP	5.451	-	I	3.581	2.45	-	-	0.70
AlAs	5.6605	0	I	3.018	2.168	2.25-2.35	0.15	0.79
AlSb	6.1355	18	I	2.223	1.589	1.897	0.12	0.98
GaP	5.45117	25	I	2.78	2.261	∿2.6	0.82	0.60
GaAs	5.65325	27	D	1.424	1.900	1.708	0.067	0.48
GaSb	6.09593	-	D	0.726	1.020	0.799	0.042	0.44
InP	5.86875	18	D	1.351	2.21-2.25	1.84	0.077	0.64
InAs	6.0584	18	D	0.35	∿1.7	∿1.6	0.023	0.40
InSb	6.47937	25	D	0.172	∿1.0	∿0.73	0.0145	0.40

Table 2-1. Selective properties of III-V binary compounds semiconductors.

GaAs	AlAs	$Ga_{1-x}Al_xAs$
$E_g^{\Gamma} = 1.424\text{eV at } 297\text{K}$	$E_g^{\Gamma} = 3.018\text{eV}$	$E_g^{\Gamma}(0<x<0.45) = 1.424 + 1.247x$
		$E_g^{\Gamma}(0.45<x<1.0) = 1.424 + 1.247x + 1.147(x-0.45)^2$
$E_g^{L} = 1.708\text{eV at } 297\text{K}$	$E_g^{L} = 2.25\text{–}2.35\text{eV}$	$E_g^{L} = 1.708 + 0.642x$
$E_g^{X} = 1.900\text{eV at } 297\text{K}$	$E_g^{X} = 2.168\text{eV}$	$E_g^{X} = 1.900 + 0.125x + 0.143x^2$
$m_p = 0.48 \cdot m_o$	$m_p = 0.79 \cdot m_o$	$m_p = (0.48 + 0.31x) \cdot m_o$
$m_n^{\Gamma} = 0.067 \cdot m_o$	$m_n^{\Gamma} = 0.15 \cdot m_o$	$m_n^{\Gamma} = (0.067 + 0.083x) \cdot m_o$
$m_n^{L} = 0.55 \cdot m_o$	$m_n^{L} = 0.67 \cdot m_o$	$m_n^{L} = (0.55 + 0.12x) \cdot m_o$
$m_n^{X} = 0.85 \cdot m_o$	$m_n^{X} = 0.78 \cdot m_o$	$m_n^{X} = (0.85 - 0.07x) \cdot m_o$
$E_g^{\Gamma} = 1.519 - 5.045 \times 10^{-4} T^2/(204 + T)$		

Table 2-2. Energy band gaps and density-of-states effective masses for GaAs, AlAs, and $Ga_{1-x}Al_xAs$.

2-1-3. Valence band structure.

In the absence of spin-orbit splitting, the highest point of the uppermost valence band is at Γ and is sixfold-degenerated including spin degeneracy. When the spin-orbit effects are included, this band split into a fourfold degenerate band (Γ_8) and a doubly degenerate band (Γ_7) by an energy $\overline{\Delta}_o$ (the zone center spin-orbit splitting). For points away from k=0, the symmetry is lower and the Γ_8 band is further split into two doubly degenerate band called heavy hole (v_1) and light hole (v_2) band. The Γ_7 band at at the zone center is known as the split-off band (v_3).

Dresselhause (1955) gave an approximate expression for the heavy- and light-hole energy surface in terms of the valence band parameters.

$$E(\vec{k}) = -(\hbar^2/2m_o)\left[Ak^2 \pm \{B^2k^4 + C^2(k_x^2k_y^2 + k_y^2k_z^2 + k_z^2k_x^2)\}^{1/2}\right], \quad (2\text{-}3)$$

where A, B, and C are valence band parameters. These bands (the upper sign corresponds to v_2 and the lower to v_1) are approximations to the more accurate band, and are only valid near k=0.

There are various parameters, which can represent the valence band structure: L, M, and N (which often appear in the text books.) and γ_1, γ_2, and γ_3(the Luttinger's valence band parameters, Luttinger, 1956). The relationship between these parameters are given by;

$$A = (1/3)(L + 2M) + 1, \tag{2-4}$$

$$B = (1/3)(L - M) , \tag{2-5}$$

$$C = (1/3)\{N^2 - (L - M)^2\}, \tag{2-6}$$

and

$$A = -\gamma_1, \tag{2-7}$$

$$B = A(\mu - \frac{6}{5}\delta), \tag{2-8}$$

$$C = A\delta(5\mu - \delta), \tag{2-9}$$

with

$$\mu = (6\gamma_3 + 4\gamma_2)/(5\gamma_1), \tag{2-10}$$

$$\delta = (\gamma_3 - \gamma_2)/\gamma_1 . \tag{2-11}$$

Table 1-3 contains values for γ_1, γ_2, and γ_3 given by Lawaetz (1971), together with the equivalent L, M, N, A, B, and C^2.

Using Luttinger's valence band parameters, the effective masses of v_1, v_2, and v_3 bans are represented as follows: The effective mass m_3 of the split-off band Γ_6^+ is given by

$$m_3/m_o = (\gamma_1 + Fy)^{-1} , \tag{2-12}$$

where

$$y = \bar{\Delta}_o/3(E_g^\Gamma + \bar{\Delta}_o) , \tag{2-13}$$

$$F = -E_p/E_g^\Gamma . \ (*) \tag{2-14}$$

---

*) The representation for E_p is complex. The details are omitted here.

The v_1 and v_2 band are strictly anisotropic as shown in Fig. 1-3. However, it is convenient to determine the average effective masses of these valence bands, because these v_1 and v_2 bands are usually assumed to be spherical and to be expressed by the scalar effective masses. The average light hole and heavy hole effective masses are given by

$$m_2/m_o = (\gamma_1 + \bar{\gamma})^{-1} , \tag{2-15}$$

$$m_1/m_o \sim (1 + 0.05\gamma_h + 0.164\gamma_h^2)^{2/3}/(\gamma_1 - \bar{\gamma}), \tag{2-16}$$

where

$$\bar{\gamma} = (2\gamma_2^2 + 2\gamma_3^2)^{1/2} , \tag{2-17}$$

$$\gamma_h = 6(\gamma_3^2 - \gamma_2^2)/\bar{\gamma}(\gamma_1 - \bar{\gamma}) . \tag{2-18}$$

These effective masses are also listed in Table 1-3. (*)

---

*) The heavy and light hole effective masses calculated by equations 2-15 and 2-16 are 0.62 and 0.074,respectively, when one use the parameters given by Lawaetz (1971). However, $m_1 \sim 0.48$ and $m_2 \sim 0.067$ have been used as more reliable values in many reportes. Consequently, the Luttinger's valence band parameters should be recalculated.

	-L	-M	-N	-A	-B	C^2	γ_1	γ_2	γ_3	m_1/m_o	m_2/m_o	m_3/m_o
AlP	4.73	4.34	6.87	3.47	0.130	15.7	3.47	0.06	1.15	0.63	0.20	0.29
AlAs	8.21	3.44	9.33	4.03	1.59	21.4	4.04	0.78	1.57	0.76	0.15	0.24
AlSb	9.30	3.03	10.3	4.12	2.09	22.2	4.15	1.01	1.75	0.94	0.14	0.29
GaP	9.14	3.23	9.93	4.20	1.97	21.2	4.20	0.98	1.66	0.79	0.14	0.24
GaAs	18.4	3.77	19.6	7.63	4.86	56.7	7.65	2.41	3.28	0.62	0.074	0.15
GaSb	29.1	4.55	31.2	11.7	8.19	122.6	11.80	4.03	5.26	0.49	0.046	0.14
InP	15.6	3.11	16.5	6.28	4.17	38.9	6.28	2.08	2.76	0.85	0.089	0.17
InAs	54.2	3.87	55.6	19.7	16.8	186.5	19.67	8.37	9.29	0.60	0.027	0.089
InSb	98.9	4.58	101.0	35.0	31.4	437.5	35.08	15.64	16.91	0.47	0.015	0.107
Si	6.80	4.43	8.61	4.22	0.790	27.84	4.22	0.39	1.44	0.53	0.16	0.24
Ge	31.5	5.75	33.9	13.3	8.57	163.4	13.35	4.25	5.69	0.35	0.043	0.092

Table 2-3.

Valence band parameters of III-V compounds, Si, and Ge (Lawaetz, 1971: Wiley, 1975).

2-1-4. (GaAl)As/GaAs heterostructure.

The heterostructure generally means the multilayers of different semiconductor films on a suitable semiconducting substrate. Each layer generally has a different energy band gap and different physical properties. For example, in laser diodes, the active layer is sandwiched between grad layers, which have wider energy band gaps and smaller refractive indices than those of the active layer. This structure is generally called a Double-Hetero(DH) structure, and it exhibits both carrier and optical confinement actions. Of the various opto-electronic devices which are formed by III-V compound semiconductor alloys, the heterostructure has been widely utilized. It is noted that each layer which makes up the heterostructure must have the same lattice parameter in order to avoid the interface-state effects. It is a general requirement to have less than a 0.3% lattice mismatch between each layer in order to produce a predicted properties of a heterostructure. Since the lattice mismatch between GaAs and AlAs is about 0.13%, the heterostructure constructed by $Ga_{1-x}Al_xAs$ and GaAs can produce a good heterostructure. In fact, the first reported DH laser diode was formed by a (GaAl)As/GaAs heterostructure (see Sec. 7-2.). Furthermore, there are no other combinations between binary and ternary solid solutions such as that between GaAs and $Ga_{1-x}Al_xAs$ (see Table 2-1.). Recently, the heterostructure using III-V quaternary alloys such as in the InGaAsP/InP system has received wide attention for the production of high performance opto-electronic devices.

2-2. Various epitaxial growth techniques for III-V compound semiconductors.

'Epitaxial growth' means the growth technique of solid solutions on suitable substrates, and the solid solutions have the same lattice strucuture and the same lattice constant as the substrates. Most of the electronic devices fabricated using III-V compound semiconductors have a heterostructure, and require the development of heteroepitaxial growth of thin multi-layers of III-V solid solutions.

There are three epitaxial growth techniques that are of interest for III-V compound semiconductors. Growth on single-crystal substrates from metallic solutions in a graphite boat, This is called liquid phase epitaxy (LPE), and is the most com commonly used process for heterostructure devices. The technique called molecular beam epitaxy (MBE) is one in which beams of atoms and molecules from effusion ovens in an ultra-high-vacuum system impinge on a heated substrate. Chemical vapor deposition (CVD) is epitaxy by the transport of reactant species in a flowing gas stream to the substrate where a deposition reaction occurs.

In this work : the $Ga_{1-x}Al_xAs$ layers in PART II and the (GaAl)As/GaAs heterostructure solar cells in PART IV were prepared by LPE. Chapter 3 summarizes the details of LPE. The $(Al_xGa_{1-x})_yIn_{1-y}As$ layers on InP substrates in PART III were prepared by MBE. The details of MBE techniques are discussed in Chap. 8.

There are four different CVD techniques, i.e., the water-vapour transport process, the halide process, the hydride process, and the metal-organic-(MO)-CVD technique. Of these processes the MO-CVD technique has been taken attention, since Rockwell group reported (GaAl)As/GaAs DH laser diodes fabricated using this technique in 1978.

Table 2-4 summarizes the distinctive features of each epitaxial growth technique.

	LPE	MBE	CVD	MO-CVD
System cost	normal	very expensive	normal	expensive
Mass productivity	inferior	inferior	superior	superior
Automatic control for epitaxial growth	very difficult	possible and easy	difficult	somewhat difficult
Possibility of growth on large area substrate	somewhat difficult	somewhat difficult	easy	easy
Growth possibility with III-V alloys	YES, but very difficult	YES, easy	YES, but impossible for the III^{n}-V system	YES, probably easy
Controllability of the doping profile in the epitaxial layer	YES, but difficult	YES, easy	YES	YES
Substrate temperature	700-900°C	400-500°C	700-800°C	600-700°C
Growth rate (μm/min)	0.1-10	0.005-0.05	0.01-0.5	0.005-1.5
Thickness uniformity	normal	superior	normal	superior
Surface flatness	normal	superior	superior	superior
The lowest carrier density (cm^{-3})	10^{13}	10^{15}	10^{13}	10^{15}
Crystal quality	superior	normal	somewhat superior	normal

Table 2-4. Comparison of various epitaxial growth techniques.

PART II

BEHAVIOUR OF II-COLUMN IMPURITIES IN $Ga_{1-x}Al_xAs$.

CHAPTER 3.

FUNDAMENTALS OF LIQUID PHASE EPITAXY.

3-1. Introduction.

Liquid phase epitaxy (LPE) is widely used for the preparation of III-V ternary and quaternary alloys. The $Ga_{1-x}Al_xAs$ layers described in chapters 4 ∿ 6 and (GaAl)As/GaAs heterostructures described in chapters 10 and 11 were prepared on GaAs wafers by LPE. In this chapter, the fundamentals of LPE such as the phase equilibria and the growth process are summarized.

3-2. Phase equilibria in III-V systems.

In LPE growth of ternary (and quaternary) compound films, it is obviously desirable to be able to predict theoretically the dependence of the ternary crystal composition on the liquid composition at various temperatures. The ternary system phase diagrams have been determined by many authors, and reviewed in the literature (Casey, 1978; Kressel, 1977).

The liquidus isotherms for the Al-Ga-As ternary at 800°C, 900°C, and 1000°C are given in Fig. 3-1 with the triangular cordinates generally used for ternaries. For LPE growth of $Ga_{1-x}Al_xAs$, the liquidus and solidus isotherms at the Ga-rich corner are important. In Appendix A, the general

Fig. 3-1.

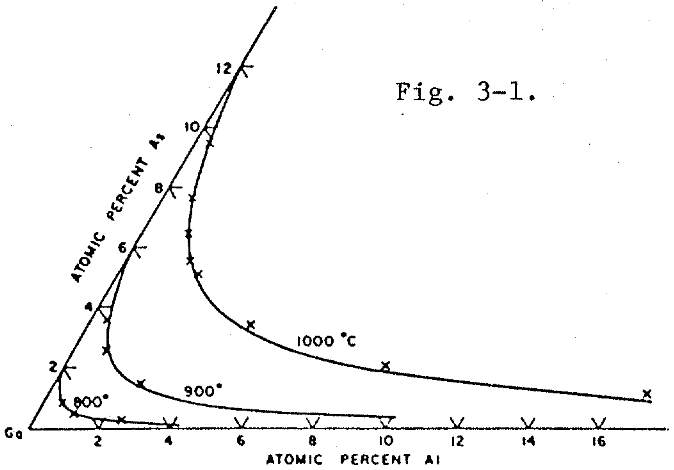

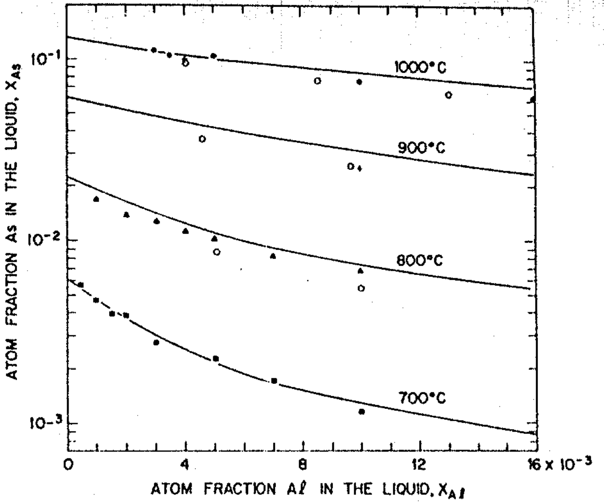

Fig. 3-2(a)

Fig. 3-2(b)

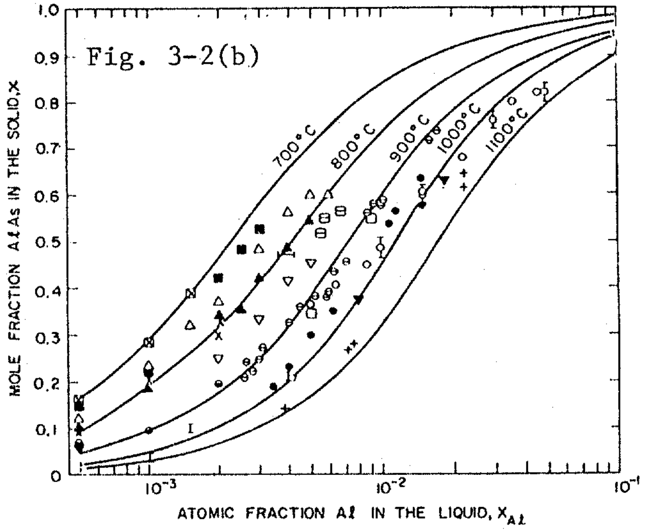

Fig. 3-1. ↑

The solbility of As as a function of the Al composition in the solution at 1000, 900, and 800°C. The solid lines are theoretically calculated values.

Fig. 3-2. ⟶

(a) The liquidus isotherms in Al-Ga-As system.
(b) The solidus composition in $Ga_{1-x}Al_xAs$ as a function of liquidus composition.

The solid lines are theoretically calculated values.

formulae for the III^n-V system is derived. The phase diagram for the Al-Ga-As ternary system can be determined as a special case of the deviation Appendix A.* Figure 3-2 shows the liquidus curve (a) and the solidus composition as a function of the liquidus composition (b) at the Ga-rich corner. Using these results,the liquidus composition at a given temperature and for a given solid composition can be obtained (see Fig. 3-8).

3-3. Impurity incorporation in LPE.

Table 3-1 lists the ionization energies for various dopants in GaAs divided into three major categories, namely simple donors, simple acceptors, and complex levels involving the group IV atoms. Transition metals are listed separately. Of these dopants, n-type Sn, Si, and Te, and p-type Zn (used in this work), Mg, Ge, and Be (used in this work) are normally used in LPE.

Although the distribution coefficients of Te and Se are very high (5-10 at 750°C) (Kang, 1968; Greene, 1971), that of Sn is low (about 10^{-4} at 750°C) (kang, 1968). Silicon exhibits amphoteric behaviour in GaAs and this behaviour is particularly dependant on the growth temperature.

*) In Appendix A, the phase diagram for Al-Ga-As can be obtained by putting n = 2 in equations A-1 to A-5.

Ionization Energy of Transition Metals in GaAs[a]

	Ionization energy		
Element	From photoluminescence at 20 and 4 K	From electroluminescence at 77 K	From electrical measurements
Cr	0.85	—	0.79
Mn (acceptor)	0.114, 0.112		0.094
Fe	~0.2 and 0.5	0 36	0.52, 0.37
Co	0.58	0.345	0.16
Ni	—	0.35	0.21
Cu	0.170, 0.155 0.165	—	0.145
Ag	0.239	—	0.235

Impurity Ionization Energies in GaAs

Type	Element	E_i (eV)	Remarks
Simple donors	S_{As}	0.00610	
	Se_{As}	0.00589	
	Te_{As}	0.0058	
	Sn_{Ga}	0.006	
	C_{Ga}	Similar to Sn	
	Ge_{Ga}	0.00608	
	Si_{Ga}	0.00581	
	Cr	Shallow	LPE material
	O	Similar to Sn	LPE material only
	Pb_{Ga}	Shallow	LPE material
Simple acceptors	Cd_{Ga}	0.0345	
	Zn_{Ga}	0.029	
		0.032	
		0.030	
		0.034	
	Mg_{Ga}	0.030	
		0.028	
	Be_{Ga}	0.030	
		0.028	
	C_{As}	0.026	
		0.025	
	Sn	0.2 ± 0.02	Believed to be Sn_{As}
		0.171	
	Pb	~0.12	
	Ge_{As}	0.038	
	Si_{As}	0.035	
Complex centers	Ge (acceptor)	~ 0.08	LPE and MG material
	Si (acceptor)	~ 0.1	LPE material
	Si (acceptor)	~ 0.22	LPE material
		0.23	Si ion-implanted GaAs

Table 3-1. Various dopants in GaAs.

Consequently, tin was used as a n-type dopant throughout this work because of its small distribution coefficient.

Figure 3-3 shows the doping characteristics of Sn in GaAs at 765°C measured by the author. The donor concentration was determined from the slope of the C^{-2}-V curve. The distribution coefficient at 765°C is 3×10^{-4}, which is the same value as that previously reported by many authors (Harris, 1969; Solomon, 1968, Vilms, 1972). Using these results, the carrier concentration in the n-GaAs epitaxial layer can be controlled by controlling the weight of tin in the growth melt in the LPE process.

3-4. The epitaxial growth technique.

3-4-1. The liquid phase epitaxy system.

(1) System description.

Figure 3-4 shows a block diagram and an overview of the LPE system used in this work, which incorporated the conventional sliding boat technique. The quartz reactor tube is 50 mm in diameter and 1 m long. The furnace has three zones (each about 15 cm long), controlled by three separate thermo-controllers. The right hand end of the reactor tube is connected to the clean bench. The charging of Ga and other sources into the graphite boat is performed on the clean bench.

(2) The graphite boat.

The graphite boat is shown in Fig. 3-5. The boat consists of four parts —— the holder, the slider, the barrel,

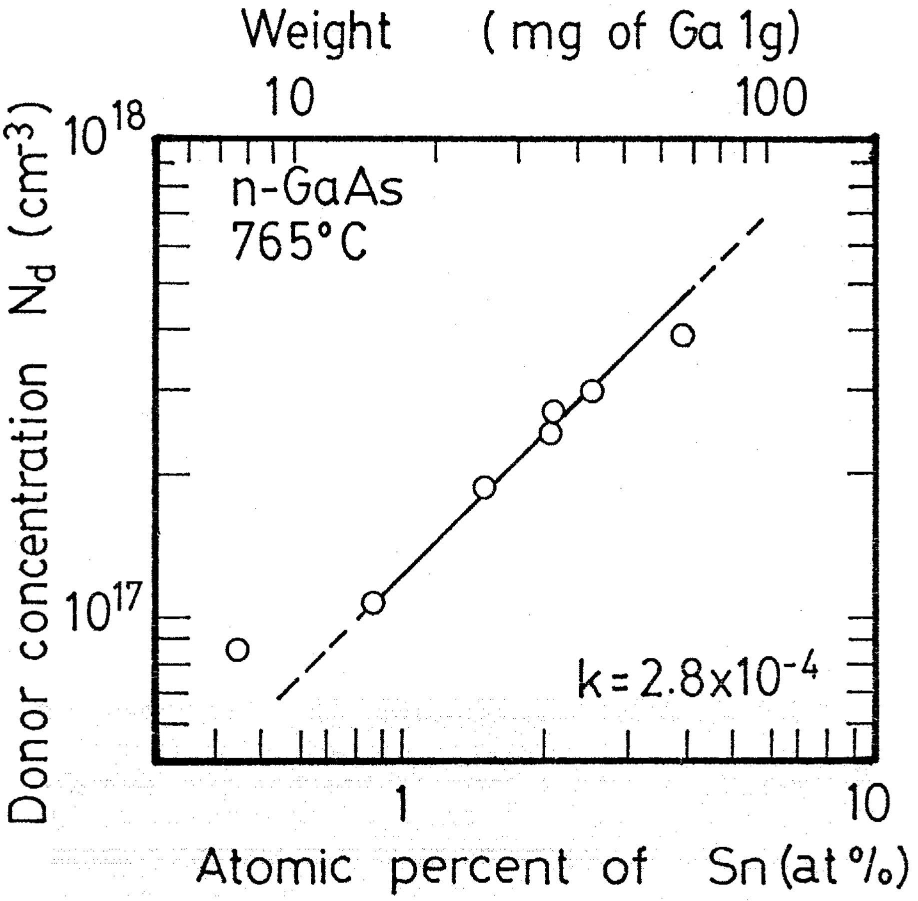

Fig. 3-3.

Donor concentration as a function of Sn concentration in the growth melt. The epitaxial growth conditions were (1) initial growth temperature; 765°C, (2) cooling rate; 1.0°C/min, and (3) growth duration; 15 min . The donor concentration were determimed from the slope of the C^{-2}-V curves.

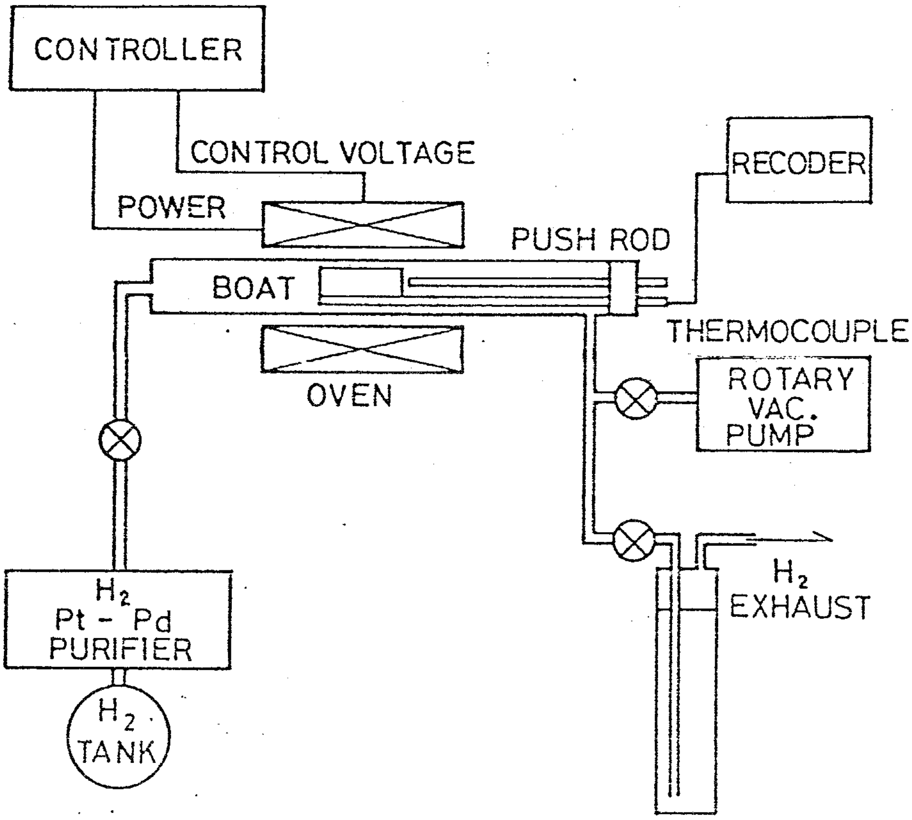

(a) Block diagram.

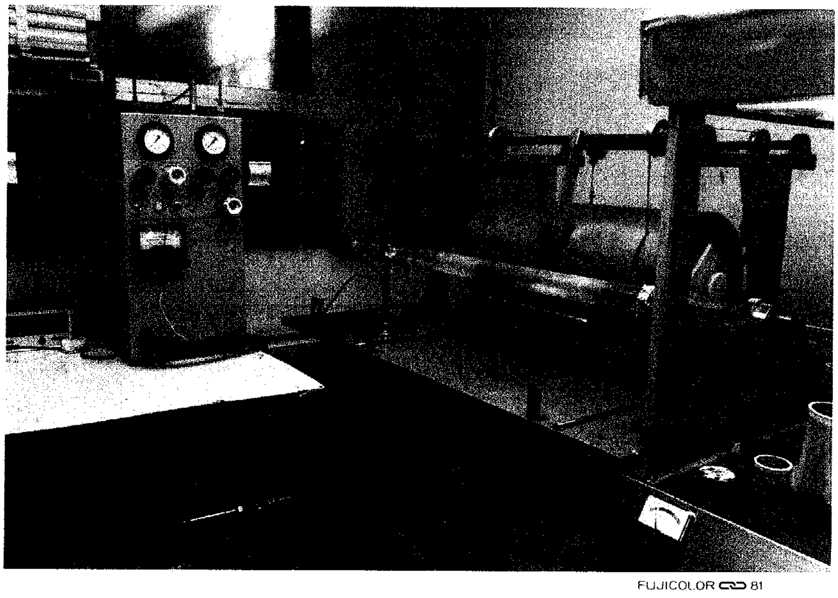

(b) Overview.

Fig. 3-4. The liquid phase epitaxy system.

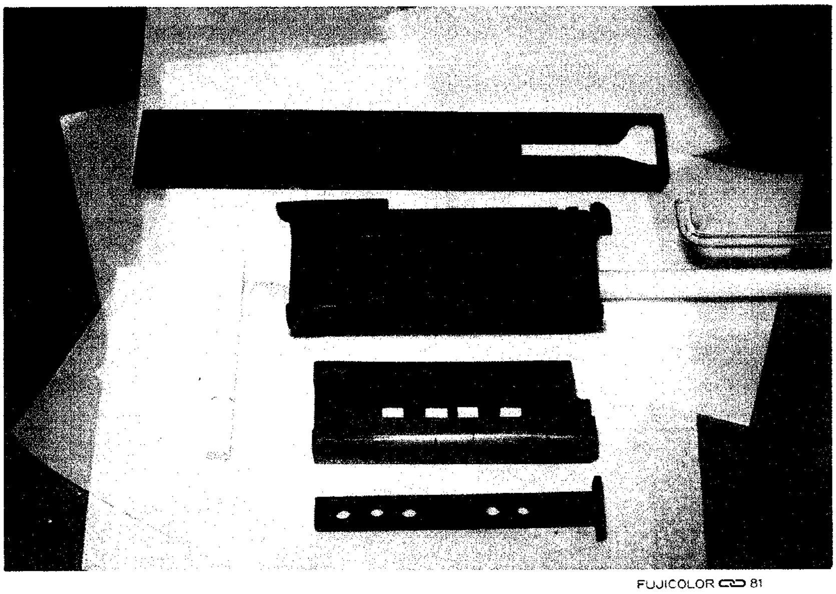

Fig. 3-5. The graphite boat.

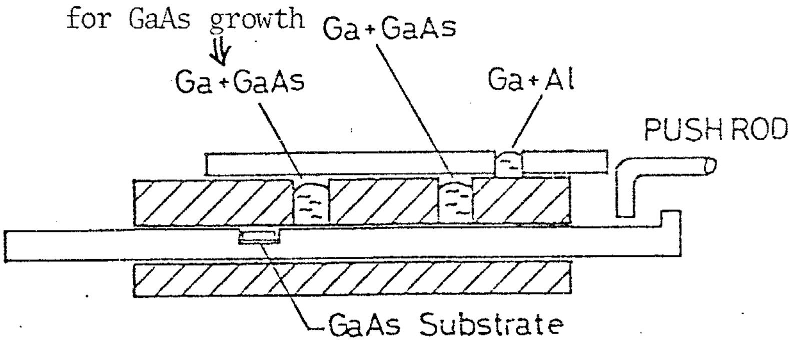

Fig. 3-6.

Aspects of the Al mixing method. The solution for (GaAl)As is separated into two parts, ——Ga+GaAs and Ga+Al. These solutions are mixed a few minutes before the growing process.

and the Al barrel. The substrate, of surface area 7x11 mm^2, is set on the slider.

The Al mixing method, which was originally developed by Konagai (1976b) to reduce the effects of the oxidization of Al, was utilized for the growth of $Ga_{1-x}Al_xAs$ with a large Al composition. In this method, the solution is separated into two parts, Ga + Al and Ga + GaAs, as shown in Fig. 3-6. The upper solution of Ga + As drops into the lower solution of Ga + GaAs a few minutes before the substrate is brought into contact with the melt at the growth temperature. Smooth (GaAl)As layers were obtained by this technique, as the mixed solution containing a large quantity of Al makes contact with substrate without contamination by Al oxide slag.

3-4-2. The epitaxial growth process.

The flowchart for the growth process is shown in Fig. 3-7. The process details are as follows:

(1) GaAs substrate.

In general, the GaAs substrate were (100) or (111)B oriented wafers. Undoped ($n = 10^{16} cm^{-3}$) GaAs wafers were used for the electrical measurement, n^+-GaAs ($>2x10^{18} cm^{-3}$) for the solar cells, and Cr doped semi-insulating substrates for the monolithic solar cell arrays.

(2) Weighing the charging materials.

As indicated above, the solutions consisted of Ga, GaAs, Al, and appropriate dopants. Typically, the Ga charge was 1 g or 2 g throughout this research programme. The weight of GaAs and Al in a saturated liquid solution of Ga-Al-As at a

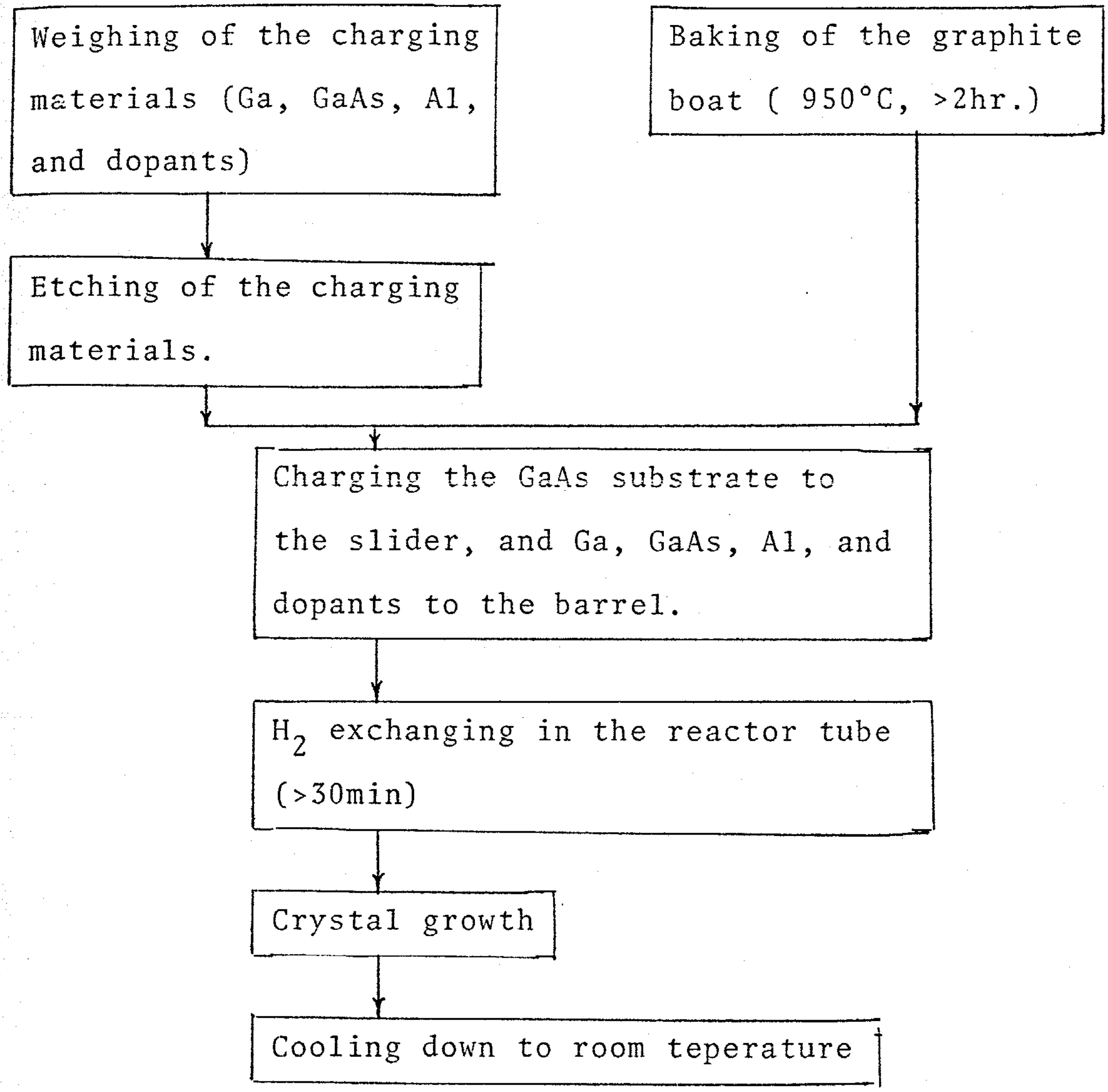

Fig. 3-7.

Crystal growth process of the liquid phase epitaxy.

temperature can be calculated by using the results shown in Fig. 3-2. Figure 3-8 shows the weight of GaAs and Al in 1 g Ga melt as a function of the Al solid composition.

Table 3-2 shows the weight of GaAs and Al in 1 g of Ga and the thickness of the epitaxial layers for several growth temperatures.

(3) Temperature programme during crystal growth.

Figure 3-9 shows the typical temperature programme for (GaAl)As/GaAs p-p-n solar cells (see Chap. 10). It takes about 15 min to heat the graphite boat to about 750°C from room temperature. After 15 min soaking, the crystal growth of n-GaAs is started by bringing the substrate into contact with the solution of Ga + GaAs + Sn. With this programme, typical thickness of n-GaAs and p-$Ga_{0.2}Al_{0.8}As$ are 6 μm and 1.6 μm, respectively. After crystal growth, the graphite boat is cooled down to room temperature, taking about 20 min . Following this, the next crystal growth process can be started. The thickness of the epitaxial layer depends on the growth temperature and figure 3-10 shows the thickness of Be doped p-$Ga_{0.2}Al_{0.8}As$ as a function of the initial growth temperature.

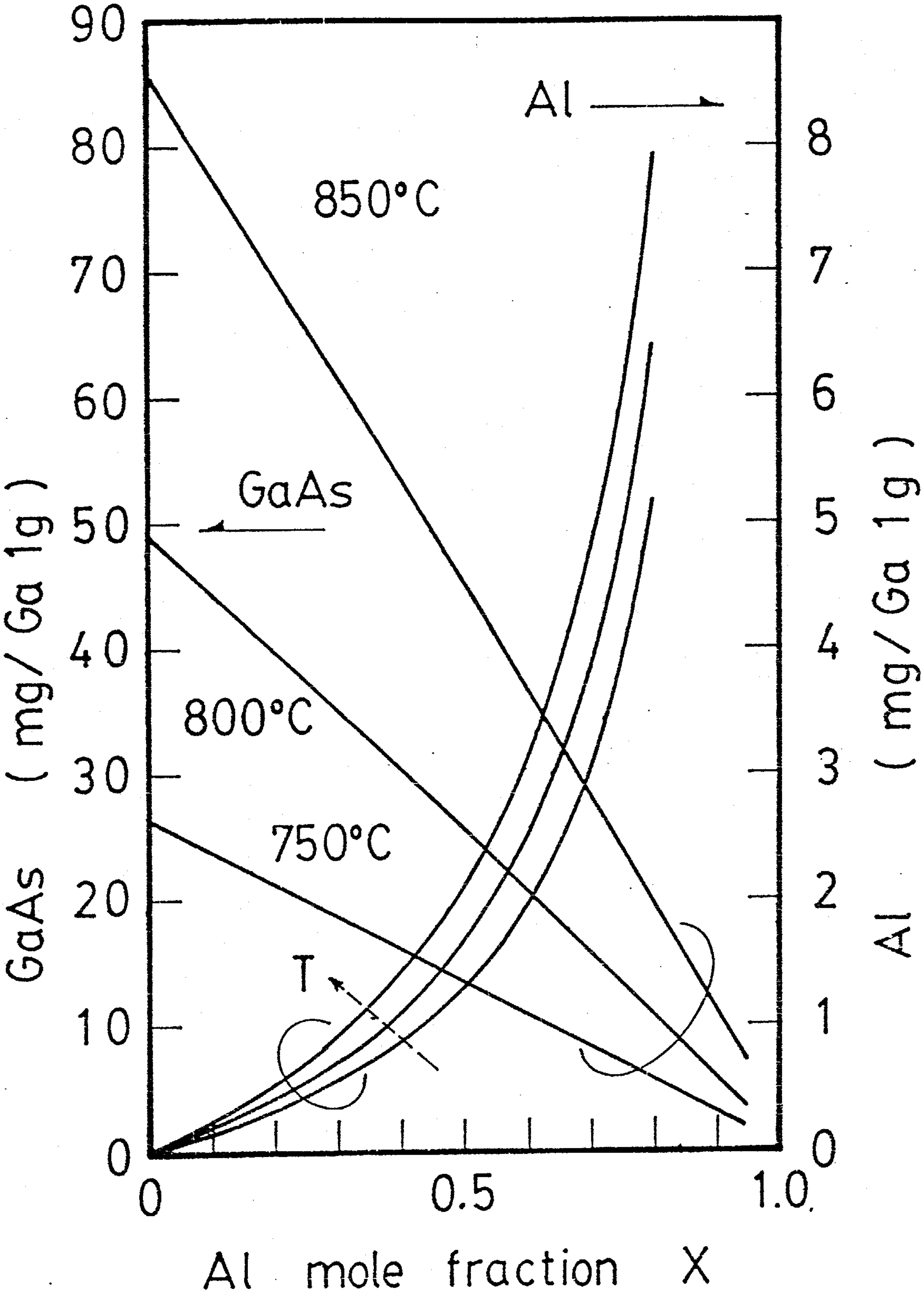

Fig. 3-8.

The weight of GaAs and Al in a saturated liquid solution of Ga-Al-As as a function of Al composition in the corresponding solid solution, obtained from the phase diagram caluculations.

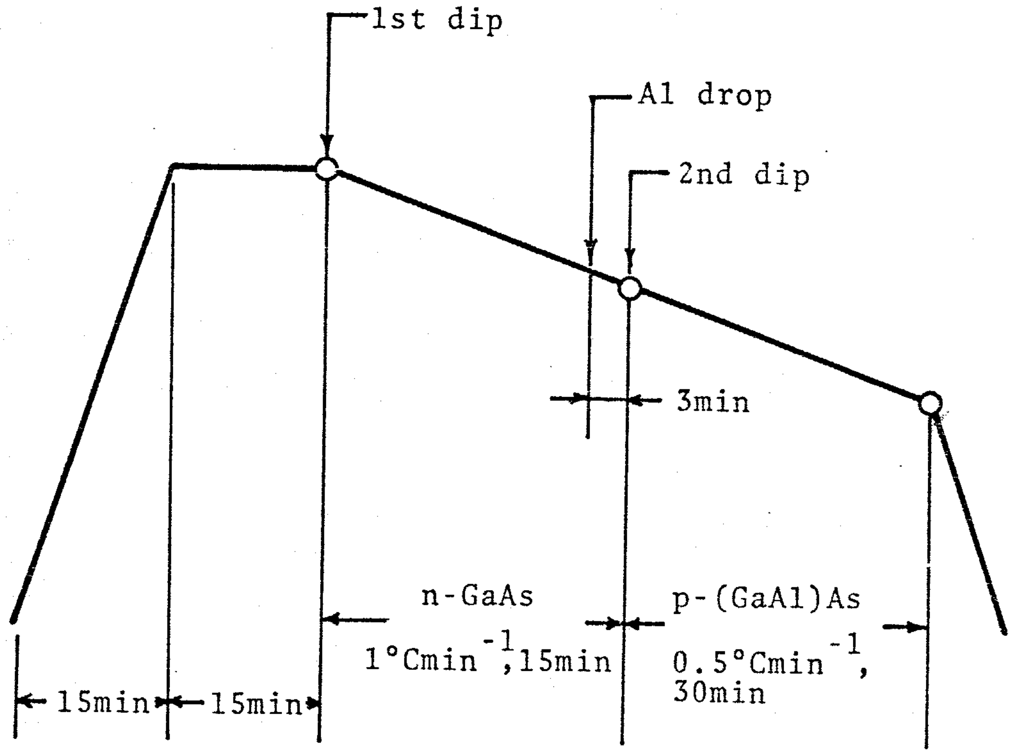

Fig. 3-9.

Typical temperature programme for the (GaAl)As/GaAs p-p-n solar cells.

Mole fraction X	Contents (mg in 1g of Ga) Al	GaAs	Dopant	Temperature T (°C)	Thickness d (μm)
0.5	4.0	50.6	8.0(Zn)	850*	5.61
0.6	6.0	43.7	7.8(Zn)	850*	3.63
0.75	8.0	30.9	4.2(Zn)	850*	2.97
0	0	33±3	25±3(Sn)	765**	6-7
0.8	6.0	6.0	0.043(Be)	750*	1.6

Table 3-2.
Weight of GaAs and Al in 1 g of Ga for several epitaxial layer temperatures and thicknesses.
*) Cooling rate; 0.5°C/min, Duration; 30min.
**) Cooling rate; 1.0°C/min, Duration; 15min.

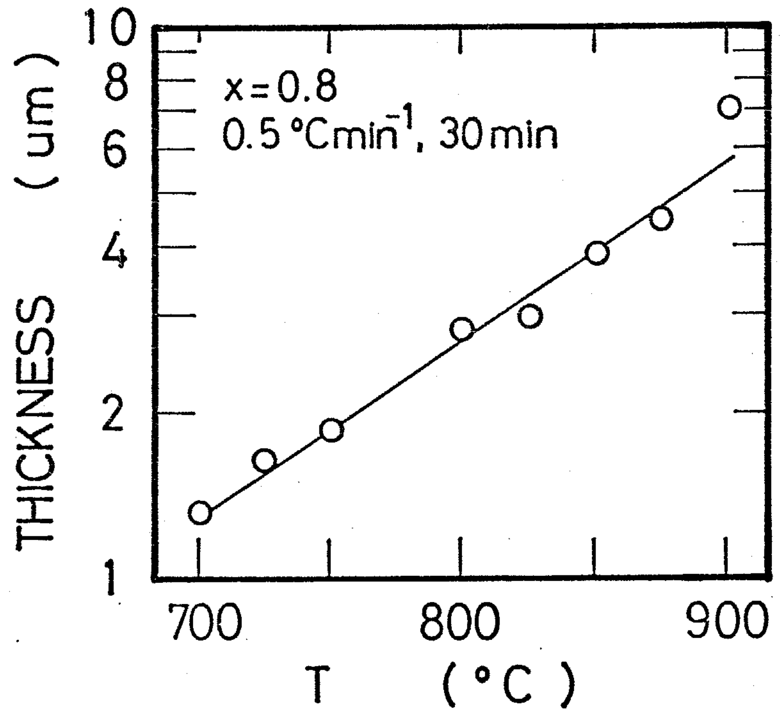

Fig. 3-10.
Thickness of $Ga_{0.2}Al_{0.8}As$ epitaxial layer .vs. initial growth temperature. The growth conditions were (1) cooling rate; 0.5°C/min, (2) duration; 30min, and (3) Be concentration; 0.043at%.

3-5. Summary.

The $Ga_{1-x}Al_xAs$ layers and (GaAl)As/GaAs heterostructures used in this work were prepared on GaAs wafers by the liquid phase epitaxy (LPE) method. The fundamentals of LPE are described in this chapter.

For epitaxial growth by LPE, theoretical phase diagram must be determined at first. The phase diagram calculation method is discussed in Sec. 3-2.

The LPE apparatus used in this work consisted of the conventional horizontal-sliding boat system. The epitaxial growth process, weights of the charge materials in the growth melt and the temperature programme, are summarized in Sec.3-4.

CHAPTER 4.

DIFFUSION OF II-COLUMN IMPURITIES INTO GaAs DURING THE LPE-GROWTH PROCESS.

4-1. Introduction.

P-type dopant diffusion during LPE growth is widely and positively utilized in (GaAl)As/GaAs heterostructure devices.

Although diffusion in the usual closed-ampoule-annealing-technique has been reported by many researchers*, diffusion during LPE growth has not been investigated to the author's knowledge and in particular there has been no reported study of II-column impurity diffusion during LPE growth. In this chapter, the diffusion of II-column impurities such as Zn and Be during LPE growth of Be or Zn doped p-$Ga_{0.2}Al_{0.8}As$ is discussed thoroughly. In Sec. 4-3, the experimental investigation of the diffusion coefficient into GaAs is described. The junction depth in the (GaAl)As/GaAs solar cells described in PART III,is controlled using these results. The results will also be utilized in the preparation of other heterostructure devices. The diffusion process is discussed in Sec. 4-4.

---

*) The diffusion coefficient obtained in the usual closed-ampoule-annealing-technique was reviewed by Yarbrough (1968) and Casey (1973b).

4-2. Features of impurity diffusion during the LPE growth process.

In this section, the main features of impurity diffusion during the LPE growth process are clarified.

Figure 4-1 shows schematically the epitaxial grwoth process for Be (or Zn) doped p-$Ga_{1-x}Al_xAs$. Epitaxial growth starts when the substrate is brought into contact with the melt (Fig. 4-1a). The melt consists of Ga, Al, As, and Be (or Zn). During the epitaxial growth, beryllium (or zinc) is diffused into the n-GaAs substrate to form the p-GaAs region. Consequently, a GaAs p-n structure with a p-(GaAl)As layer is formed by the growth of p-(GaAl)As.

For the preparation of (GaAl)As/GaAs heterostructure solar cell, the Al composition in the surface p-$Ga_{1-x}Al_xAs$ layer is fixed at 0.8 throughout this chapter.

4-3. Diffusion of II-column impurities into GaAs during the LPE growth process of p-$Ga_{0.2}Al_{0.8}As$.

4-3-1. Diffusion of beryllium.

The epitaxial $Ga_{0.2}Al_{0.8}As$ layers were grown on undoped n-GaAs substrates, whose carrier concentration was about $10^{16}cm^{-3}$. The growth conditions were as follows;

1. intitial growth temperature T_i : 700-900°C,
2. cooling rate α : 0-0.5°C·min^{-1},
3. growth duration t : 10-120 min ,

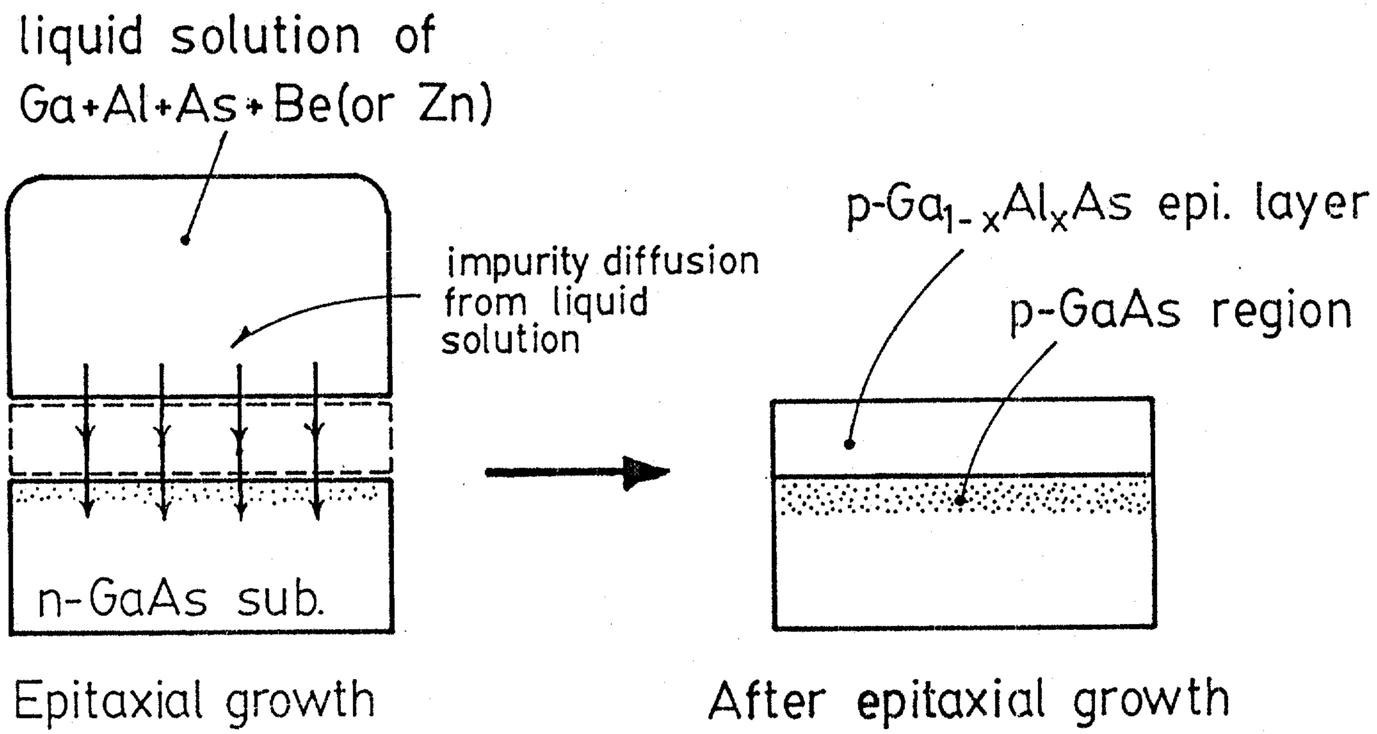

Fig. 4-1.
LPE growth of p-$Ga_{1-x}Al_xAs$ onto an n-GaAs substrate. The p-GaAs region is formed by Be (or Zn) diffusion during the growth process of the p-$Ga_{1-x}Al_xAs$ epitaxial layer. Consequently, the GaAs p-n structure is formed in the n-GaAs substrate. The Al composition of the $Ga_{1-x}Al_xAs$ epitaxial layer is fixed at 0.8 throughout this chapter.

and 4. beryllium concentration in the growth melt C_{Be}: 0.01-0.3 at% .

The room temperature Hall mobility, resistivity, and carrier concentration of the p-GaAs region for the following growth conditions $T_i = 750°C$, $\alpha = 0.5°C \cdot min^{-1}$, and $C_{Be} = 0.043$ at% , were $137 cm^2V^{-1}s^{-1}$, $0.031\Omega \cdot cm$, and $1.5x10^{18} cm^{-3}$, respectively. These properties are typical of the (GaAl)As/GaAs solar cells described in PART III.

The thickness of the p-GaAs region was revealed by staining a cleaved cross-section with HF + HNO_3 (∿50 : 1) for 10-20sec and then measured with an optical microscope . A solution of 1 N-NaOH($50cm^3$) + H_2O_2($3.7cm^3$) was used for the measurement of the thinner p-GaAs region. The etching rate of this solution is very low ($3000Å \cdot min^{-1}$ at 20°C), and consequently the n-GaAs substrate is accurately exposed. The surface p-(GaAl)As layer was removed by HF before the measurement of the thickness of p-GaAs region. The breakdown voltage between two tungsten needles set up on the surface was measured to determine whether the surface was p- or n-type. The breakdown voltage V_b of the p-GaAs region is less than 5 V , whereas V_b for the n-GaAs substrate is 10-20V. Thus, the change in V_b between p-GaAs and n-GaAs makes it easier to measure the thickness of the p-GaAs region.

For constant cooling rate, growth duration, and Be concentration, the thickness of the Be-diffused p-GaAs region was found to increase with increasing temperature. Figure 4-2 shows the thickness of the p-GaAs region as a function of the growth temperature for a cooling rate of

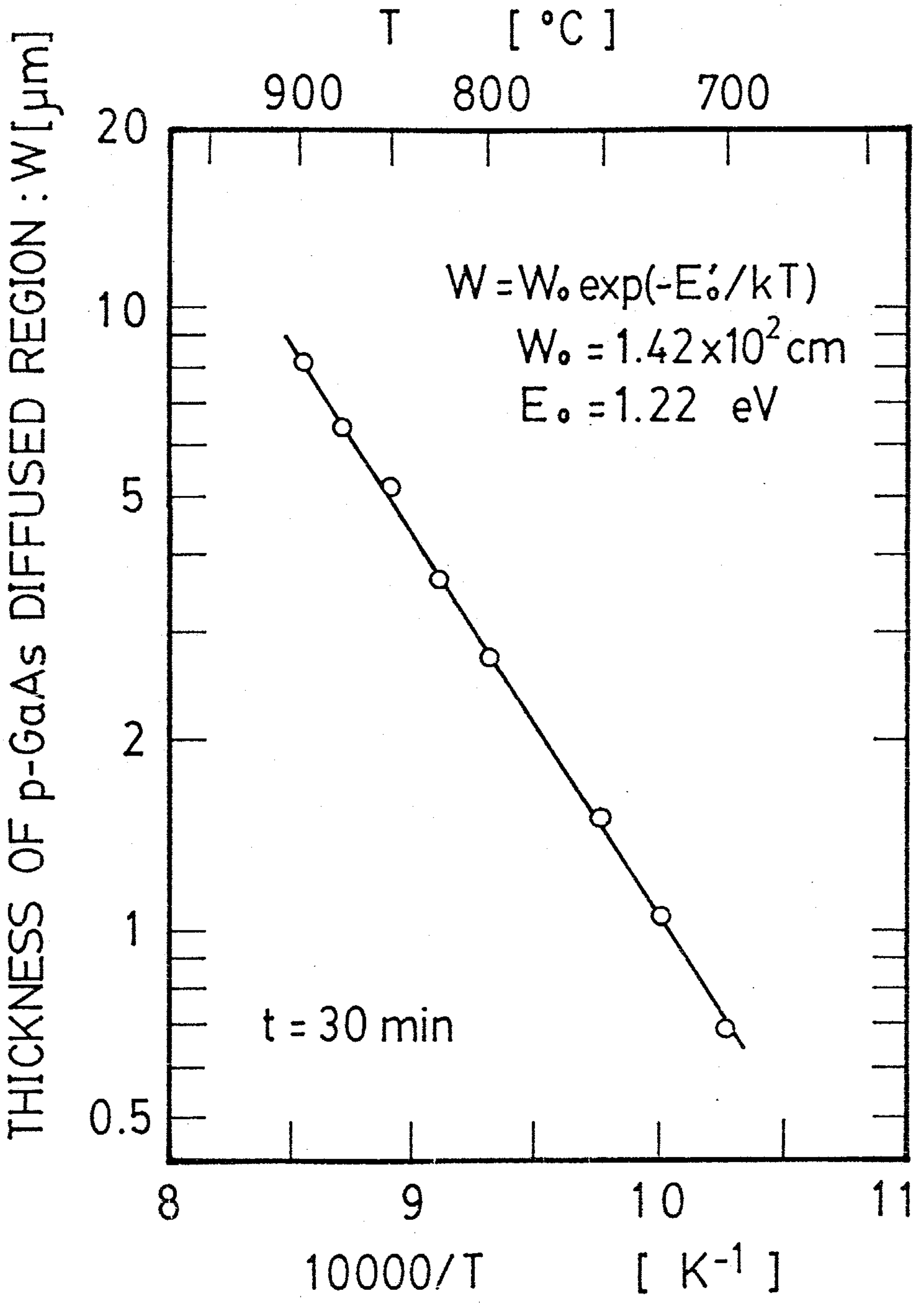

Fig. 4-2.

Temperature dependence of the thickness of the Be diffused p-GaAs region. The growth conditions were (1) cooling rate; 0.5°C/min, (2) growth duration; 30 min, and (3) Be concentration in the growth melt; 0.043at%.

0.5°C min, growth duration of 30 min , and Be concentration of 0.043 at%. The temperature dependence of the thickness takes the form

$$W = W_o \cdot \exp(-E_o'/kT), \qquad (4\text{-}1)$$

where $W_o = 1.42 \times 10^2$ cm and $E_o' = 1.22$eV.

With the other growth parameters held constant, the thickness of the p-GaAs region also increases with incresing growth duration 't', i.e., diffusion time. Figure 4-3 shows the thickness of the p-GaAs region as a function of the growth duration at a temperature of 750°C. For a given Be concentration in the growth melt, the thickness of the p-GaAs region was found to be proportional to the square root of the diffusion time and to satisfy the empirical relation,

$$W\ (\mu m) = 0.33 \cdot t(\min)^{1/2} - 0.45. \qquad (4\text{-}2)$$

In the evaluation of the diffusion coefficient, it is usual to assume the equation,

$$W = (D_w \cdot t)^{1/2}, \qquad (4\text{-}3)$$

where W is the thickness of the p-GaAs region, t is the diffusion time, and D_w is the diffusion coefficient. The subscript 'w' indicates that the diffusion coefficient is determined from the thickness. Using this relation and the results in Fig. 4-2, D_w is represented by

$$D_w = D_{wo} \exp(-E_{wo}/kT), \qquad (4\text{-}4)$$

where $D_{wo} = 11.2 \text{cm}^2 \text{s}^{-1}$ and $E_{wo} = 2.43$eV.

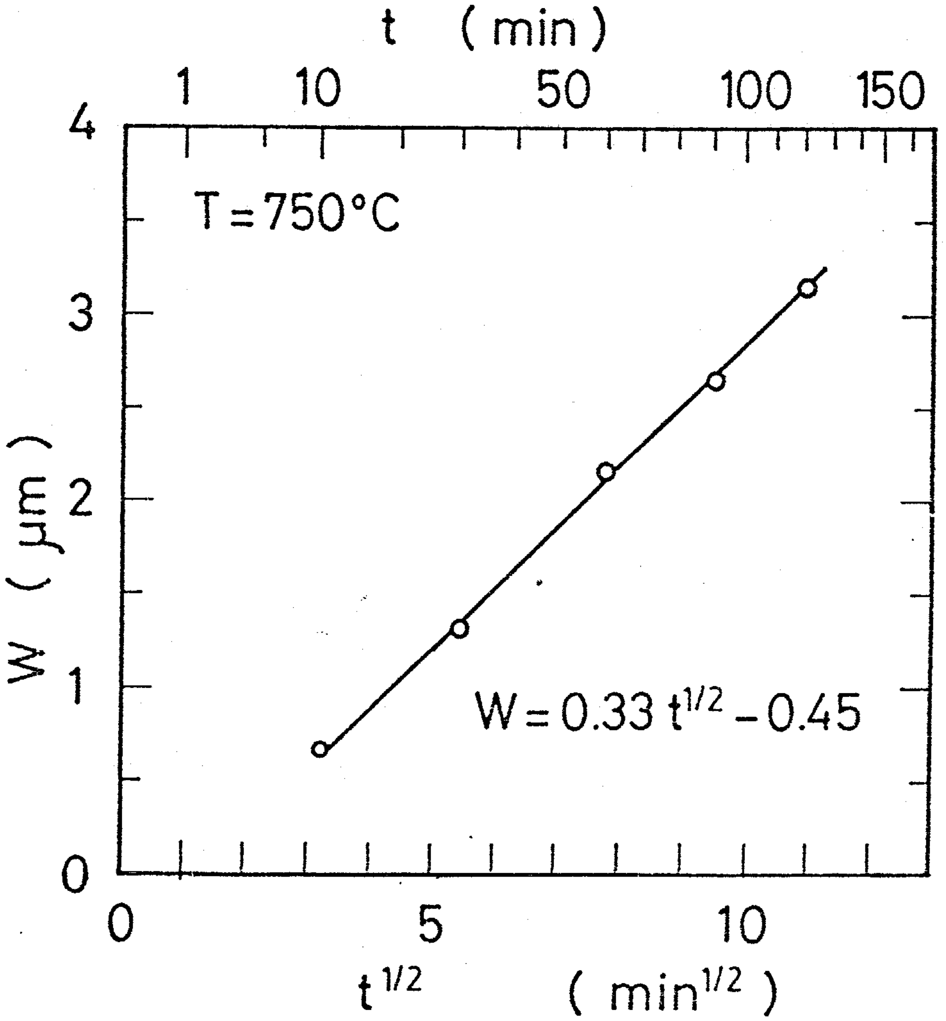

Fig. 4-3.

Time dependence of the thickness of the p-GaAs region. The growth conditions were (1) growth temperature; 750°C, (2) cooling rate; 0°Cmin^{-1}, and (3) Be concentration in the growth melt; 0.043at%.

However, the accurate value of the diffusion coefficient must be determined from the carrier profile in the p-GaAs region. Consequently, the profile of the free-carrier concentration was determined as follows:

Following removal of a few thousand angstroms of the p-GaAs layer using the slow etchant ($H_2O + NaOH + H_2O_2$), resistivity, Hall mobility, and free-carrier concentration were measured by the van der Pauw method. By repeating these measurements, the free-carrier concentration of the removed p-GaAs region can be calculated from the change of resistivity, Hall mobility, and free-carrier concentration as a function of the distance from the surface. Details of this calculation are discussed in Sec. 6-2-2.

Figure 4-4 shows the profiles of the free-carrier concentration in the p-GaAs region as a function of the distance from the surface. If the diffusion process can be treated as the diffusion in a semi-infinite medium, the carrier profile is given by

$$p(x) = p_{sur} \cdot \mathrm{erfc}\{x/2(D_p t)^{1/2}\}, \qquad (4\text{-}5)$$

where p_{sur} is the surface free-carrier concentration, x the distance from the surface, t the diffusion time, and D_p the diffusion coefficient. The subscript 'p' indicates that D_p is the diffusion coefficient obtained from the free-carrier profile. Fitting the profile to the error-function complement (Eq. 4-5), the diffusion coefficient D_p can be determined. The values obtained are shown in Fig. 4-4. Figure 4-5 shows the free carrier concentration profiles for two samples

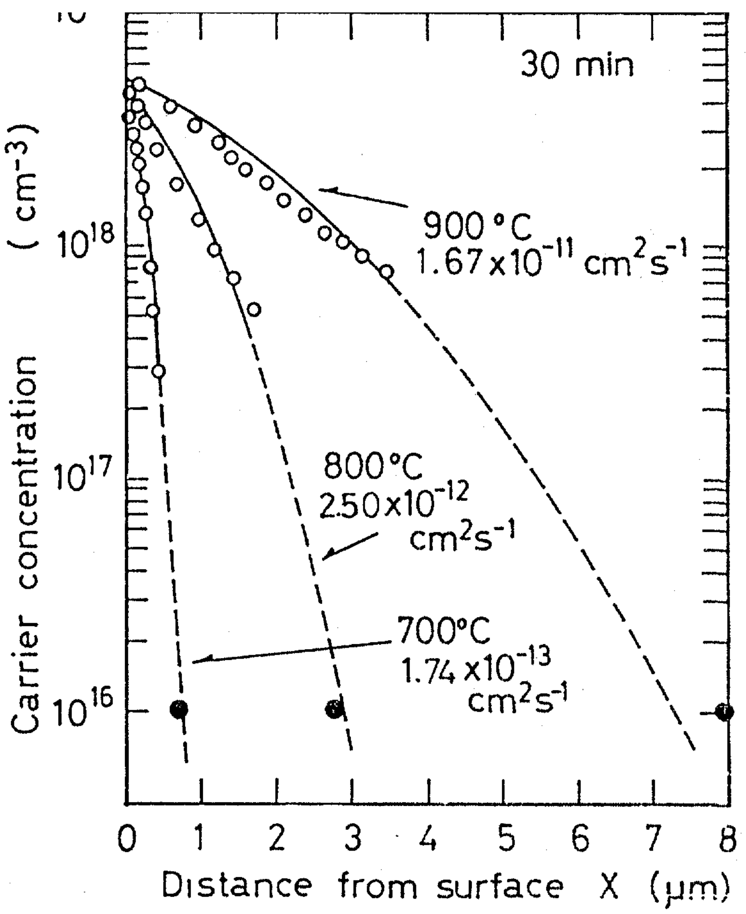

Fig. 4-4.
The free-carrier density profiles in the Be diffused p-GaAs region with growth temperature as a parameter. The abscissa is the distance from the p-GaAs surface.

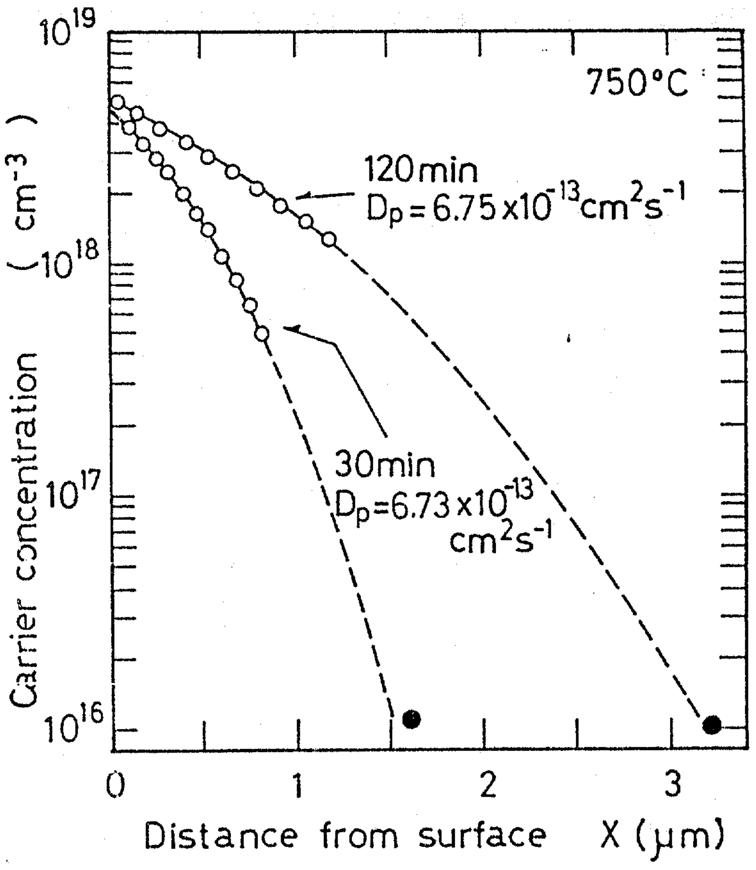

Fig. 4-5.
The free-carrier density profiles in the Be diffused p-GaAs region with growth duration as a parameter. The abscissa is the distance from the p-GaAs surface.

which have different diffusion times of 30 min and 120 min. The diffusion coefficient for these two samples is the same, which is coincident with the results shown in Fig. 4-3. The black dots in Fig. 4-4 and Fig. 4-5 indicate the thickness of the p-GaAs region measured by the above mentioned techniques (Staining-etching and observation using the optical microscope, or slow etchant method). Since the carrier concentration of undoped n-GaAs wafer is about $1\times10^{16}cm^{-3}$, these black dots are plotted at the level of $10^{16}cm^{-3}$. The extrapolations of the error-function complement cross the black dots in these figures. These results confirm that the diffusion process can be treated as the diffusion in the semi-infinite medium.

Figure 4-6 shows the diffusion coefficients which were obtained from (1) the thickness (Fig. 4-2 and Eq. 4-3) and (2) the carrier profile (Fig. 4-4 and Eq. 4-5).

N. B. Although these two lines were obtained from the same samples, there exists an apparent discrepancy in the absolute value. This discrepancy is caused by an overestimation of the diffusion coefficients from the thickness. The relation $W = (D_w t)^{1/2}$ in Eq. 4-2 assumed a profile which is shown in as a broken curve in Fig. 4-7. However, the correct profile is indicated by the solid curve in this figure, and the p-n junction is lying at the $10^{16}cm^{-3}$ level. If the surface free-carrier concentration was about $4\times10^{18}cm^{-3}$, the relation $D_w = 17.1\times D_p$ applied as seen Fig. 4-7. From Fig. 4-6, D_{wo} and D_{po} are $11.2cm^2s^{-1}$ and $0.655cm^2s^{-1}$, respectively. The ratio D_{wo}/D_{po} is 17.1, which is in agreement with the above.

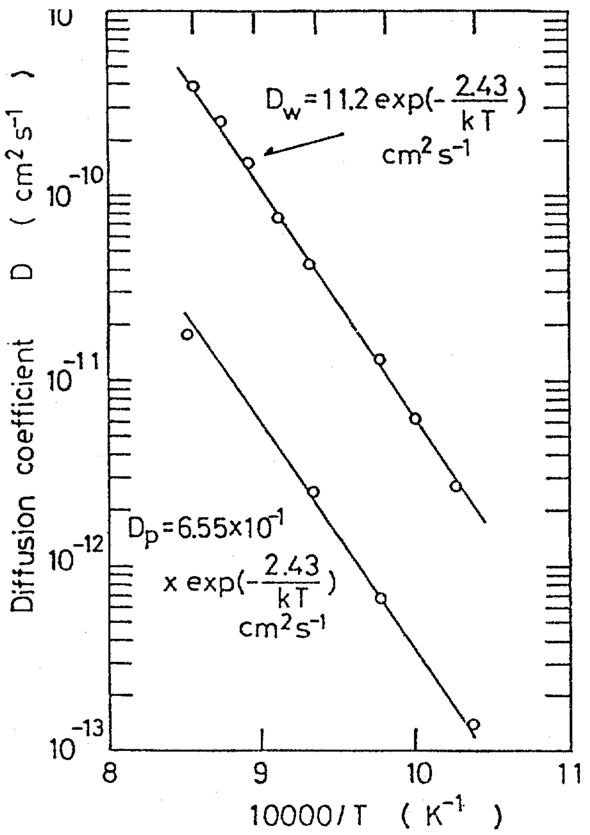

Fig. 4-6.

The diffusion coefficients of Be as a function of growth temperature. Detailed growth conditions were the same as in Fig. 4-2. The subscripts 'w' and 'p' means that the diffusion coefficients were determined from the thicknesses and the carrier profiles, respectively (see text).

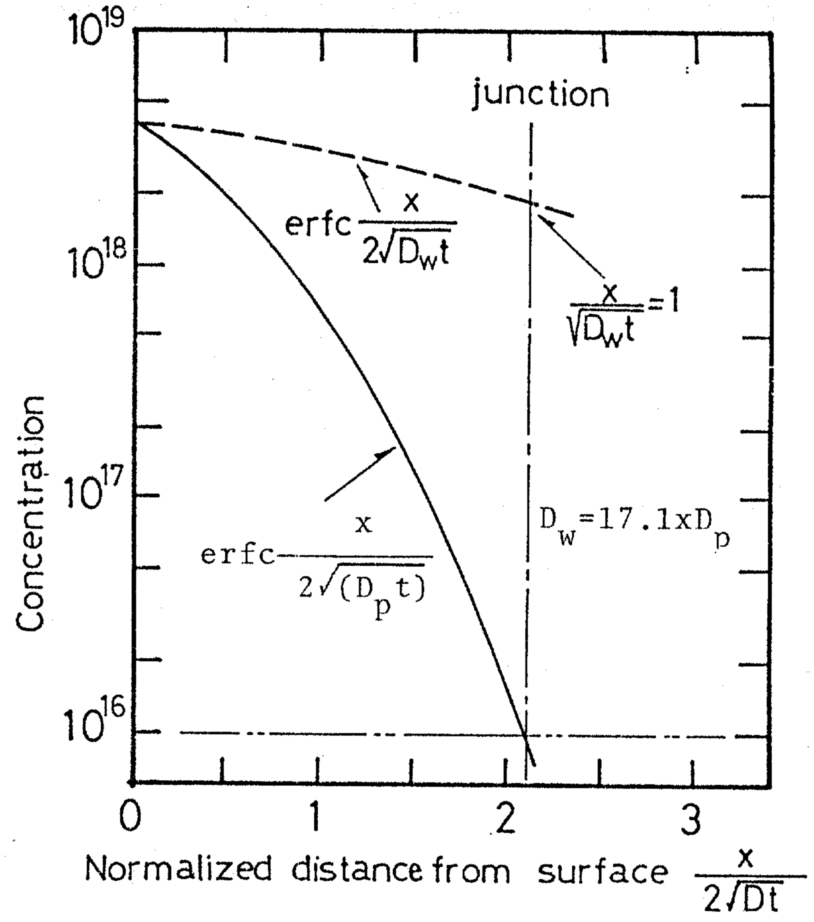

Fig. 4-7.

The discrepancy between D_w and D_p (see text).

Hence, the apparent difference between D_p and D_w is not real and is explained by the above discussion. Here, it should be pointed out that the diffusion coefficient must be determined from the carrier profile, because there is an overestimation of the diffusion coefficient from the relation $W = (Dt)^{1/2}$.

4-3-2. Diffusion of zinc.

Figure 4-8 shows the temperature dependence of the Zn diffusion coefficient which was determined from the carrier profiles. The diffusion coefficient of Be is about ten time times higher than that of Zn in the temparature range above 750°C as shown in this figure. Table 4-1 summarized the diffusion coefficients (D_w and D_p) for Be and Zn.

If $p_{sur} < 6\text{x}10^{18}\text{cm}^{-3}$, $D = D_o \cdot \exp(-E_o/kT)$.

For Be : $D_o = 11.2\ \text{cm}\cdot\text{sec}^{-1}$ and $E_o = 2.43$ eV.

For Zn : $D_o = 1.31\text{x}10^{-5}\text{cm}\cdot\text{sec}^{-1}$ and $E_o = 1.49$ eV.

Table 4-1.

Diffusion coefficients of Be and Zn during LPE growth process, which were determined from the carrier profiles. P_{sur} is the surface free-carrier concentration (see Sec. 4-3).

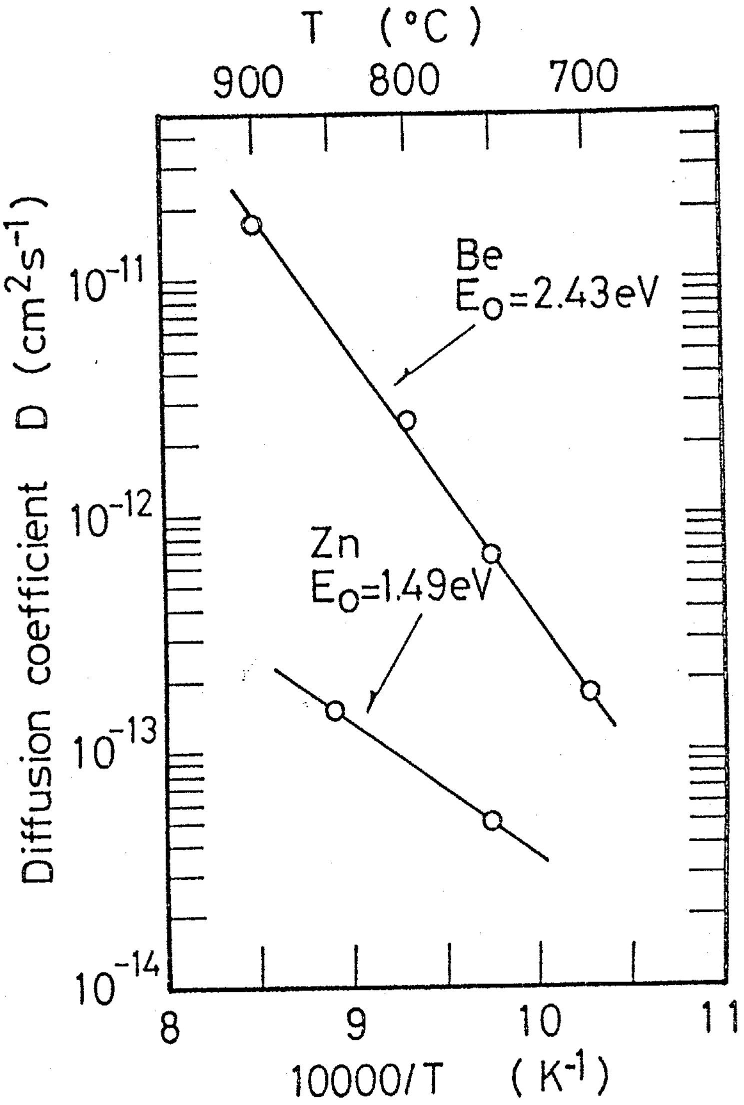

Fig. 4-8.

Diffusion coefficients of Zn and Be as function of growth temperature (They were determined from carrier profiles.).

4-4. Discussion.

4-4-1. Diffusion of Be into $Ga_{1-x}Al_xAs$.

The impurity diffusion described in this chapter occured simultaneously with the epitaxial growth of p-$Ga_{0.2}Al_{0.8}As$ as shown in Fig. 4-1. The effect of this epitaxial layer on the impurity diffusion is discussed in this section.

Figure 4-9 shows the thickness of p-$Ga_{1-y}Al_yAs$ formed by Be diffusion during the LPE growth of p-$Ga_{0.2}Al_{0.8}As$. The thickness of the p-$Ga_{1-y}Al_yAs$ diffused region increases linearly with increasing 'y' values. In other words, the diffusion coefficient of $Ga_{1-y}Al_yAs$ increases with increasing 'y'.* The extrapolated thickness of the p-$Ga_{0.2}Al_{0.8}As$ region is greater than ten microns. Thus, it is natural to expect that this diffusion occurs directly from the Ga + Al + As + Be liquid solution, i.e., the p-$Ga_{0.2}Al_{0.8}As$ epitaxial layer can be treated as a transparent film for the impurity diffusion during LPE growth, since the diffusion coefficient of Be in $Ga_{0.2}Al_{0.8}As$ is much larger (about 50 times according to the extrapolation of Fig. 4-9) than that in GaAs.

*) An increased diffusion coefficient for Zn in $Ga_{1-x}Al_xAs$ (produced by the usual closed-ampoule-annealing-technique) was reported by Flat(1977) and Lee(1978). Lee(1978) suggested that the increased diffusion coefficient was due to a reduction in the lattice vacancies as x increased because of the higher binding energy between Al and As than that between Ga and As.

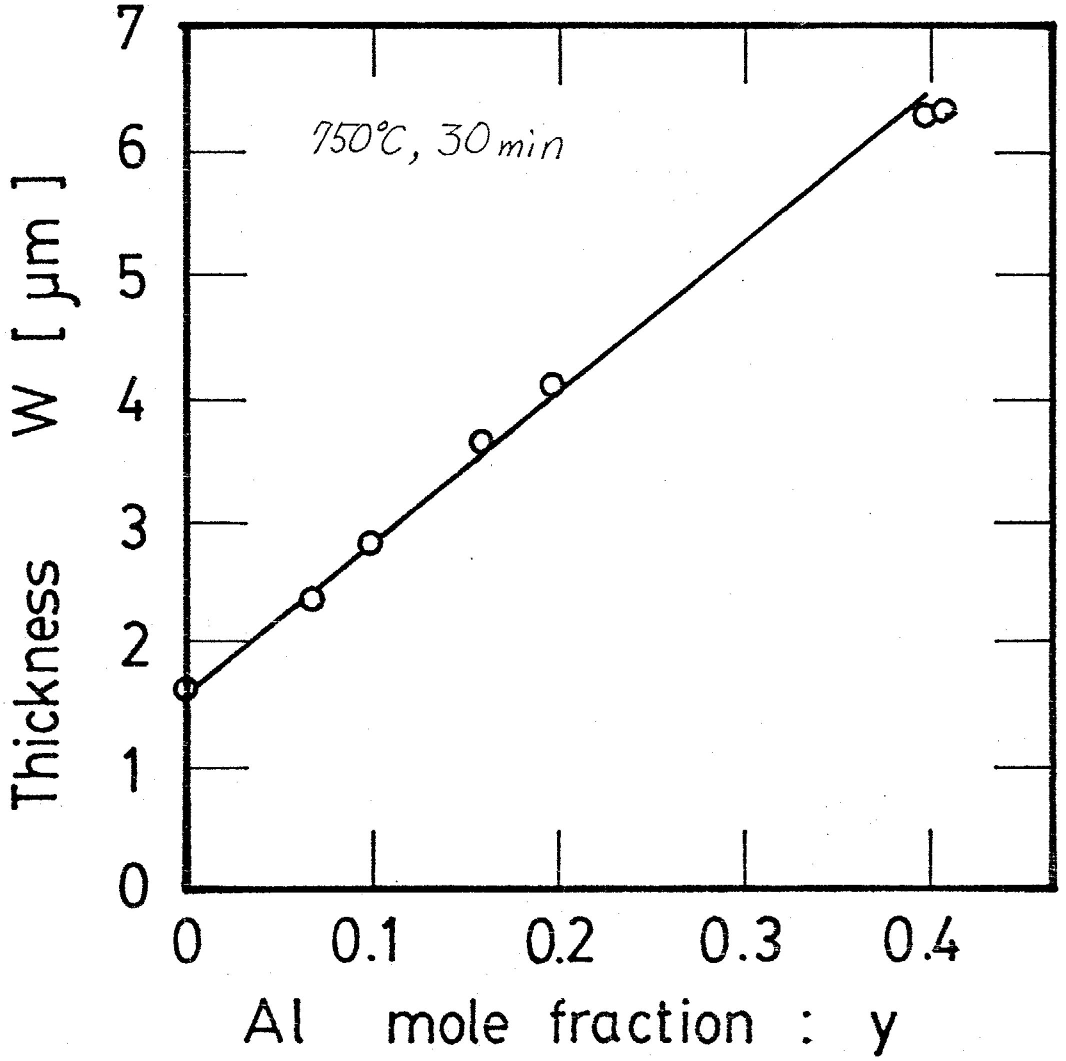

Fig. 4-9.

The thickness of the p-$Ga_{1-y}Al_yAs$ diffused region as a function of the Al composition 'y'. The p-$Ga_{1-y}Al_yAs$ region was formed in the epitaxial $Ga_{1-y}Al_yAs$ layer on a GaAs substrate by Be diffusion during LPE growth process of Be doped p-$Ga_{0.2}Al_{0.8}As$. The growth conditions for Be doped p-$Ga_{0.2}Al_{0.8}As$ were (1) $T_i = 750°C$, (2) $\alpha = 0.5°C/min$, (3) $t = 30$ min , and (4) $C_{Be} \sim 0.04at\%$.

4-4-2. The relation between the diffusion coefficient and the surface free-carrier concentration.

The error-function complement is assumed to represented the profiles of the free-carrier concentration in the previous section. In Fig. 4-4 and Fig. 4-5, the thickness of the p-GaAs region corresponds to the point of intersection of the error-function complement and the concentration value of $10^{16}\mathrm{cm}^{-3}$. If the profiles were represented by the error-function complement, the following relation between W and p_{sur} would be satisfied,

$$N_d/p_{sur} = \mathrm{erfc}\{W/2(Dt)^{1/2}\}, \tag{4-6}$$

where W : the thickness of p-GaAs region,

p_{sur}: the free-carrier concentration at the p-GaAs surface,

N_d : the free-carrier concentration in the undoped n-GaAs substrate.

Figure 4-10 shows the relation between N_d/p_{sur} and W for Be diffusion at 750°C for 30min. The broken line shows the error-function complement (Eq. 4-6) with $D=6.6\mathrm{cm}^2\mathrm{sec}^{-1}$ and 30min. The open circles represent the experimentally observed values. The experimentally observed values with $p_{sur}>6\times10^{18}\mathrm{cm}^{-3}$ apparently deviate from the broken line, while those with $p_{sur}<6\times10^{18}\mathrm{cm}^{-3}$ agree with the broken line. Figure 4-11 shows the thickness of the p-GaAs region formed by Be diffusion as a function of Be concentraiton in a growth melt. The thickness increases rapidly, for values of C_{Be} above 6×10^{-1}at%. This result quantitatively agrees with that shown in Fig. 4-10 .

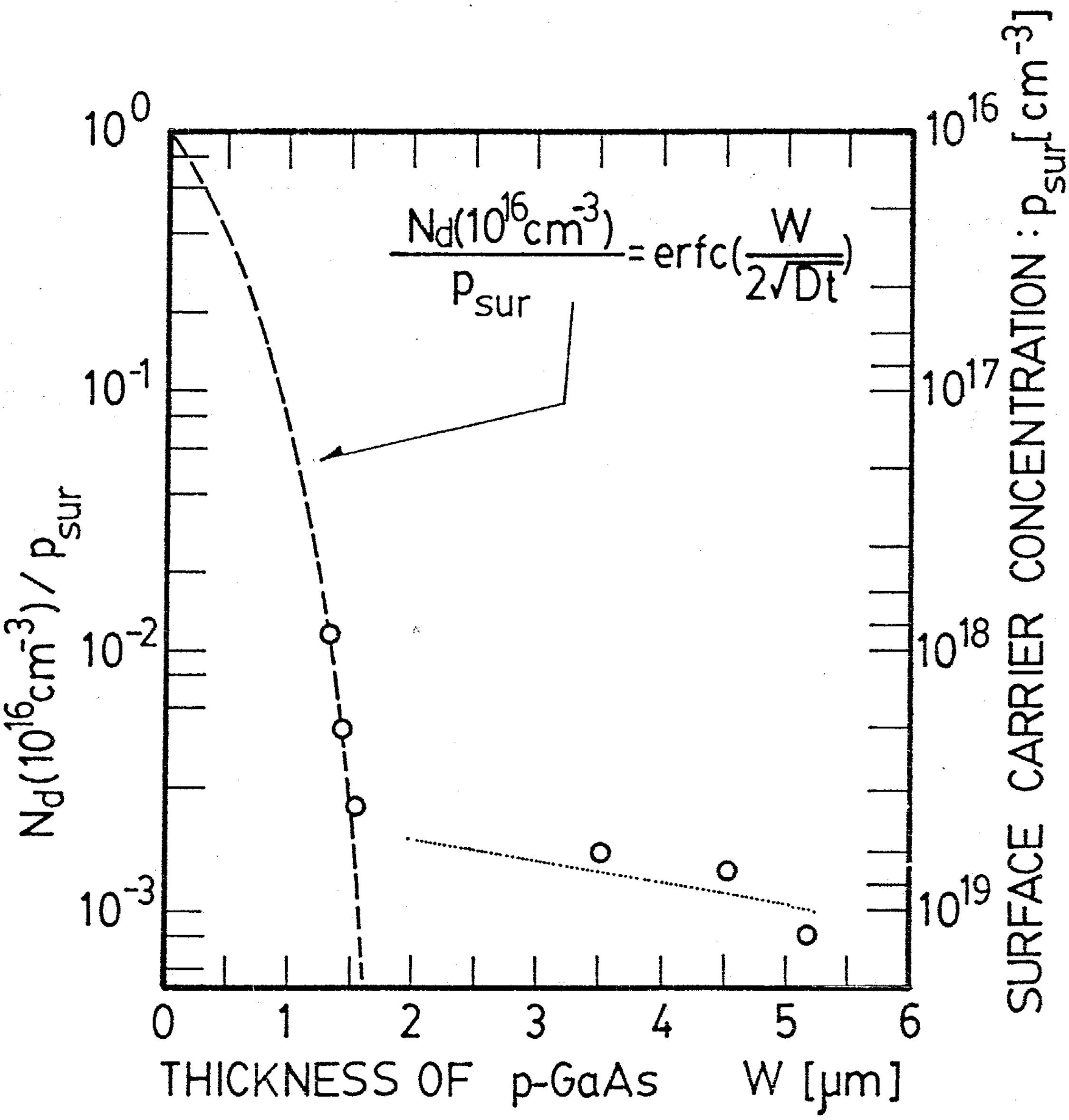

Fig. 4-10.

The relation between (N_d/p_{sur}) and the thickness of p-GaAs diffused region (see text). The growth conditions were the same as those applying in Fig. 4-11.

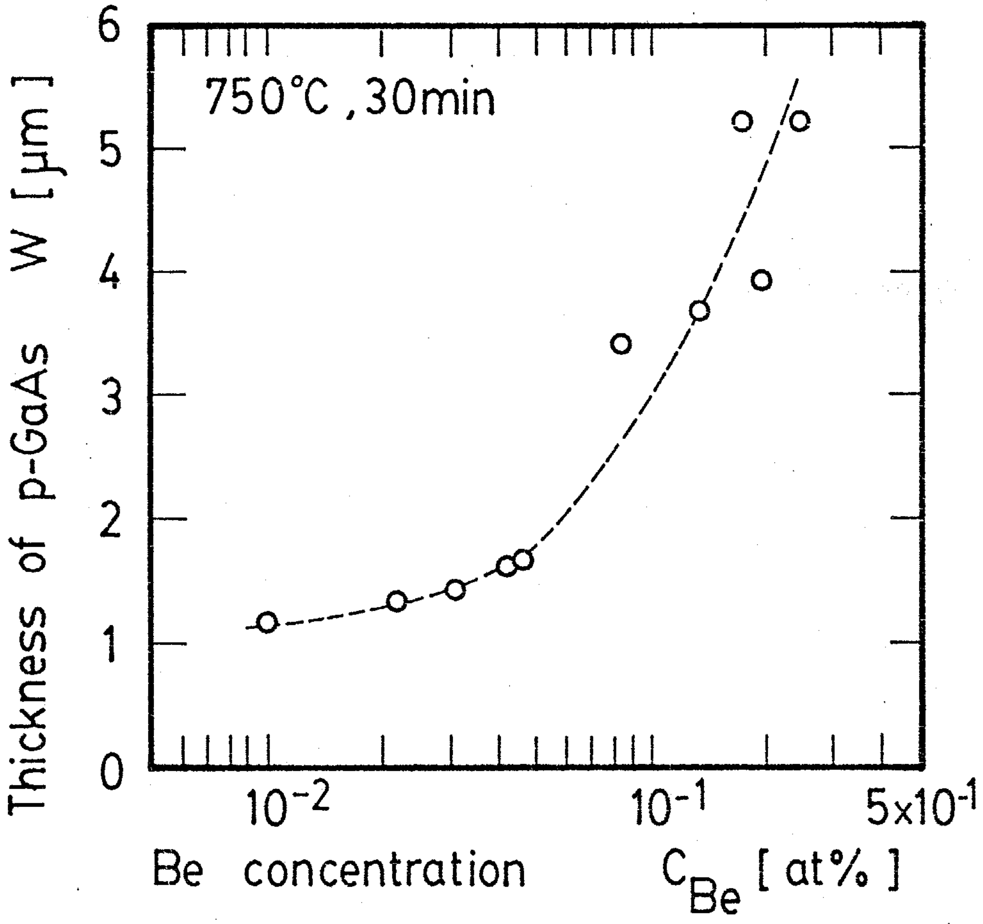

Fig. 4-11.

The thickness of the p-GaAs diffused region as a function of the Be concentration in the growth melt. The growth conditions for Be doped p-$Ga_{0.2}Al_{0.8}As$ were (1) T_i=750°C, (2) α=0.5°$Cmin^{-1}$, and (3) t=30min, respectively.

These results can be summarized as follows:

1. (1) If $p_{sur} < 6\times10^{18}\text{cm}^{-3}$ (the results in Sec. 4-3 satisfy this condition), Be diffusion can be explained by a constant diffusion coefficient.
2. (2) If $p_{sur} > 6\times10^{18}\text{cm}^{-3}$, Be diffusion can not be represented by a constant diffusion coefficient, and explanation involves the concentration dependent diffusion process, i.e., the so-called interstitial-substitutional diffusion process (Casey, 1973b; Weisberg, 1963).

Fortunately, for device preparation the doping level of p-GaAs in p-n junctions is generally in the region $(1\text{-}2)\times10^{18}\text{cm}^{-3}$. Hence, it is not necessary to take account of the more complex diffusion process (i.e., the interstitial-substitutional model) when preparing p-n junctions by the diffusion process during LPE growth.

4-5. Summary and conclusion .

Although p-type impurity diffusion during the LPE growth process is widely used for (GaAl)As/GaAs heterostructure devices, there have no previous studies of the process. In this chapter, the diffusion of Be and Zn, which occurs simultaneously with the LPE growth of p-type $Ga_{0.2}Al_{0.8}As$, was discussed.

It was established that the diffusion must be evaluated using diffusion coefficients obtained from carrier profiles, because the diffusion coefficients obtained from the usual relation $W = (Dt)^{1/2}$ are larger than the correct values.

Comparing the diffusion coefficients of Be and Zn, it is shown that the diffusion coefficient of Be is about ten times higher than that for Zn in the temperature range above 750°C.

For Be diffusion, the following results and criteria apply; If the surface free-carrier concentration is lower than about $6\mathrm{x}10^{18}\mathrm{cm}^{-3}$, the treatement of diffusion is simple, i.e., diffusion can be expressed as diffusion from a semi-infinite source and the free-carrier concentration profiles are represented by the error-function complements. With regard to temperature dependence, the diffusion coefficient takes the form

$$D = D_o \exp(-E_o/kT),$$

where $D_o = 0.655\mathrm{cm}^2/\mathrm{sec}$ and $E_o = 2.43\mathrm{eV}$ for Be diffusion in the temeprature range from 700°C to 900°C. The diffusion coefficient is constant with respect to diffusion time, i.e., the thickness of the p-GaAs region increases linearly with the square root of the diffusion time.

If the surface free-carrier concentration is higher than about $6 \times 10^{18} cm^{-3}$, the anomalous diffusion behaviour was observed, i.e., the diffusion can no longer represented by a constant diffusion coefficient and a concentration- dependent diffusion process is necessary to explain diffusion.

CHAPTER 5.

ANALYSIS OF HOLE MOBILITY IN III-V COMPOUND SEMICONDUCTORS.

5-1. Introduction.

Carrier mobility has been among the most important indices in studying, characterizing, and assessing semiconducting materials. The analysis of hole mobilities in III-V binary compounds is well established and account for the measured mobility data. However, there has been little analytical work on the hole mobility of III-V ternary alloys.

In this work, it was recognized firstly that previous analytical expressions related to the drift mobility whereas the experimentally observed values related to the Hall mobility. In Sec. 5-2, expressions, which enables the drift and Hall mobilities to be calculated separately, are proposed (MTBT model). These are obtained by the expanding the conventional two-band transport model. In ternary (and quaternary) alloys, the so-called alloy scattering exists. Consequently, this scattering is considered in the calculations.

In Sec. 5-3, material parameters for ternary alloys are discussed. Practical calculations using formulae presented in Sec. 5-2, are carried out for p-$Ga_{1-x}Al_xAs$.
These calculations show that the room temperature Hall mobility is strongly affected by the exixtense of alloy scattering.

5-2. Formularization of the Hall mobility.

5-2-1. Modified two-band transport (MTBT) model.

As discussed in Sec. 2-1-3, the valence band is characterized by heavy hole (v_1), light hole (v_2), and split-off (v_3) bands. Each band is doubly degenerated because of the spin degeneracy. The valence band structure is schematically shown in Fig. 5-1. Since the split-off band is separated by an energy Δ_o ($\Delta_o = 0.34$eV for GaAs), it may be ignored for the hole transport, and it is usual to assume that only holes in the v_1 and v_2 bands can contribute to the transport properties. Furthermore, these two band (v_1 and v_2) are usually characterized by concentrations p_1 and p_2, scalar effective masses m_1 and m_2, and corresponding drift mobilities μ_1 and μ_2, where the subscripts '1' and '2' indicate that each values is for the heavy hole (v_1) and light hole (v_2) bands, respectively. This two-band model has been successfully employed to explain the lattice mobility in some III-V binary compounds (Wiley, 1970; Neumann, 1978) and it

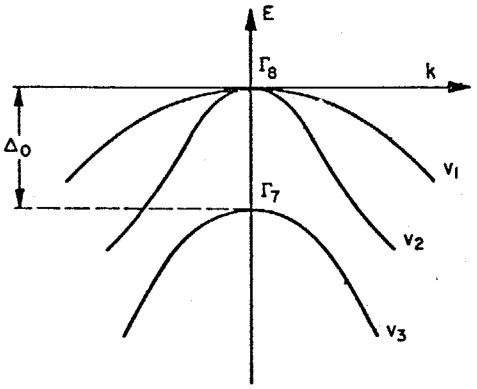

Fig. 5-1.

Features of the energy band structure relevant to hole transport.

also plays a fundamental part in the MTBT model.

Using the MTBT model, the total drift and Hall mobilities were derived as follows:

(1) The drift and Hall mobilities corresponding to each scattering mechanism were expressed using the appropriate heavy hole drift mobility.

(2) The total drift and Hall mobilties were derived using Matthiessen's rule.

Details of derivations:

——— MTBT (Modified Two-Band Transport) model ———

The conductivity σ^i, Hall coefficient R^i, and Hall mobility μ_H^i for each scattering mechanism are given by (Neumann, 1978)

$$\sigma^i = \sigma_1^i + \sigma_2^i = e(p_1\mu_1^i + p_2\mu_2^i) = ep\mu_D^i , \qquad (5\text{-}1)$$

$$R^i = \frac{1}{(\sigma^i)^2} \{R_j^i(\sigma_1^i)^2 + R_j^i(\sigma_2^i)^2\} , \qquad (5\text{-}2)$$

$$\mu_H^i = \sigma^i \cdot R^i , \qquad (5\text{-}3)$$

where

'1' and '2' : the lower subscripts '1' and '2' indicate heavy and light holes, respectively,

'i' : the superscript 'i' indicates each of the scattering mechanism,

p : $p = p_1 + p_2$, (5-4)

R_j^i (j=1,2) : corresponding Hall coefficient due to heavy (j=1) and light (j=2) holes.

R_j^i (j=1,2) can be written as

$$R_j^i = \frac{1}{ep_j} \cdot \frac{<(\tau_j^i)^2>}{<\tau_j^i>^2} \quad , (j=1,2) \qquad (5\text{-}5)$$

where τ_j^i is the corresponding relaxation times.

Equations 5-1 to 5-3 can be reduced to

$$\mu_D^i = f_D^i \cdot \mu_1^i \quad , \qquad (5\text{-}6)$$

$$\mu_H^i = f_H^i \cdot \mu_1^i \quad , \qquad (5\text{-}7)$$

$$R^i = (1/ep) \cdot (\mu_H^i/\mu_D^i), \qquad (5\text{-}8)$$

$$f_D^i = \frac{c^i + r^{3/2}}{1 + r^{3/2}} \quad , \qquad (5\text{-}9)$$

and
$$f_H^i = \frac{\beta(c^i)^2 + r^{3/2}}{c^i + r^{3/2}} \cdot \alpha_1^i \quad , \qquad (5\text{-}10)$$

where

μ_1^i : the heavy hole <u>drift</u> mobility due to the scattering mechanism 'i',

$$r = m_1/m_2 \quad , \qquad (5\text{-}11)$$

$$c^i = \mu_2^i/\mu_1^i \quad , \qquad (5\text{-}12)$$

$$\beta^i = \alpha_2^i/\alpha_1^i \quad , \qquad (5\text{-}13)$$

nd
$$\alpha_j^i = <(\tau_j^i)^2>/<\tau_j^i>^2 \qquad (j = 1,2) \qquad (5\text{-}14)$$

he relation $p_1/p_2 = (m_1/m_2)^{3/2}$ is used in the derivation f equations 5-6 to 5-10.

Hence, the total drift and Hall mobilities can be btained using Matthiessen's rule,

$$(\mu_D^{total})^{-1} = \sum_i (\mu_D^i)^{-1} , \tag{5-15}$$

$$(\mu_H^{total})^{-1} = \sum_i (\mu_H^i)^{-1} . \tag{5-16}$$

The following scattering mechanisms were taken into ccount in the numerical calculations.

(1) Acoustic and nonpolar optical phonon (AC,NPO) scattering,

(2) Polar optical phonon (PO) scattering,

(3) Ionized impurity (II) and neutral impurity (NI) scattering,

(4) Alloy (ALLOY) scattering as an additional scattering occuring in ternary and quaternary alloys.

The factors f_D^i and f_H^i, and the expressions for each of the cattering mechanisms are given in the following sections.

-2-2. Estimation of f_D^i and f_H^i .

In order to obtain the total drift and Hall mobilities, t is necessary to estimate f_D^i and f_H^i in equations 5-6 to 5-10. n this section, expressions for f_D^i and f_H^i for each scattering echanism are given. Simple account of intra- and inter- and scattering is taken.

When μ_1^i and μ_2^i are calculated using the standard xpressions for each mobility, and the v_1 and v_2 bands are assumed o completely decoupled, the ratio $c^i = \mu_2^i/\mu_1^i$ reduces to a imple power of r, depending on the mass dependence of the cattering mechanism under consideration. Thus, the c^i's are:

1. $c = r^{5/2}$ for AC,NPO scattering,
2. $c = r^{3/2}$ for PO scattering,
3. $c = r^{1/2}$ for II scattering,
4. $c = r$ for NI scattering,

ıd 5. $c = r^{5/2}$ for ALLOY scattering.

owever, it is known that the decoupled band approximation may nly be particularly varid for ionized impurity scattering Costato, 1973a).

In the case of scattering mechanisms for which the ıterband scattering is uncertain, the following approximation s used, which acknowledges the presence of interband cattering (Wiley, 1975). In this approximation, one writes

$$1/\tau_1 = 1/\tau_{11} + 1/\tau_{12} \qquad (5\text{-}17)$$

nd

$$1/\tau_2 = 1/\tau_{22} + 1/\tau_{21} \ , \qquad (5\text{-}18)$$

here τ_{ij} is a relaxation time associated with scattering from and i to band j. If the τ_{ij} differ primarily in the density f final states, then transitions with final states in the eavy-hole band will be dominant and one can write

$$1/\tau_{11} \sim 1/\tau_{21} >> 1/\tau_{22} \sim 1/\tau_{12}, \quad m_1 > m_2 \qquad (5\text{-}19)$$

n this approximation, one has

$$\tau_1 \sim \tau_2 \ . \qquad (5\text{-}20)$$

sing the approximation of equal relaxation times, $_1^i = e<\tau_1^i>/m_1$, and $\mu_2^i = e<\tau_2^i>/m_2$. Thus,

$$c^i = r \qquad (\tau_1 = \tau_2), \qquad (5\text{-}21)$$

nd

$$\beta^i = 1 \ , \qquad (5\text{-}22)$$

ince the relaxation times may have the same energy dependence. hen this approximation was used to estimate f_D^i and f_H^i, it was ssumed that

$$\alpha_1^i = 1 \ , \qquad (5\text{-}23)$$

or simplicity. This approximation was used in the estimation f f_D^i and f_H^i for (1) neutral impurity and (2) alloy scattering.

<u>For acoustic and nonpolar optical phonon scattering</u>, ^i_D and f^i_H were estimated as follows:

Costato (1974) has made explicit allowance for interband attering for AC.NPO mobility due to the deformation potential attering. The drift mobilities of heavy and light holes re given by

$$(\mu_i^{AC.NPO})^{-1} = (\mu_o)^{-1}\cdot\left(\frac{m_i}{m_o}\right)^{\frac{5}{2}}\cdot\left\{1 + \left(\frac{m_j}{m_i}\right)^{3/2}\right\} \qquad (5\text{-}24)$$

$$(\ i=1,2,\quad j=2,1\ ),$$

ere

$$\mu_o = \frac{2^{3/2}\pi^{1/2}e\hbar^4\rho\bar{u}^2}{3(m_o)^{5/2}(kT)^{3/2}E_{AC}^{\ 2}}\ S(\Theta,\ \eta,\ T)\quad , \qquad (5\text{-}25)$$

(the meaning of each variable is given in Eq. 5-33.)

ing Eq. 5-24, f^i_D and f^i_H reduce to

$$f^i_D = \frac{r^{5/2}(1 + r^{1/2})}{(1 + r^{3/2})^2} \qquad (5\text{-}26)$$

d

$$f^i_H = \frac{r^2}{(1 + r^{3/2})}\quad . \qquad (5\text{-}27)$$

Eq. 5-27, $\alpha_1^{AC.NPO} = 1$ is assumed. (α_1=3π/8~1.18 for re acoustic phonon scattering. Hence, the approximation $^{C.NPO}_{1}$=1 has no drastic effect on the calculations.)

<u>For polar optical phonon scattering</u>, f^i_D and f^i_H were timated as follows:

It is well known that the Boltzmann transport equation uld be simply solved , if the energy dependent relaxation me were defined However, the energy dependent relaxation time can not be defined for polar optical phonon scattering, because the scattering between electrons (or holes) and optical phonons is not elastic. Hence, many researchers reported the various solution of the Boltzmann equations for PO mobility using the variational method (Howarth, 1953; Eherenreich, 1957, 1959) and the iterative method.

The expressions for PO miblity have been obtained for conduction band electrons that have s-like atomic wave functions, whereas holes in the valence band have p-like wave functions. Wiley (1971) showed that PO mobility of heavy holes was approximately twice larger than than that of electrons, i.e. the PO mobility of carriers which have p-like wave functions was about twice larger than those with s-like wave functions.

Thus, for the PO mobility of holes in the valence band, intra- and interband scattering can not be neglected, and the total Hall and drift mobilities can not be simply obtained as indicated in equations 5-6 to 5-10.

As there are many difficulties involved in the estimation of PO mobility for holes in the valence band, Kranzer's results were used in this work for mobility estimation. Kranzer (1976) calculated the PO mobility, taking account of the intra- and inter-band scattering. According to his results:

$$\mu_D^{PO} \sim \begin{cases} 1.12 \cdot \mu_1^{PO} & (T \sim \Theta) \quad , \\ 1.24 \cdot \mu_1^{PO} & (T \sim \Theta/5) , \end{cases} \tag{5-28}$$

and

$$\mu_H^{PO} \sim \begin{cases} 1.8 \cdot \mu_D^{PO} & (T < \Theta/2) \\ 1.6 \cdot \mu_D^{PO} & (T > \Theta/2) \end{cases} , \qquad (5\text{-}29)$$

where

$$\mu_1^{PO} = 2 \cdot \mu_o^{PO} \quad (\mu_o^{PO} : \text{PO mobility for electrons}). \qquad (5\text{-}30)$$

Since PO mobility decreases with increasing temperature, PO mobility is relatively significant at high temperature $(T>\Theta/2)$. Hence, the following relations were used in these calculations.

$$\mu_D^{PO} \sim 1.16 \cdot \mu_1^{PO} \qquad (5\text{-}31)$$

and $\mu_H^{PO} \sim 1.6 \times 1.16 \cdot \mu_1^{PO}$. (5-32)

5-2-3. Expressions for each scattering mechanism.

N.B., the variables and constants that appeared in the text without definition have their usual meanings. T is the temperature in 'K'.

For lucidity, all formulae appearing in this section are restricted to the nondegenerate limit case. Although extention to the degenerate case is straightforward, except in the case of PO mobility* (Neumann, 1978), this is omitted here. Results from expressions for the nondegenerate case must be valid, since holes are not degenerate if the free-carrier concentration exceeds about $3 \times 10^{18} \mathrm{cm}^{-3}$ because of the large effective mass of band v_1 holes in III-V compounds.

(1) Acoustic and nonpolar phonon scattering.

For AC.NPO drift mobility of heavy holes, the formula which was derived for electrons in nondegenerate parabolic bands was usually used (Wiley, 1970), and this was characterized by phenomenological deformation potentials E_{AC} and E_{NPO}.

$$\mu_1^{AC.NPO} = \frac{2^{3/2}\pi^{1/2}e\hbar^4\rho\bar{u}^2}{3(m_1)^{5/2}(kT)^{3/2}E_{AC}^2} \cdot S(\Theta, \eta, T) \qquad (5\text{-}33)$$

---

*) The formula for the PO mobility of electrons accounting arbitrary degeneracy was reported by Ehrenreich (1957).

$$= 3.1752\times10^{-5} \frac{\rho\,\bar{u}^2}{(m_1/m_o)^{5/2} E_{AC}^2 T^{3/2}} S(\Theta,\eta,T) \quad (\mathrm{cm^2V^{-1}sec^{-1}}),$$

with

$$S(\Theta,\ \eta,\ T) = \int_o^{\infty} \frac{x\cdot\exp(-x)\ dx}{1+C\{(1+\Theta/xT)^{1/2} + \exp(\Theta/T)(1-\Theta/xT)^{1/2}\}}, \tag{5-34}$$

$$C = \frac{1}{2}\cdot\left(\frac{\Theta}{T}\right)\left\{\exp\left(\frac{\Theta}{T}\right) - 1\right\}^{-1}, \tag{5-35}$$

$$\eta = (E_{NPO}/E_{AC})^2, \tag{5-36}$$

where

ρ (g$\cdot$cm^{-3}) : the material density,

$\bar{u}$ (cm$\cdot$sec^{-1}) : the average sound wave velocity defined in Eq. 5-37,

E_{AC} (eV) : the acoustic deformation potential,

E_{NPO} (eV) : the optical phonon deformation potential,

Θ (K) : the characteristic temperature of the optical phonons ($k\Theta = \hbar\omega_o$).

In computing the integral 5-34, the term $(1-\Theta/xT)^{1/2}$ (which arises from phonon emission) must be set equal to zero when $\Theta/xT > 1$. Figure 5-2 shows the temperature dependence of the function S.

The average sound velocity is given by (Wiley, 1975)

$$\bar{u}^2 = \frac{1}{3}u_T^2 + \frac{1}{3}u_L^2 \quad , \tag{5-37}$$

where u_L and u_T are the velocities of the longitudinal and transverse sound waves, respectively. They are given by

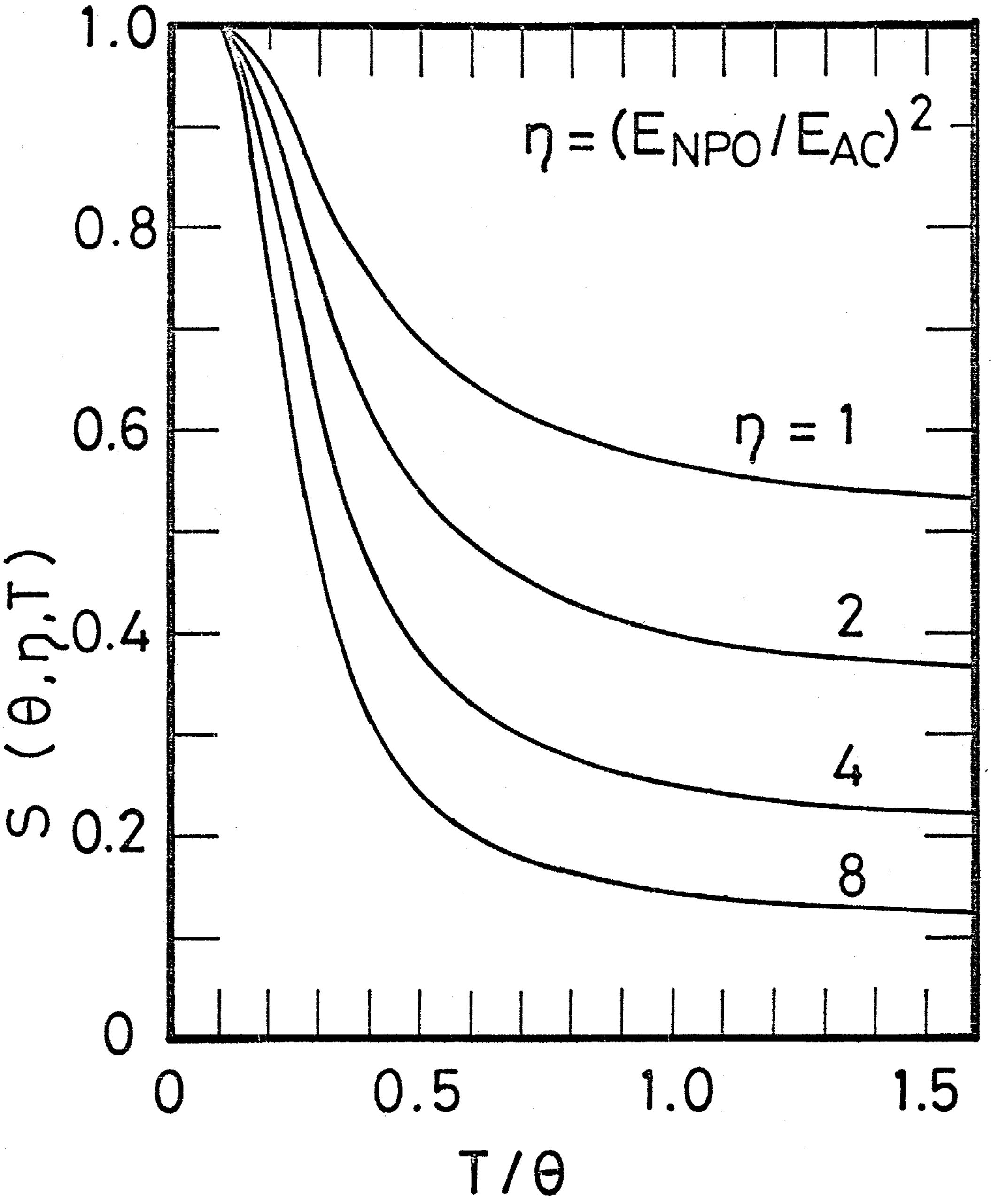

Fig. 5-2.

Temperature dependence of the function S(Θ, η, T) obtained from Eq. 5-34.

$$u_L = (C_L/\rho)^{1/2} \quad \text{(the longitudinal sound velocity)}, \tag{5-38}$$

and $$u_T = (C_T/\rho)^{1/2} \quad \text{(the transverse sound velocity)}, \tag{5-39}$$

with

$$C_L = \frac{1}{5}(3C_{11} + 2C_{12} + 4C_{44}), \tag{5-40}$$

and $$C_T = \frac{1}{5}(C_{11} - C_{12} + 3C_{44}), \tag{5-41}$$

where C_{ij} are the elastic constants.

(2) Polar optical phonon scattering.

The formula for the PO mobility μ_o^{PO} (see Eq. 5-30) which has s-like symmetry is given by (Ehrenreich, 1957)

$$\mu_o^{PO} = \frac{2^{7/2}}{3\pi^{1/2}} \cdot \frac{h\varepsilon_o^2 M v_a \omega_L (kT)^{1/2}}{(m_1)^{3/2}(e^*)^2 e} \cdot \left[\frac{G_p(\eta_F, z)\{\exp(z)-1\}}{(2/\pi^{1/2})F_{1/2}(\eta_F)}\right], \tag{5-42}$$

$$= 0.1982 \cdot (T/300)^{1/2}(e/e^*)^2(m_o/m_1)^{3/2}(10^{22}M)(10^{23}v_a) \cdot$$

$$(10^{-13}\omega_L) \cdot \left[\frac{G_p(\eta_F, z) \ \exp(z)-1}{(2/\pi^{1/2})F_{1/2}(\eta_F)}\right] \ (\mathrm{cm}^2\mathrm{V}^{-1}\mathrm{sec}^{-1}),$$

where

ε_o : the permitivity of free space,

M (g) : the reduced mass of the unit cell,

v_a (cm^3) : the volume of the unit cell ($v_a = a_o^3/4$, a_o: lattice constant) ,

ω_L (sec^{-1}) : the angular frequency of zone-center LO phonons ($h\omega_L = k\Theta$),

e* (c) : the Callen's effective charge,

η_F : the reduced Fermi energy,

$F_{1/2}(\eta_F)$: the Fermi integral.

For the nondegenerate limit, the final functions in Eq. 5-42 reduce to

$$\frac{G_p(\eta_F,\ z)\{\exp(z)-1\}}{(2/\pi^{1/2})F_{1/2}(\eta_F)} \longrightarrow \{\exp(z)-1\}\cdot G(z)\ . \qquad (5\text{-}43)$$

If the screening effect is neglected, G(z) is given by (Howarth, 1953)

$$G(z) = G^{(n)}(z)\Big|_{n\to\infty} \qquad (5\text{-}44)$$

$$G^{(n)}(z) = \frac{\exp(-z/2)}{z}\cdot\left[\frac{\{\Gamma(5/2)\}^2}{\delta_{00}} + \sum_{i=2}^{n}\frac{\{\Delta_\gamma^{(i-1)}\}^2}{\Delta^{(i-1)}\Delta^{(i)}}\right], \qquad (5\text{-}45)$$

where

$\Delta^{(i)}$: the determinant $|\delta_{rs}|$ broken off at i rows and i columns,

$\Delta_\gamma^{(i-1)}$: the determinant formed by replacing the last column of $\Delta^{(i)}$ by $\Gamma(5/2)$, $\Gamma(7/2),\cdots,\Gamma(i+3/2)$.

δ_{rs} is given by

$$\delta_{rs} = \int_0^\infty [2\{y^{r+s+1} + (y+z)^{r+s+1}\}\sinh^{-1}\surd(y/z) - \{y^r(y+z)^s + (y+z)^r y^s\}\{(2y+z)\sinh^{-1}\surd(y/z) - \surd(y(y+z)\}]\cdot\exp(-y)\ dy. \qquad (5\text{-}46)$$

Figure 5-3 shows $G^{(n)}(z)$ as a function of z. In the practical calculations, $G^{(4)}(z)$ was used for G(z). The PO mobility generally decreases with increasing temperature. The temperature dependence of μ_o^{PO} is not simple except at high temperatures ($T > 1.5\Theta$), where it approaches $T^{-1/2}$ (Wiley, 1970).

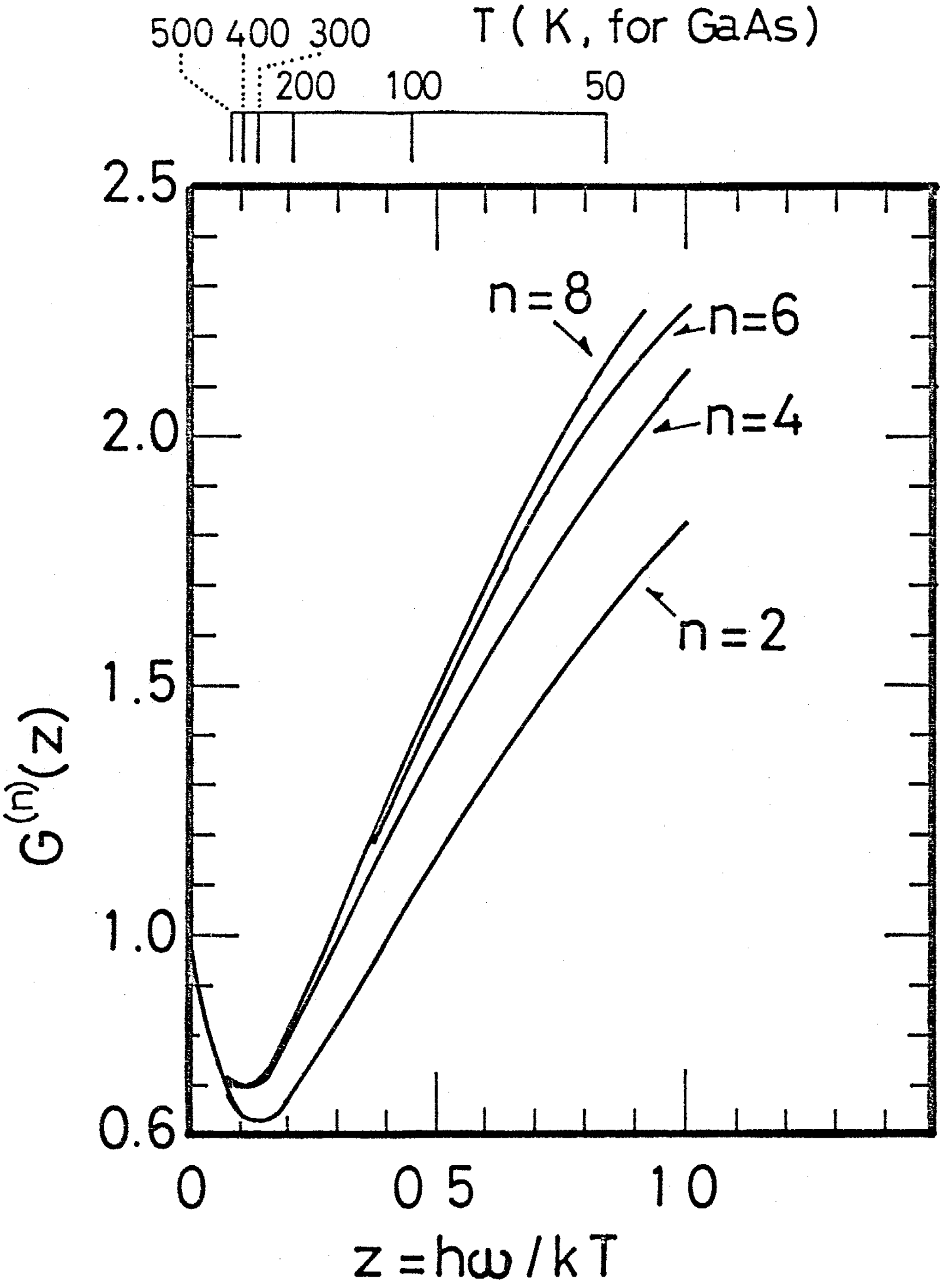

Fig. 5-3.

Temperature dependence of the function $G^{(n)}(z)$ given by Eq. 5-45. In practical calculations, $G^{(4)}(z)$ was used as G(z) (see Eq. 5-44).

The Callen's effective charge is given by

$$(e^*)^2 = \varepsilon_o M\omega_L^2 V_a \ (\varepsilon_\infty^{-1} - \varepsilon_s^{-1})^{-1} , \qquad (5\text{-}47)$$

where ε_s and ε_∞ are the static and dynamic dielectric constants, respectively. For GaAs, e^*/e is about 0.2.

(3) Ionized Impurity scattering.

For the ionized impurity scattering, the so-called Brooks-Herring formula which was known derived from nondegenerate s-like wave functions was used. According to Wiley's discussion (1975), μ_1^{II} is given by

$$\mu_1^{II} = W\cdot\mu_o^{II} , \qquad (5\text{-}48)$$

where μ_o^{II} is the Brooks-Herring formula, and W is a factor of order unity ($1 < W < 2$) which account for the p-like symmetry of the hole wave functions. In the practical calculations, W was set to 1.0 for simplicity. The Brooks-Herring formula is given by

$$\mu_o^{II} = \frac{128\pi(2\pi)^{1/2}\varepsilon_o^2\varepsilon_s^2(kT)^{3/2}}{e^3(m_1)^{1/2}\ N_i}\{\ln(1+b) - \frac{b}{1+b}\}^{-1} , \qquad (5\text{-}49)$$

$$= 3.284\text{x}10^{15}\ \frac{\varepsilon_s^2\ T^{3/2}}{N_i(m_1/m_o)^{1/2}}\{\ln(1+b) - \frac{b}{1+b}\}^{-1}$$

$$(\text{cm}^2\text{V}^{-1}\text{sec}^{-1}),$$

where

$$b = \frac{24\varepsilon_o\varepsilon_s m_1(kT)^2}{e^2h^2p'} , \qquad (5\text{-}50)$$

$$= 1.294\text{x}10^{14}\cdot(m_1/m_o)\varepsilon_s T^2/p'$$

$$p' = p + (N_A - N_D - p)(p + N_D)/N_A , \qquad (5\text{-}51)$$

$$N_i = p + 2N_D, \qquad (5\text{-}52)$$

N_A (cm^{-3}) : the acceptor concentration,
N_D (cm^{-3}) : the unintentionary doped donor concentration,
and p (cm^{-3}) : the free-carrier concentration.

(4) Neutral impurity scattering.

μ_1^{NI} is given by

$$\mu_1^{NI} = (e^3/h^3)(m_1/20p_N)(1/4\pi\varepsilon_o\varepsilon_s) \qquad (5\text{-}53)$$
$$= 1.435\text{x}10^{22}\{(m_1/m_o)/(\varepsilon_s p_N)\} ,$$

where

$$P_N = N_A - N_D - p . \qquad (5\text{-}54)$$

(5) Alloy scattering.

Alloy scattering refers to the scattering present in alloys due to the random distribution of component atoms among the available lattice sites. This scattering is in addition to the normal scattering mechanisms present in nonalloy materials. An expression for the alloy scattering was first derived by Brooks (See, Chandra, 1980). In this work, the formula derived by Harrison was used for calculations. Harrison (1976a) assumed the crystal to have a uniform background potential with a square well of depth ΔE_{ALLOY} at random sites associated with one of the alloying constituents. The square well potential was assumed to extend over a spherical region of radius equal to the nearest-neighbor separation, a choice admitted as being somewhat arbitrary. In Harrison's paper, the energy dependent relaxation time was derived ($\tau_{Alloy} \propto \varepsilon^{-1/2}$). Using Harrison's results, μ_1^{ALLOY} is given by

$$\mu_1^{ALLOY} = \frac{32\sqrt{2}}{9\pi^{3/2}} \cdot \frac{e\hbar^4}{m_1^{5/2} v_a \{x(1-x)(\Delta E_{ALLOY})^2\}(kT)^{1/2}} , \qquad (5\text{-}55)$$

$$= 2.369\text{x}10^{-27} \cdot [(m_1/m_o)^{5/2}\{x(1-x)(\Delta E_{ALLOY})^2\}] \cdot$$

$$T^{-1/2} \quad (\text{cm}^2\text{V}^{-1}\text{sec}^{-1}) ,$$

where

ΔE_{ALLOY} (eV) : the alloy scattering potential.

The most significant parameter in Eq. 5-55 is the alloy scattering potential ΔE_{ALLOY}. However, an ambiguity over the choice of scattering potential remains. Various proposal for the alloy scattering potential have been made such as
(1) the difference in the energy band gaps between the bonary constituents (Tietjen, 1965; Makowski, 1973),
(2) the difference in electron affinities between the binary constituents (Harrison, 1976), and
(3) the scattering potential based on the electron negativity theory (see Littlejohn, 1978). The alloy scattering potential which is calculated by the above three methods , for example, varies from 0.12eV to 1.52eV for the $Ga_{1-x}Al_xAs$ system. Hence, it would be better to regard the scattering potential as a justfiable parameter which can be calculated from a curve-fitting process until a satisfactory theory of alloy scattering is developed.

5-3. Various parameters in ternary alloys.

In the various formulae for each mobility given in Sec. 6-2-3, certain material parameters occur, such as the effective mass, the reduced ion mass, the Callen's effective charge, and so on. The variation of these with composition must be determined if mobility calculations of ternary alloys are to be made.

Here, the ternary alloy is represented by $A_xB_{1-x}C$, for example $Al_xGa_{1-x}As$. 'x' is the mole fraction of AC in the mixed crystal. The lower subscript, A or B, generally indicates that the corresponding parameters is of the end binary compound, AC or BC, respectively.

Linear interpolations were assumed for the following parameters:

(1) the lattice parameter; $a(x)$ (Vegard' law)

(2) the heavy- and light-hole effective masses; $m_1(x)$ and $m_2(x)$,

(3) the elastic constant; $C_{ij}(x)$.

i.e., these parameters were assumed to be represented by

$$P^i(x) = x \cdot P_A^i + (1-x) \cdot P_B^i \ , \tag{5-56}$$

where P^i indicates the corresponding parameters.

The material density $\rho(x)$ is given by

$$\rho(x) = \{x\cdot W_A + (1-x)\cdot W_B + W_C\}/v_a , \qquad (5\text{-}57)$$

where W_i $(i=A, B, C)$: the mass of 'i' atom,

v_a : the unit cell volume, $v_a=\{a(x)\}^3/4$. (5-58)

The reduced mass of the unit cell $M(x)$ is given by

$$M(x)^{-1} = x\cdot W_A^{-1} + (1-x)\cdot W_B^{-1} + W_C^{-1} . \qquad (5\text{-}59)$$

The relative permitivities $\varepsilon_\infty(x)$ and $\varepsilon_s(x)$ are given by (Harrison, 1976)

$$\frac{\varepsilon_i(x) - 1}{\varepsilon_i(x) + 2} = x\cdot\frac{\varepsilon_{i,A} - 1}{\varepsilon_{i,A} + 2} + (1-x)\cdot\frac{\varepsilon_{i,B} - 1}{\varepsilon_{i,B} + 2} \quad (i=\infty, s), \qquad (5\text{-}60)$$

Fig. 6-4 shows the compositional variation of $\varepsilon_s(x)$ and $\varepsilon_\infty(x)$ as a function of x for $Ga_{1-x}Al_xAs$.

The Debye temperature $\Theta(x)$ was estimated as follows (Harrison, 1976) :

The transverse-optical mode angular frequency $\omega_T(x)$ is given by

$$\omega_T(x) = \{x\cdot\omega_{T,A}^2 + (1-x)\cdot\omega_{T,B}^2\}^{1/2} . \qquad (5\text{-}61)$$

The relation between the transverse(T)- and the longitudinal(L)-optical mode frequency is

$$\{\omega_L(x)\}^2 = \{\varepsilon_s(x)/\varepsilon_\infty(x)\}\cdot\{\omega_T(x)\}^2 , \qquad (5\text{-}62)$$

and that between $\omega_L(x)$ and $\Theta(x)$ is

$$k\Theta(x) = \hbar\omega_L(x) \quad . \tag{5-63}$$

In the practical calculations, $\omega_T(0)$ and $\omega_T(1)$ were first calculated from $\Theta(0)$ and $\Theta(1)$ using equations 5-63 and 5-64, since the Θ's of binary compounds are usually available. $\omega_T(x)$ was calculated using Eq. 5-62, and then $\Theta(x)$ was obtained from equations 5-63 and 5-64. $\omega_T(x)$, $\omega_L(x)$, and $\Theta(x)$ calculated from $Ga_{1-x}Al_xAs$ are shown in Fig. 5-5.

The Callen's effective charge $e^*(x)$ is defined in Eq. 6-47. Relationships for all the parameters appearing in Eq. 6-47 have already been given in the preceding sections. Using these formulae, the Callen's effective charge e^* was estimated. (e^*/e) varied linearly with x from 0.20 to 0.25 for $Ga_{1-x}Al_xAs$.

The material parameters for the III-V binary compounds are listed in Table 6-1.

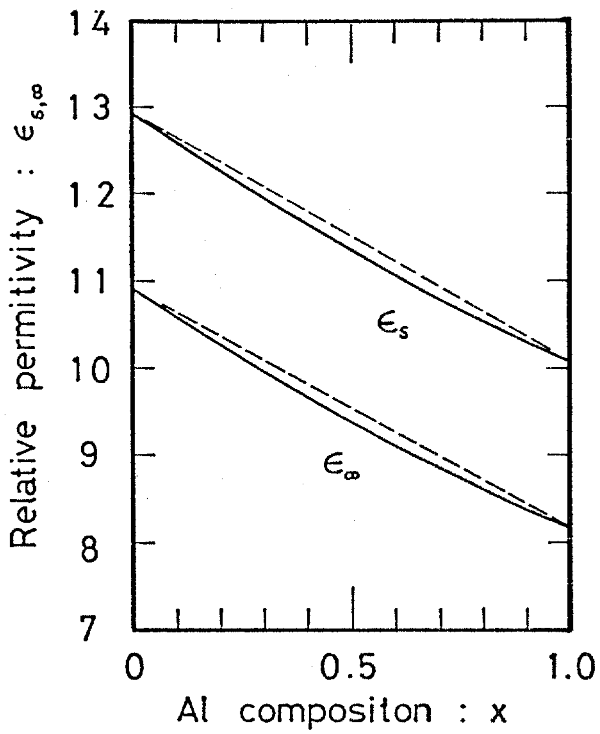

Fig. 5-4.

The relative permitivities ε_s and ε_∞ of $Ga_{1-x}Al_xAs$ as a function of x, calculated from Eq. 6-61. The dashed line is the linear interpolation.

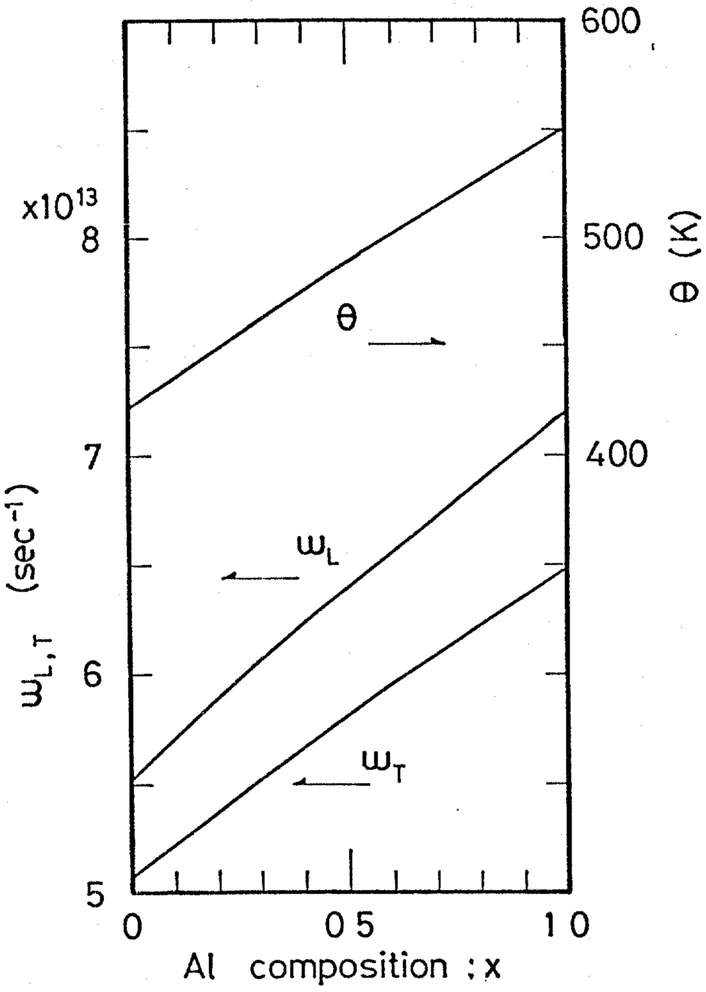

Fig. 5-5.

The Debye temperature θ, the longitudinal (ω_L) and the transverse (ω_T) optical phonon angular frequencies of $Ga_{1-x}Al_xAs$ as a function of x, calculated from equations 6-61∿6-63.

	ρ	Θ	$\overline{u}$	elastic constant (10^{11}dyn cm^{-2})					ε_s	ε_∞	e*/e
	(g·cm^{-3})	(K)	(10^5cm/s)	C_{11}	C_{12}	C_{44}	C_L	C_T			
AlP	2.40	725	5.95	13.2	6.30	6.15	15.36	5.07	9.9	7.6	0.302 ± 0.036
AlAs	3.598	550	4.55	12.5	5.34	5.42	13.40	4.49	10.06	8.16	0.248 ± 0.028
AlSb	4.26	493	3.72	8.939	4.425	4.155	10.46	3.392	12.04	10.24	0.212 ± 0.021
GaP	4.130	582	4.76	14.12	6.253	7.047	16.61	5.804	11.1	9.09	0.241 ± 0.034
GaAs	5.307	421	3.90	11.88	5.38	5.94	14.03	4.864	12.91	10.91	0.200 ± 0.028
GaSb	5.614	347	3.22	8.839	4.033	4.316	10.38	3.554	15.69	14.44	0.128 ± 0.033
InP	4.787	498	3.81	10.22	5.76	4.60	12.21	3.652	12.35	9.52	0.270 ± 0.027
InAs	5.667	350	3.09	8.329	4.526	3.959	9.975	3.136	14.55	11.98	0.221 ± 0.027
InSb	5.775	284	2.83	6.669	3.645	3.020	7.875	3.021	17.88	15.68	0.159 ± 0.027

Table 6-1. Numerical values for the physical parameters needed in the equations. The error bars quoted for e*/e are based on assumed 2% uncertainty in the relative permitivity.

5-4. Calculation results for p-$Ga_{1-x}Al_xAs$.

In sections 5-2 and 5-3, expressions were given for the Hall mobility of holes. Calculation results for the Hall mobility of p-$Ga_{1-x}Al_xAs$ ternary alloys are discussed in this section, and it is shown that the Hall mobility of p-$Ga_{1-x}Al_xAs$ at room temperature is influenced by the existence of the alloy scattering.

5-4-1. Calculation for GaAs and AlAs.

The method presented in sections 5-2 and 5-3 can be generally applied to any III-V ternary alloy. In this section, calculation results for the Hall mobility of the $Ga_{1-x}Al_xAs$ ternary alloy are discussed.

Although various parameters appearing in the equations in sections 5-2 and 5-3 are given in Sec. 5-4, several other parameters remain in order to calculate the mobility

They are :

(1) the deformation potentials: E_{AC} and E_{NPO},

(2) the acceptor and the free-carrier concentrations; N_a and p, and

(3) the alloy scattering potential; ΔE_{ALLOY}

It is usual to regard the deformation potentials as justifiable parameters which can be calculated from the curve fitting to the results for the high purity materials in the previous mobility analyses for p-type III-V binary compounds (Wiley, 1975).

However, it must be recognized that the theoretical formulae was for drift mobility whereas the experimental values are for Hall mobility in the earlier works. Since the expressions for Hall mobility are formulated in Sec. 5-2, the reconsideration for the deformation potentials is required first.

The deformation potentials E_{AC} and E_{NPO} were determined as follows:

In high purity p-GaAs ($N_a < 10^{15}cm^{-3}$), holes are scattered in the main only by the hole and phonon interaction (AC.NPO and PO phonons) at relatively high temperature ($T > 100K$). When only the AC,NPO and the PO scattering is taken into account in the mobility calculation, this is called the 'lattice limited' mobility——μ_i^{Latt}(i=D and H). The deformation potentials for p-GaAs were determined by fitting the lattice limited mobility to published Hall mobility data for p-type GaAs with low carrier concentrations where at least at higher temperatures the scattering by ionized impurities can be neglected. Best agreement was found with $E_{AC} = 3.5eV$ and $E_{NPO} = 13.2eV$,* the corresponding curve for $\mu_H^{Latt}(T)$ is shown in Fig. 5-6 together with existing experimental data. The deformation potential E_{AC} is in better accordance with the value of 3.6eV estimated on the basis of theoretical considerations (Wiley 1970a).

---

*) The corresponding η (see Eq. 5-36) is 14.22.

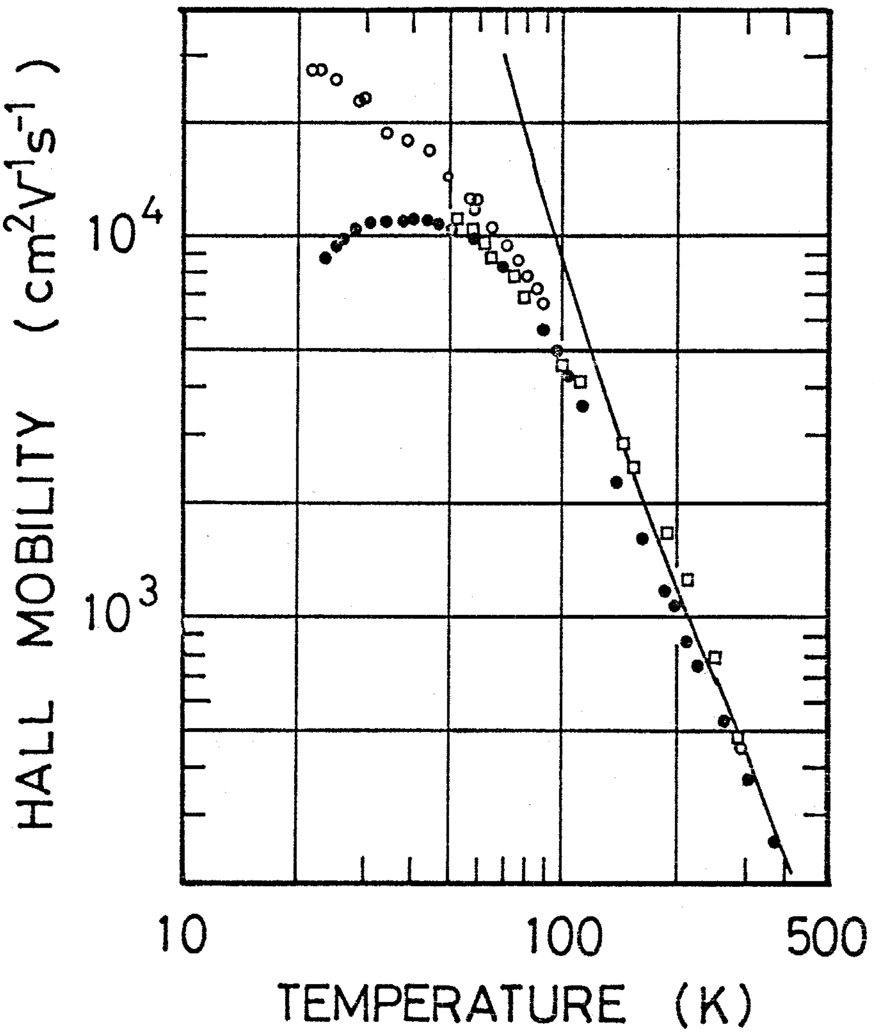

Fig. 5-6.

Comparison of the calculated Hall mobility due to the lattice scattering (AC.NPO and PO) in p-GaAs (solid curve) with experimental data, The experimental values are obtained from Zschauer (○) (1973), Mears (□) (1971), and Hill (●) (1970). The deformation potentials E_{AC} and E_{NPO} are 3.5eV and 13.2eV, respectively.

Furthermore, the E_{NPO} value for holes determined in this work is quite similar to the deformation potential E_{NPO} for electrons in the indirect conduction minimum of GaAs near the point X of the Brillouin zone which can be estimated to be about 13eV (Neumann, 1976). As expected the values $E_{AC} = 3.5$eV and $E_{NPO} = 13.2$eV found in this work agree fairly with the corresponding values obtained by Neumann (1978) (3.5eV and 12.1eV, respectively). (Neumann also formulated an expression for the Hall mobility, although it was simpler than that used in this work.)

There have been no reported measurements of hole mobilities for AlAs (nor AlP). Wiley (1975) estimated that $\mu_H^{Latt}(300K)$ for AlAs would be $200 cm^2V^{-1}s^{-1}$, although the value had uncertainty of at least 50%. The deformation potential E_{AC} and E_{NPO} were assumed to be 3.5eV and 11.9eV, respectively. For $Ga_{1-x}Al_xAs$, the deformation potentials were assumed to vary linearly with Al composition for simplicity.

In order to calculate the mobility due to the ionized impurity and the neutral impurity scattering using equations 5-49 and 5-53, it is necessary to determine the free-carrier concentration at a given temperature. Assuming the one-level impurity model, the free-carrier concentration and the neutral impurity concentrations were determined. In the one-level model, the free-carrier concentration is represented by Eq. 6-7. The acceptor energy level E_a in p-$Ga_{1-x}Al_xAs$ increases with increasing Al composition x (see Fig. 6-4.). as discussed in Chap. 6.

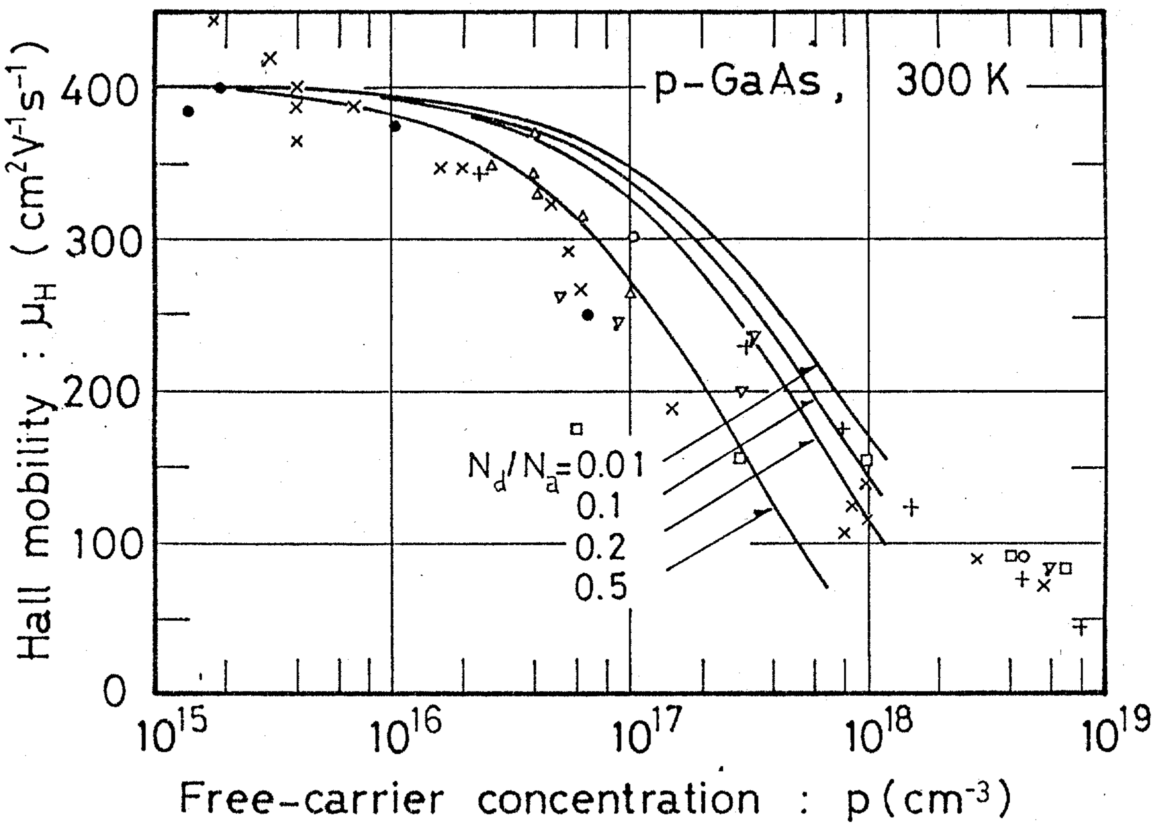

Fig. 5-7.

The concentration dependence of the Hall mobility in p-GaAs at 300K.

The experimental values are obtained from the literature (Wiley, 1975).

In the calculations of I.I. and N.I. mobilities, the experimentally observed value which is given in Fig. 6-4 was used for the acceptor energy level E_a.

Figure 5-7 shows the dependence of the Hall mobility of p-GaAs on the free-carrier concentration p at 300K together with reported experimental results. The lattice limitted mobility of p-GaAs at 300K is $400\mathrm{cm}^2\mathrm{V}^{-1}\mathrm{s}^{-1}$. With increasing free-carrier concentration the Hall mobility decreases due to I.I. scattering. The calculated Hall mobility agree fairly well with the experimental values. However, it must be noted that the Brooks-Herring formula (Eq. 5-49) can not be applied to higher impurity concentration ranges of over $(3\text{-}5)\times10^{17}\mathrm{cm}^{-3}$.

5-4-2. Component of the mobility due to alloy scattering in p-$Ga_{1-x}Al_xAs$.

Figure 5-8 shows the compositional dependence of the lattice limited Hall mobility of p-$Ga_{1-x}Al_xAs$ at 300K. As seen in this figure, the main scattering for p-$Ga_{1-x}Al_xAs$ at room temperature is caused by the AC.NPO scattering. In ternary alloys, the alloy scattering is taken into account as an additional scattering mechanism, Hoever, there is an ambiguity over the choice of the scattering potential ΔE_{ALLOY} as discussed in Sec. 5-2-3. ΔE_{ALLOY} which havs been estimated by various authors varies from 0.12eV to 1.52eV for p-$Ga_{1-x}Al_xAs$. Figure 5-9 shows the variation of ALLOY mobility with Al composition x at 300K, together with the lattice limited mobility.

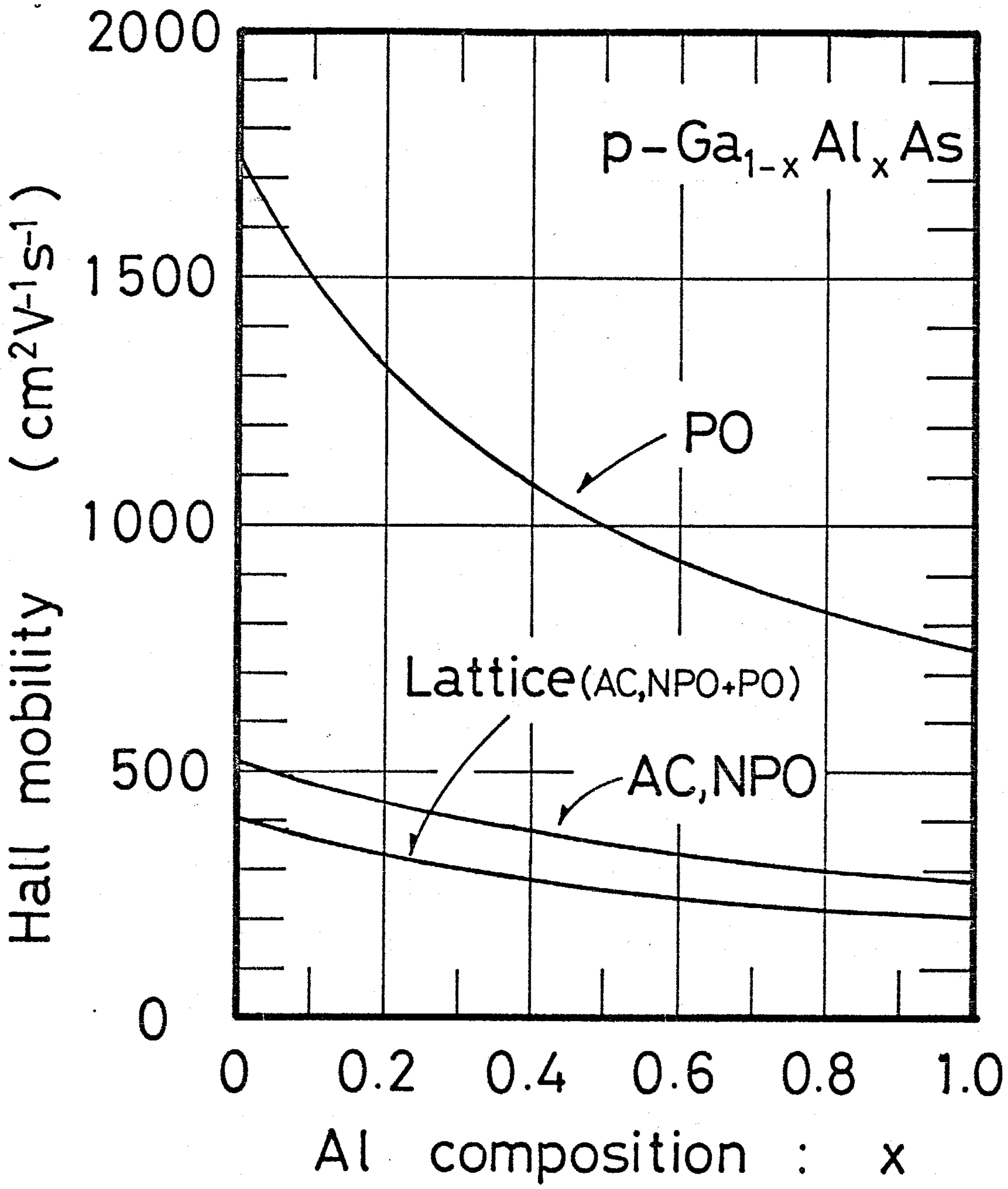

Fig. 5-8.

Compositional dependence of the lattice limited Hall mobility of p-$Ga_{1-x}Al_xAs$ at 300K.

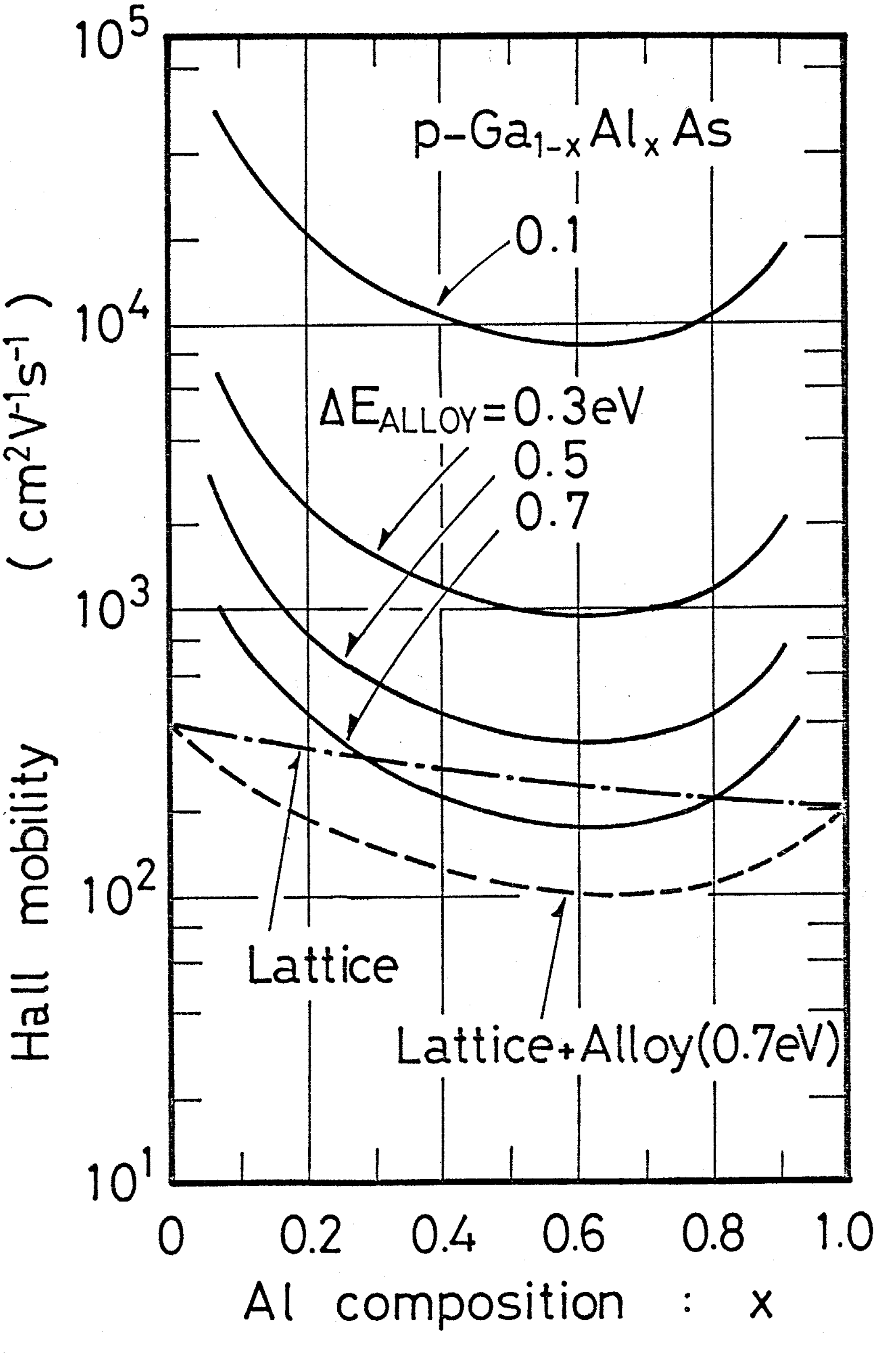

Fig. 5-9.

Compositional dependence of the ALLOY mobility with various alloy scattering potentials for p-Ga$_{1-x}$Al$_x$As at 300K.

The total Hall mobility (Lattice + Alloy) is obtained by including the ALLOY mobility with $\Delta E_{ALLOY}=0.7eV$ as seen in this figure, The total Hall mobility has a minimum value ($\sim 100 cm^2 V^{-1} s^{-1}$, at 300K) at $x \sim 0.65$. Since the experimentally observed values usually contain appropriate impurity atom concentration effects, Figure 5-10 shows the total Hall mobility, which includes I.I. and N.I. scattering ($N_a = 1x10^{16} cm^{-3}$ and $5x10^{17} cm^{-3}$, N_d/N_a is assumed to be 0.1). It can be concluded from figures 5-9 and 5-10, that there exists a clear bowing in the total Hall mobility at 300K if alloy scattering exists for the p-$Ga_{1-x}Al_xAs$ system, and since the total mobility would be dramatically affected by the existence of the alloy scattering, experimentally observed values are required in order to evaluate the alloy scattering potential quantitatively.*

In Chap. 6, it is shown that the alloy scattering potential for p-$Ga_{1-x}Al_xAs$ is about 0.7eV.

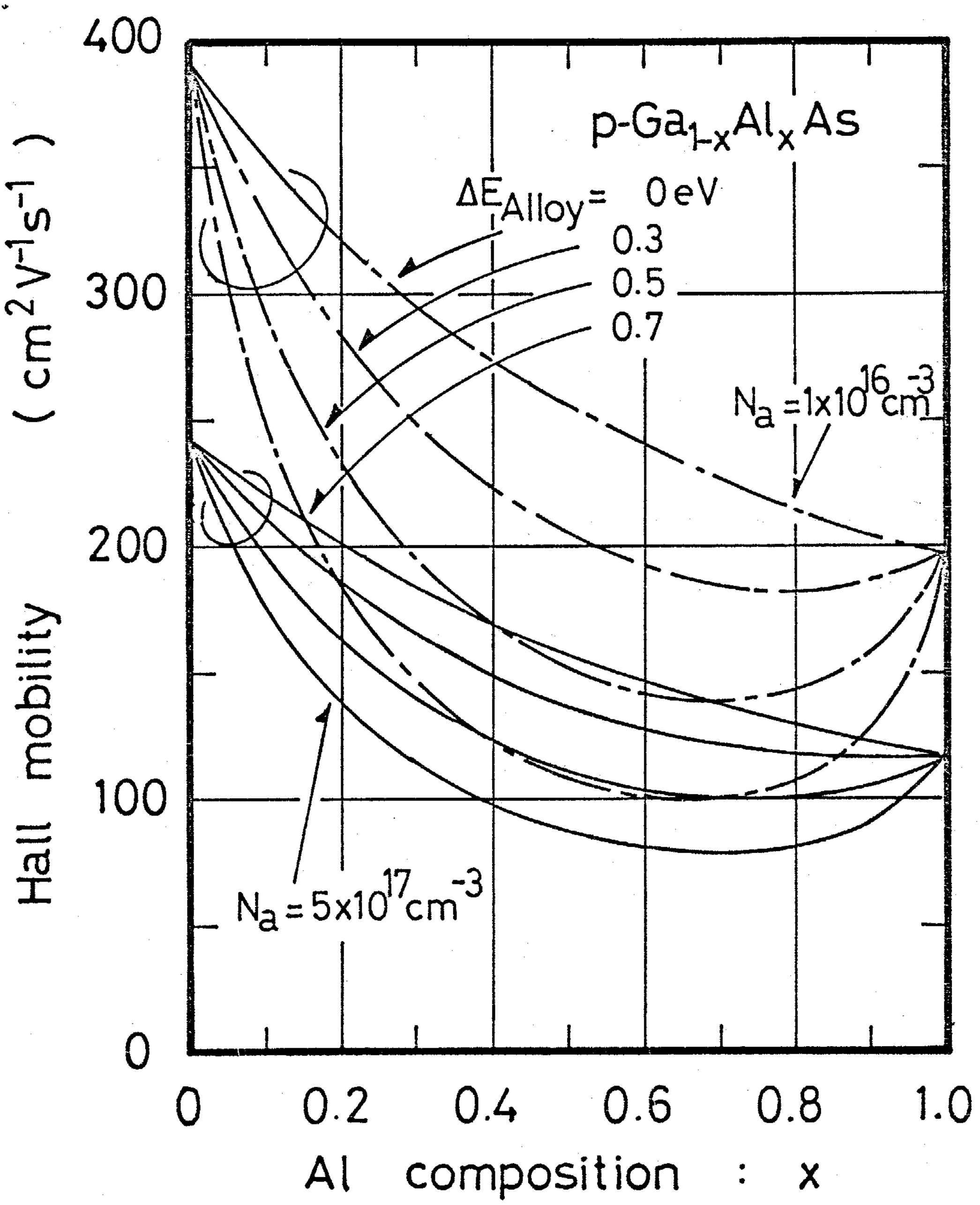

Fig. 5-10.

Compositional dependence of the total Hall mobility of p-Ga$_{1-x}$Al$_x$As, including the ALLOY scattering and I.I.+N.I. scattering.

5-5. Summary and conclusion .

The MTBT (Modified Two-Band Transport) model was proposed for analyzing the Hall mobility of p-type III-V compound semiconductor alloys. Using this model, the drift and Hall mobilities can be calculated separately. Numerical calculations of the Hall mobility were carried out for p-$Ga_{1-x}Al_xAs$, taking account of the acoustic and non-polar optical phonon, the polar optical phonon, the ionized impurity, the neutral impurity, and the alloy scattering which exists in the tenary (and quaternary) alloys.

Comparing these results with the reported Hall mobility data for p-GaAs, it was shown that the temperature and the free-carrier concentration dependences of the Hall mobility of holes in p-GaAs could be explained. The room temperature lattice limited Hall mobility (the acoustic and non-polar optical phonon scattering + the polar optical phonon scattering) of p-$Ga_{1-x}Al_xAs$ decreses with increasing Al composition from $400cm^2V^{-1}s^{-1}$ at $x = 0$(GaAs) to $200cm^2V^{-1}s^{-1}$ at $x = 1$(AlAs). The main scattering in the lattice limited mobility at 300K was caused by the acoustic and non-polar optical phonon scattering over the entire Al composition range.

The estimated alloy scattering potential varies from 0.12eV to 1.52eV, depending on the estimation method. Including the alloy scattering with the total Hall mobility calculations showed that the total Hall mobility is clearly affected by this scattering with an alloy scattering potential of 0.7eV at room temperature.

CHAPTER 6.

ELECTRICAL PROPERTIES OF p-TYPE $Ga_{1-x}Al_xAs$.

6-1. Introduction.

Prior to this work, there were only a few papars concerning systematic investigations of the electrical properties of p-type $Ga_{1-x}Al_xAs$.

In this chapter, the electrical properties of both Zn and Be doped p-type $Ga_{1-x}Al_xAs$ are discussed. The acceptor energy level, which strongly affects the transport and optical properties, is discussed theoretically and experimentally in Sec. 6-3. In Sec. 6-4, the electron diffusion length of Be doped p-$Ga_{1-x}Al_xAs$ is evaluated. The results in section 6-3 and 6-4 show that beryllium is a suitable p-type dopant for opto-electronic devices such as (GaAl)As/GaAs solar cells. The beryllium doping characteristics are described in Sec. 6-5. In Sec. 6-6, hole transport properties are discussed and it is shown that the variation of the Hall mobility of $Ga_{1-x}Al_xAs$ with Al composition can be explained by taking into account alloy scattering, and that the alloy scattering potential for $Ga_{1-x}Al_xAs$ is about 0.7eV.

6-2. Measurement of the electrical properties of p-type $Ga_{1-x}Al_xAs$.

6-2-1. Crystal growth.

Zn or Be doped p-$Ga_{1-x}Al_xAs$ epitaxial layers were grown on undoped n-GaAs substrates by LPE. The growth temperature was 850°C for the Zn doped epitaxial layers and 750°C for the Be doped layers. Typical cooling rate and growth duration were 0.5°Cmin^{-1} and 30 min, respectively.

6-2-2. Measurement techniques.

The electrical properties of the epitaxial layers were evaluated using the so-called Hall measurements.

For the Hall measurements, p-type ohmic contacts using Ag + Zn (10:1) were formed on the Zn or Be diffused p-GaAs layer, as shown in Fig. 6-1. The reverse side was coated with Au + Ge (10:1) or Au + Ge + Ni (10:1:0.5) for an n-type ohmic contact. The deposited metals were annealed at 400-500°C for 3-5min in ambient H_2 or N_2. Usually, the Hall measurements were performed for a specimen size of 3x3 mm^2 or 3x4 mm^2 with the back contact floating. However, even if one of the contacts on the p-type layer was connected with the back contact, i.e., the p-n junction was shorted, there was no effect on the observed results.

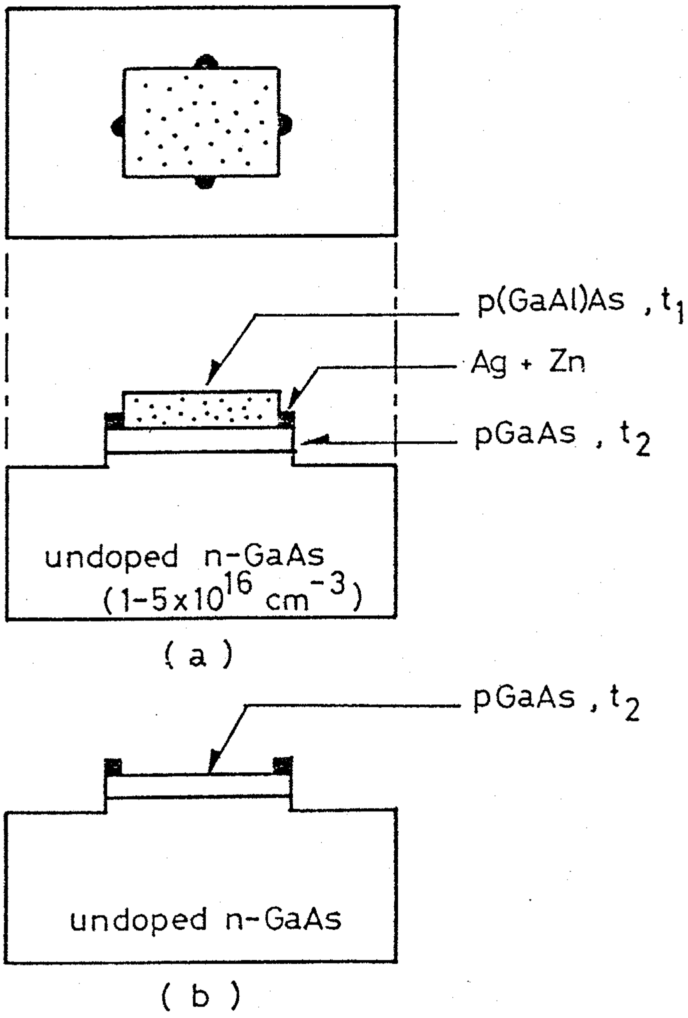

Fig. 6-1.

Sample structure for measurements of the resistivity, the hole mobility, and the free-carrier concentration. (a) First, the average resistivity and Hall coefficient of the p-(GaAl)As/p-GaAs structure were measured by the van der Pauw method. (b) After removing the p-(GaAl)As epitaxial layer, the resistivity and the Hall coefficient of the p-GaAs diffused region were measured.

The details of the measurement method follow:

First, the average resistivity ρ_{12} and the hole mobility μ_{H12} were measured in the temperature range 80-420K using the van der Pauw method. The average free-carrier concentration p_{12} was determined using

$$p_{12} = 1/(e\rho_{12}\mu_{H12}), \tag{6-1}$$

where the suffix '1' denotes the p-(GaAl)As, '2' the p-GaAs, and '12' the p-(GaAl)As/p-GaAs structure, and e is the electronic charge. Subsequently, the (GaAl)As layer was removed using a selective etchant HF, and the above-mentioned measurements for p-GaAs were repeated.

Following these measurements, the resistivity ρ_1, the hole mobility μ_{H1}, and the free-carrier concentration p_1 of the etched-off p-(GaAl)As layer were calculated by the following formulae:

$$\rho_1 = t_1/\sigma_1' , \tag{6-2}$$

$$\mu_{H1} = \Delta(R_H'/\rho^2)/\sigma_1' , \tag{6-3}$$

$$p_1 = 1/(e\rho_1\mu_{H1}), \tag{6-4}$$

where

$$\sigma_1' = \frac{t_1+t_2}{\rho_{12}} - \frac{t_2}{\rho_2} \tag{6-5}$$

$$\Delta(R_H'/\rho^2) = \frac{1}{B}\left(\frac{\Delta R_{H12}'}{\{\rho_{12}/(t_1+t_2)\}^2} - \frac{\Delta R_{H2}'}{(\rho_2/t_2)^2}\right) , \tag{6-6}$$

t_1 : the thickness of p-(GaAl)As,

t_2 : the thickness of p-GaAs,

$\Delta R_H'$: the "sheet" Hall coefficient,

B : the applied magnetic field (∿0.5T),

e : the electronic charge.

In these measurements, the p-(GaAl)As/p-GaAs structure can be regarded as a parallel combination of resistors and the Hall voltages as a parallel combination of the voltage source of each layer. When calculating the free-carrier concentration, the Hall-coefficient factor was assumed to be unity for simplicity.

The above-mentioned technique, which is basically the same as the van der Pauw method, was first developed by Petritz(1958). Petritz's method has been widely utilized to determine the carrier concentration profile of layers with complex distributions (Arizumi, 1968; Wang,1977; Kim, 1979). In chapter 4, the free-carrier profile in the p-GaAs region which was formed by impurity diffusion during the LPE growth process, was determined using this technique.

6-2-3. Determination of the acceptor energy level and the acceptor concentration.

Figure 6-2 shows the temperature variation of the resistivity, the hole mobility, and the free-carrier concentration for the Be doped p-$Ga_{0.2}Al_{0.8}As$ layer and the corresponding p-GaAs diffused region. As illustrated in Fig. 6-2(a), the resistivity of $Ga_{0.2}Al_{0.8}As$ is about ten times higher than that of the p-GaAs region. In the low temperature region

($T < 300K$), the resistivity of both layers decreases with increasing temperature due to an obvious increase in the free-carrier concentration, as shown in Fig. 6-2(c). On the other hand, the increase in resistivity in the region above 270K is caused by a decrease in hole mobility.

The variation of free-carrier concentration with temperature has been used to determine the acceptor energy level E_a and the acceptor concentration N_a for beryllium or zinc using the following equation which utilizes the Boltzmann approximation (Hutson, 1957).

$$\frac{p(p+N_d)}{N_a-N_d-p} = \frac{N_v}{g} \left(\frac{m_h^*}{m_o}\right)^{3/2} \exp\left(-\frac{E_a}{kT}\right) , \qquad (6\text{-}7)$$

where

$N_v = 2(2\pi m_o kT/h)^{3/2}$,

N_a : the acceptor concentration,

N_d : the unintentionaly doped donor concentration.

m_h^* : the hole effective mass,

m_o : the free electron mass,

g : the ground state degeneracy factor,

E_a : the acceptor energy level.

When determining the acceptor energy level and concentration, the following assumptions were made:

(a) Equation 6-7 was considered valid for the present case as (GaAl)As is not degenerate.

(b) The hole effective mass was considered to be $0.5m_o$, independent of x for simplicity.

(c) The degeneracy factor g was taken to be 4 (the same as for p-type semiconductors with a doubly degenerate valence band at k = 0).

(d) The variation of free-carrier concentration as shown in Fig. 6-2(c) can be partly accounted for by impurity band conduction in the low temperature region. However, this has not been considered in the determination of N_a and E_a.

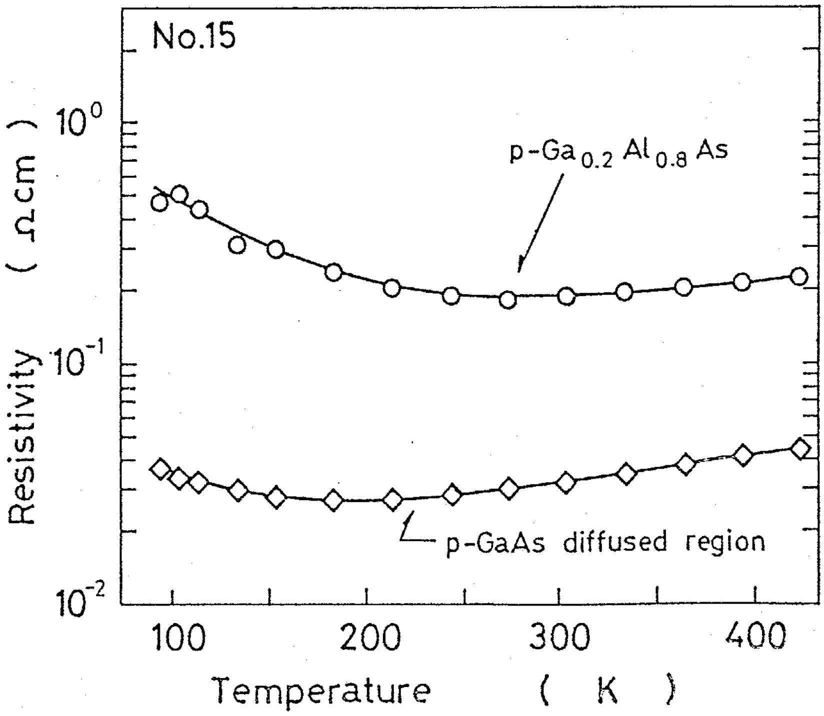

Fig. 6-2(a)

Fig. 6-2.

Variation of (a) the resistivity, (b) the hole mobility, and (c) the free-carrier concentration with temperature for the Be doped p-Ga$_{0.2}$Al$_{0.8}$As and p-GaAs diffused region.

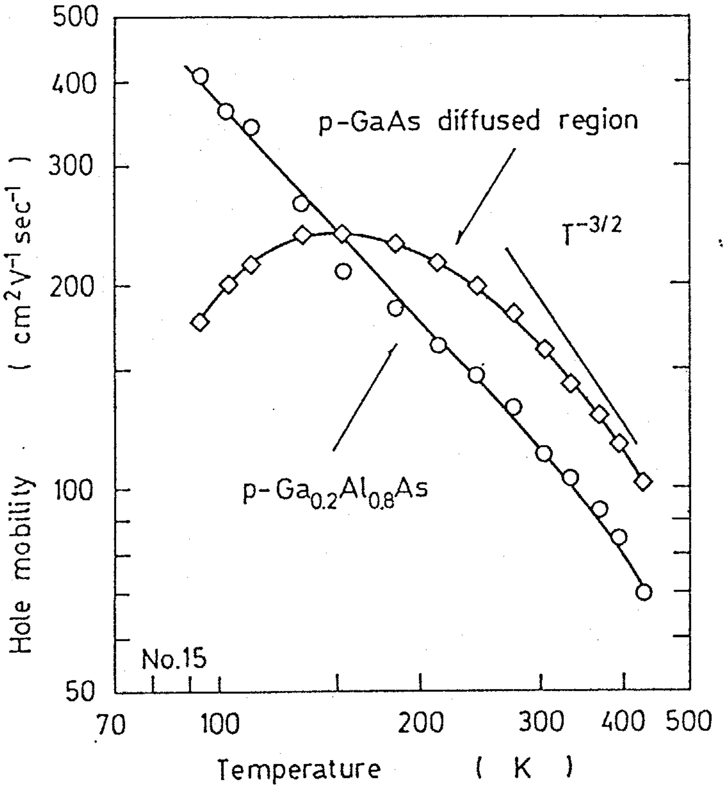

Fig. 6-2(b).

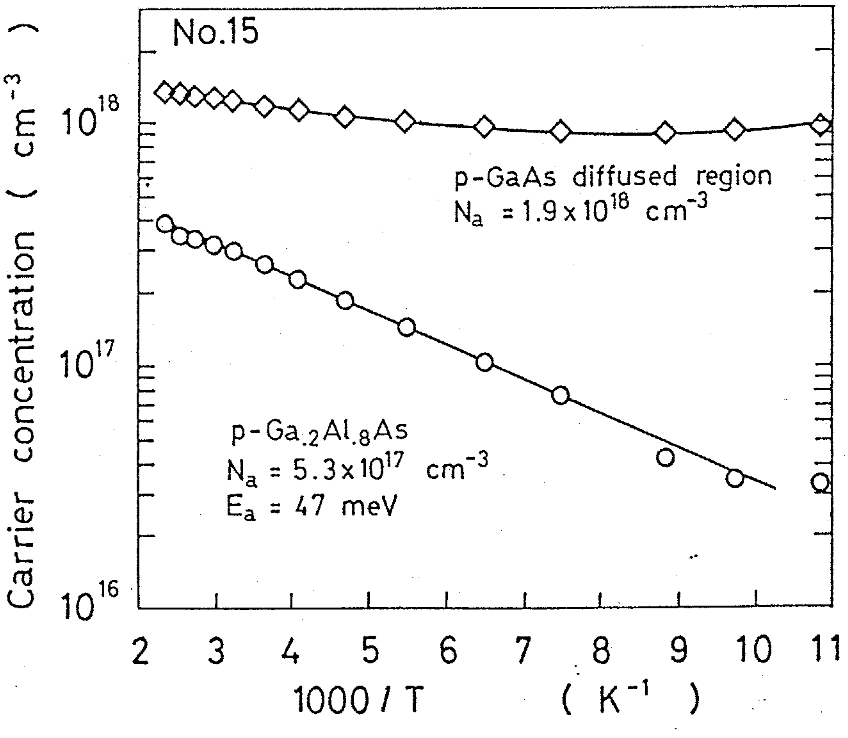

Fig. 6-2(c).

6-3. The acceptor energy level in $Ga_{1-x}Al_xAs$.

The optical and transport properties of semiconductors are strongly affected by the presence of charged impurities, owing to the bound states that such impurities produce in the forbidden gap. In this section, the acceptor energy level in $Ga_{1-x}Al_xAs$ is discussed theoretically and experimentally.

6-3-1. Theoretical estimation.

It is well known that the band structure has a simple minimum in the conduction band and a degenerated maximum in the valence band. Therefore, donor states are easily investigated whereas a complex analysis is required for acceptor states. Here, the acceptor energy level in $Ga_{1-x}Al_xAs$ is estimated according to Baldereschi and Lipari's hydrogenic model (1973).

The acceptor center is described with a Coulomb potential screened by the dielectric constant of the host crystal. Assuming also that the kinetic energy is well described in the effective-mass approximation, the acceptor Hamiltonian is

$$\begin{aligned} H = {} & (\gamma_1+\tfrac{5}{2}\gamma_2)\frac{p^2}{2m_o} - \frac{\gamma_2}{m_o}\,(p_x^2J_x^2+p_y^2J_y^2\ p_z^2J_z^2)^2 \\ & - \frac{2\gamma_3}{m_o}\,(\{p_xp_y\}\{J_xJ_y\}+\{p_yp_z\}\{J_yJ_z\}+\{p_zp_x\}\{J_zJ_x\}) \\ & - e^2/(4\pi\varepsilon r), \end{aligned} \qquad (6\text{-}8)$$

where

$\{ab\} = (ab+ba)/2$,

$\varepsilon = \varepsilon_o \varepsilon_r$,

ε_o : the permitivity of free space,

ε_r : the crystal static dielectric constant,

m_o : the free electron mass,

e : the electronic charge,

$\gamma_1, \gamma_2, \gamma_3$: the Luttinger's valence band parameters (Luttinger, 1956),

$\vec{p}$: the hole linear momentum operator,

$\vec{J}$: the angular monentum operator corresponding to spin $\frac{3}{2}$.

This Hamiltonian can be thought of as describing a particle with spin 3/2 in a Coulomb potential. The first term is the particle kinetic energy, the second and third terms represent a kind of "spin-orbit" interaction, and the last term is the external potential. Using this acceptor Hamiltonian, the acceptor energy level E_a, i.e., the binding energy of the ground state, is given by

$$E_a = R_o\, K(\mu) \ , \tag{6-9}$$

$$R_o = \left\{\frac{e^4 m_o}{2\hbar^2 (4\pi\varepsilon_o)^2}\right\}\cdot\left\{\frac{1}{\varepsilon_r^2 \gamma_1}\right\} \quad \text{(the effective Rydberg)},$$

$$\mu = (6\gamma_3+4\gamma_2)/5\gamma_1,$$

where $K(\mu)$ is the acceptor energy spectrum as a function of the parameter μ, and has been calculated by the variational method for the strong spin-orbit coupling($\bar{\Delta}_o=\infty$) and the weak spin-orbit coupling ($\bar{\Delta}_o=0$) (Baldereschi and Lipari, 1973).

Figure 6-3 shows their calculated results for the acceptor energy spectrum as a function of μ in the strong spin-orbit coupling limit (Detailed values are also tabulated in Table III of their paper.).

In the calculation of E_a, the exact values of the parameters for $Ga_{1-x}Al_xAs$ have not been reported yet. Hence, the values for the Luttinger's valence band parameters of $Ga_{1-x}Al_xAs$ were assumed to vary linearly with the Al composition x. The static dielectric constant ε_r was assumed to vary parabolically with x, since Casey (1974) reported that the refractive index of $Ga_{1-x}Al_xAs$ varied linearly with x.

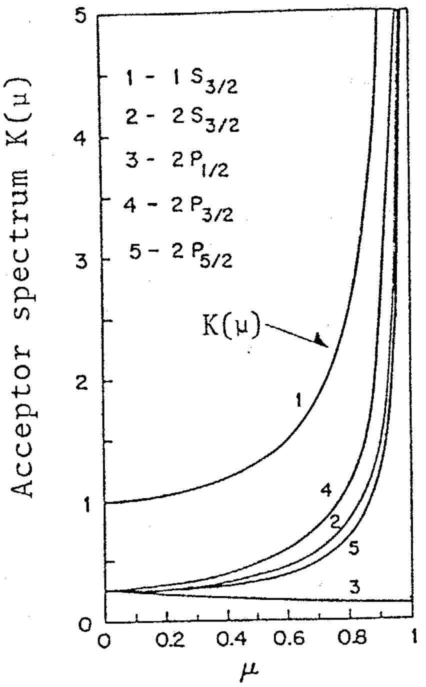

Fig. 6-3.

Calculated acceptor energy spectrum as a function of μ in the strong spin-orbit coupling limit ($\Delta_0 = \infty$) (Baldereschi, 1973).

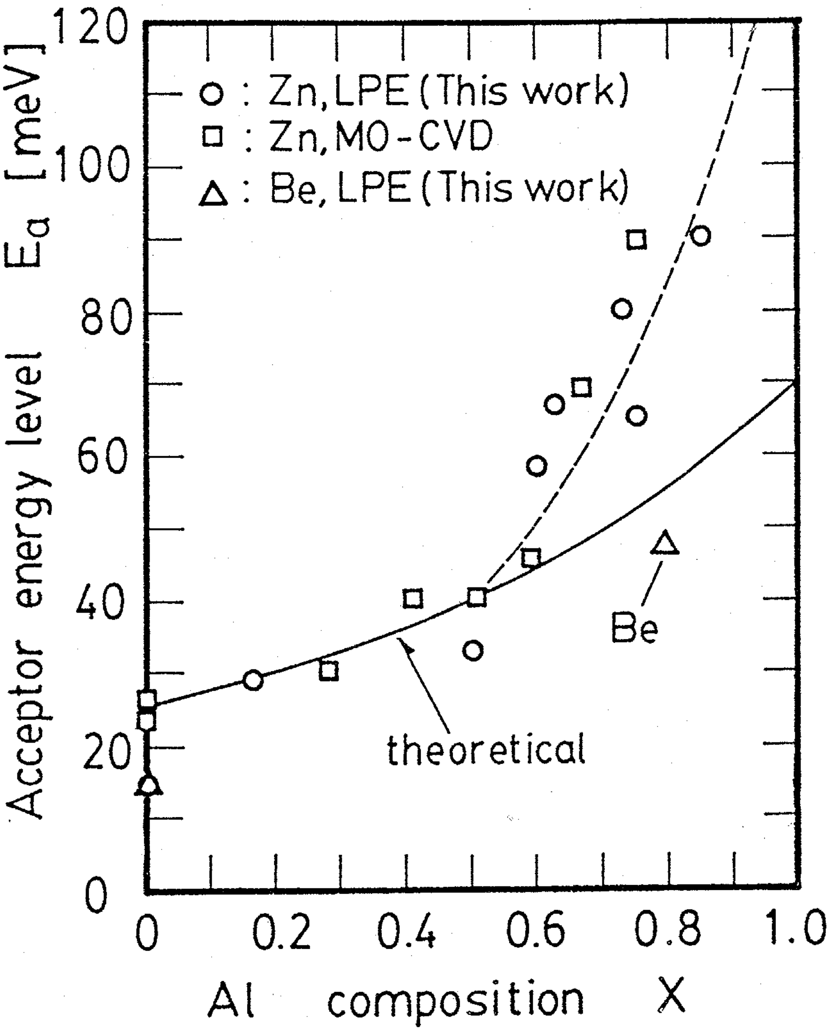

Fig. 6-4.

The acceptor energy level in $Ga_{1-x}Al_xAs$. The solid curve represents the theoretical values calculated using Eq. 6-9. The circles represent the values observed in LPE Zn doped $Ga_{1-x}Al_xAs$ samples, which were determined from the free-carrier concentration variation with the inverse temperature. The squares represent the values observed in Zn doped MO-CVD samples (Yang, 1981). The triangles are the values observed in LPE Be doped $Ga_{1-x}Al_xAs$ samples.

The solid line in Fig. 6-4 shows the acceptor energy level which was calculated using Eq. 6-9. The calculated acceptor energy level in $Ga_{1-x}Al_xAs$ increases from 25.6meV at x=0 (GaAs) to 70.4meV at x=1 (AlAs). This increase in the acceptor energy level with increasing Al composition is mainly due to the decrease in the dielectric constant with increasing Al composition.

N.B., since the impurity atoms are assumed to be the hydrogenic atoms which produce the Coulomb potential (see Eq. 6-8), the theoretical curve can not explain the so-called chemical shift. However, the acceptor energy levels in GaAs, which were observed in the photoluminescence measurements, generally increase with increase in the atomic number for II-column acceptors (see review paper of Kamiya, 1976). These results could lead one to expect that the acceptor energy level for Be is smaller than that for Zn in $Ga_{1-x}Al_xAs$.

6-3-2. Comparison with experimental results.

In Fig. 6-4, the acceptor energy levels for Zn and Be, which were obtained experimentally, are also illustrated. In the case of the acceptor energy level for Zn, the circles indicate the values of the LPE samples (this work), while the squares indicate values for the MO-CVD samples reported recently by Yang (1981a).

Very similar results are obtained both for the LPE and MO-CVD samples. The acceptor energy levels for Zn agree fairly well with the theroretical values when $x<\sim0.5$. However, they increase more rapidly than the theoretical values when $x>\sim0.5$. Extrapolating the experimental acceptor energy levels produces a value of 140meV for Zn at $x=1.0$. This is about twice the theoretical value at $x=1$. This rapid increase in the acceptor energy leval for Zn for $x>0.5$ may be attributed to the direct-indirect transition of $Ga_{1-x}Al_xAs$ (Yang, 1981b) or to the so-called chemical shift.

Since the acceptor energy level increases with Al composition x, the free-carrier concentration at room temperature (i.e., the holes that are thermally ionized from the acceptor atoms) will decrease with increasing x, if the acceptor concentration is constant. Figure 6-5 shows the acceptor concentration N_a (open cirles) and the free-carrier concentration (open squares) for Zn doped $Ga_{1-x}Al_xAs$ as a function of Al composition. These films were formed at 850°C and the weight of Zn in the Ga-Al-As melt was 8mg/1 g of Ga, independent of the Al composition. The increase in the acceptor energy concentration N_a with increasing x may be caused by an increase in the segregation coefficient of Zn for $Ga_{1-x}Al_xAs$ with increasing x. The free-carrier concentration at room temperature decreases with increasing x, although the acceptor concentration increases with increasing x. This could be explained by the increase in the acceptor energy level for Zn with increasing as predicted above.

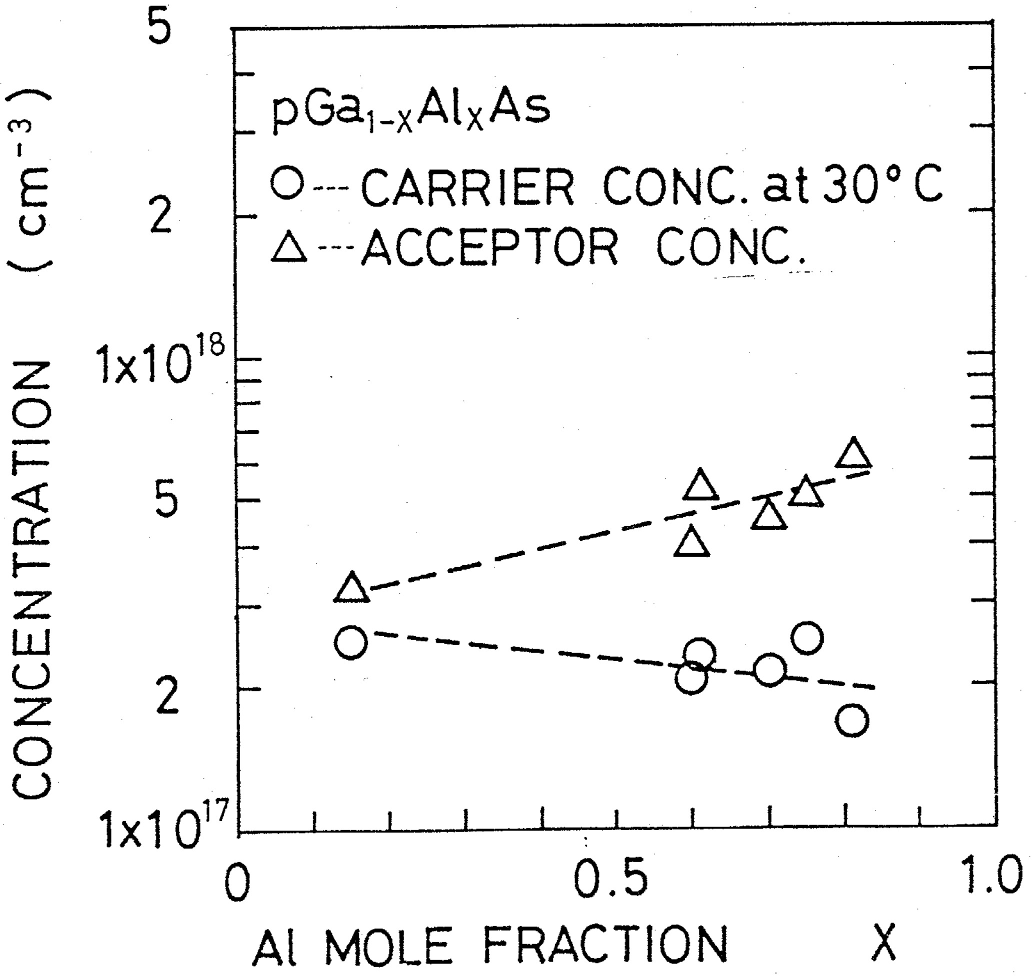

Fig. 6-5.

The acceptor concentration N_a and the free carrier concentration at room temperature as a function of Al composition. The weight of Zn in Ga-Al-As melt is 8mg/1g of Ga independent of Al composition. The epitaxial $Ga_{1-x}Al_xAs$ layers were grown at 850°C

The acceptor energy level for Be at x=0.8 is also illustrated in Fig. 6-4, and is 47meV, This value is about half that for Zn at x=0.8. This small acceptor energy level agrees with the behaviour in GaAs as discussed in Sec. 6-2-1. Thus, it may be expected that the resistivity of p-(GaAl)As can be reduced using Be as a p-type dopant, since the free-carrier concentration at room temperature is increased because of its small acceptor energy level in (GaAl)As.

For the preparation of (GaAl)As/GaAs solar cells (see Chap. 10), a p-type dopant which can produce a small acceptor energy level at $x \gtrsim 0.8$ is required in order to reduce the sheet resistance. Hence, it can be stated that beryllium is a more suitable p-type dopant for (GaAl)As/GaAs solar cells.

The increase in the acceptor energy ionization energy E_i in $Ga_{1-x}Al_xAs$ with x was first reported by SpringThorpe (1975) for Ge.* In addition to this work, the increase in the acceptor energy level E_a in $Ga_{1-x}Al_xAs$ was reported for Mg (Mukai, 1979), for Be (Fujita, 1980), and for Zn (Yang, 1981). However, the research work reported here represented the first publication of the increase of E_a together with the relevant theoretical calculations.

*) SpringThorpe (1975) defined the ionization energy E_i as $p \propto \exp(-E_i/2kT)$ for simplicity.

**) Following the completion of the research programme described here, Fujita (1980) reported the increase of E_a for Be in $Ga_{1-x}Al_xAs$ for various Al compositions, whereas E_a for Be was evaluated only at $x = 0.8$ in the author's work.

6-4. The minority carrier diffusion length.

The minority carrier diffusion length is one of the most significant physical parameters in the design of electronic devices. The electron diffusion length of Zn- or Ge doped p-GaAs has been reported by many researchers (Casey, 1973; Ettenberg, 1975).

The electron diffusion length L_n in the p-GaAs region was evaluated using the SEM beam-induced current technique (Konagai, 1976b). The beam energy was 20keV and the induced current was measured point by point as the electron beam was scanned perpendicularly across the junction (Fig. 6-6). The measured region was the Be diffused p-GaAs in the undoped n-GaAs epitaxial layer. The thickness of the p-GaAs region was about 7μm. The room temperature free-carrier concentration was about $1\times10^{18}cm^{-3}$ on average. L_n was determined from the relation $L \propto \exp(-X/L_n)$, where X is the distance from the p-n junction. The rapid decrease of the induced current near the junction shown in Fig. 6-6 may be due to surface recombination effects (Hackett, 1972). The value of L_n obtained from the slope remote from the junction influence is 4.3μm. It should be noted that the free-carrier concentration is not uniform throughout the whole p-GaAs layer as discussed in Chap. 3. The free-carrier concentration at the hetero-interface between p-(GaAl)As and p-GaAs, i.e., for $X\sim7\mu m$ in Fig. 6-6, is about $2\times10^{18}cm^{-3}$ and that at the junction is about $10^{16}cm^{-3}$. Thus the free-carrier concentration increases from about $5\times10^{17}cm^{-3}$ at 4μm to about $2\times10^{18}cm^{-3}$ at 7μm.

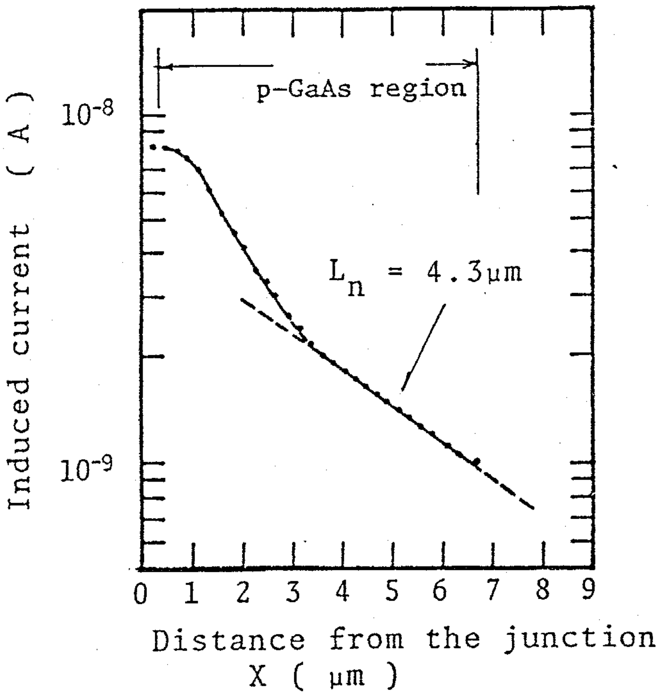

Fig. 6-6.

Measurement of the electron diffusion length.

Induced current vs. Distance from the junction (V_{ac}=20keV).

The free-carrier concentration in p-GaAs is 1x10^{18}cm^{-3} on average.

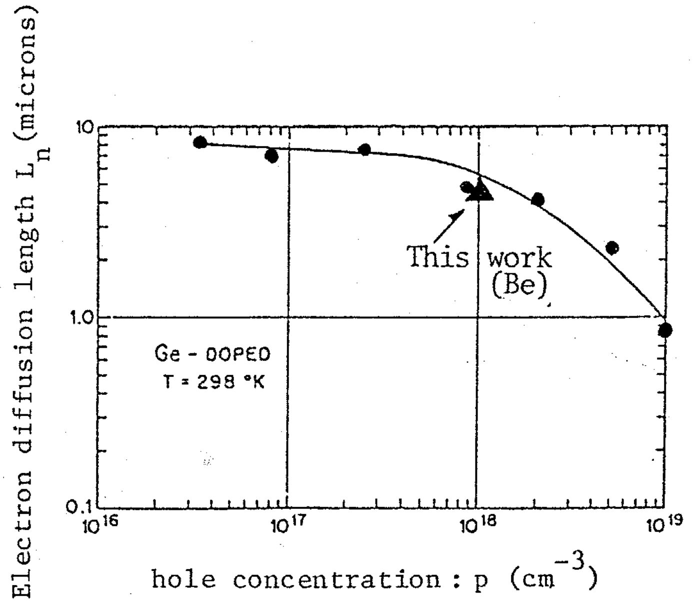

Fig. 6-7.

Electron diffusion length in p-GaAs as a function of hole concentration.

● : Ge doped p-GaAs (Casey, 1973).

▲ : Be doped p-GaAs (this work).

There is no previously reported value for the diffusion length in Be-doped p-GaAs. However, the above value is comparable to that for Zn doped p-GaAs (Ettenberg, 1975). Figure 6-7 shows the electron diffusion length of Ge doped p-GaAs obtained by Casey (1973). As shown in this figure, $L_n = 4.3\mu m$ is compatible with these results.

Kawakami (1973) reported $L_n \sim 5\mu m$ independent x when $0<x<0.3$ for Ge doped p-$Ga_{1-x}Al_xAs$. L_n for Be doped p-$Ga_{0.9}Al_{0.1}As$ ($p \sim 1x10^{18}cm^{-3}$) was evaluated using the same technique in this work. L_n (Be doped, $x = 0.1$) was about $5.0\mu m$.

Since the electron diffusion length of Be doped p-(GaAl)As is compatible with that of Ge or Zn doped (GaAl)As reported previously, a high performance can be expected from Be doped elecronic devices. In Chap. 10, it is shown that the conversion efficiencies of Be doped (GaAl)As/GaAs solar cells are in excess of 20%, that is comparable or higher than that obtained using other p-type dopants such as Zn.

6-5. Beryllium doping characteristics for $Ga_{0.2}Al_{0.8}As$.

Although beryllium will be used as a p-type dopant for (GaAl)As/GaAs heterostructure devices, the doping characteristics of the LPE layers have not yet been investigated. However, the beryllium doping characteristics for $Ga_{1-x}Al_xAs$ with x=0.8 were thoroughly investigated.

The variation of the room temperature free-carrier concentration and resistivity of p-$Ga_{0.2}Al_{0.8}As$ with Be concentration C_{Be} in the growth melt of Ga-Al-As are illustrated in Fig. 6-8. The free-carrier concentration is approximately proportional to the Be concentration C_{Be} in the range 0.02-0.2 at%, and thus can be controlled by C_{Be} in the range $3x10^{17}cm^{-3}$ $-3x10^{18}cm^{-3}$. The distribution coefficient k for Be in $Ga_{0.2}Al_{0.8}As$ was found to be about 0.03 using the room temperature free-carrier concentration. Recently, Fujita (1980) reported the distribution coefficient for Ge in $Ga_{1-x}Al_xAs$. The value k=0.03 at x=0.8 obtained in this work agrees with Fujita's results. The resistivity decreases with increasing C_{Be}. It is not inversely proportional to C_{Be} because of the decrease in the mobility with increasing free-carrier concentration. The Hall mobility of Be doped p-$Ga_{0.2}Al_{0.8}As$ is discussed in the next section.

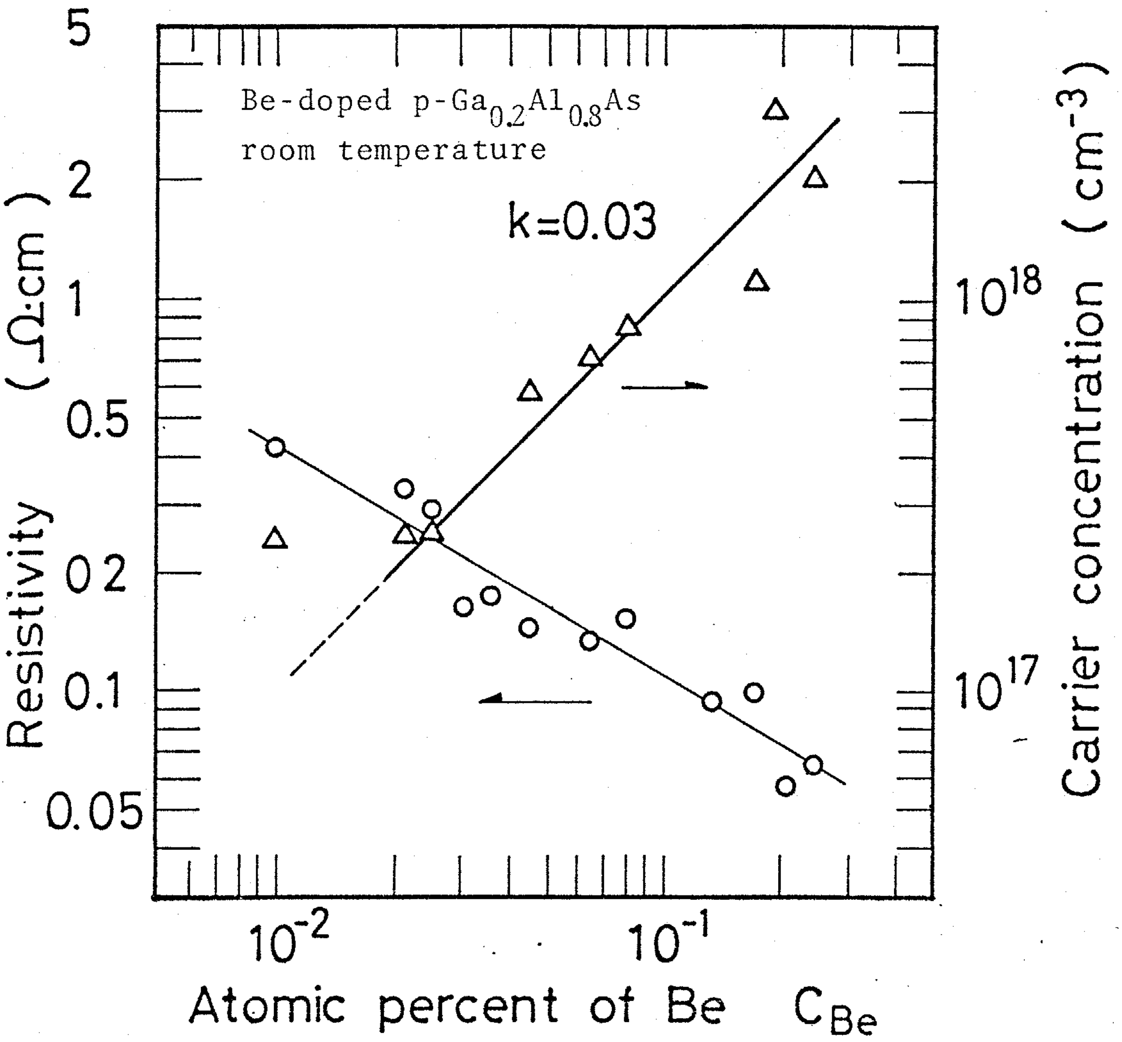

Fig. 6-8.

Room temperature free-carrier concentration and resistivity of Be doped p-$Ga_{0.2}Al_{0.8}As$ as a function of Be concentration in the growth melt. The p-$Ga_{0.2}Al_{0.8}As$ layers were growth at 750°C.

6-6. The alloy scattering effect for hole transport in p-$Ga_{1-x}Al_xAs$.

In chapter 5, it was shown that the Hall mobility of p-$Ga_{1-x}Al_xAs$ was influenced by the existence of alloy scattering at room temperature. The alloy scattering potential which was theoretically estimated varied from 0.12eV to 1.52 eV depnding on the estimation method. The alloy scattering potential was determined by comparing it with the experimental data obtained in this work.

Figure 6-9 shows the Hall mobility of Zn doped p-type $Ga_{1-x}Al_xAs$ as a function of the Al composition. The acceptor concentration for these samples was about $5x10^{17}cm^{-3}$. Theoretically calculated Hall mobilities are also shown in this figure. The acoustic and non-polar optical phonon (AC.NPO), the polar optical phonon (PO), the ionized impurity (II), and the alloy (ALLOY) scatterings as an additional scattering in ternary alloys, were taken into account in the numerical calculations. The three curves in Fig. 6-9 are (1) LATTICE (AC.NPO + NPO), (2) LATTICE + II, and (3) LATTICE + II + ALLOY mobility. In the calculation of the II scattering, $N_a = 5x10^{17}cm^{-3}$ and $N_d/N_a = 0.1$ were assumed. Although the neutral impurity scattering was also calculated, no effect on the total mobility was observed. The compositional dependence of the observed Hall mobility can not be explained by including LATTICE + II scattering only. However, by including the alloy scattering in the total Hall mobility calculation, fairly good agreement was obtained as shown in this figure.

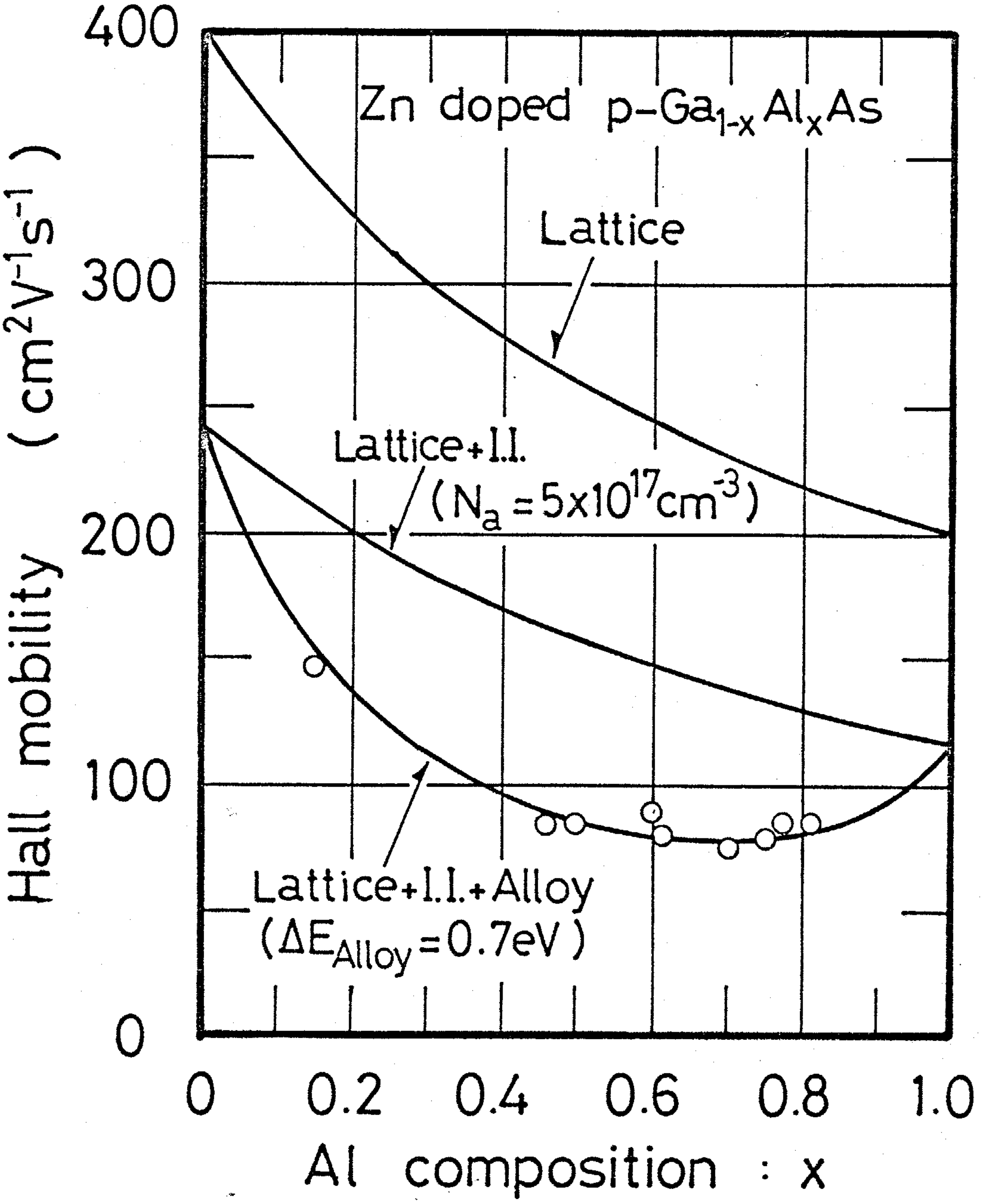

Fig. 6-9.

Compositional dependence of the Hall mobility of Zn doped p-$Ga_{1-x}Al_xAs$ with $N_a \sim 5\times10^{17}cm^{-3}$ at room temperature. The solid curves represented theoretically calculated values (see text).

Best agreement was found for an alloy scattering potential $\Delta E_{ALLOY} = 0.7eV$. Chandra (1980) reported $E_{ALLOY} = 0.44eV$ (on average) for high purity undoped n-$Ga_{1-x}Al_xAs$ ($x < 0.18$). However, the alloy scattering potential ΔE_{ALLOY} for p-$Ga_{1-x}Al_xAs$ determined in this work agree with one of the previously reported theoretical values, i.e., the energy band gap difference between GaAs and AlAs ($E_g^{X,AlAs} - E_g^{\Gamma,GaAs} = 0.74eV$).

Figure 6-10 shows the room temperature Hall mobility of Be doped p-$Ga_{0.2}Al_{0.8}As$ as a function of the free-carrier concentration, together with the theoretically calculated values. In the numerical calculations, the acceptor energy level E_a was assumed to be 47meV (see Fig. 6-4). The experimental data agree with the theoretical results using $\Delta E_{ALLOY} = 0.7-0.8eV$.

This work was the first to show that the compositional dependence of the Hall mobility in p-$Ga_{1-x}Al_xAs$ can be explained by the existence of alloy scattering. More detailed work will be required to explain the temperature dependence of the Hall mobility of p-$Ga_{1-x}Al_xAs$ ternary alloys. *

---

*) Temperature dependence of the Hall mobility for $X = 0.15$, including the alloy scattering component, is explained in this work.

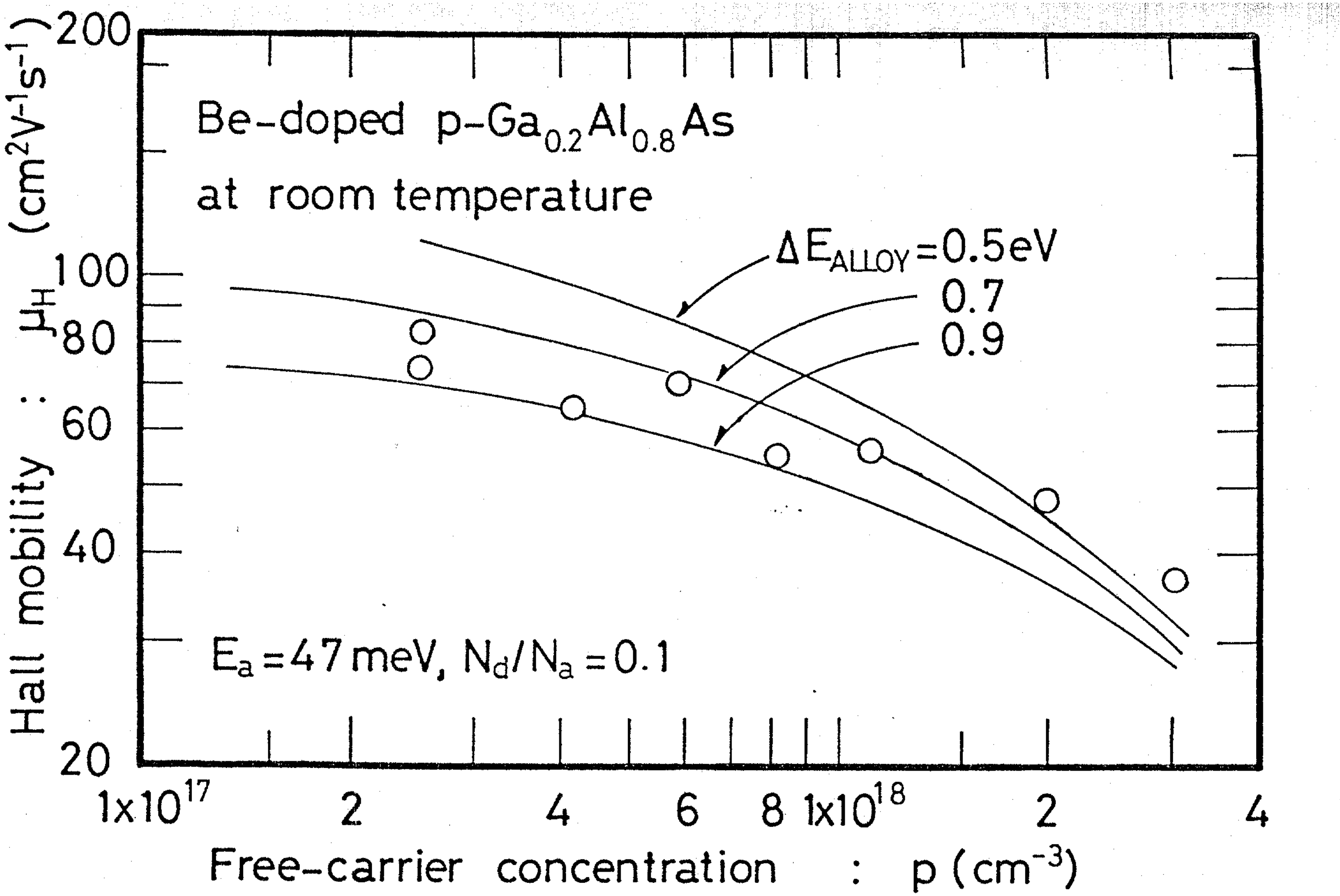

Fig. 6-10.

The Hall mobility of Be doped p-$Ga_{0.2}Al_{0.8}As$ as a function of the free-carrier concentration. The solid curves are theoretically calculated.

6-7. Summary and conclusions.

A systematic investigation of the electrical properties of both Zn and Be doped p-$Ga_{1-x}Al_xAs$ are described in this chapter.

The acceptor energy level is discussed first. Using the modified hydrogenic model, which takes into account the valence band structure, it was shown that the acceptor energy level in $Ga_{1-x}Al_xAs$ increases with increasing Al composition. The acceptor energy level for Zn in $Ga_{1-x}Al_xAs$, which was obtained from the free-carrier concentration variation with the inverse temperature, agrees with the theoretical estimation for $x < 0.5$ and reaches about 140meV at $x = 1.0$(AlAs). Zinc produces a relatively deep level whereas beryllium produces a relatively shallow level of 47meV at $x = 0.8$. Beryllium would be a more suitable p-type dopant when relatively low resistivity films with low acceptor concentration are required such as in (GaAl)As/GaAs solar cells.

The electron diffusion length of Be doped p-GaAs was evaluated using the SEM beam-induced current technique. The observed electron diffusion length was 4.3 μm for $p \sim 1\times10^{18}cm^{-3}$, and this value is comparable with that observed for other p-type dopants such as Zn and Ge.

Beryllium doping characteristics were investigated, and the free-carrier concentration was controlled from $3\times10^{17}cm^{-3}$ to $3\times10^{18}cm^{-3}$ by the Be concentration in the LPE growth melt. The distribution coefficient of Be in $Ga_{0.2}Al_{0.8}As$ was found to be 0.03

Comparing the observed Hall mobility of Zn doped p-$Ga_{1-x}Al_xAs$ with the theoretically calculated Hall mobility, it was shown that the compositional variation of the Hall mobility at room temperature can be explained by the existence of alloy scattering, and that the alloy scattering potential is 0.7eV for hole transport in p-$Ga_{1-x}Al_xAs$.

PART III

DEVELOPMENT OF III-III-III-V QUATERNARY SEMICONDUCTORS.

Chapter 7. Development of new III-III-III-V quaternary semiconductors.

Chapter 8. Crystal growth and physical properties of $(Al_xGa_{1-x})_yIn_{1-y}As$ lattice matched to an InP substrate grown by molecular beam epitaxy.

CHAPTER 7.

DEVELOPMENT OF NEW III-III-III-V QUATERNARY COMPOUND SEMICONDUCTORS.

7-1. Introduction.

In this chapter, the requirement for the development of III-III-III-V quaternary semiconductors for opto-electronic devices operating in the infra-red and visible wavelength region is explained. The expected fundamental properties of these materials are discussed briefly in Sec. 7-3.

Although the requirement for the development of these materials is clear, there have been no previous reports concentrating on the epitaxial growth. It is shown in Sec. 7-4, that the conventional liquid phase epitaxy is not suitable for the preparation of these materials. This is confirmed by the phase equilibria calculations. Molecular beam epitaxy is shown to be the most suitable growth technique for these materials.

7-2. Historical background and the necessity for the development of III-V quaternary compound semiconductors.

The optical communication system has become neccessary in order to cope with the increase in communication volume. The main devices from which an optical communication system is constructed are the laser diode or light emitting diode as light source, the optical fiber as transmission medium, and the photodetectors. The research and development of laser diodes for optical communications has been in progress since the 1960's. The most significant studies were the single heterostructure (SH) and double heterostructure (DH) heterostructure (GaAl)As/GaAs laser diodes in 1970 (Hayashi, 1970; Goodwin, 1970). The high performance (GaAl)As/GaAs laser diodes were improved throughout the 1970's. However, it became clear in the latter part of the 1970's that the transmission loss of optical fibers appeared at wavelength of 1.1 - 1.3 μm. Consequently, the development of laser diodes gradually shifted from the (GaAl)As/GaAs system to the InGaAsP/InP system for which the emission wavelength is 0.9- 1.5 μm. On the other hand, optical semiconductor devices for the consumer and the industrial field require light emitting diodes and laser diodes which emit visible lights(<750 nm). Naturally, high performance photodetectors are required to complement the light emitting devices. In summary, the greatest requirement for optical devices for the 1980's is for those constructed from the material whose energy band gap wavelength region is less than 750 nm (for the visible region) and greater than 1.0 μm (for the infra-red region). It is also preferable that the direct energy band gap should be in the required wavelength region.

The III-V compound semiconductors have energy band gaps which comply with above requirements.

On of the most successful optical semiconductor devices is the DH laser diode. Several other devices are also constructed using the heterostructure. However, an important problem in heterostructure devices is the lattice mismatch at the interface between the materials. In DH laser diodes, for example, rapid degradation of the laser is caused by only 0.1% lattice mismatch between the grad layer and the active layer. The lattice constant and the energy band gap can vary independently with the proportion of each constituent in the III-V quaternary solid solutions.

Therefore, development of III-V quaternary semiconductor alloys is necessary in order to obtain an energy band gap in the infra-red and visible wavelength region, and to improve the optical semiconductor device performance.

The latter part of this section discusses the classification of III-V ternary and quaternary semiconductor alloys.

The elements, which form III-V solid solutions, lies near the metal-nonmetal boundary of the periodic chart as shown in Fig. 7-1, which includes the IIa and VIa elements. The III-V compound semiconductors of interest in this work are those between Al, Ga, and In (group-III) and P, As, and Sb (group-V). Although solid solutions can be formed which contain B or N, these materials are not considered in this study.

III-V compound semiconductor alloys are categorized in the following groups, ——binary, ternary, and quaternary alloys. Although there are solid solutions which have five or more elements, such as (AlGaIn)AsP and (AlGaIn)AsPSb, discussions of these materials is neglected, because there are too many

IIb	IIIa	IVa	Va	VIa
	^{5}B	^{6}C	^{7}N	^{8}O
	^{13}Al	^{14}Si	^{15}P	^{16}S
^{30}Zn	^{31}Ga	^{32}Ge	^{33}As	^{34}Se
^{48}Cd	^{49}In	^{50}Sn	^{51}Sb	^{52}Te

Fig. 7-1.

A portion of the periodic chart showing the elements.

	Group	n*	Example
Binary	III-V	9	GaAs, InP
Ternary	III-III-V	9	(GaAl)As, (InGa)As
	III-V-V	9	Ga(AsP), In(AsP)
Quaternary	III-III-III-V	3	(AlGaIn)As, (AlGaIn)P
	III-V-V-V	3	In(AsPSb)
	III-III-V-V	9	InGaAsP, GaAlAsP

Table 7-1.

Classification of III-V semiconductors.

The pentagonary and the hexagonary alloys are neglected.

n* : Number of possible combinations.

unknown physical parameters to estimate the physical properties of these materials.

There are two sets of III-V ternary solid solutions and three sets of III-V quaternary alloys as shown in Table 7-1. In these alloys, more than one group-III element is distributed randomly on the group-III lattice sites or more than one group-V element is distributed on the group-V lattice sites. The alloys crystallize in the zinc-belnde structure. The notation most frequently used, and that adopted in this work, is $A_x^{III}B_{1-x}^{III}C_y^{V}D_{1-y}^{V}$ with A^{III} and B^{III} for the group-III elements and with C^V and D^V for the group-V elements. If A, B, and C are group-III elements and D is a group-V element, the notation $(A_x^{III}B_{1-x}^{III})_yC_{1-y}^{III}D^V$ is convenient (Casey, 1978). A similar notation is used for the solid solutions of III-V-V-V.

In ternary solid solutions, the crystal lattice constant generally varies linearly with the composition, and this behaviour can be reasonably assumed to occur also in quaternary solid solutions (Vegard's law). Linear variation with composition does not, in general, occur for the other properties. However, when detailed data are unavailable it is often necessary to use linear interpolation.

An additional degree of freedom in lattice matched III-V heteristructures may be found in quaternary crystalline solid solutions, namely, that the energy band gap and the lattice constant vary independently with compositions. $(Al_xGa_{1-x})_yIn_{1-y}As$ is, for example, lattice matched to InP for all values of x when $y = 0.47$, and has a direct energy band gap which increases linearly with x from 0.73eV to 1.55eV.

7-3. The expected physical properties of III-III-III-V quaternary alloys and their applications.

In this section, the fundamental physical properties of III-III-III-V quaternary solid solutions, which can be estimated from the end ternary solid solutions, are discussed.

7-3-1. Lattice constant and energy band gap.

The lattice constant and the energy band gap variation with composition are the primary properties of interest when considering the heterojunction. The assumption that the lattice constant of quaternary solid solutions varies linearly with composition, is known to be a good approximation (Vegard's law). With regard to the energy band gap, it is important to know not only the energy difference from the valence band to the lowest conduction band, but also the energy separation of the various conduction band minima. Therefore, it is useful to know the compositional dependence of the Γ, L, and X conduction band minima. The variation of the energy band gap with composition can often represented by

$$E_g = a + bx + cx^2, \tag{7-1}$$

for a ternary solid solution $A^{III}_x B^{III}_{1-x} C^V$ or $A^{III} C^V_x D^V_{1-x}$. The factor 'c' is termaed the bowing parameter, and has been treated theoretically by Van Vechten (1970). Of the 18 conceivable ternary systems among the group-III and group-V elements, the experimental data are available for more than half. The variation of the energy band gap, when the experiemental data are unavailable, is assumed to vary linearly with composition. Table 7-2 summarized the reported band gaps at the Γ, X, and L points for the 18 possible ternary systems.

According to Vegard's law, the lattice constant a(x,y) for $(A_x^{III}B_{1-x}^{III})_yC_{1-y}^{III}D^V$ quaternary solid solutions is represented by

$$a(x,y) = xy\cdot a_{AD} + y(1-y)\cdot a_{BD} + (1-y)\cdot a_{CD}, \qquad (7\text{-}2)$$

where a_{AD}, a_{BD}, and a_{CD} are the lattice constants of the binary compounds AD, BD, and CD, respectively. Thus, the lattice constant of $(Al_xGa_{1-x})_yIn_{1-y}As$ is represented using Eq. 7-2 as follows;

$$a(x,y) = 5.66022\cdot xy + 5.65321\cdot y(1-y) + 6.0584\cdot(1-y). \qquad (7\text{-}3)$$

When this alloy is lattice-matched to InP(a = 5.86875 Å), the relationship between x and y is

$$y = 0.18965/(0.40519\cdot x - 0.00899)$$
$$\sim 0.47 \text{ (for all values of x).} \qquad (7\text{-}4)$$

Therefore, $(Al_xGa_{1-x})_yIn_{1-y}As$ can be lattice matched to InP when y = 0.47 for all values of x. Hence, the variation of any physical property with composition for $(Al_xGa_{1-x})_yIn_{1-y}As$ can be represented as a function of x alone. This due to the fact that AlAs and GaAs have nearly the same lattice constant (see Table 2-1.).

The energy band gap $E_g(x,y)$ of $A_x^{III}B_{1-x}^{III})_yC_{1-y}^{III}D^V$ can be

Ternary Alloy	Type of Energy Band *	Γ (eV)	X (eV)	L (eV)
$Al_xGa_{1-x}P$	D → I	-	-	-
$Al_xGa_{1-x}As$	D → I	$1.424+1.247x$ $(x<0.45)$ $1.424+1.247x+$ $1.147(x-0.45)^2$ $(x>0.45)$	$1.900+0.125x+0.143x^2$	$1.708+0.642x$
$Al_xGa_{1-x}Sb$	D → I	$0.726+1.129x+0.368x^2$	$1.020+0.492x+0.077x^2$	$0.799+0.746x+0.334x^2$
$Al_xIn_{1-x}P$	D → I	$1.351+2.23\ x$	-	-
$Al_xIn_{1-x}As$	D → I	$0.360+2.012x+0.698x^2$	-	-
$Al_xIn_{1-x}Sb$	D → I	$0.172+1.621x+0.43\ x^2$	-	-
$Ga_xIn_{1-x}P$	D → I	$1.351+0.643x+0.768x^2$	-	-
$Ga_xIn_{1-x}As$	D → D	$0.35\ +0.63\ x+0.45\ x^2$	-	-
$Ga_xIn_{1-x}Sb$	D → D	$0.172+0.139x+0.415x^2$	-	-
$Al\ P_xAs_{1-x}$	I → I	-	-	-
$Al\ P_xSb_{1-x}$	I → I	-	-	-
$AlAs_xSb_{1-x}$	I → I	-	-	-
$Ga\ P_xAs_{1-x}$	D → I	$1.424+1.150x+0.176x^2$	$1.977+0.355x+$ $0.211 \cdot x(x-1)^2$ (77K)	$1.802+0.93x+$ $0.160 \cdot x(x-1)^2$ (77K)
$Ga\ P_xSb_{1-x}$	D → I	-	-	-
$GaAs_xSb_{1-x}$	D → D	$0.726-0.512x+1.2\ \ x^2$	-	-
$In\ P_xAs_{1-x}$	D → D	$0.360+0.891x+0.101x^2$	-	-
$In\ P_xSb_{1-x}$	D → D	-	-	-
$InAs_xSb_{1-x}$	D → D	$0.18-0.41\ x+0.58\ x^2$	-	-

Table 7-2.

The reported energy band gaps at the Γ, X, and L points for the 18 possible III-V ternary systems at room temperature.

*) D : Direct energy band

I : Indirect energy band.

obtained by interpolation between the energy band gaps of the end ternary solid solutions. $E_g^i(x,y)$ ($i = \Gamma$, X, and L) can therefore be represented by

$$E_g^i(x,y) = (1-x)\cdot E_g^i(0,y) + x\cdot E_g^i(1,y), \qquad (7\text{-}5)$$

where $i = \Gamma$, X, and L. In Eq. 7-5, the bowing factor is neglected for simplicity and because there are some ternary a alloys for which the bowing parameter 'c' has not be determined experimentally (see Table7-2.). The energy band gap $E_g^i(x,y)$ ($i = \Gamma$, X, and L) of $A^{III}(B_x^V C_{1-x}^V)_y D_{1-y}^V$ can be represented in the same manner as that for $(A_x^{III} B_{1-x}^{III})_y C_{1-y}^{III} D^V$.

The lowest energy band gap of $(Al_xGa_{1-x})_yIn_{1-y}As$ can be written as follows using the values listed in Table 7-1.

$$E_g^\Gamma(x,y)\ (\mathrm{eV}) = (1-x)\cdot(0.35 + 0.63y + 0.45y^2) + x\cdot(0.36 + 2.49y) \text{ for } 0.68 > y > 0,$$

and $$E_g^\Gamma(x,y)\ (\mathrm{eV}) = (1-x)\cdot(0.35 + 0.63y + 0.45y^2) + x\cdot(1.81 + 0.353y) \text{ for } 1.0 > y > 0.68. \qquad (7\text{-}6)$$

Figure 7-2 shows the energy band gap and lattice constant contours superimposed on the x-y composition plane. The compositional plane is a triangle for $(A_x^{III} B_{1-x}^{III})_y C_{1-y}^{III} D^V$ and $A^{III}(B_x^V C_{1-x}^V)_y D_{1-y}^V$ rather than a square as in the case of $A_x^{III} B_{1-x}^{III} C_y^V D_{1-y}^V$. The relationship between the lattice constant and the energy band gap is shown in Fig. 7-3. The data for $(Al_xGa_{1-x})_yIn_{1-y}P$ and $In_{1-x}Ga_xAs_{1-y}P_y$ are also shown in this figure. It can be seen that (AlGaIn)As lattice matched to InP has a wider direct energy band gap than that of the InGaAsP/InP system, and that (AlGaIn)P lattice matched

(a)

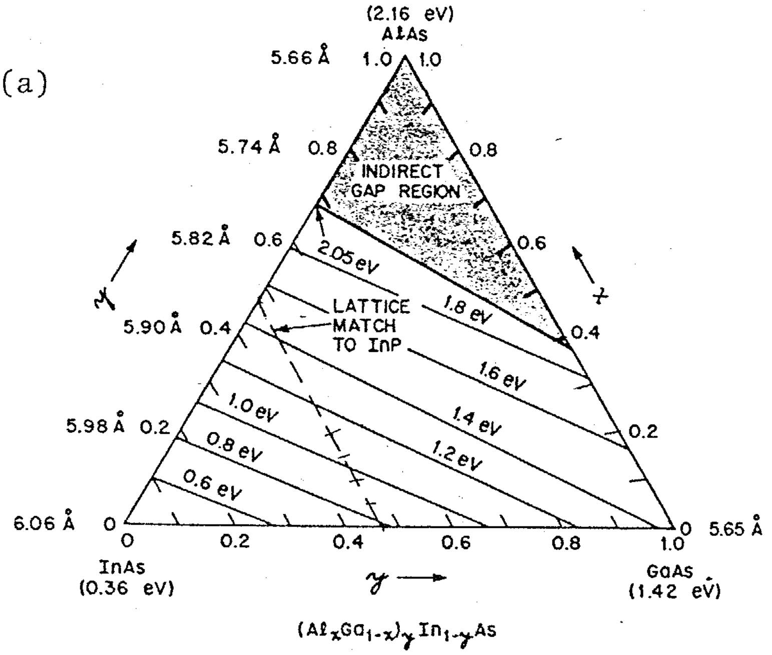

(b)

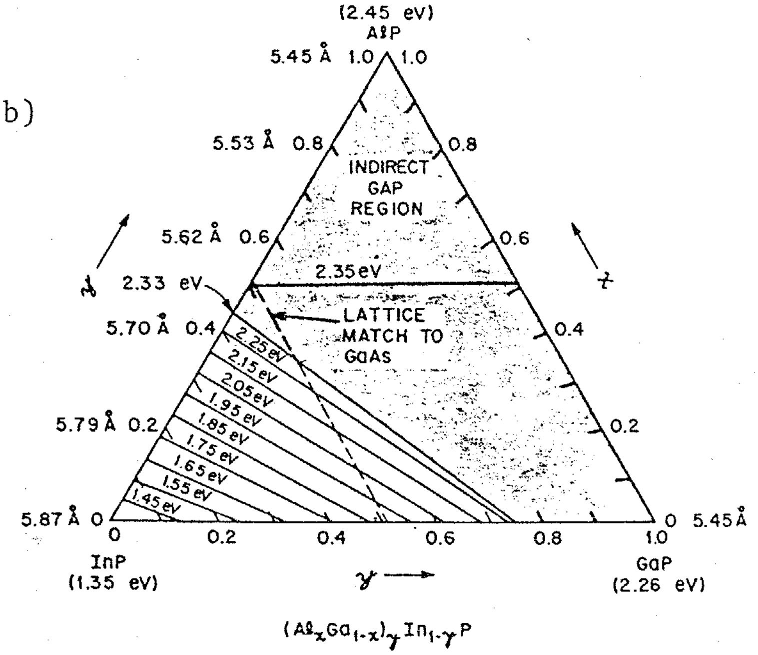

Fig. 7-2.
The x-y compositional planes for $(Al_xGa_{1-x})_yIn_{1-y}As$ and $(Al_xGa_{1-x})_yIn_{1-y}P$ at 300K. The solid lines are constant direct-energy band-gap values by a linear extrapolation of E_g from the end ternary solid solutions. The dashed lines represent the InP lattice constant (in (a)) and the GaAs lattice constant (in (b)).

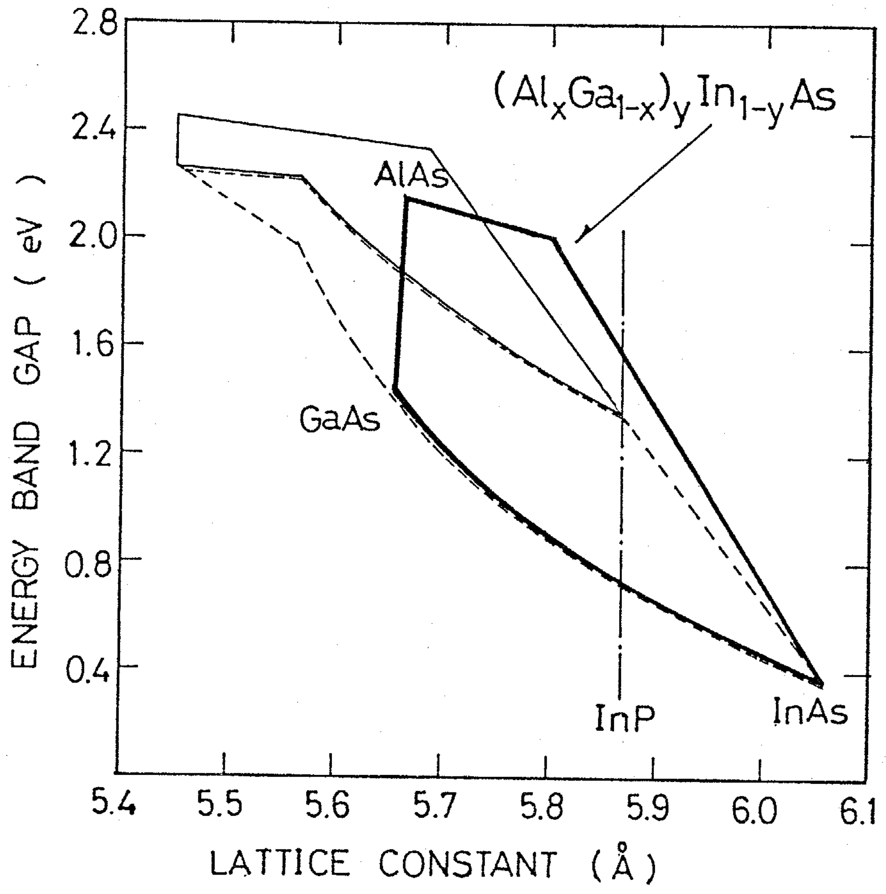

Fig. 7-3.

The relationship between the lattice constant and the energy band gap of three quaternary III-V semiconductors.

Thick line (▬▬) : (AlGaIn)As in this work.

Thin lime (——) : (AlGaIn)P.

Broken line(–––) : InGaAsP.

GaAs has a wider direct energy band gap than that the (GaAl)As/GaAs system. It is noteworthy that $(Al_xGa_{1-x})_yIn_{1-y}P$/GaAs is the only III-V material which produces a laser diode operating in the visible wavelength region ($\lambda < 750$ nm). It is clear that these III-III-III-V materials are amongst the most attractive materials for opto-electronic devices operating in the infra-red and visible wavelength regions as discussed in Sec. 7-2.

The energy band gap of $(Al_xGa_{1-x})_yIn_{1-y}As$ lattice matched to InP as a function of composition is shown in Fig. 7-4.

The direct energy band gap of this material increases with x from 0.73eV to 1.55eV.

7-3-2. Application to opto-electronic devices.

One of the most useful application of these materials the DH laser diode. Heterostructures utilizing the $y = 0.47$ $(Al_xGa_{1-x})_yIn_{1-y}As$ quaternary are of particular interest. Structures on an InP substrate of

$$n\text{-}(Al_{x'}Ga_{1-x'})_{0.47}In_{0.53}As/n\text{- or } p\text{-}(Al_xGa_{1-x})_{0.47}In_{0.53}As/ /p\text{-}(Al_{x'}Ga_{1-x'})_{0.47}In_{0.53}As$$

with $x' > x$ would give laser emission from 0.73eV to 1.35eV for values of x up to 0.8. The prospect of laser emission in the 1.2-1.3 μm range is an interesting possibility for this system. The avalanche photodiode with a super-lattice structure is also available using this system (Cappasso, 1981).

The heterostructure constructed with $y = 0.53$ $(Al_xGa_{1-x})_yIn_{1-y}P$ would give laser emission from 1.8eV to 2.15eV for values of x up to 0.8.

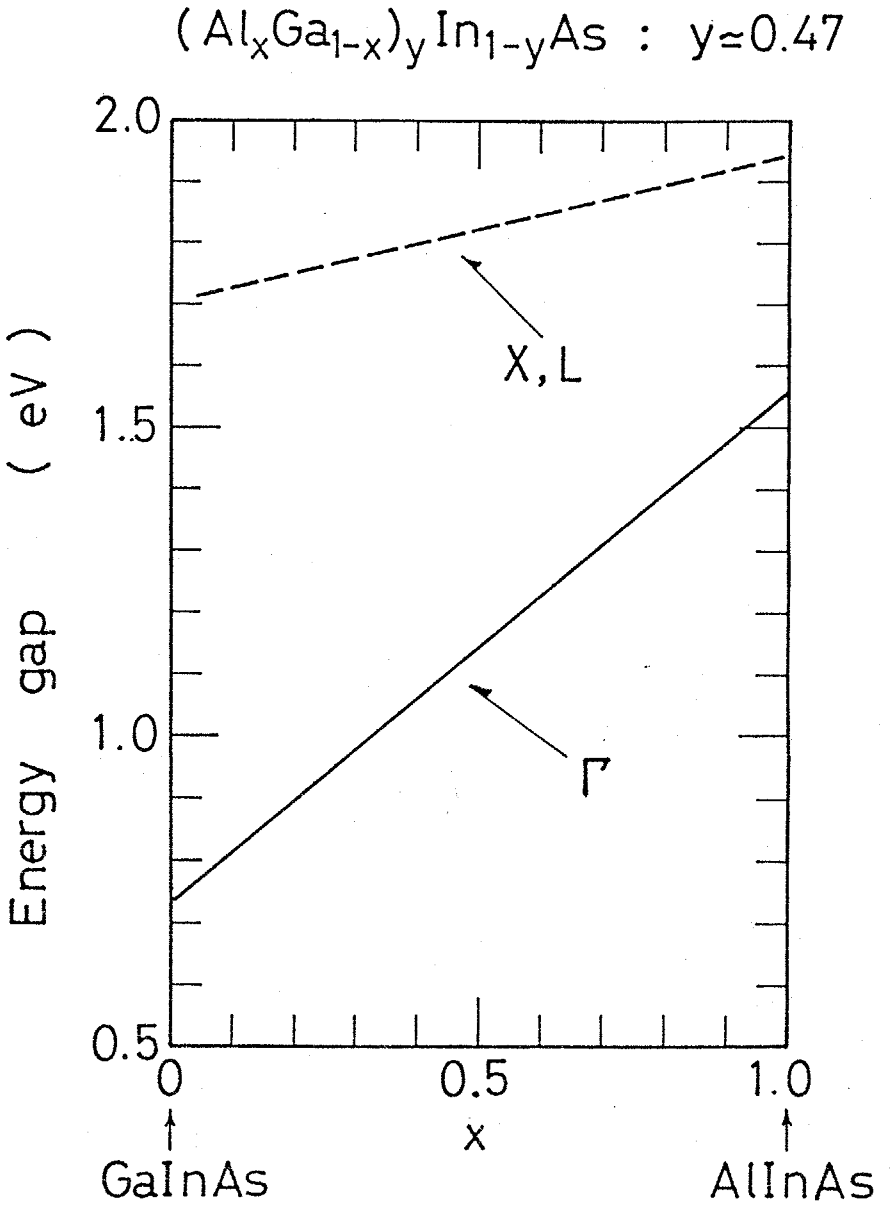

Fig. 7-4.

The energy band gaps of $(Al_xGa_{1-x})_yIn_{1-y}As$ lattice matched to InP as a function of x, calculated using Eq. 7-3 to Eq. 7-6. The X and L point energy band gaps gaps are of approximately the same value.

7-4. Possibility of epitaxial growth of III-III-III-V quaternary alloys.

The III-III-III-V quaternary solid solutions are new candidates for the manufacture of opto-electronic devices operating in the visible and infra-red wavelength region as discussed in the previous section. Consequently, it is important to consider the crystal growth techniques for these materials. It is concluded in the following discussions that MBE is a more suitable epitaxial growth technique than LPE $(Al_xGa_{1-x})_yIn_{1-y}As$.

7-4-1. Liquid phase epitaxy.

When preparing III-V compounds using liquid phase epitaxy, it is first necessary to calculate the phase equilibria. The liquidus-solidus phase diagram of III-III-III-V compounds can be calculated using the quasi-regular solution approximaion. Details of the quasi-regular solution approximation are described in Appendix A. Figure 7-5 shows the results of the phase equilibria calculations at 640°C for an (AlGaIn)As quaternary alloy lattice matched to InP. In the LPE process for this alloy using an InP substrate, the liquidus melt consists of Al, GaAs, InAs, and In. The required amounts of Al, GaAs, and InAs for 0.4g of In are shown in Fig. 7-6. As can be seen from Fig. 7-5 and Fig. 7-6 the required amount of Al is very small over the entire range of x for the lattice matched ~~condi~~ condition. This situation is confirmed by calculating the compositional change in the epitaxial layer.

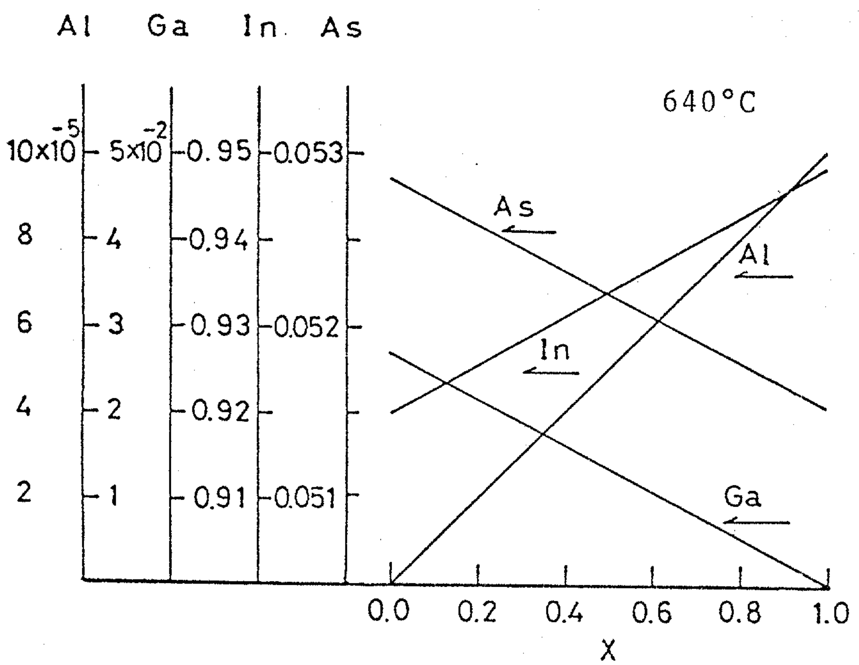

Fig. 7-5.
Results of the phase equilibria calculations at 640°C for $(Al_xGa_{1-x})_yIn_{1-y}As$ lattice matched to InP. The horizontal scale is x, and y is given by Eq. 7-4. The vertical axes give the composition of the liquid in equilibrium with this solid. Note there are four differnt vertical scales and also that not all the scales begine at zero.

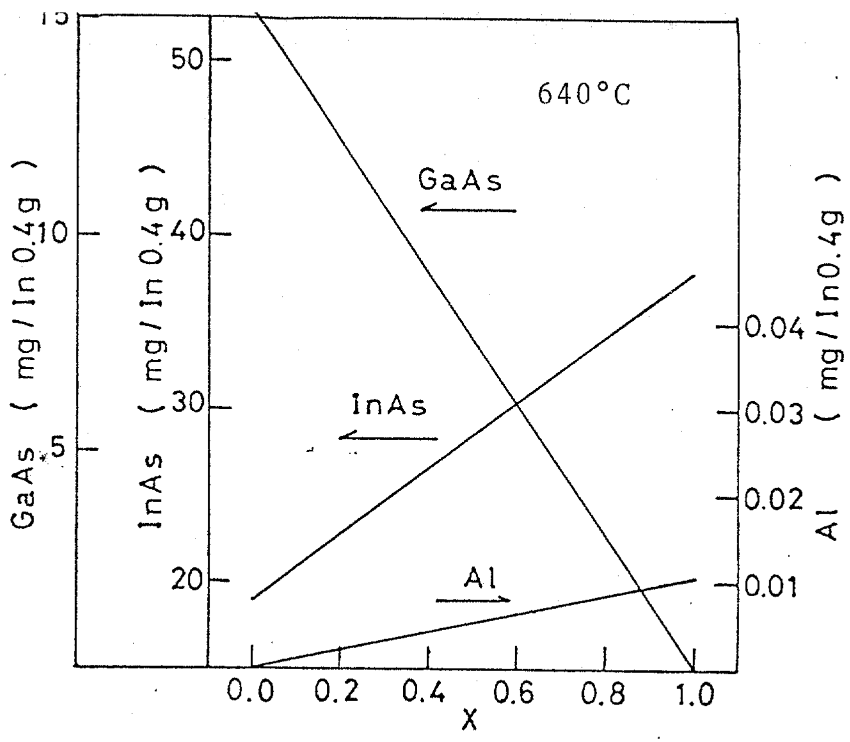

Fig. 7-6.
Amount of Al, GaAs, and InAs in the equilibrium liquid solution at 640°C. The solvent is indium (assumed to be 0.4 g). ›e 0.4g.

he compositional change in the epitaxial layer can be alculated using the quasi-equilibrium process (Ilegems, 1974; sozumi, 1977, Ijuin, 1976). Figure 7-7 shows the com- ositional change in $(Al_xGa_{1-x})_yIn_{1-y}As$ during the cooling rocess from 700°C. The Al mole fraction in the solid solution ecreases rapidly due to the depletion of Al in the liquid olution. It can be concluded, from the above results, that he epitaxial growth of an $(Al_xGa_{1-x})_yIn_{1-y}As$ quaternary solid olutions on an InP substrate is very difficult because of the mall amount of Al in the equilibrium liquid solution. This ituation derives from the large segregation coefficient of Al. urthermore, the epitaxial growth of these materials was xperimentally impossible by the usual LPE method.

Although the above discussions are restricted to the $Al_xGa_{1-x})_yIn_{1-y}As$/InP system, the calculation for $Al_xGa_{1-x})_yIn_{1-y}P$ quaternary solid solutions shows that the pitaxial growth of these alloys is more difficult than for $Al_xGa_{1-x})_yIn_{1-y}As$.

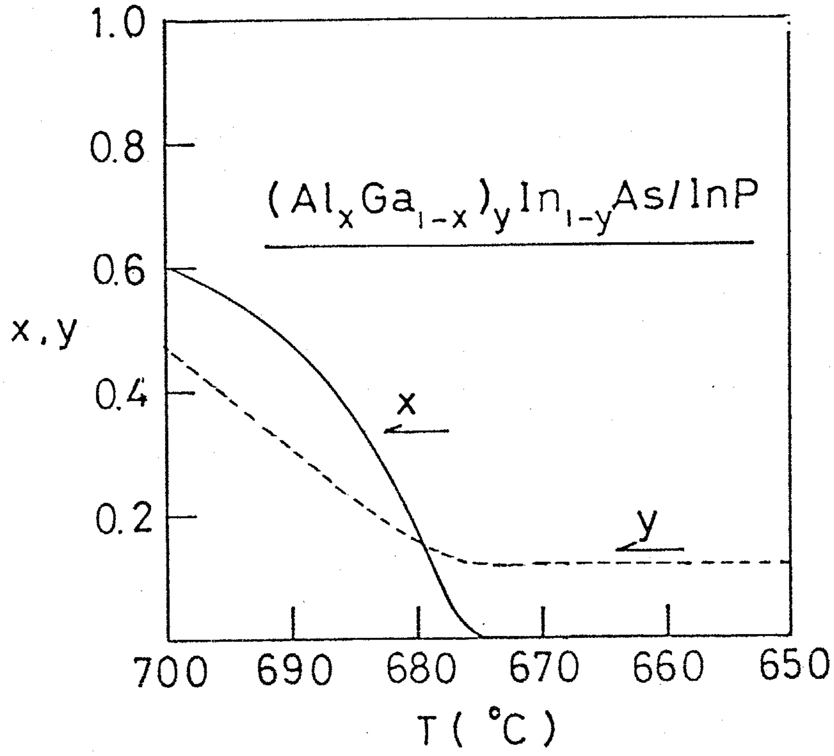

Fig. 7-7.

Compositional change in $(Al_xGa_{1-x})_yIn_{1-y}As$ during the cooling process from 700°C. The quasi-equilibrium process is assumed in the calculation.

At 700°C the solid solution is $x=0.6$ and $y=0.47$, which is lattice matched to InP. The rapid decrease of the Al mole fraction in the solid solution is due to the depletion of Al in the liquidus melt.

7-4-2. Molecular beam epitaxy.

Molecular beam epitaxy (MBE) is a growth technique in which epitaxial layers are produced by impinging thermal beams of molecules or atoms upon a heated substrate under ultra-high vacuum conditions. As MBE is essentially a non-equilibrium growth process, the composition in the epitaxial layer can be easily controlled by the flux of each molecular beam. When $Ga_{1-x}Al_xAs$ is grown on a GaAs substrate, there are three molecular beams, namely Ga, Al, and As.
The sticking coefficient of group-III elements is generally about one. Hence, the arsenic beam flux is usually greater than the required quantity, because the sticking probability of As depends on the availability of unsaturated group-III elements of Ga and Al. Consequently, the Al composition in the $Ga_{1-x}Al_xAs$ epitaxial layer is controlled by the ratio of the flux of the Al molecular beam and to that of the Ga beam. The III-III-III-V quaternary alloys, such as (AlGaIn)As, have only one group-V element, and the composition of the group-III elements can be controlled by the fluxes of the group-III molecular beams. On the other hand, III-III-V-V quaternary alloys, such as InGaAsP, have more than one group-V element, and the compositional control is more difficult than that for a III-III-III-V quaternary alloy, because the sticking probability of the group-V elements depends on the availability of unsaturated group-III elements as discussed above. Furthermore, the vapour pressure of the group-V elements is generally higher than that of group-III elements.

Hence, it is concluded that the growth of III-III-III-V uateranry alloys is possible using MBE, and is easier than the sual LPE method, because MBE is essentially a non-equilibrium rowth process.

-5. Summary and conclusion .

III-V quaternary semiconductor alloys are classified into hree sets, namely III-III-III-V, III-III-V-V, and III-V-V-V. $Al_xGa_{1-x})_yIn_{1-y}As$ and $(Al_xGa_{1-x})_yIn_{1-y}P$ lattice matched to uitable substrates (InP and GaAs, respectively) which belong o the III-III-III-V solid solutions are expected to be used aterials for opto-electronic devices operating in the infra-ed (0.9÷1.6 µm) and visible (<0.75 µm) wavelength regions, espectively.

Liquid phase epitaxy and molecular beam epitaxy are onsidered as epitaxial growth techniques for these materials. rom a calculation of the phase equilibria, it was shown that t is difficult to produce these materials using the conventional onventional LPE method because of the large segregation oefficient of Al. On the other hand, MBE in which epitaxial ayers are grown by impinging thermal beams of molecules upon heated substrate, is shown to be the most suitable growth echnique.

CHAPTER 8.

CRYSTAL GROWTH AND PHYSICAL PROPERTIES OF $(Al_xGa_{1-x})_yIn_{1-y}As$ LATTICE MATCHED TO InP SUBSTRATES GROWN BY MOLECULAR BEAM EPITAXY.

8-1. Introducition.

III-III-III-V quaternary alloys are one of the most promising materials for opto-electronic devices in the infra-red and visible wavelength region. As discussed in the previous chapter, MBE is a suitable growth technique for these materials.

In this chapter, the first reported preparation of $(Al_xGa_{1-x})_yIn_{1-y}As$ is described. Preparation was by the MBE technique. $(Al_xGa_{1-x})_yIn_{1-y}As$ is a III-III-III-V quaternary alloy and is a suitable material for the infra-red wave-legth region. In Sec. 8-2, fundamentals of the MBE are summarized. In Sec. 8-3 and Sec. 8-4, the epitaxial growth and fundamental physical properties of $(Al_xGa_{1-x})_yIn_{1-y}As$ lattice matched to an InP substrate are discussed.

8-2. Fundamentals of molecular beam epitaxy.

8-2-1. What is molecular beam epitaxy ?

The essential components for a MBE system for $Ga_{1-x}Al_xAs$ are illustrated in Fig. 8-1. However, implemetation which is discussed in Sec. 8-3, is more complex than this drawing implies. Molecular beam epitaxy (MBE) is the epitaxial growth technique on a heated single crystal substrate (GaAs in Fig. 8-1) placed in an ultra-high vacuum ($\lesssim 10^{-9}$ torr) through the reaction of a number of different molecular beams (Ga, Al, As, and dopants) of differing intensities. Each furnace contains a crucible that holds one of the constituent elements or compounds of the desired epitaxial film. The temperature of each furnace is chosen to generate a molecular beam of the appropriate intensity. By choosing appropriate furnace and substrate temperatures,stoichiometric epitaxial films of the desired chemical composition can be obtained. The beam flux at the substrate is abruptly changed and stopped by individual shutters placed between each furnace and the substrate. When III-V compounds are grown, the epitaxial growth was carried out in an excess group-V element flux, because a fortuitous dependence of the sticking probability on unsaturated group-III elements allows stoichiometric III-V compounds to be obtained simply.

The strength of the MBE process lies mainly in its unprecedental precision in controlling dopant concentration and epitaxial thickness in layers as thin as a few tens of angstroms, with an exceptional interface morphology and uniformity of the epitaxial layer thickness that is easily reproducible. Furthermore, as the MBE chamber is maintained in an ultrahigh vacuum, instruments for various surface analysis techniques can be contained in the system.

MBE has various distinguishing features and advantages

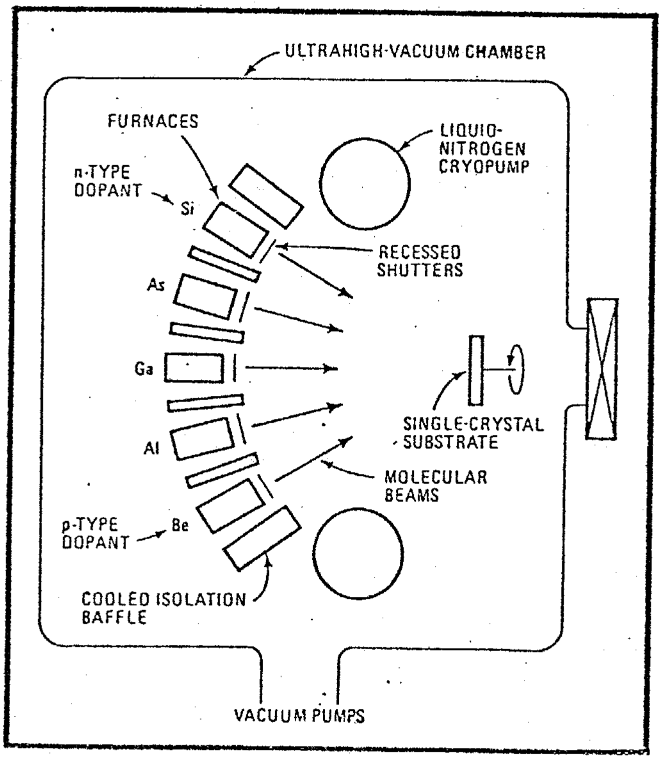

Fig. 8-1.

Molecular beam epitaxy. In molecular beam epitaxy, film growth takes plase in ultrahigh vacuum. Molecular beams with different intensities and chemistries are focused on a heated substrate. The diagram shows the essential components for molecular growth of (GaAl)As.

Group III-V	GaAs, GaP, GaSb, AlAs, InAs, InP, InSb, AlGaAs, GaInP, GaAsSb, GaAsP InGaAsP, AlGaInAs*, AlGaInP**
Group IV	Ge, Ge-Si, Si
Group II-VI	CdSe, CdS, CdTe, ZnSe, ZnS, ZnTe, ZnSeTe
Group IV-VI	PbSe, PbS, PbTe, SnTe, PbGeTe, PbSeTe, PbGeTe, PbSeTe, PbSnSe, PbSnTe
Metal	Al, Au, Ag

Table 8-1.

Semiconductors and metals grown by molecular beam epitaxy.

*) Preparation of AlGaInAs was first reported independently by the author and the Cornell University group in Sept.,1981.

*) Preparation of AlGaInP was also reported in Sept., 1981.

compared with LPE and VPE, and it is no over simplification to say that these arise only from that fact that MBE take place in an ultrahigh vaccum environment.

As many review papers (Luscher, 1977, 1980; Panish, 1980) have been published concerning MBE, further discussions are omitted. Each of the various epitaxial growth techniques, MBE, LPE, VPE, and MO-CVD, has advantages and disadvantages in preparing epitaxial layers for specific devices and a comparison of these techniques was summarized in Table 2-4.

It is worth emphasizing that MBE is a particularly technique for the development of new materials, because the epitaxial film can be easily formed by the impinging molecular beams on the heated substrate.

8-2-2. Device applications using molecular beam epitaxy.

Fabrication of a variety of microwave and opto-electronic devices using MBE has been described in the literature with increasing frequency over the past eight years. During this period, steady improvement in materials and growth process has resulted in performance and fabrication yields that are the equivalent of or that exceed those of similar discrete devices grown by other epitaxial growth techniques.

Several planar isolation processes unique to MBE have been developed by scientists at Bell Lab. and employed in the fabrication of both of the above device categories. These techniques, along with selective ion implantations, promise unique monolithic integration capability. In addition, the precision of MBE has been applied to the development of totally new materials and devices in both the microwave and opto-electronic fields. These studies indicate a greate potential for unique and significant commercial applications.

Specific examples of devices fabricated using MBE illustrate the process's important capabilities. Table 8-1 lists most of the materials that have been grown by MBE. Of the various materials that have been grown by MBE, GaAs and (GaAl)As have been most extensively studied, and many literautures have reported the preparation of DH laser diodes and FETs with high electron mobility.

(GaAl)As/GaAs DH laser diodes have been studied at Bell Lab. (Tsang, 1979), and this work has shown that MBE can produce high quality (GaAl)As/GaAs heterostructures similar to those prepared by LPE. FETs with high electron mobility, termed HEMT (High Electron Mobility Transistor), have been studied at Fujitsu Lab. In this device, electrons are confined in a high-purity n-GaAs region by using a (GaAl)As/GaAs heterostructure (Miura, 1980; Hiyamizu, 1980). Their work has received wide attention because they have shown that the precision of MBE in controlling epitaxial thickness in layers enables the preparation of FET in which quantum-mechanics-effect are utilized.

8-3. Epitaxial growth of $(Al_xGa_{1-x})_yIn_{1-y}As$ on InP substrates.

8-3-1. The molecular beam epitaxy system.

Figure 8-2 shows the MBE system used in this work. Principle components of this MBE system are (1) the main chamber, (2) the vacuum pumps (ion pump, Ti sublimation pump, and sorption pump.), (3) the specimen-exchange vacuum load lock, (4) the chemical analysis equipment (QMS and MEED), and (5) the temperature control unit.

The main vacuum chamber, which is made of steel, is 50cm in diameter and about 50cm tall and is always maintained at 10^{-9}torr by the 500 litter/sec ion pump. The chamber contains the heated substrate holder and six effusion cells for epitaxial growth, and the QMS and the MEED gun for chemical analysis.

The substrate exchange load lock is an integral part of this system, and it is not necessary to expose the main chamber to atmospheric pressure when changing specimens. Hence, for periods of weeks the main chamber remains unbroken. When one of the effusion cells is empty (usually the arsenic cell), it becomes necessary to expose the main chamber to atmospheric pressure in order to load the constituent element into the effusion cell.

In order to obtain high purity films, it is necessary to reduce contamination from the effusion cell, etc.. The effusion cells are made of pyrolytic BN and the heaters are made of tantalum. Five of the effusion cells (the exception

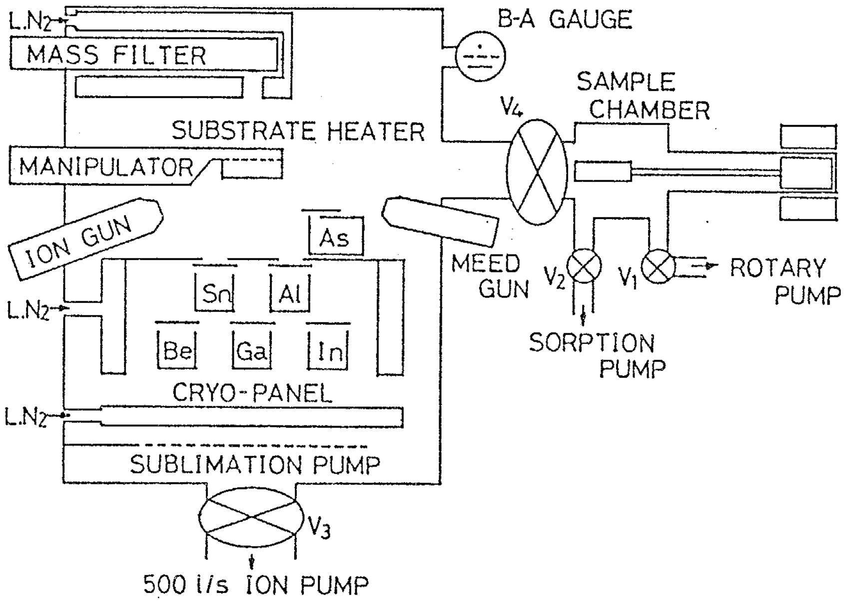

(a) block diagram.

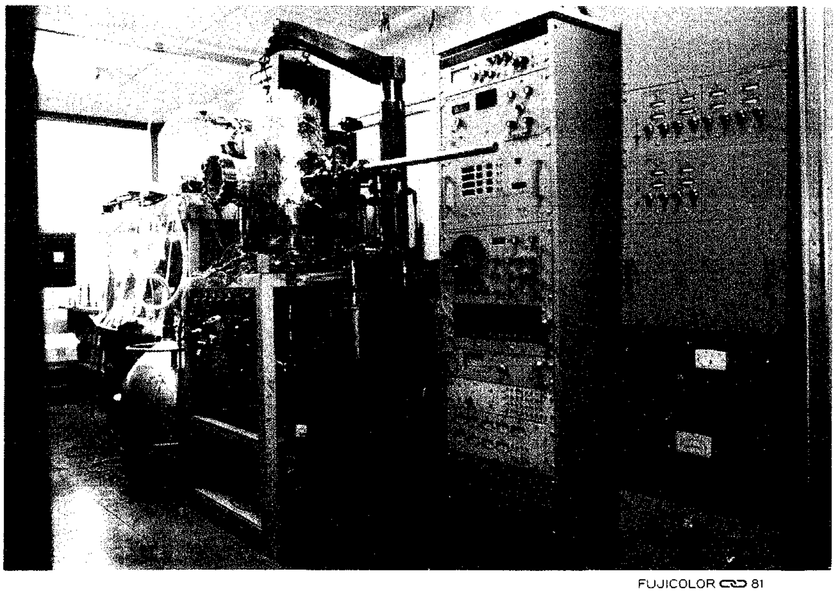

(b) Overview.

Fig. 8-2. The MBE system used in this work.

being the arsenic cell) are surrounded by liquid-nitrogen-cooled baffles to reduce the contamination from the heated effusion cells.

8-3-2. The epitaxial growth process.

The flow chart for the epitaxial growth of (AlGaIn)As by MBE is shown in Fig. 8-3.

The substrates were (100) n^+-InP wafers or (100) Fe-doped semi-insulating InP wafers and the surface area was usually 5x5mm^2.

Before crystal growth of a required film, the substrate was heated to about 30°C higher than the growth temperature, and was simultaneously exposed to an arsenic beam for surface cleanig. This technique is usual for the MBE process.

The intensities of each constituent element were controlled by the effusion cell temperatures, and the effusion cell temperatures were determined from the usual vapour pressure curves. Figure 8-4 shows the temperatures of each effusion cell and substrate at epitaxial growth. The growth rate for (AlGaIn)As was about 0.7-1.0μm/hr for $0<x<0.5$ and $y=0.47$.

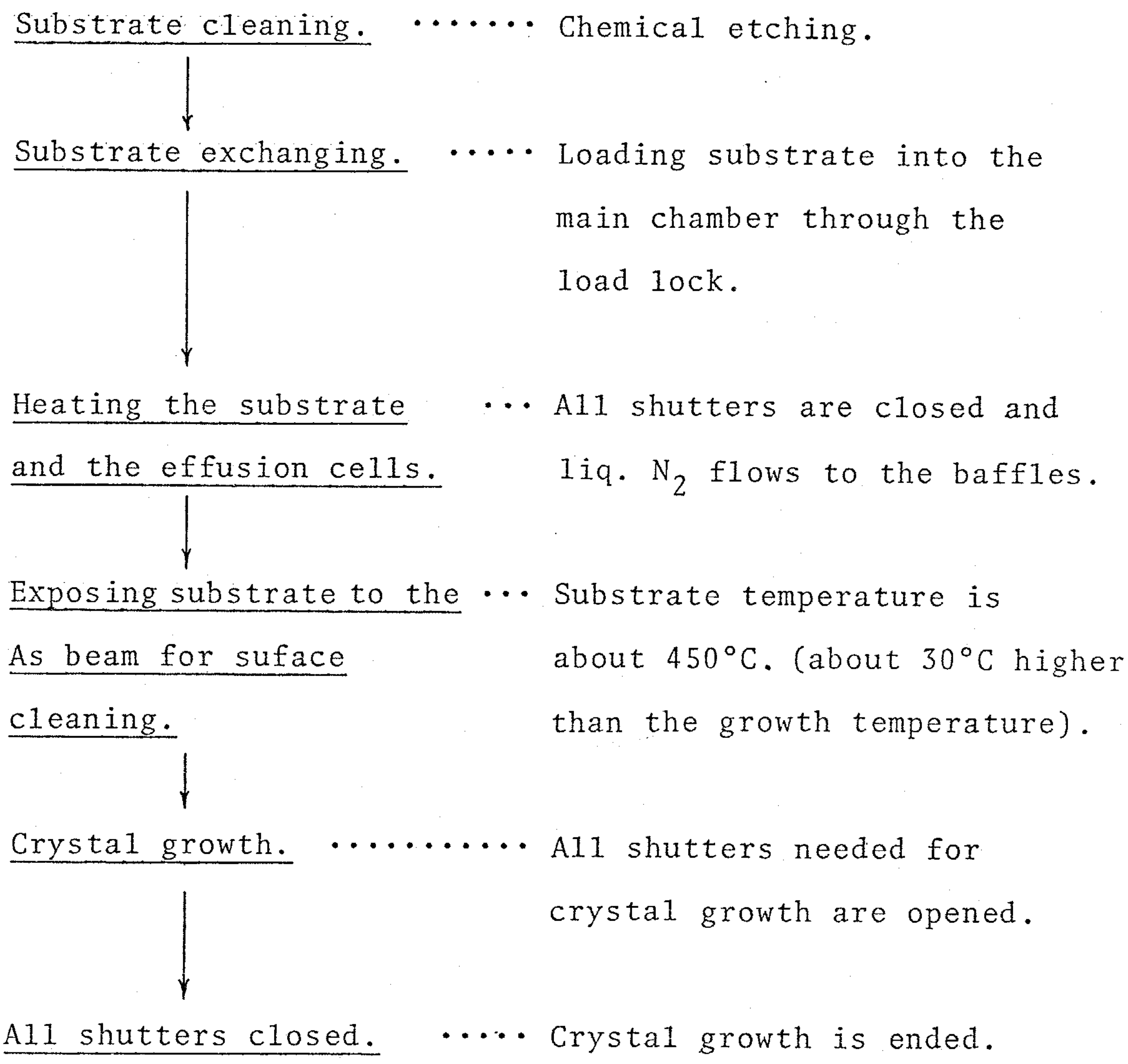

Substrate cleaning. ······· Chemical etching.

Substrate exchanging. ····· Loading substrate into the main chamber through the load lock.

Heating the substrate and the effusion cells. ··· All shutters are closed and liq. N_2 flows to the baffles.

Exposing substrate to the As beam for suface cleaning. ··· Substrate temperature is about 450°C. (about 30°C higher than the growth temperature).

Crystal growth. ············ All shutters needed for crystal growth are opened.

All shutters closed. ····· Crystal growth is ended.

Fig. 8-3.

The epitaxial growth process.

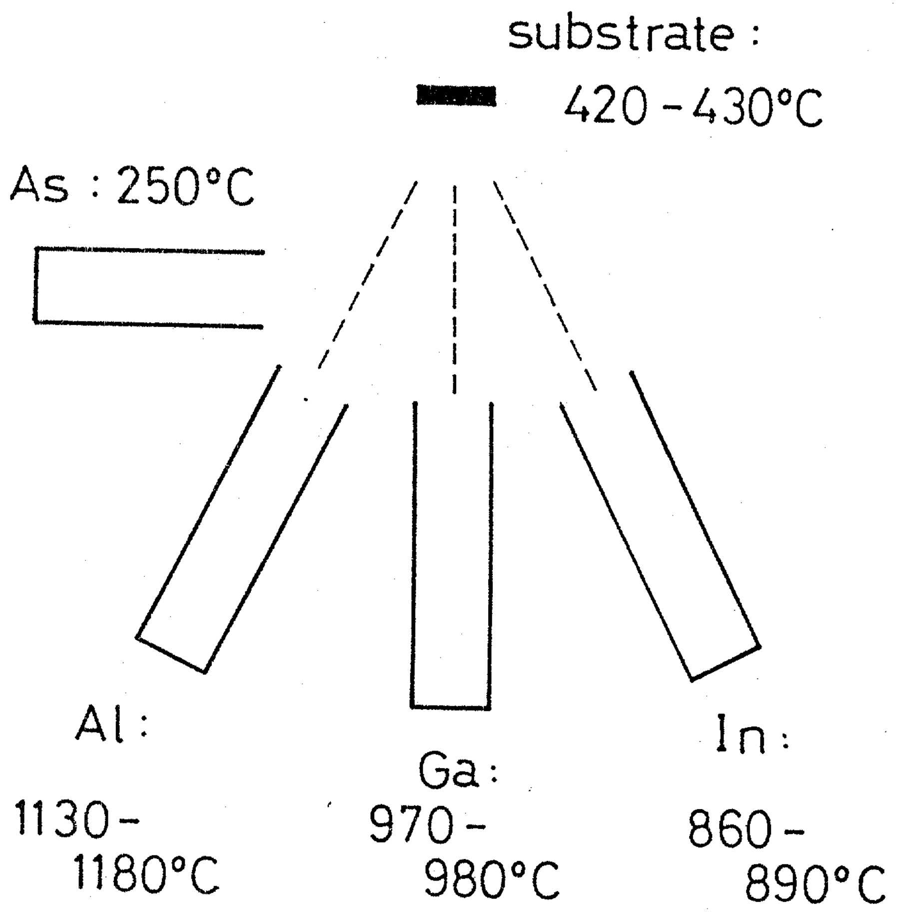

Fig. 8-4. Temperatures of each effusion cell and substrate.

8-3-3. Crystal growth of $(Al_xGa_{1-x})_yIn_{1-y}As$.

Figure 8-5 shows typical X-ray diffraction curves of $(Al_xGa_{1-x})_yIn_{1-y}As$ on InP substrates when $\Delta a/a \sim 0.4\%$ and $\Delta a/a < 0.05\%$ (very close lattice matched to InP). Epitaxial layers with less than 0.1% lattice-mismatch were selected. Their physical properties are evaluated in this section and in Sec. 8-4.

The RHEED patterns of the $(Al_xGa_{1-x})_{0.47}In_{0.53}As$ epitaxial layers indicated that the layers consisted of a single crystal. Figure 8-6 shows a typical RHEED pattern which was observed at V_{ac}=50keV.

In many studies concerning the epitaxial growth of (InGa)As on an InP substrate, poor surface morphologies were observed (Kawamura, 1981). However, good surface morphologies were obtained for $(Al_xGa_{1-x})_{0.47}In_{0.53}As$ on InP in this work. Figure 8-7 shows a typical photograph of the epitaxial layer placed on blue section paper. As the surface is mirror-like, the epitaxial surface reflects section lines. Figure 8-8 shows the surface morphology by SEM at magnifications of $2x10^3$ and $1x10^4$. In these photographs, the white parts are dust particles remaining on the epitaxial surface. Even at a magnification of 10^4, no structual features can be observed.

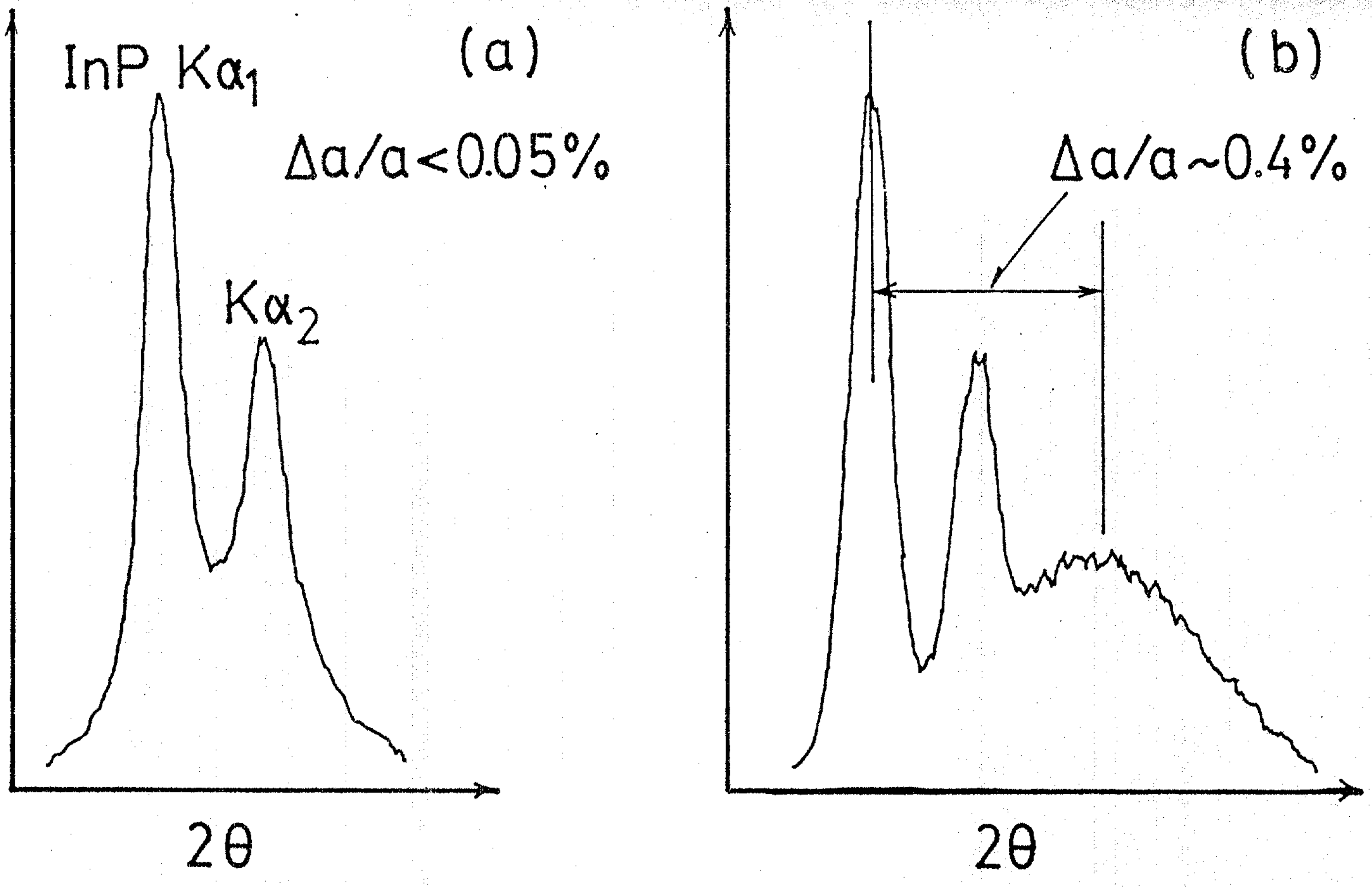

Fig. 8-5.

Typical X-ray diffraction curves. The lattice mismatches between the epitaxial layer and the InP substrate are $\Delta a/a<0.05\%$ in (a) and $\Delta a/a\sim 0.4\%$ in (b).

Fig. 8-6.

The RHEED pattern of $(Al_{0.5}Ga_{0.5})_{0.47}In_{0.53}As$ on a (100) n^{+}-InP substrate (V_{ac}=50keV).

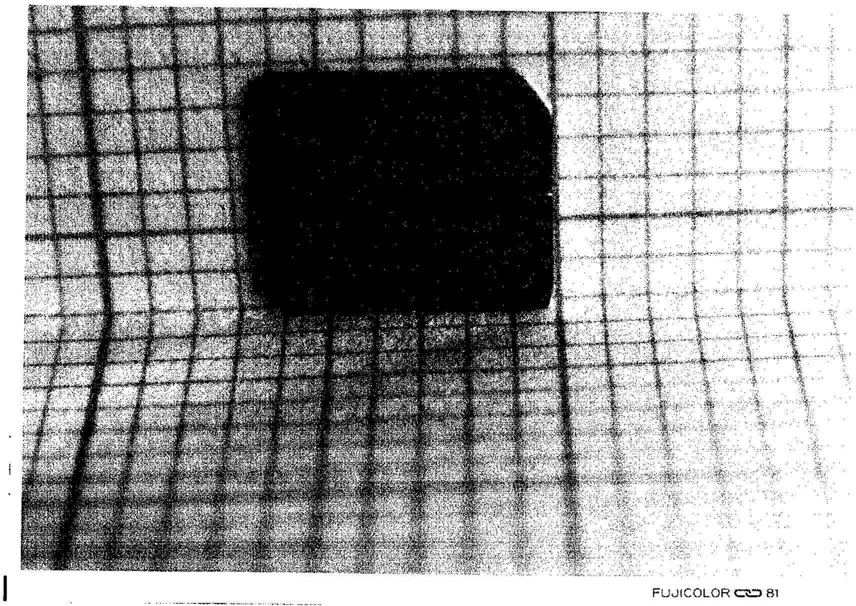

Fig. 8-7.

$(Al_{0.7}Ga_{0.3})_{0.47}In_{0.53}As$ on an InP substrate, which is placed on a blue section paper.

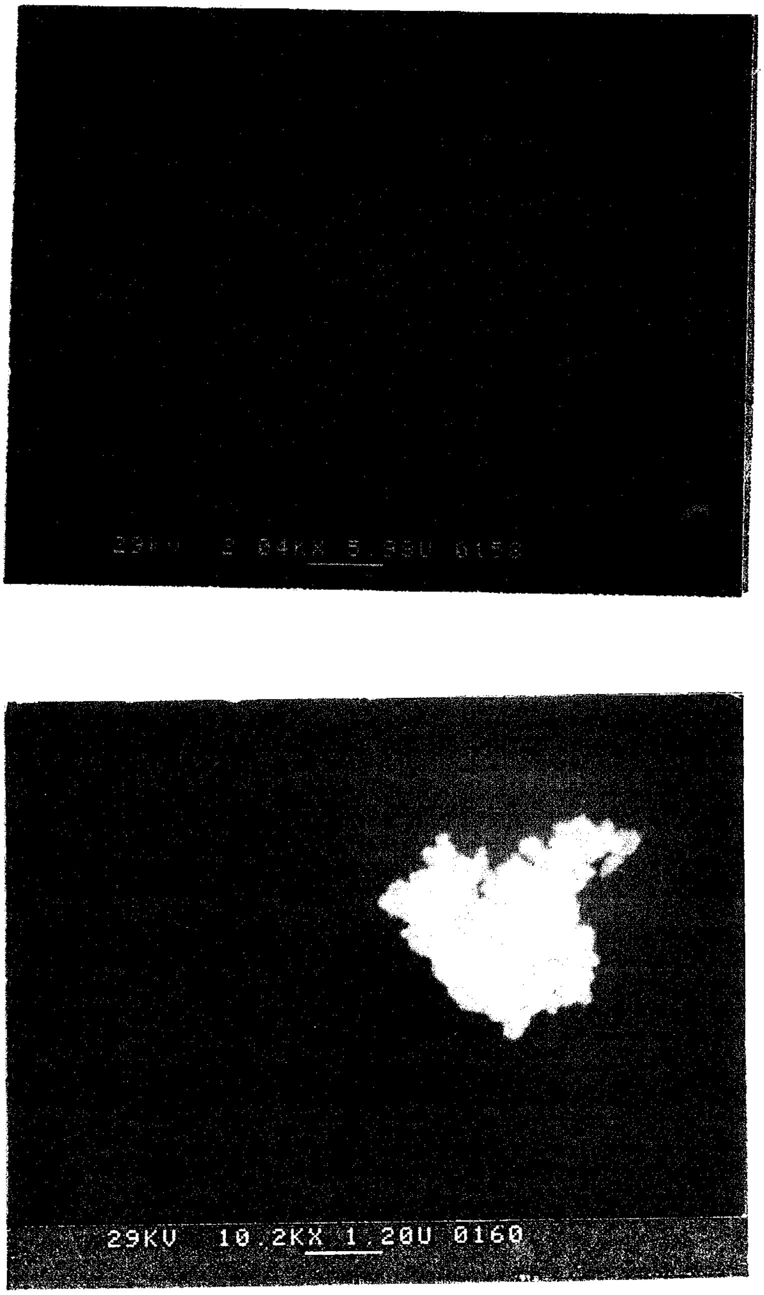

The SEM inspection of $(Al_{0.7}Ga_{0.3})_{0.47}In_{0.53}As$ on an InP substrate. The white parts are the dust remaining on the epitaxial surfaces. No structual features can be observed at a magnification of 10^4.

8-4. Fundamental physical properties of $(Al_xGa_{1-x})_yIn_{1-y}As$, lattice matched to InP substrates.

8-4-1. Energy band gap.

One of the primary physical properties is the compositional dependence of the energy band gap. The energy band gaps were evaluated from the absorption edges.
The absorption coefficient was obtained from measurements of the room temperature transmittance. As the energy band gap of InP (1.35eV) is larger than that of $(Al_xGa_{1-x})_{0.47}In_{0.53}As$ when $x<0.75$, the transmittance could be measured with monochromatic light incident on the mirror-polished InP side.

Taking account of multiple reflection, the total transmittance is given by

$$T = (1-R_1)(1-R_2)(1-R_3)\exp(-\alpha_1 d_1-\alpha_2 d_2) / [\{1-R_1R_2\exp(-2\alpha_1 d_1)\}\{1-R_2R_3\exp(-2\alpha_2 d_2) - R_1R_3(1-R_2)^2\exp(-2\alpha_1 d_1-2\alpha_2 d_2)], \qquad (8\text{-}1)$$

here $R_1 = \{(n_1-1)/(n_1+1)\}^2$,
$R_2 = \{(n_1-n_2)/(n_1-n_2)\}^2$,
$R_3 = \{(n_2-1)/(n_2-1)\}^2$,
α_1 : the absorption coefficient of InP,
α_2 : the absorption coefficient of the quaternary alloy,
n_1 : the refractive index of InP,
n_2 : the refractive index of the quaternary alloy,
d_1 : the thickness of InP,
d_2 : the thickness of the quaternary alloy.

If the photon energy is smaller than the energy band gap of InP (1.35eV) and n_1 and n_2 have nearly the same values (within 10%), Equation 8-1 reduces to

$$T = \{(1-R_1)(1-R_3)\exp(-\alpha_2 d_2)\} / \{1-R_1R_3\exp(-2\alpha_2 d_2)\}. \quad (8\text{-}2)$$

Assuming $n_1=3.337$ and $n_2=3.54$, the absorption coefficient coefficient α_2 for $(Al_xGa_{1-x})_{0.47}In_{0.53}As$ is calculated from Eq. 8-2 and the transmittance T.

Figure 8-9 shows the square of the absorption coefficients for several samples as a function of the incident photon energy. As the relation

$$\alpha = A^* \cdot (h\nu - E_g)^{1/2} \quad (8\text{-}3)$$

is satisfied, $(Al_xGa_{1-x})_{0.47}In_{0.53}As$ has a direct energy band gap as predicted in Chap. 7. (The factor A* is (2.7-3.9)x $10^4 cm \cdot eV^{-1/2}$ for $0 \le x \le 0.5$.) Hence the energy band gap could be determined from the absorption edge. Figure 8-10 shows the energy band gap variation with Al composition x. The broken line in this figure is the expected energy band gap (Γ point), which is the same as that shown in Fig. 7-4. Open circles are the experimentally observed values which agree with the predicted values. Thus, it was demonstrated that $(Al_xGa_{1-x})_{0.47}In_{0.53}As$ is a promising material for opto-electronic devices operating in the infra-red wavelength region.

Figure 8-11 shows the photoluminescence spectrum of $(Al_{0.5}Ga_{0.5})_{0.47}In_{0.53}As$ at 77K excited by a 4880A Ar laser. The peak energy was 1.107eV, which coincided with the energy

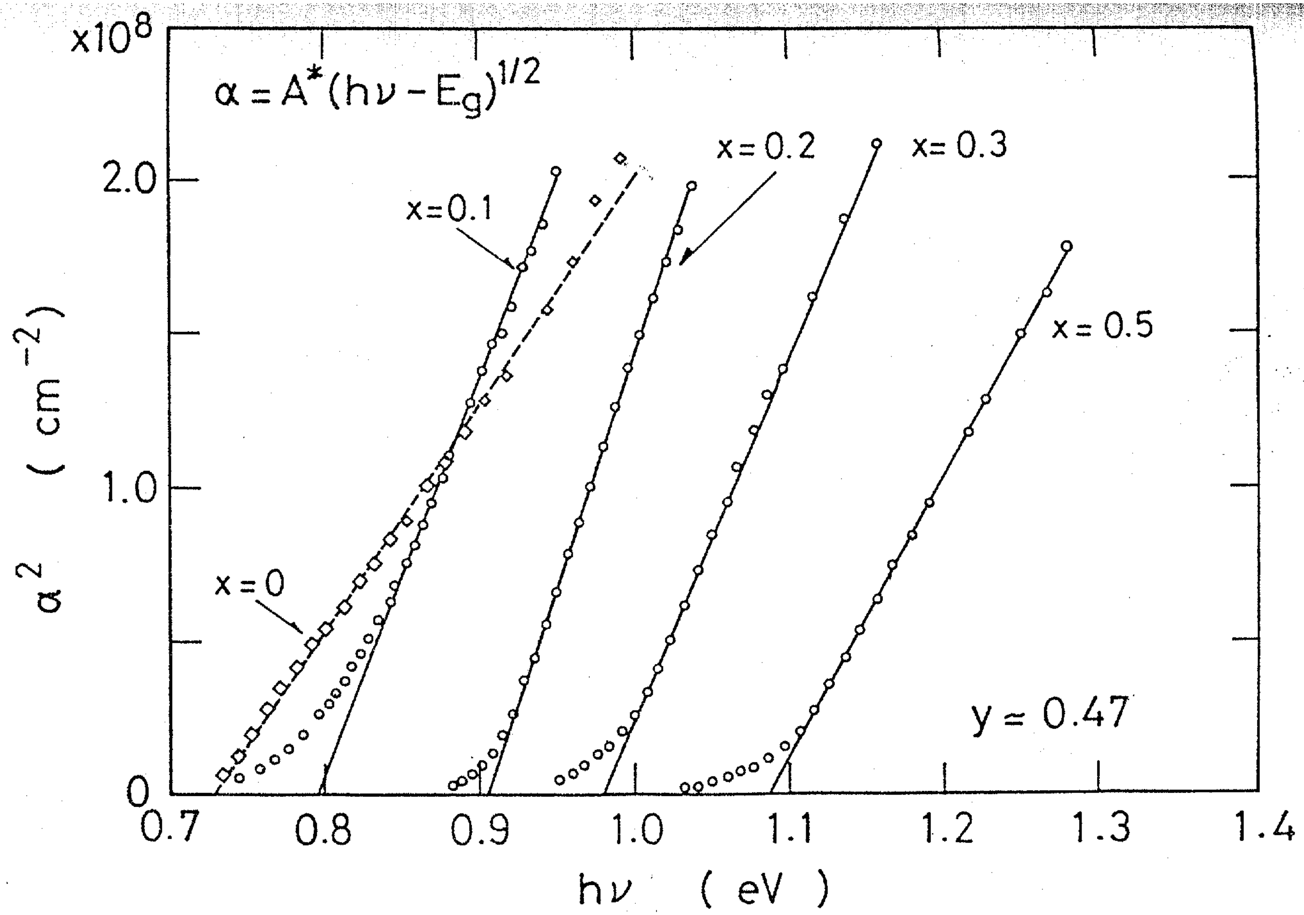

Fig. 8-9.

The square of the absorption coefficients of several $(Al_xGa_{1-x})_{0.47}In_{0.53}As$ epitaxial layers as a function of the incident photon energy.

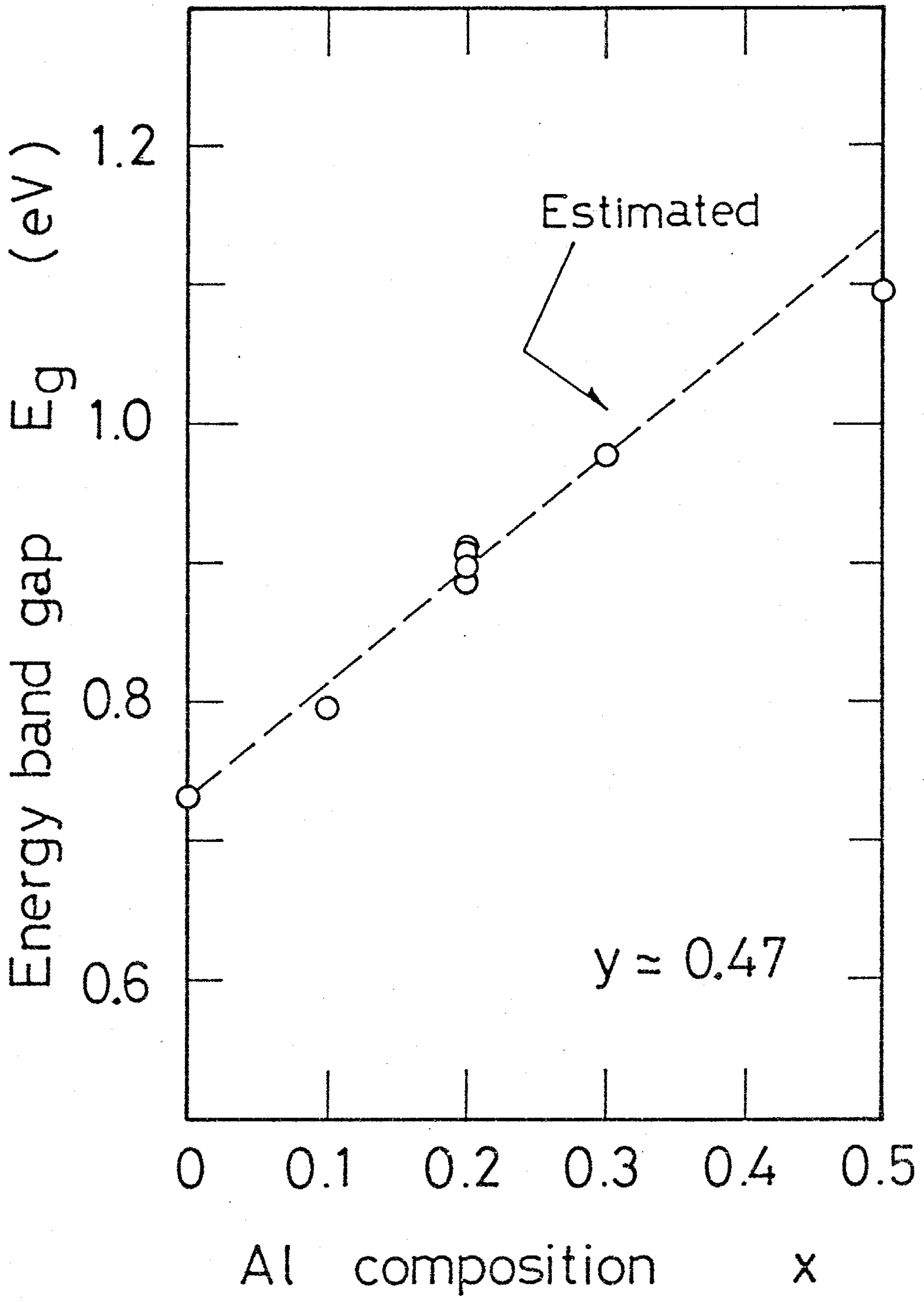

Fig. 8-10.

The room temperature energy band gap variation with Al composition x. The broken line is the expected value (see Fig. 7-4.).

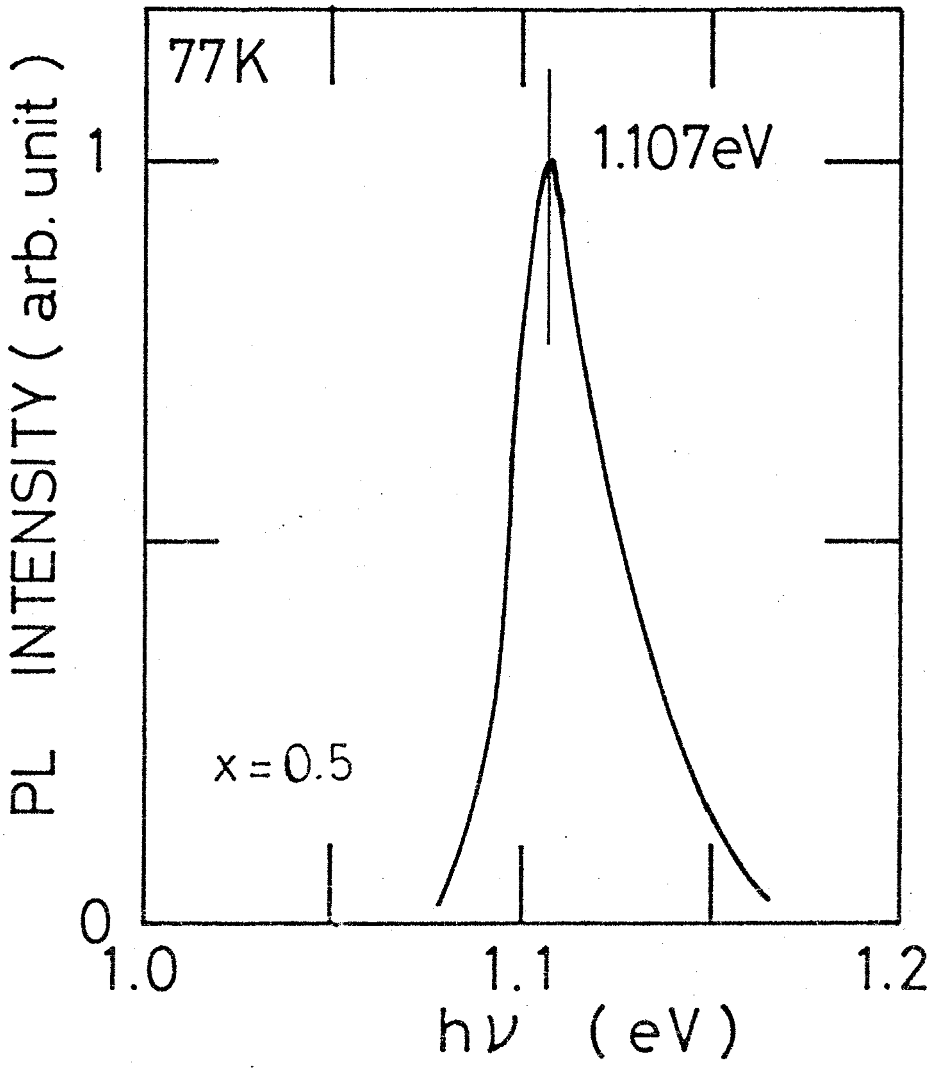

Fig. 8-11.

The photoluminescence spectrum of $(Al_{0.5}Ga_{0.5})_{0.47}In_{0.53}As$ at 77K excited by a 4880Å Ar laser.

band gap obtained from the absorption edge measurements.

8-4-2. Electrical properties.

$(Al_xGa_{1-x})_{0.47}In_{0.53}As$ is a promising material for the infra-red wavelength region. However, the potential of this material can not be realised unless p-type and n-type layers can be prepared.

For the first stage, the electrical properties of the undoped and Be doped layers were evaluated by van der Pauw measurements at room temperature.

Table 8-2 summarizes the room temperature characteristics. Using beryllium, the p-type layer can be easily obtained with a free-carrier concentration of $2 \times 10^{18} cm^{-3}$. Although the undoped layer exhibited high resistivity, the undoped layer has n-type conduction and the room temperature electron mobility is about $1200 cm^2V^{-1}sec^{-1}$.

Undpoed (n-type)	$\rho \sim 50\ \Omega cm$	$\mu = 1200\ cm^2V^{-1}sec^{-1}$
Be-doped (p-type)	$p = 2 \times 10^{18} cm^{-3}$	$\mu = 22\ cm^2V^{-1}sec^{-1}$

Table 8-2.

Electrical properties at room temperature (x=0.1, y=0.47).

8-5. Summary and conclusion .

$(Al_xGa_{1-x})_yIn_{1-y}As$ can be lattice matched to InP for $y=0.47$, and is one of the promising materials for opto-electronic devices in the infra-red wavelength region as discussed in Chap. 7.

In this chapter the epitaxial growth of $(Al_xGa_{1-x})_{0.47}In_{0.53}As$ $(0<x<0.7)$ on InP substrates using molecular beam epitaxy is described. The films consisted of single crystal and exhibited good surface morphologies. The energy band gaps of the epitaxial layers were determined from the absorption edge. The relation between the absorption coefficient and the incident photon energy satisfied $\alpha=A^*(h\nu-E_g)^{1/2}$, and these films have a direct energy band gap as predicted in Chap. 7. The undoped films with $x=0.1$ showed n-type conduction and possessed a room temperature electron mobility of $1200cm^2V^{-1}sec^{-1}$. Using beryllium, p-type films could be obtained. These results showed, as expected, that $(Al_xGa_{1-x})_{0.47}In_{0.53}As$ is a promising III-V material for the infra-red wavelength region.

This work was the first preparation in the world of $(Al_xGa_{1-x})_yIn_{1-y}As$ on InP substrates. Hence, more detailed work concerning the electrical properties required in order to fabricate opto-electronic devices.

MBE has a good precision in controlling the epitaxial thickness in layers as its primary distinguishing feature. MBE is a suitable epitaxial growth technique for opto-electronic device fabrications, because these devices require very thin (1000-2000Å) epitaxial layers.

Previously, MBE for III-V semiconductor alloys was mainly utilized for device preparation. However, this work has demonstrated that MBE can equally used for the production of unkown materials which can not be easily prepared by LPE. It is particularly significant that this work has shown that MBE is a useful technique for material development.

PART IV

DEVELOPMENT OF HIGH CONVERSION EFFICIENCY GaAs BASED SOLAR CELLS

Chapter 9. Current status of solar cell research and development.

Chapter 10. Development of high conversion efficiency (GaAl)As/GaAs heterostructure solar cells.

Chapter 11. Development of monolithic series-connected multi-junction GaAs solar cell array.

CHAPTER 9.

CURRENT STATUS OF SOLAR CELL RESEARCH AND DEVELOPMENT.

9-1. Introduction.

In this chapter, the requirements for solar cell R&D are discussed first. The current status of R&D of GaAs based solar cells, which are discussed in chapeters 10 and 11, is also described. Finally, techniques for evaluating solar ~~ce~~ cells are briefly summarized.

9-2. Utilization of solar energy.

Necessity for solar cell development.

Looking back over the history of human prosperity, there has been a spectacular increase of energy requirements with the progress of civilization. In particular, steam-power generation has produced the industrial progress of this century. However, as is well known that the oil crisis has cast a shadow over industrial prosperity. Although industrial prosperity does not provide everything for humankind, it is no exaggeration to say, that it supports culture, civilization, and human ~~wel~~ welfare. Thus, it is essential for man to develop alternative energy source to replace petroleum. As there are few natural resource in Japan, the development of alternative sources is one of the most important Japanese requirements.

The electric power generation system using nuclear reactors is one of such alternative energy source, and some nuclear power stations have been built in Japan, and in many other countries. Though the safety of nuclear power stations has been established, the environmental damage caused by, for example warm cooling-water, has not been overcome. It is necessary to develop and to demonstrate the completely 'safe' nuclear power generation system.

However, it is also necessary to develop an essentially 'safe and clean' energy source. One possible 'safe and clean' energy source is the energy produced by the sun. The energy from the sun is inexhaustible unlike peteroleum. A conversion system from solar (light) energy to electricity is required, since solar energy is essentially the sum of constituent photon energies while the most convenient form of energy is electrical energy.

There are two normal conversion methods,

(1) The thermal conversion system;

(Light → Thermal energy → Electricity),

(2) The solar cell system; (light → Electricity).

The first system generates electricity using the conventional steam turbine engine, while the steam is thermally generated using solar energy. A 10^3kW pilot plant in which this thermal conversion system is used was completed and tested in Niho-cho, Kagawa-prefecture, in 1981. The second system converts solar power directly into electricity using the so-called solar cells. The solar cell is a light-electricity converter which uses the photovoltaic effect in a semiconductor p-n junction.

Although the so-called energy crisis could not fully solved by the development of solar cell systems, it is generally considered that solar cells with a high conversion efficiency are required as an additional .alternative energy source to petroleum.

Efficiency of solar cells in the conversion of solar to electrical energy.

The solar irradiance in terms of the number of photons is shown in Fig. 9-1. The spectrum outside the earth's atmosphere and at the earth's surface is different. The degree to which the atmosphere affects the sunlight received at the surface is defined quantitatively by the 'air mass - AM'. Thechnically, the air mass(AM) is equal to the secant of the angle of the sun to the zenith, measured at sea level, or in other words the pathlength that a ray of sunlight must traverse compared to the shortest path it could take. The air mass zero (AM0) means the spectrum outside the earth's atmosphere which has a total incident power integrated over all wavelength of about $135\text{-}140 \mathrm{mW \cdot cm^{-2}}$ at the earth's mean distance from the sun. The AM1 spectrum represents the sun light at the earth's surface for optimum weather conditions with the sun at the zenith, leading to a total incident power of slightly over $100 \mathrm{mW \cdot cm^{-2}}$. The major differences between the sunlight in space and the light received at the earth's surface are in the ultraviolet and infra-red content. Ultraviolet light is filtered out by ozone in the upper layers of the atmosphere, and infra-red is removed from the spectrum by water vapour and CO_2. Aerosol particles scatter light of short wavelength more than that of long wavelength.

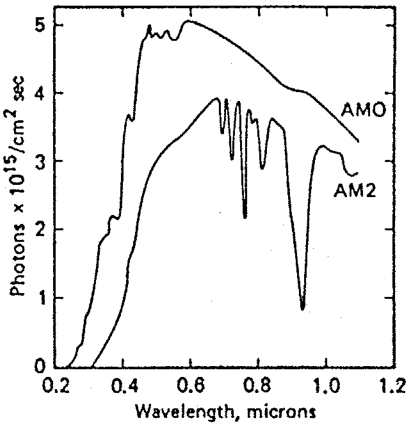

Fig. 9-1.

Solar irradiance in photons per cm^2 per second in a 100A band width for outer space (AM0) conditions and for average weather conditions on earth (AM2).

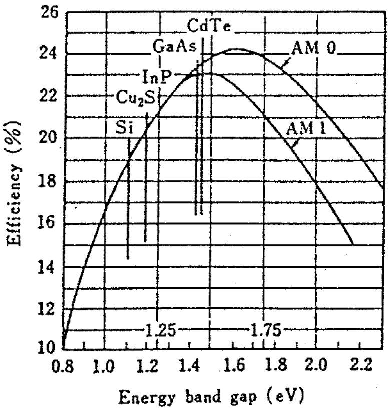

Fig. 9-2.

Theoretical efficiency vs. the energy band gap of materials. (After Loferski, 1956)

Materials with large band gaps yield higher open circuit voltages,but they also produce lower photo-currents because the sunlight at low energies (long wavelength) is not absorbed. On the other hand, materials with small band gaps yield lower open circuit voltages but higher photo-currents. Consequently there exists an optimum band gap for solar cells. Loferski (1956), by making simple assumptions, made the first estimations of the conversion efficiency of solar cells as a function of the energy band gap. Figure 9-2 shows his theoretically estimated conversion efficiencies as a function of band gap. As seen from this figure, silicon is not the optimum material and higher efficiencies can be expected in other materials such as GaAs, CdTe, InP,and so on. However, in practise the only solar cells with over 20% efficiency are GaAs based solar cells as discussed in the following sections.

9-3. Research and development of solar cells.

The electric power generation system using solar cells consists of solar cells which generate the electricity, electric storage batteries, and D-A converters in order to connect the system to the commercial supply lines. The performance of a photo-generated power system is mostly dependent on the solar cell performance and many researchers are involved with solar cell research and development (R&D). This R&D activity divides into two groups,

(1) R&D of high conversion efficiency solar cell,

(2) R&D of low cost solar cell (0.5 - 1$/pW*).

Although these two R&D terms are in practise contrary to each other, it is nevertheless one of the most important objectives to obtain low cost solar cells possessing a high conversion efficiency. R&D of large area solar cells is, of course, one of the most major subjects for practical applications.

In this section, recent progress of Si and compound semiconductor solar cells is summarized. The current situation of GaAs based solar cells is discussed in the following section. Details of solar cell R&D and photo-generated power systems have been reviewed in the literature (Takahashi, 1980; Hovel, 1975a).

9-3-1. Si solar cells.

Although many types of Si solar cells (Si p-n, MIS SnO_2/Si heterostructure, etc.) have been developed over the last ten years, the successful technologies are restricted to CZ single crystalline, ribbon crystalline, and casting polycrystalline Si. The conversion efficiencies obtained with these Si solar cells vary from 8% to 14% depending on the technology. However, these Si technologies are the strongest candidates for the photo-generated power system, because the cell area is very large, 2-5 inch in diameter, compared with

---

*) 'pW' means ' peak watts'. The DOE goal is 0.5$/pW by 1985 for large area single crystalline silicon solar cells.

other solar cells such as amorphous Si and compound semiconductor solar cells.*

As an alternative to single or poly crystalline materials, amorphous silicon (a-Si) has become very attractive over the last two or three years. a-Si solar cells can be fabricated much more cheaply than the other Si solar cells, because the fabrication process is simple and a-Si can be deposited on any substrate.** R&D of the above single and poly crystalline Si solar cells is mainly carried forward in foreign countries such as in U. S. A. In contrast R&D of a-Si solar cells is vigorously pursued in Japan. The reported conversion efficiencies of a-Si solar cells are 6.5-7% for small area device and 5-6% for large area devices ($5x5cm^2$ or $10x10cm^2$). The future of the a-Si solar cell, if it survives as a solar cell material for large scale photo-generated power systems, depends on further studies, including the elucidation of its physical properties, such as the localized state density in the forbidden gap.

*) Recent progress of sigle and poly cryatalline Si solar cells is reviewed by Matsuzawa (1981) and Saitoh (1981).

**) Recent progress of a-Si solar cells is reviewed by Hamakawa (1981). Konagai (1981) reviewed amorphous materials in general.

9-3-2. Compound semiconductor solar cells.

The theoretical conversion efficiency depends fundamentally on the energy band gap of the material, and silicon is not the optimum material for solar cells as is shown in Fig. 9-1. The higher conversion efficiencies are expected with materials such as Cu_2S, InP, CdTe, and the subject of this thesis—GaAs. Table 9-1 lists the recent progress with compound semiconductor solar cells. If GaAs based solar cells are excluded from this Table, one can see that there is currently no material which can compete with Si solar cells, although various materials have been tried. The performance of GaAs based solar cells is partially summalized in this Table. Table 9-2 gives more detailed informations regarding the progress of GaAs based solar cells.

9-4. Status of GaAs based solar cells.

GaAs is the only material which currently exhibites a high conversion efficiency of over 20% as indicated in Sec. 9-2. The excellent performance and a brief history of GaAs based solar cells are summarized in this section.

Firstly, it is important to clarify the distinctive features of GaAs solar cells compared with Si solar cells, which are as follows:

(a) High conversion efficiency.

(b) Potentiality for producing thin film solar cells.

The absorption coefficient of Si is low because Si

Type		Device area mm^2	Voc volts	Isc mAcm^{-2}	F.F.	η %	Illumination mWcm^{-2}	Year	
(GaAl)As/GaAs	S	10	0.976	27.8	0.76	21.9	AM1	(1978)	IBM
p-p-n	S	—	0.980	29.7	0.86	17.2	AM0	(1976)	Hughes
	S	100	0.96	30.3	0.803	17.2	AM0	(1978)	Rockwell
	S	56.3	—	—	0.74	19.9	541suns	(1980)	Varian
			—	—	0.65	17.6	1094suns		
	S	6	0.987	22.9	0.83	24.7	76	(1979)	Tokyo Inst. Tech.
	S	25	1.006	21.9	0.84	21.6	85	(1979)	Mitsubishi
GaAs $n^+/p/p^+$	S	49	0.99	24.5	0.82	20	AM1	(1978)	MIT
GaAs MIS	S	—	—	—	—	17	—	(1977)	JPL
	P	900	0.5	18	0.675	6.1	AM1	(1979)	Southern Methodist Univ.
GaAs (monolithic) heterojunction	S	22	3.96	18.3	0.625	13.9	82	(1980)	Varian
GaAs (monolithic) p-n homojunction	S	20	4.30	12.1	0.74	10.6	73	(1980)	Tokyo Inst. Tech.
InP $n^+/p/p^+$	S	9.3	0.779	26.5	0.72	14.8	AM1	(1980)	MIT
nCdS/nInP/pInP	S	—	0.64	18	0.73	10.4	81.1	(1980)	Chiba Univ.
nCdS/pInP/nInP	S	3.6	0.72	23.2	0.63	11.9	94	(1978)	Rockwell
ITO/InP	S	—	0.69	23.4	0.65	12.4	85	(1978)	Rockwell
Au/nInP MIS	S	6.3	0.46	17.2	0.76	6.01	AM1	(1980)	Rensselaer Polytech. Inst.
Al/pInP MIS	S	—	0.78	18.9	—	14.0	AM2	(1980)	Tokyo Inst. Politech.
nCdS/pInP	P	—	0.46	13.5	0.68	5.7	AM2	(1977)	Bell Lab.
InGaAsP/InP	S	—	0.52	18.8	0.612	8.7	69	(1980)	Nagoya Inst. Tech.
CdS/Cu_2S	P	88.4	0.516	21.8	0.71	9.15	88	(1978)	Univ. Delaware
CdS/Cu_xS	P	90	0.46	14.4	0.67	8.9	50	(1980)	Matsushita
CdS/CdTe	P	100	0.75	14.0	0.58	8.7	70	(1978)	Matsushita
CdS/CdTe	P	18	0.68	12.7	0.38	4.7	71	(1980)	Matsushita
$Cu/CuBr/Cu_2O$	P	65	0.37	8.3	—	1.76	AM1	(1980)	Joint Center for Graduate Study
Mg/Zn_3P_2	S	0.25	0.50	19.0	0.64	6.08	AM1	(1978)	Inst. Energy Conversion
Mg/Zn_3P_2	P	0.25	0.385	18.4	0.47	4.0	AM1	(1978)	Inst. Energy Conversion
$Al/pWSe_2$	S	—	0.51	11.0	0.62	4.2	83	(1978)	Univ. Constance Fachbereich
Pt/InSe	S	—	0.56	13.3	0.61	5.7	80	(1979)	Univ. Valencia
$In_{0.2}Se_{0.8}/SnO_2$	A	—	—	—	—	2.8	—	(1980)	Univ. Osaka Pref.
$Cu/pCuGaSe_2$	S	—	0.41	16.5	—	4	—	(1980)	Inst. Venezolano de Invest. Cientificas
$CuInSe_2/CdS$	P	120	0.49	25	0.54	6.6	100	(1978)	SERI
$CuInSe_2/CdS$	P	20	0.45	22	0.51	5.1	AM1	(1980)	Brown Univ.
$CuIn_{0.3}Ga_{0.7}Se_{1.2}Te_{0.8}/CdS$	S	20	0.65	29	0.69	13	AM1	(1980)	Brown Univ.
$CuIn_{0.3}Ga_{0.7}Se_{1.2}Te_{0.8}/ITO$	S	10	0.72	31	0.55	12.3	AM1	(1980)	Brown Univ.
$p^+Ga_{0.7}Al_{0.3}AsSb/p\text{-}nGa_{0.9}Al_{0.1}Sb/nGaSb$	S	2.5	0.285	16	0.562	1.9	AM0	(1980)	Rockwell
			0.41	886	0.47	2.3	45.6suns		
$(CH)_x/nSi$	O	3.85	0.55	18.2	0.32	4.3	72	(1980)	Tokyo Inst. Tech.

S: single crystal　P: polycrystal　A: amorphous　O: organic semiconductor

Table 9-1.

Compound semiconductor solar cell performances.

Area (cm^2)	V_{oc} (V)	I_{sc} ($mAcm^{-2}$)	F.F.	η (%)	Illumination[a] P_{in}($mWcm^{-2}$)	CR[b]	Research Institute	Author	Year	Comments
(1) (GaAl)As/GaAs p-p-n heterostructure.										
0.1	0.955	19.5	-	20.3	AM2/T/74	-	IBM	Woodall	(1972)	LPE
	0.965	21.3	-	16.3	AM1/T/98	-				First paper
∿0.1	1.105	33.1	0.745	18.5	AM0/S/134.8	-	IBM	Woodall	(1975)	LPE
	0.976	27.8	0.760	21.9	AM1/T/93.9	-				
0.14	∿1.1	$31x10^3$	-	19.5	- /T/ -	1735suns	Varian	James	(1975)	LPE
1	0.96	30.3	0.803	17.2	AM0/S/ -	-	Rockwell	Sahai	(1976)	LPE
	-	25	-	21	- /T/92.4	-				
4	1.00	26.7	0.83	16.3	AM0/S/ -	-	Hughes	Kamath	(1976)	LPE
0.29	0.955	24.5	0.70	12.8	AM0/S/128	-	Rockwell	Dupuis	(1977)	MO-CVD without AR
0.785	-	-	-	24.0	AM2/T/80	-	Rockwell	Sahai	(1978)	LPE
	-	-	0.822	24.7	AM2/T/80	178suns				
1	∿1.2	-	-	16.3	AM0/S/135.3	912suns	Hughes	Ewan	(1978)	LPE
	∿1.2	-	-	60.0	AM1/S/100	1006suns				
0.56	1.141	$21x10^3$	0.792	23.3	AM1.5/T/85.4	945suns	Varian	Vander Plas	(1978)	LPE

Table 9-2. (1)

(continued to next page)

Area (cm^2)	V_{oc} (V)	I_{sc} $(mAcm^{-2})$	F.F.	η (%)	Illumination[a)] P $(mWcm^{-2})$	CR[b)]	Research institute	Author	Year	Comments
0.563	1.01	20.9	-	-	AM2/S/ -	-	Varian	Nelson	(1978)	MO-CVD
	1.15	$16x10^3$	0.757	19.1	AM2.1/T/77.4	933suns	Varian	Nelson	(1978)	MO-CVD
0.06 $\sim$0.12	0.959	25.5	0.83	20.3	AM1/S/100	-	THIS WORK		(1979)	LPE
	1.080	248	0.82	26.3	AM1.9/T/79	10.6suns				
	0.984	25.4	0.83	20.7	AM1/S/100	-				
	0.987	22.9	0.83	24.7	AM1.9/T/76	-				
	1.020	23.6^3	0.845	21.5	AM1/T/94.5	-	Mitsubishi	Yoshida	(1979)	LPE
0.06	1.11	$1.6x10^3$	0.82	21.2	AM1.5/T/85	78suns	THIS WORK		(1980)	LPE
0.563	$\sim$1.1	$21x10^3$	0.65	17.6	- /T/$\sim$80	1094suns	Varian	Sexena	(1980)	MO-CVD Packaged cell
1	1.05	$17x10^3$	-	17.6	- /T/84.5	1025suns	Mitsubishi	Mitsui	(1981)	LPE without water cooling
(2) (GaAl)As/GaAs graded band gap.										
-				$\sim$14	- /T/ -	-	T.I.T	Konagai	(1975)	LPE
(3) $Ga_{0.08}Al_{0.92}As/Ga_{0.86}Al_{0.14}As$ p-p-n										
0.58	$\sim$1.2	$15.9x10^3$	-	15.5	- /T/ -	899suns	Varian	Moon	(1978)	LPE
(4) n-AlAs/p-GaAs										
2$\sim$3	0.85	27.0	0.8	18.5	AM1.5/T/90-95	-	Bell	Johnston	(1976)	Chroride transport CVD

Table 9-2. (2)

(continued to next page)

Area	V_{oc} (V)	I_{sc} ($mAcm^{-2}$)	F.F.	(%)	Illumination[a] P_{in} ($mWcm^{-2}$)	CR[b]	Research Institute	Author	Year	Comments
(5) (GaAl)As/GaAs monolithic cascade.										
0.012	2.13	12.89	0.735	15.1	AM0/S/ -	-	Research Triangle Institute	Bedair	(1981)	LPE without AR
	2.05	10.7	-	16.4	AM1/-/ -	-				
(6) Monolithic series connected.										
0.20	3.90	18.3	0.625	13.9	-/T/82	-	Varian	Borden	(1980)	p-p-n hetero.
0.20	3.0	16.3	0.76	7.5	AM1/S/100	-	THIS WORK		(1980)	SB[c]
0.25	4.30	12.1	0.74	10.6	AM2/S/73	-				p-n homo.
0.20	3.58	12.1	0.77	11.4	AM2/S/73	-				p-n homo.
0.20	3.55	24.3	0.70	15.0	AM1/S/100	-	THIS WORK		(1981)	p-p-n hetero.
(7) n^+/p GaAs homojunction.										
0.5	0.97	25.6	0.81	20.5	AM1/-/ -	-	MIT	Fan	(1978b)	Ga+$AsCl_3$ CVD
0.49	0.99	24.5	0.82	20	AM1/-/ -	-	MIT	Botzler	(1978)	"
0.045 ~0.095	0.92	23	0.76	16	AM1/S/100	-	MIT	Fan	(1979b)	MBE
0.028 ~0.047	0.79	20.4	0.73	12	AM1/S/100	-	MIT	Fan	(1979a)	Ion Implantation
0.5	~1.08	-	~0.76	~20	AM1/S/ -	125suns	MIT	Turner	(1981)	Ga+$AsCl_3$ CVD

Table 9-2.(3)

(continued to next page)

Area	V_{oc} (V)	I_{sc} (mAcm^{-2})	F.F.	(%)	Illumination[a)] P_{in}(mWcm^{-2})	CR[b)]	Research Institute	Author	Year	Comments
1	0.976	25.5	0.78	19.4	AM1/S/ -	-	JPL	Stirn	(1981)	MO-CVD GaAs sub.
0.0236	0.998	23.5	0.785	18.4	AM1/S/ -	-				p$^+$-Ge sub.
0.093	0.76	24.4	0.63	11.7	AM1/S/ -	-	MIT	Gale	(1981)	Ge coated Si substrate
(8) Thin film (single crystalline)										
p-n GaAs	0.82	12.5	0.67	8.7	AM2/T/ -	-	TIT	Konagai	(1976c)	PFT (LPE)
n(GaAl)As/pGaAs	0.88	16.9	0.77	13.5	AM2/T/ -	-				
p-n GaAs	∿0.9	-	-	9.1	AM2/T/80	-	TIT	Kanagai	(1978)	PFT (LPE)
	∿1.05	-	-	9.4	AM2/T/80	109suns				
(GaAl)As/GaAs p-p-n	0.90	18.6	0.78	18.7	- /T/72	-	TIT	Sugimoto	(1979)	PFT (LPE)
n$^+$/p GaAs	-	-	-	15	AM1/-/ -	-	MIT	Fan	(1980b)	CLEFT (Ga+ AsCl$_3$ CVD)
n$^+$/p GaAs	-	-	-	17	- /-/ -	-	MIT	Fan	(1981)	CLEFT (Ga+ AsCl$_3$ CVD)

Table 9-2. Progress in the development of GaAs based solar cells.

a) Illumination ; Air mass value/Solar simulator or Terrestrial Insolation/Input power.

b) CR ; concentration ratio.

c) SB ; Schottky barrier.

has an indirect energy band gap. Hence, Si thickness of more than 100μm is required for adequete solar absorption. On the other hand, a GaAs film of only several microns provides sufficient solar absorption as GaAs a direct energy band gap. Figure 9-3 shows the conversion efficiencies for various materials as a funciton of thickness.

c) Potentiality for operation under high sunlight concentration conditions.

As the energy band gap of GaAs is 1.43eV, which is larger than that for Si (1.1eV), the decrease in the conversion efficiency is small at an operating temperature of 200-300°C. Consequently, GaAs solar cells can be operated under high sunlight concentration conditions (such as 1000suns).

d) Tolerance of exposure to radiant rays.

As GaAs has a short carrier life time and the active region of GaAs solar cells is thin because of the direct energy band gap (see (b) above), GaAs solar cells can be operated under radiant ray irradiation. Consequently, it is expected that GaAs based solar cells will be used in space.

e) Potentiality for a higher conversion efficiency with a wider spectral response.

Although the spectral response of solar cells is determined by the energy band gap of the material, this spectral region can be widened by two or more p-n junctions of different energy band gaps using the heterostructure, and also a higher conversion efficiency in excess of 30% is expected with such structures.

The first reported GaAs solar cell was a Cd or Zn diffused p-n homojunction device (Jenny, 1956; Gobat, 1962). However, the conversion efficiencies of these devices were only 6-11% because of the large surface recombination velocity at the front surface of p-GaAs (10^6-10^7cm sec^{-1}). The first device with over 20% efficiency was reported by Woodall and Hovel (1972). Figure 9-4 shows the device structure, which consists of a GaAs p-n structure with a heteroface of p-$Ga_{1-x}Al_xAs$ ($x > 0.8$). This heteroface is transparent to much of the solar spectrum and provides a low suface recombination velocity at front surface of the p-GaAs. Since this report, work on (GaAl)As/GaAs solar cells has been reported by Rockwell, Hughes, and Varian in the U. S. A. and by the author and Mitsubishi in Japan, and high conversion efficiencies in excess of 20% were obtained as listed in Table 9-2. Recently, GaAs solar cells have been fabricated by MO-CVD.

As the cost of a GaAs wafer is very expensive (about ten times more expensive than a Si wafer), operation under sunlight concentration conditions can lead to greater cost reduction in GaAs solar power systems than in Si systems. James (1975) first reported the performance under concentration conditions (735suns). R&D of (GaAl)As/GaAs solar cells has been directed towards the development of concentrator type solar cells, and many reports have been produced as listed in Table 9-2.

$n^+/p/p^+$ GaAs homojunction solar cells have been extensively studied at MIT (Fan, 1978a-b, 1979a-b, Bozler, 1979) and at JPL (Stirn, 1981), and both institutes reported a high conversion efficiencies up to 20%. Furthermore, Fan (1980) reported

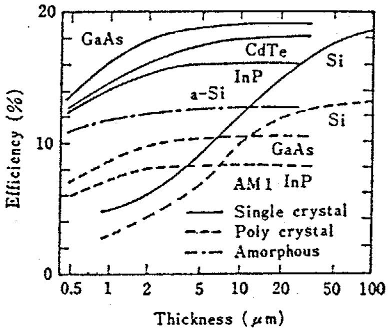

Fig. 9-3.

AM1 efficiencies for different base thickness.

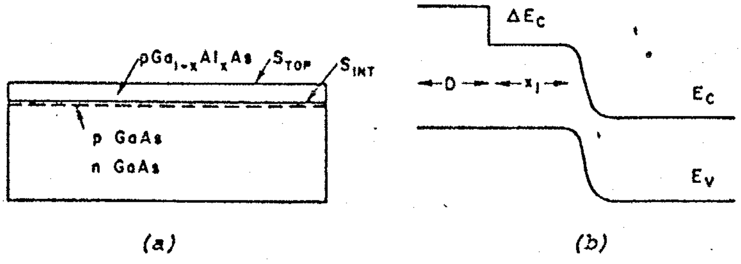

Fig. 9-4.

(GaAl)As/GaAs p-p-n solar cell: (a) structure, (b) energy band diagram.

these homojunction solar cells have a higher resistance to 1-MeV electron radiation than the usual (GaAl)As/GaAs solar cells.

MIS structure solar cells have been extensively studied, since the fabrication process for MIS solar cells is easier than that for the junction type solar cells (Stirn , 1975a-b, 1976, 1977a-b; Yeh, 1978). They reported an efficiency of 12-17% using single crystal GaAs wafers. However, the polycrystalline GaAs MIS solar cells have an efficiency of only 6-6.5% as reported by many workers (Chu S.S., 1978a-c; Dapkus, 1978; Russel, 1978). The poly crystalline GaAs MIS solar cells can not be used for photo-generated power systems, unless the leakage at the grain boundary can be overcome and a low cost manufacturing process established.

The most promising process for the reduction of low cost GaAs solar cells is PFT establised by Konagai (1976b-c, 1978) and CLEFT established by Fan (1981).
Since the solar cells obtained by these processes are single crystal and very thin (5-20μm), high conversion efficiencies of over 20% can be expected.
Results reported are 18.7% for a (GaAl)As/GaAs heterostructure solar cell by PFT (Sugimoto, 1979), and 15% for a n^+/p homojunction solar cell by CLEFT (Fan, 1981), respectively.

Therefore, it could be concluded, that research on GaAs based solar cells is going to be directed towards;
(1) The development of higher conversion efficiencies under high concentrating conditions (greater than 1000suns),
(2) The development of a large area device greater than

$2 \times 2\,cm^2$ or 1 inch diam. cell,

(3) an understanding of the damage caused by electron and proton irradiation, and

(4) The development of a low cost fabrication process with high conversion efficiency such as PFT or CLEFT.

Furthermore, it is also necessary to develop the solar cells with a large output voltage and small current. These devices are required, not only for consumer photo-cells, but also for concentrator solar cells. The monolithic series-connected multi-junction solar cell arrays satisfy this requirements.

9-5. Evaluation of solar cell performance.

The performance of a solar cell is fundamentally assessed by the energy conversion efficiency and the spectral response.

Energy conversion efficiency.

Figure 9-5 shows the I-V curve for a solar cell under illumination. The energy conversion efficiency is evaluated as follows:

$$\text{Conversion efficiency} = \frac{V_m \times I_m}{A_{total} \times P_{in}} \times 100\ (\%),$$

$$\text{Active conversion efficiency} = \frac{V_m \times I_m}{A_{active} \times P_{in}} \times 100\ (\%),$$

where V_m, I_m ; the output voltage and the output current density at maximum power,

P_{in} ; the incident power density,

A_{total} ; the cell area including the electrodes, etc. whose are exhibites zero photovoltaic effect at the cell surface,

A_{active} ; the cell area excluding the electrodes.

The fill factor F.F. is defined as

$$F.F. = (V_m \times I_m)/(V_{oc} \times I_{sc}),$$

where I_{sc} ; the short circuit current density,

V_{oc} ; the open circuit voltage.

As discussed in Sec. 9-1, the incident light has various spectral distributions depending on the air mass value. The air mass value during measurement must be stated. In this work, the cell performance were measured using a solar simulator, and the incident power density was calibrated by thermopile. Consequently, the cell performance is evaluated using the following values.

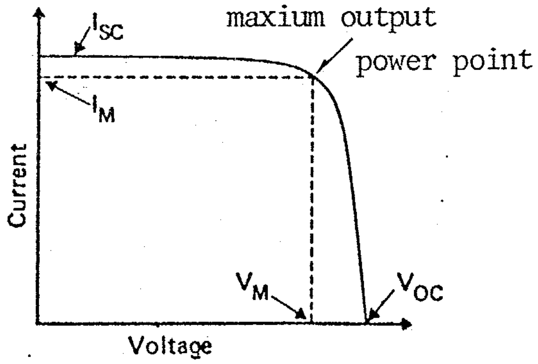

Fig. 9-6.

Voltage and current output from an illuminated solar cell.

(1) Open circuit voltage : V_{oc} (V)
(2) Short circuit current : I_{sc} ($mA \cdot cm^{-2}$)
(3) Fill factor : FF
(4) Conversion efficiency : η (%)
(5) Input power : P_{in} ($mW \cdot cm^{-2}$)
(6) Measurement condition : Light source,
Air mass value.

Spectral response

The spectral response is evaluated by the collection efficiency. The collection efficiency at a given wavelength is defined as the ratio of the number of electrons flowing in the external circuit, to the number of incident photons under short circuit conditions.

9-6. Summary.

A solar power system using solar cells should be developed as an alternative energy source to petroleum. Although various types of solar cell have been investigated and developed, the GaAs based solar cells is the only device with a high conversion efficiency of over 20%.

It is shown that the performance of solar cells can be evaluated using the conversion efficiency and the spectral response.

CHAPTER 10.

DEVELOPMENT OF HIGH CONVERSION EFFICIENCY (GaAl)As/GaAs HETEROSTRUCTURE SOLAR CELLS.

10-1. Introduction.

In this chapter, the conventional (GaAl)As/GaAs p-p-n solar cells using Be as a p-type dopant and (GaAl)As/(GaAl)As p-p-n solar cells, in which the active region were formed by $Ga_{1-y}Al_yAs$ ($0 \leq y \leq 0.4$), were fabricated and tested.

The fundamental device structure and the fabrication process are described in sections 10-2 and 10-3. The performance of Be doped (GaAl)As/GaAs p-p-n solar cells is discussed in Sec. 10-4, and it is shown that Be doped devices exhibit high performances with and without sunlight concentration.

As discussed in Chap. 9, the conversion efficiency of single junction solar cells is about 25% at best. In studies of methods for obtaining higher conversion efficiencies than the usual single junction solar cells, it had been predicted that the (GaAl)As/GaAs based monolithic cascade solar cell, in which two or more junctions of different energy band gaps are connected perpendicularly to the substrate surface*, should

---

*) N.B., in the monolithic series connected solar cell array discussed in Chap. 11, several solar cells are series-connected planarly on the substrate.

possess a conversion efficiency of over 30%.** In this cascade solar cell, the top cell consists of $Ga_{1-y}Al_yAs$ ternary alloys . In Sec. 10-6, the performance of (GaAl)As/(GaAl)As p-p-n solar cells, which may be used as the top cell of a monolithic cascade solar cell, is discussed.

10-2. Device structure of (GaAl)As/GaAs p-p-n solar cells.

The (GaAl)As/GaAs p-p-n solar cell consists of a GaAs p-n structure with a heteroface of $p\text{-}Ga_{1-x}Al_xAs$ ($x > 0.8$). This solar cell is called the heteroface solar cell. The structure and corresponding energy band diagram is shown in Fig. 10-1. Photons impinge from the left and the wide band gap semiconductor acts as a window that admits photons of energy less than its band gap E_{g1}. Those photons with an energy between E_{g1} and E_{g2} (the band gap of the smaller band gap material, GaAs) create carriers in the GaAs p-n homojunction. If the absorption coefficient is relatively high in the lower gap material, as in GaAs, the carriers are generated within the junction transition region, or close to it. Consequently,

**) Various theoretical analyses of cascade solar cells were reported in the Proc. 14th IEEE Photovoltaic Specialists Conference (1980).

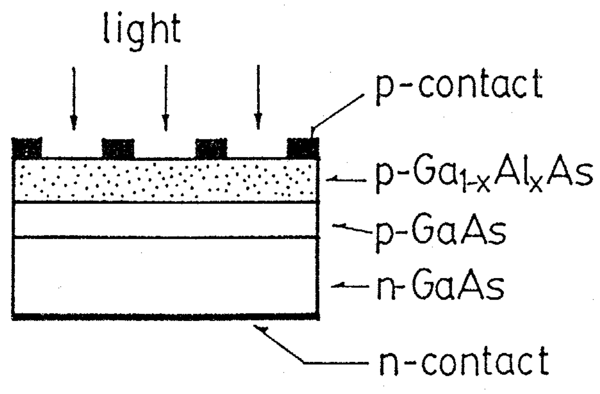

(a) structure

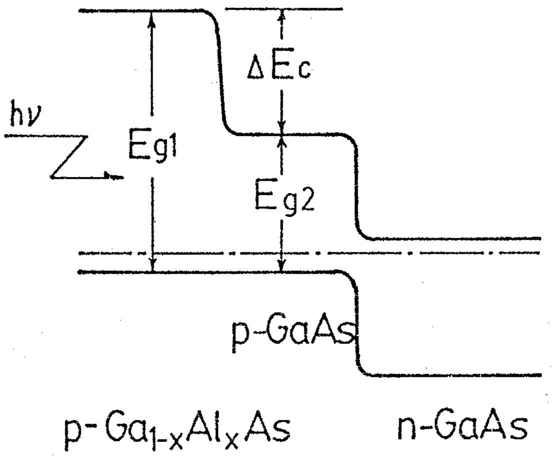

(b) energy band diagram

Fig. 10-1.

p-$Ga_{1-x}Al_xAs$/p-GaAs/n-GaAs heteroface solar cell ($x>0.8$).
(a) structure, and (b) energy band diagram.

the collection efficiency is quite high. The reason for the GaAlAs-GaAs heteroface cell improvement over the GaAs homojunction cell is that the heterojunction-interface recombination velocity ($<10^3$cm s^{-1}) is less than the surface recombination velocity for GaAs (10^6-10^7cm$\cdot$s^{-1}) (Ettenberg, 1976). The barrier ΔE_c in the p-$Ga_{1-x}Al_xAs$/p-GaAs/n-GaAs structure shown in Fig. 10-1, does not impede the flow of carriers. Therefore, the I-V characteristic of the cell is essentially that of the p-n homojunction with V_{oc} and I_{sc}, depending upon the number of photons collected by the homojunction.

Hence, the (GaAl)As/GaAs p-p-n solar cell should possess a conversion efficiency of the ideal p-n GaAs homojunction solar cell. Furthermore, high converison efficiencies of over 20% have been reported by many authors as described in the previous chapter.

For the (GaAl)As/(GaAl)As p-p-n solar cells discussed in Sec. 10-6, a GaAs p-n structure as shown in Fig. 10-1 (the region with energy band gap E_{g2}), was formed by a $Ga_{1-y}Al_yAs$ p-n structure. The energy band gap of $Ga_{1-y}Al_yAs$ increases from 1.43eV to 1.92eV with increasing Al composition 'y' from 0 to 0.4. Since the simple theoretical calculation predicted that the optimum band gap of the top cell in a (GaAl)As/GaAs based two-junction cascade solar cell should be 1.6~1.7eV (see footnote in Sec. 10-1.), the device characteristics of (GaAl)As/(GaAl)As p-p-n solar cells were investigated for Al compositions of $0 < y < 0.4$. These investigations are described in Sec. 10-6.

0-3. Fabrication of (GaAl)As/GaAs p-p-n solar cells.

The GaAs based solar cells discussed in this chapter were abricated on GaAs substrates. Each layer was grown by the PE method. The LPE growth conditions and the fabrication rocess of solar cells are discussed in this section.

0-3-1. Crystal growth.

The p-$Ga_{1-x}Al_xAs$/p-GaAs/n-GaAs heterostructure was formed n a (100) n^+-GaAs substrate by growing Sn doped n-GaAs and Be oped p-$Ga_{1-x}Al_xAs$ at about 750°C. Beryllium was diffused nto the n-GaAs epitaxial layer during the growing process of -$Ga_{1-x}Al_xAs$ to produce a GaAs p-n structure. The Al omposition of the surface layer was fixed between 0.8 and 0.9. sing the results shown in Fig. 3-3, the Sn concentration n the growth melt was determined to be $(2\text{-}3)\times10^{17}cm^{-3}$. he Be concentration in the growth melt was about 0.04at%. he thickness of the p-GaAs which was formed by Be diffusion as about 1.5-2.0 μm, which is the optimum thickness for he production of a high photocurrent, when the electron iffusion length is about 4-5 μm.

Table 10-3 summarizes the detailed growth conditions.

		1st (n-GaAs)	2nd (p-$Ga_{1-x}Al_xAs$)
Initial temperature	:	760-775°C	750°C
Cooling rate.	:	0.5-1.0°$Cmin^{-1}$	0-0.5°$Cmin^{-1}$
Duration	:	15-50 min	20-30 min
Al compostion	:	-	0.8-0.9
Thickness	:	5-7 μm	0.3-2 μm
Doping level	:	$(2-5)x10^{17}cm^{-3}$	$(0.5-1)x10^{18}cm^{-3}$
Substrate: $(100)n^+$-GaAs (Si or Te doped),			$2x10^{18}cm^{-3}$.

Table 10-1.

Growth conditions for (GaAl)As/GaAs p-p-n solar cells.

10-3-2. Fabrication process.

Figure 10-2 shows the fabrication process of the solar cells. For each process the usual photolithographic technique was used.

A Ag + Zn (10:1) front grid contact was formed on the p-GaAs, not on the p-(GaAl)As, because the ohmic contact resistance for p-$Ga_{1-x}Al_xAs$ ($x > 0.8$) is higher than that for GaAs, and also because the adherence of ohmic contact metals to GaAs is better than the that to (GaAl)As. For a concentrator cell, the front grid contact was formed as a comb pattern. The width of each grid was 10 μm or 20 μm, and the width of the bus line was 100 μm. The obscuration was less than 10%. In process (4) in Fig. 10-2, the front grid pattern was coated with a thick layer of gold (1-3 μm), by an electroplating technique, in order to reduce the grid strip resistance for the concentrator solar cells. Finally, Sb_2O_3 was vacuum-evaporated as an AR (anti-reflection) coating to reduce reflection loss. The refractive index of Sb_2O_3 is 1.94-1.97 and the reflection at 630nm (Sb_2O_3, 800 Å) is less than 1%. Hence, the Sb_2O_3 AR coating could be considered as the most suitable for a one layer coating. The cell area of the concentrator cell was either 2x3 mm^2 or 4x3 mm^2.

(1)

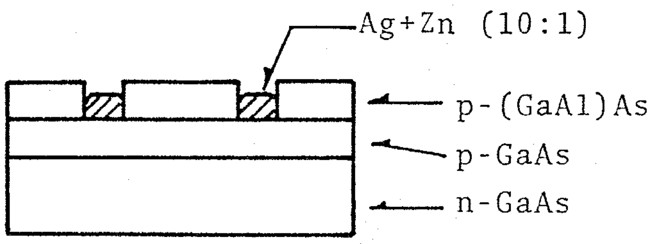

Formation of front contacs.

(2)

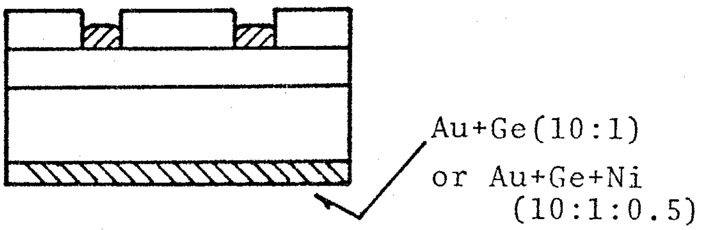

Formation of n-contact.

(3) Anealing (450°C, 5min, N_2 ambient)

(4)

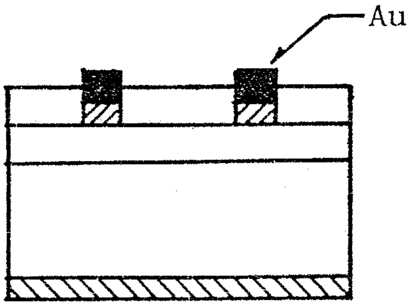

Formation of thick gold (1-3μm) on the front grid pattern.
(for the concentrator cell)

(5)

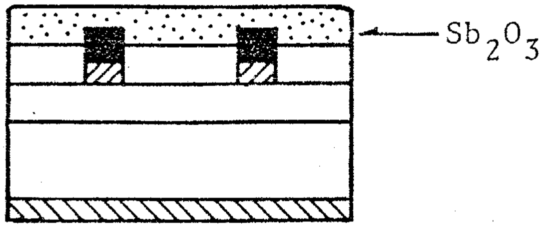

Anti-reflection coating.

Fig. 10-2.

Fabrication process of the (GaAl)As/GaAs p-p-n solar cell.

10-4. Device performance of conventional p-(GaAl)As/p-GaAs/n-GaAs solar cells using beryllium as a p-type dopant.

As pointed out in Chap. 6, the acceptor energy level for Be in $Ga_{0.2}Al_{0.8}As$ is smaller than that for Zn. Hence a higher performance under solar concentration conditions is expected from Be doped solar cells than from Zn or the other dopant doped solar cells. In this section, the cell characteristics of Be doped conventional (GaAl)As/GaAs solar cells are discussed.

10-4-1. Energy conversion efficiency.

Figure 10-3 shows the I-V characteristics of Zn doped and Be doped (GaAl)As/GaAs p-p-n solar cells under AM1 solar simulator insolation ($100mWcm^{-2}$). The conversion efficiency is 21.1% for the Be doped solar cell. This efficiency is comparable to that previously reported for this type of solar cell (see Table 9-2.). The characteristics of Be doped solar cells compared with Zn doped solar cells are summarized in Table 10-2. In this Table, the diode quality factor 'n' was obtained from the slope of the dark I-V curve at room temperature. The diode quality factor n is about 1.3-1.5 for Be doped solar cells. The adequate fill factor of 0.83 to 0.87 for these devices may be due to the low diode quality factor.

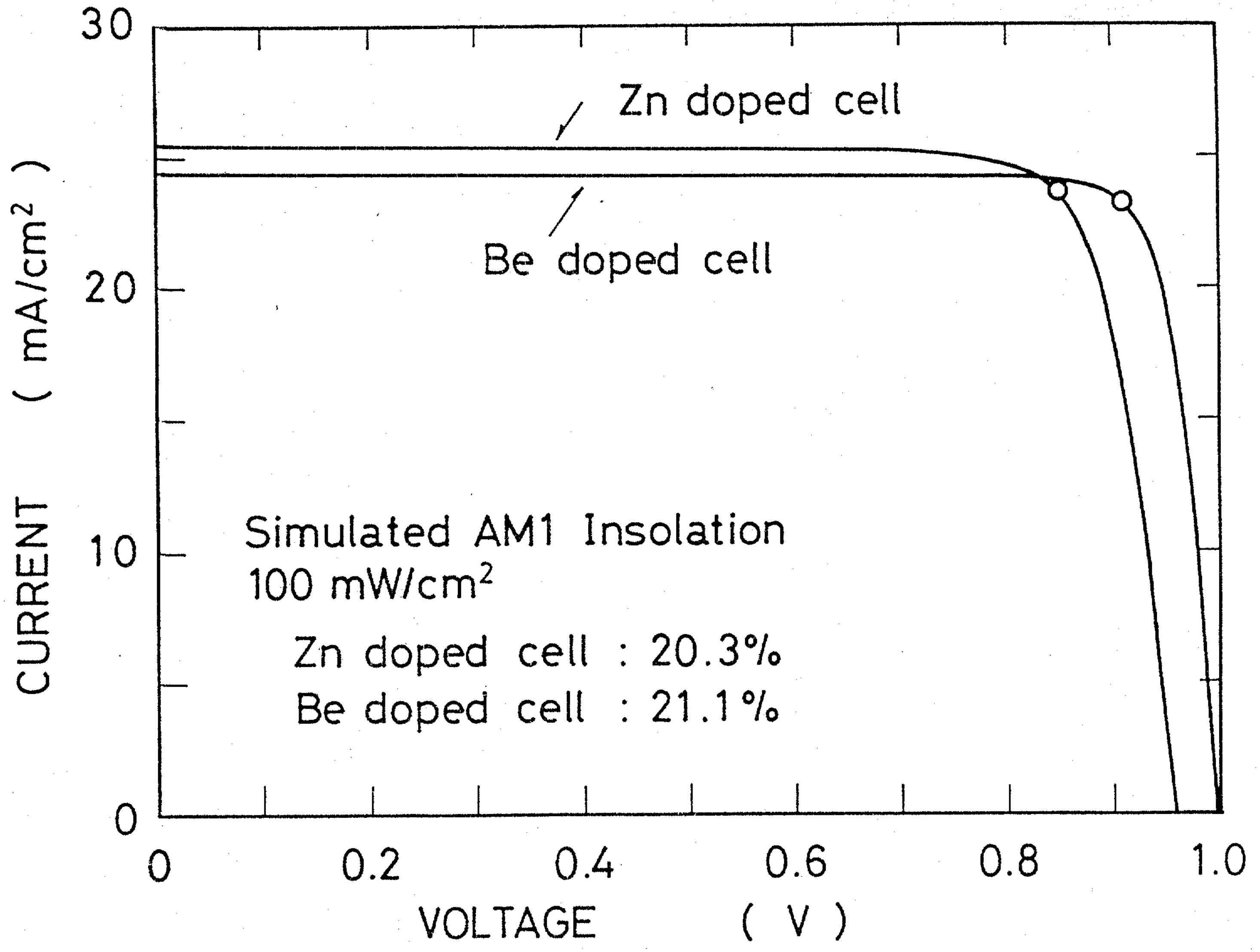

Fig. 10-3. Current-voltage characteristics of Be doped and Zn doped (GaAl)As/GaAs solar cells (AM1, 100mWcm^{-2}, Solar simulator).

Dopant	Cell No.	V_{oc} (V)	I_{sc}^{***} $(mA \cdot cm^{-2})$	F.F.	η^{***} (%)	P_{in} $(mW \cdot cm^{-2})$	AM	n^{**}
Be	36	0.984	25.4	0.83	20.7	100	1*	1.3
		0.987	22.9	0.83	24.7	76	1.3	
	42	0.994	24.4	0.87	21.1	100	1*	1.25
	49	1.00	23.0	0.84	19.4	100	1*	1.4
Zn	25	0.959	25.5	0.83	20.3	100	1*	1.7
		0.970	23.4	0.82	23.7	78.4	1.9	

Table 10-2.

Photovoltaic characteristics of Be and Zn doped (GaAl)As/GaAs p-p-n solar cells.

*) solar simulator.

**) The diode quality factor was obtained from the dark I-V curve.

***) calculated for active area (coverage about 10%).

10-4-2. Device performance under solar concentration conditions.

One of the Be doped (GaAl)As/GaAs solar cells was placed in the concentrator assembly and tested under terrestrial sunlight concentration conditions. The device, which was placed on a 1 mm thick Cu plate, was cooled by water flowing beneath the Cu plate.

The photovoltaic characteristics (V_{oc}, FF, and η) and cell temperature as a function of the concentration ratio are shown in Fig. 10-4. Detailed characteristics are summarized in Table 10-3. The concentration ratio C is assumed to be the ratio of the short circuit current under solar concentration to that without concentration. The cell temperatures were estimated from V_{oc}-I_{sc} plots superimposed on the dark I-V curves for various temperatures (Charan, 1979). This cell has a peak efficiency at a concentration ratio of about 100 and the efficiency decreases for higher concentrations due to the decrease in F.F. The highest output power of about $5 \cdot \mathrm{Wcm}^{-2}$ and the corresponding conversion efficiency of about 15% were obtained at 400 suns.

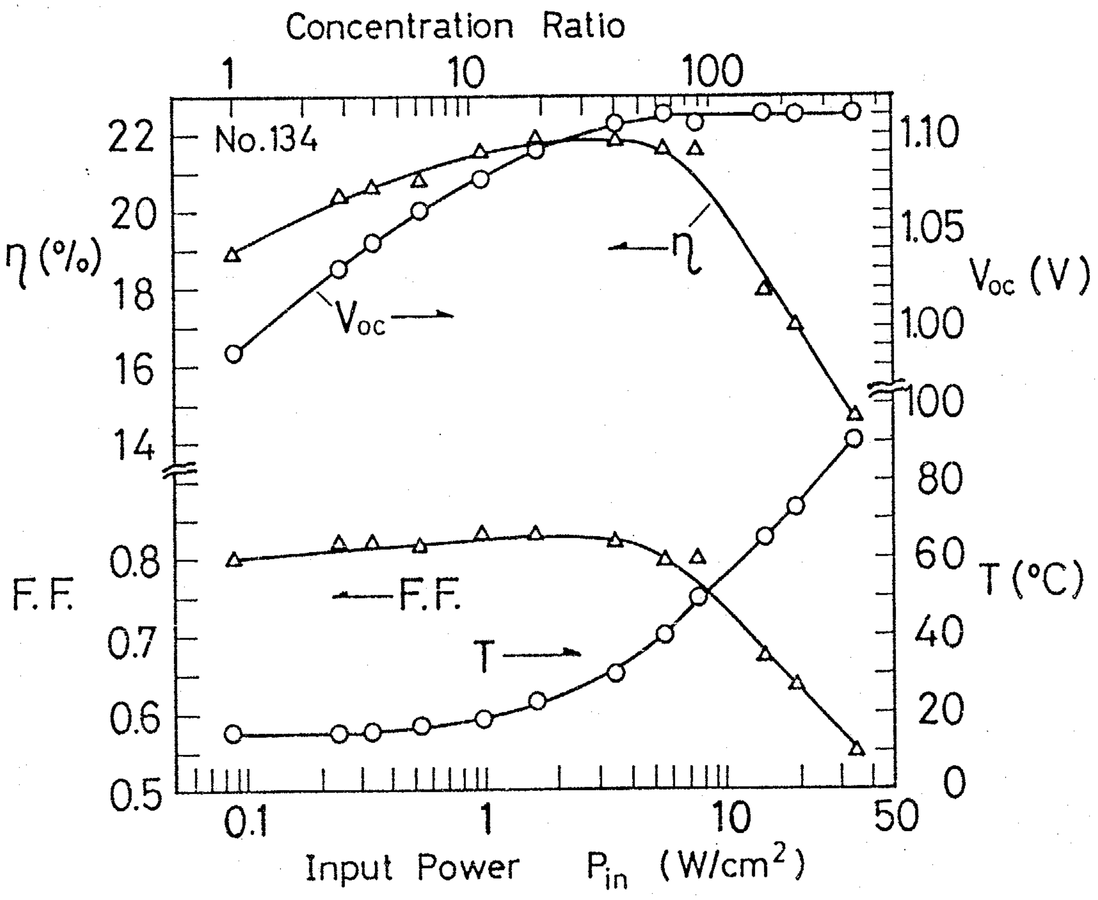

Fig. 10-4.

The photovoltaic characteristics under solar concentration conditions as a function of the concentration ratio.

C^*	P_{IN} (Wcm^{-2})	V_{OC} (V)	I_{SC} (Acm^{-2})	F.F.	η (%)	P_{OUT} (Wcm^{-2})
1	0.085	0.987	0.021	0.80	18.9	0.016
40	3.5	1.11	0.83	0.82	21.8	0.754
78	6.6	1.11	1.60	0.80	21.2	1.41
395	33.7	1.11	8.12	0.55	14.6	4.92

Table 10-3.

Concentration dependence of Be doped (GaAl)As/GaAs p-p-n solar cells (Cell No. 134).

*) Concentration ratio C and input power density P_{in} were assumed as $C = I_{sc}^{conc}/I_{sc}^{o}$ and $P_{in} = C \times P_{in}^{o}$, where I_{sc}^{conc} is the short circuit current density under solar concentration, I_{sc}^{o} the short circuit current without concentration, and P_{in}^{o} is the input power density of direct sunlight.

10-5. Device performance of p-$Ga_{1-x}Al_xAs$/p-$Ga_{1-y}Al_yAs$/n-$Ga_{1-y}Al_yAs$ ($x > 0.8$, $0 \leq y \leq 0.4$) solar cells.

In this section, the characteristics of (GaAl)As/(GaAl)As p-p-n solar cells in which the active region was formed by $Ga_{1-y}Al_yAs$ ($0 < y < 0.4$), are discussed. These devices were formed on n^+-GaAs substrates and fabricated in the same manner as that described in Sec. 10-3.

Before discussing the performance of this type of solar cell, it is noted that the thickness of p-$Ga_{1-y}Al_yAs$, formed by Be diffusion during the LPE growth of p-$Ga_{1-x}Al_xAs$ ($x > 0.8$), was not optimum for the production of the highest photocurrent except in the case $y = 0$. The thickness of the p-$Ga_{1-y}Al_yAs$ region increases with increasing Al composition 'y', because these devices were formed under the same growth conditions. Hence, the devices discussed in this section have various p-$Ga_{1-y}Al_yAs$ thicknesses depending on the Al composition 'y', and the p-$Ga_{1-y}Al_yAs$ thickness is given in Fig. 4-9. An AR coating was not deposited in order to provide easier device inter-comparison.

Figure 10-5 shows the open circuit voltage as a function of Al composition 'y'. The error bars relate to data from 4 to 6 samples. V_{oc} increases with increasing 'y', because of the increase in the energy band gap. Here, the voltage ratio VR(y) is defined as

$$VR(y) = V_{oc}(y)/E_g^{\Gamma}(y) \quad . \tag{10-1}$$

.(y) slightly decreases from 0.70 to 0.68 with increasing 'y' om 0 to 0.4. The increase in the energy band gap is sufcient to explain the increase in V_{oc}. The slight decrease VR(y) with increasing 'y' may be due to the drastic decrease I_{sc} as shown in Fig. 10-6. The solid curve in Fig. 10-6 presents theoretically calculated values[*] using the experintally observed thickness of p-$Ga_{1-y}Al_yAs$, which is given in g. 4-9. These theoretical values agree with the observed I_{sc}.[**] pointed out in this section, the thickness of p-$Ga_{1-y}Al_yAs$ s not optimized to produce the highest short circuit current. e broken curve in this figure represents the theoretically timized values for the thickness of p-$Ga_{1-y}Al_yAs$. e optimized thickness has little compositional dependence, and 1.5-2μm, depending on the electron diffusion length in the $Ga_{1-y}Al_yAs$ region.

Figure 10-7 shows the energy conversion efficiency as a nction of 'y'. The conversion efficiency decreases rapidly th increasing 'y' due to the drastic derease of I_{sc} with creasing 'y'. The solid curve and the broken curve represent eoretically calculated values without and with optimization r the thickness of p-$Ga_{1-y}Al_yAs$ as in Fig. 10-6.

) See Appendix B.

) The reflection loss effect at the front surface of p-(GaAl)As was included in the numerical calculations.

The agreement between the observed and the theoretically calculated values (using the observed thickness of p-$Ga_{1-y}Al_yAs$) indicates that the device performance, if the thickness of the active region was optimized, can be predicted by the broken curves in figures 10-6 and 10-7.

The results in this section could be utilized for the design and preparation of (GaAl)As/GaAs based monolithic cascade solar cells.

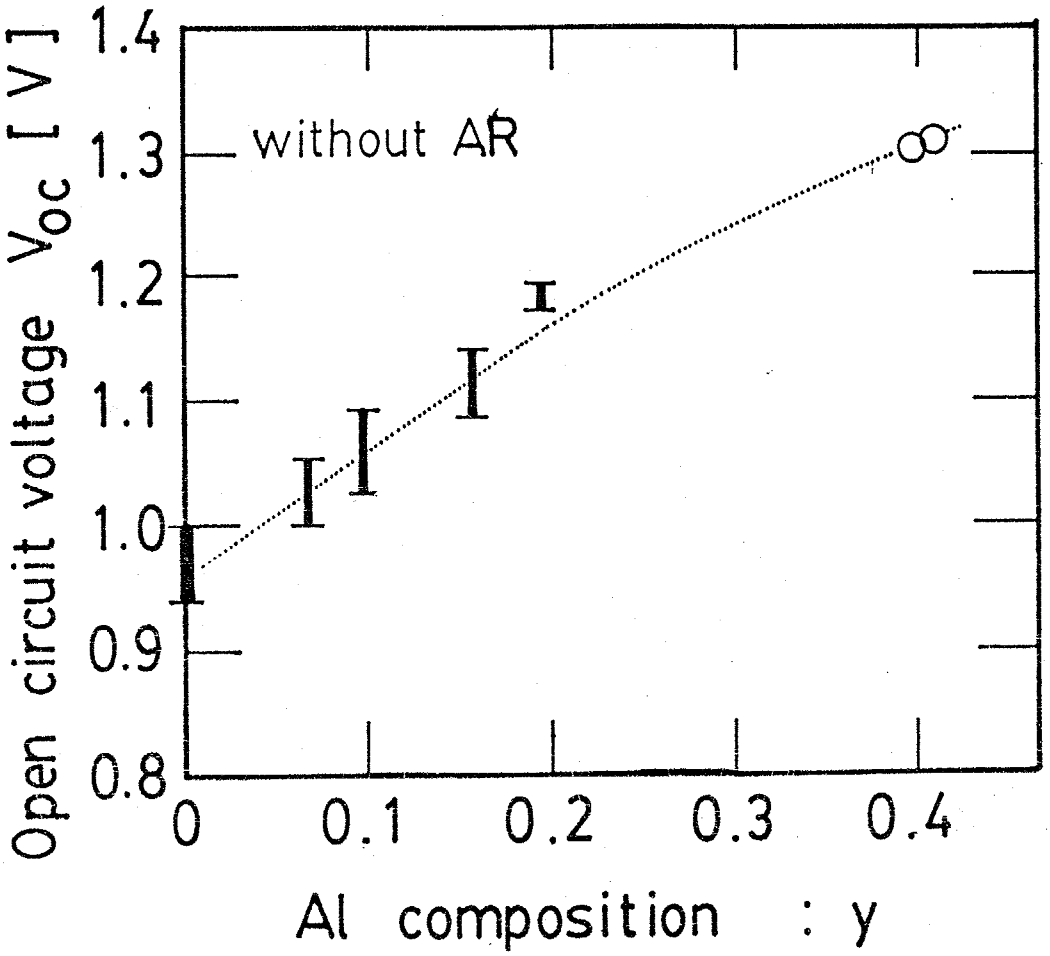

Fig. 10-5.

The open circuit voltage of the (GaAl)As/(GaAl)As p-p-n solar cells as a function of Al composition 'y', measured using AM 1 solar simulator. Each error bar contains the data of several samples.

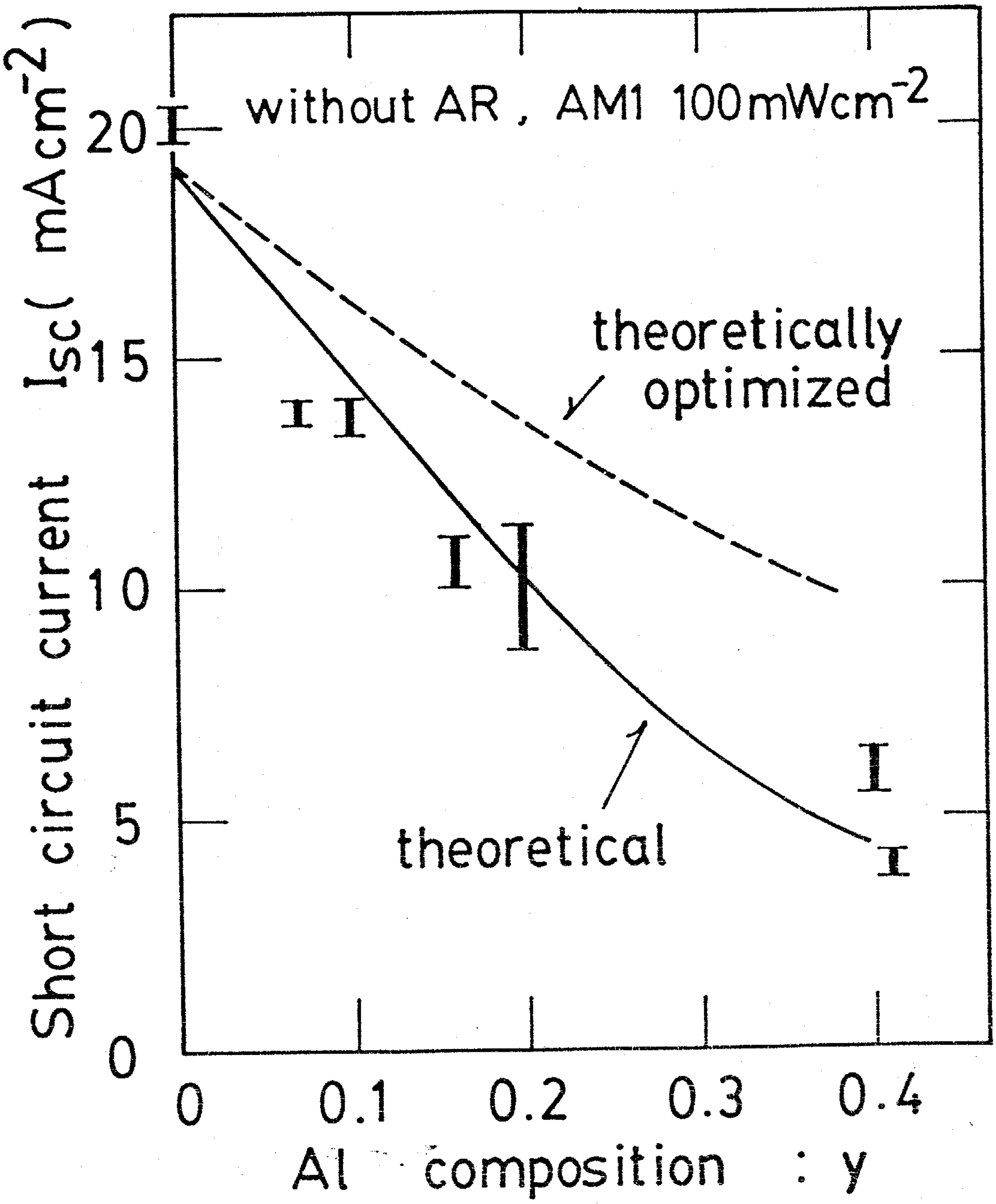

Fig. 10-6.

The short circuit current of the (GaAl)As/(GaAl)As p-p-n solar cells as a function of Al composition 'y'. Each error bar contains the data of several samples. The solid and broken curves are theoretically calculated (see text).

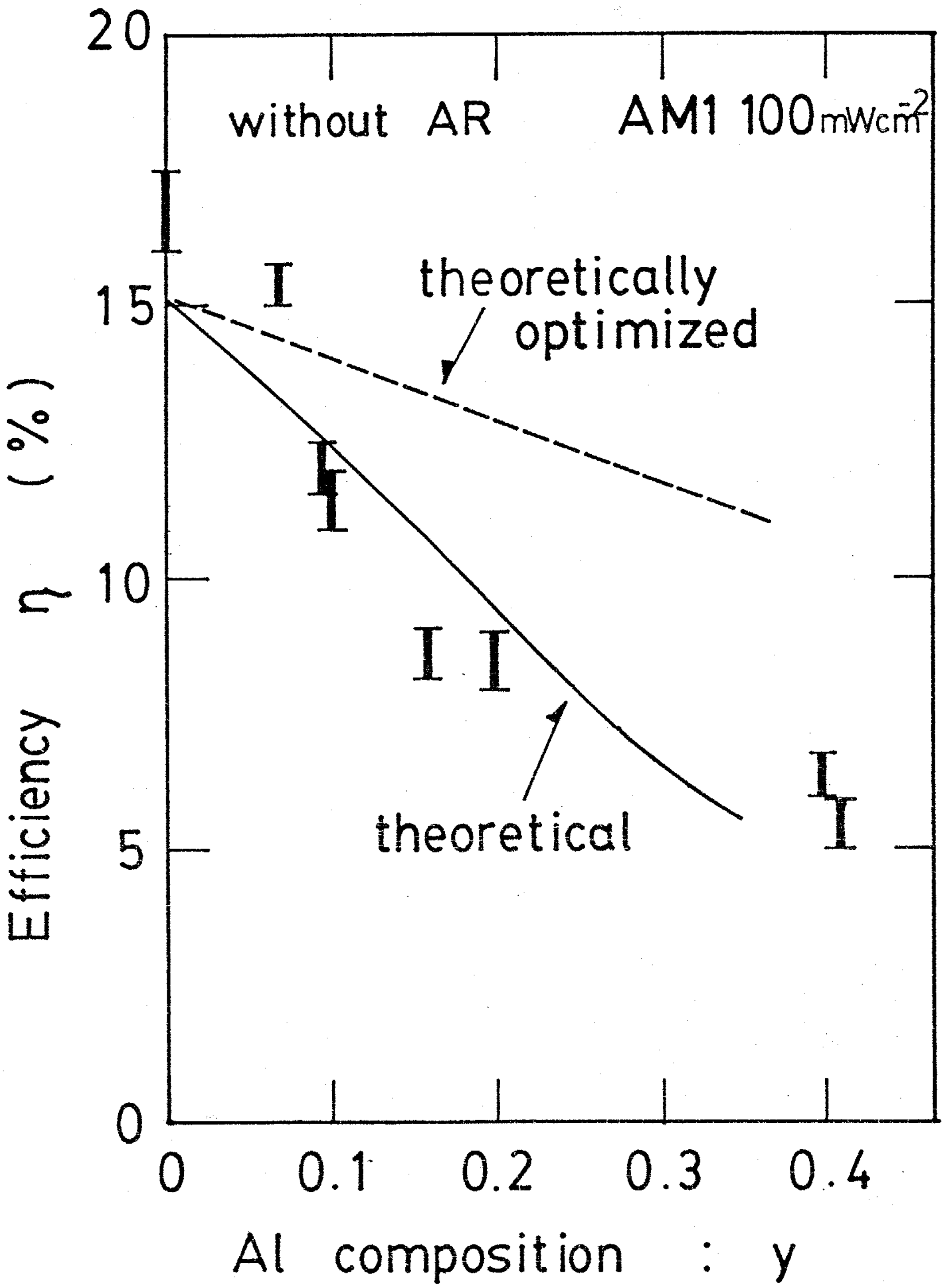

Fig. 10-7.

The conversion efficiency of the (GaAl)As/(GaAl)As p-p-n solar cells as a function of Al composition 'y'. Each error bar contains the data of several samples. The solid and broken curves are theoretically calculated values (see text).

10-6. Summary and conclusion .

As shown in Chap. 6, beryllium is a suitable p-type dopant for (GaAl)GaAs solar cells. In this chapter, Be doped (GaAl)As/GaAs p-p-n solar cell performance was discussed. The Be doped solar cells exhibited high conversion efficiencies of over 20%, as predicted from the large electron diffusion length, which was described in Chap. 6. When placed in a concentrator assembly, the device produced an output power of $5W\cdot cm^{-2}$ at 400 suns .

Finally, the (GaAl)As/(GaAl)As p-p-n solar cells, in which the active region was formed by $Ga_{1-y}Al_yAs$ p-n structure, were fabricated and tested. It was demonstrated that these devices could be used as the top cell of (GaAl)As/GaAs based cascade solar cells.

CHAPTER 11.

DEVELOPMENT OF MONOLITHIC SERIES-CONNECTED MULTI-JUNCTION GaAs SOLAR CELL ARRAYS.

11-1. Introduction.

As discussed in the previous chapters, the (GaAl)As/GaAs p-p-n solar cell has a high conversion efficiency in excess of 20%. These are the highest conversion efficiency developments. However, the output voltage of a solar cell is limited by the energy band gap of the constituent material, e.g., the open circuit voltage is about 1 V in (GaAl)As/GaAs solar cells. Recently, the development of a solar cell array with a high output voltage integrated onto a single wafer has become necessary for use in solar power systems and in photocells for consumer use.

Borden (1980) has shown that the monolithic series-connected solar cell array on a wafer has various advantages over the single junction solar cell when used in tracking concentration arrays and spectral splitters, e.g., the small degradation caused by non-uniform illumination in the solar cell array. The monolithic GaAs solar cell array was first fabricated by Borden (1980) with an efficiency of 13.6% under AM2 sunlight. However, the cell performance was limited due to the fabrication process, which is more complicated for a monolithic solar cell array than that for the usual solar cell.

For example, the formation of the insulating layer, preventing the interconnecting metal from shortage the junction at the edge of each subcell, is complex.

Three types of monolithic GaAs solar cell arrays formed on Cr-doped semi-insulating GaAs wafers were fabricated and tested in this work. In order to explore the fabrication process, the Schottky barrier type(SB) and p-n homojunction type solar cell arrays were fabricated as starting points for the monolithic GaAs solar cell arrays. This is described in Sec. 11-2 and Sec. 11-3. The (GaAl)As/GaAs p-p-n heterostructure type device is discussed in Sec. 11-4.

One of the major problems in a monolithic solar cell array formed on a semi-insulating GaAs wafer is junction shortage at the edge of each subcell, caused by the interconnecting metal. This problem does not occur in the SB type cell array. In the p-n homojunction type cell array, this difficulty can overcome by forming a p-GaAs region at the edge of each subcell. Additional Zn diffusion was proposed in order to solve this problem in the (GaAl)As/GaAs heterostructure type device. This process obviate the necessity for an insulating layer at the edge of each subcell in order to prevent junction shortage.

11-2. The Schottky barrier type monolithic GaAs solar cell array.

The Schottky barrier type monolithic solar cell array formed on a GaAs wafer was considered first in order to establish the fabrication process, because the junction can formed simply by metal evapolation onto the n-GaAs layer and the barrier metal can also be used as the interconnecting metal.

Figure 11-1 shows a schematic diagram of this array consisting of a number of rectangular subcells. Each subcell was 4 mm wide and 1 mm long and was connected in series. The number of subcells was usually 3, 4, or 5. The spacing between subcells was 100 μm.

A (100) Cr-doped semi-insulating GaAs wafer with a 5 μm n-GaAs epitaxial layer was used as the starting material. The n-GaAs epitaxial layers were deposited in the usual Ga + $AsCl_3$ CVD system, and the room temperature carrier concentration was $(1\text{-}10)\times10^{16}\mathrm{cm}^{-3}$. The interconnecting junctions were formed by the following process and the usual photolithographic technique was used for each fabrication stage.

(1) Ohmic contacts (Au + Ge + Ni) formation on the n-GaAs layer.

(2) n-GaAs mesa-etching. (each subcell was isolated electrically.)

(3) Deposition of gold for both the barrier and the interconnecting metal.

(4) Deposition of Sb_2O_3 for the AR coating.

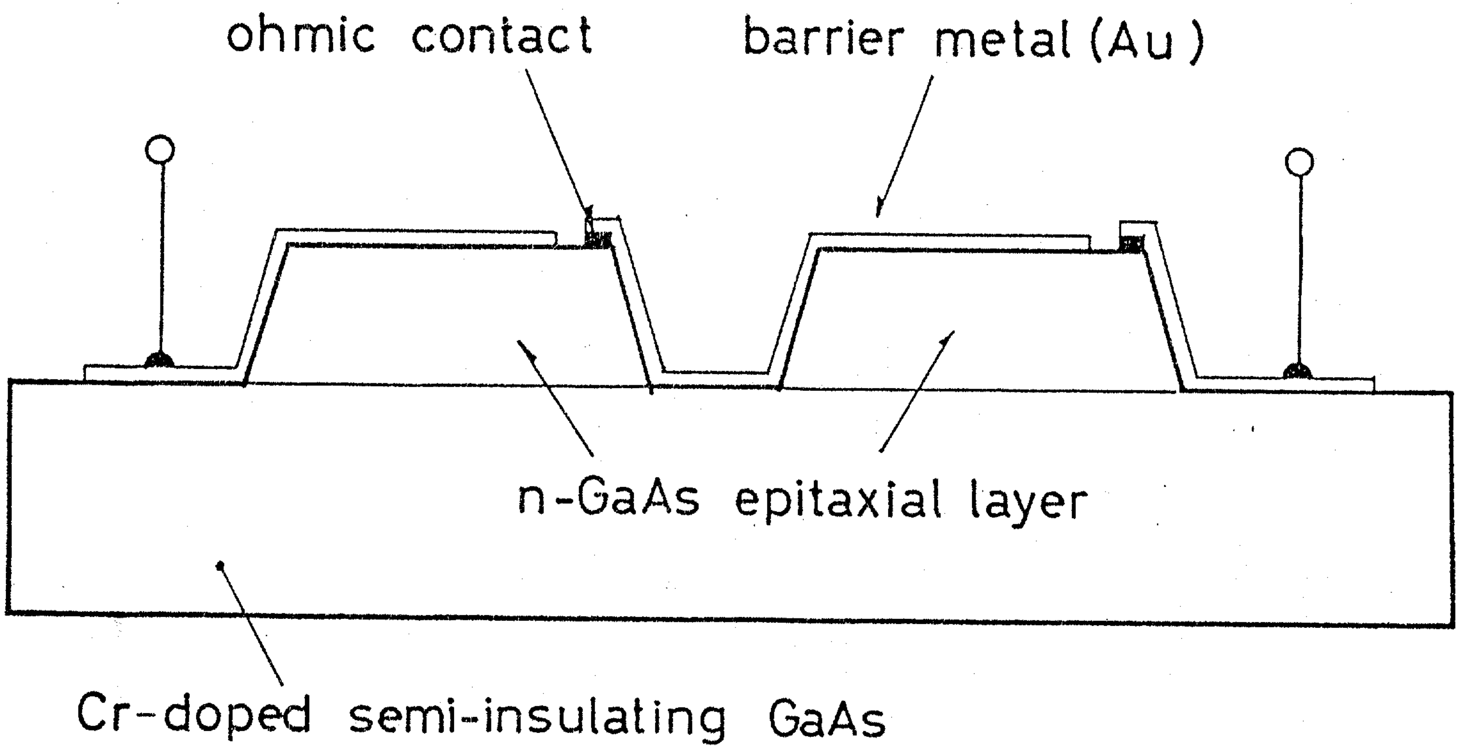

Fig. 11-1.

Schematic diagram of a Schottky barrier type monolithic series-connected solar cell array integrated on a semi-insulating GaAs wafer.

One of the most important processes is the n-GaAs mesa-etching process which ensures that the each subcell is electrically isolated. When a GaAs surface is etched using a rectangular mask, the cross-section perpendicular to the substrate surface is generally trapezoidal. The cross-section of the n-GaAs layer of a monolithic solar cell array formed on a single wafer must be mesa-type trapezoid as shown in Fig. 11-1 in order to connect each subcell across the groove via the interconnecting metal. Each subcell was oriented as shown in Fig. 11-2 and was connected in series, parallel to the $\langle 0\bar{1}1 \rangle$ direction. A $H_2SO_4 + H_2O_2 + H_2O$ (1 : 10 : 1, 0-5°C) solution was used for the groove etching precess. This satisfied the above condition. The photographs in Fig. 11-2 show the (011) and $(0\bar{1}1)$ cleaved cross sections which were obtained using this etching. These results are similar to those reported by Iida (1971).

Before deposition of the gold film for the barrier metal, the GaAs surface was cleaned using a solution of $H_2SO_4 + H_2O_2 + H_2O$ (10 : 1 : 1, 30°C) for 10 - 15sec. The sheet resistance was controlled at 80-100Ω/□.

Figure 11-3 shows the current-voltage characteristic of a SB type solar cell array. The detailed cell performances are summarized in Table 11-1. The current density (normalized current) I is defined as

$$I = I^{ARRAY}/S, \qquad (11\text{-}1)$$

where I^{ARRAY} is the current which flows through the cell array and S is the effective subcell area ($S = 1 \times 4$ mm^2).

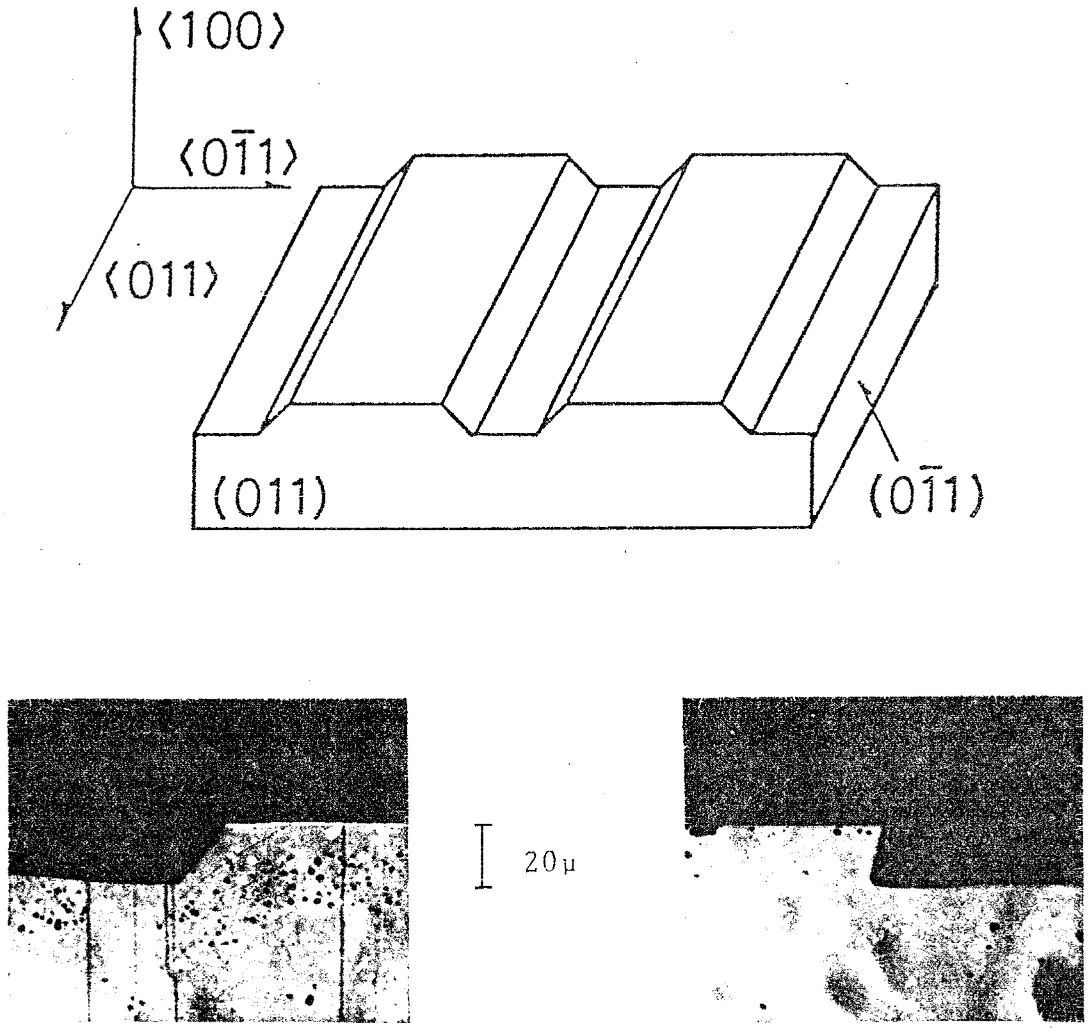

(011)

(0$\bar{1}$1)

Fig. 11-2.

Schematic cross-sections of a monolithic GaAs solar cell array. The Photographs show the cleaved cross-sections obtained using a $H_2SO_4 + H_2O_2 + H_2O$ (1:10:1, 5°C) solution.

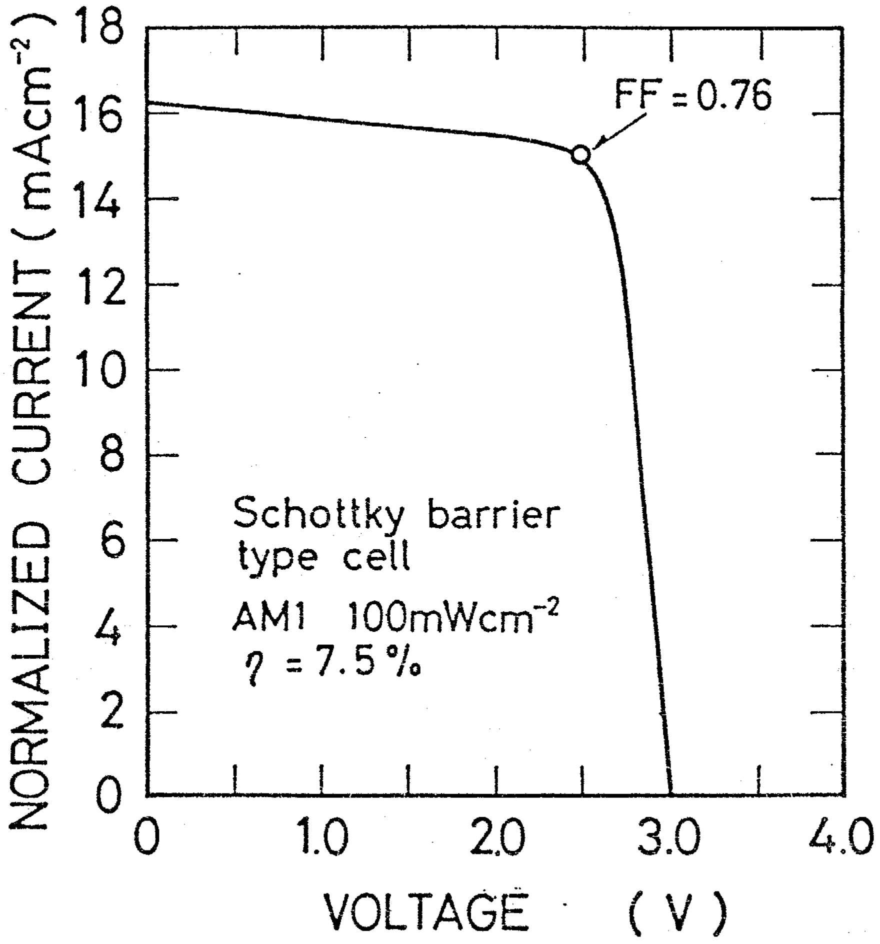

Fig. 11-3.

The current-voltage characteristic of the Schottky barrier type device under simulated AM1 insolation (100mWcm^{-2}), m is the number of subcells. The open circuit voltage and the conversion efficiency are 3.0V and 7.5%, respectively.

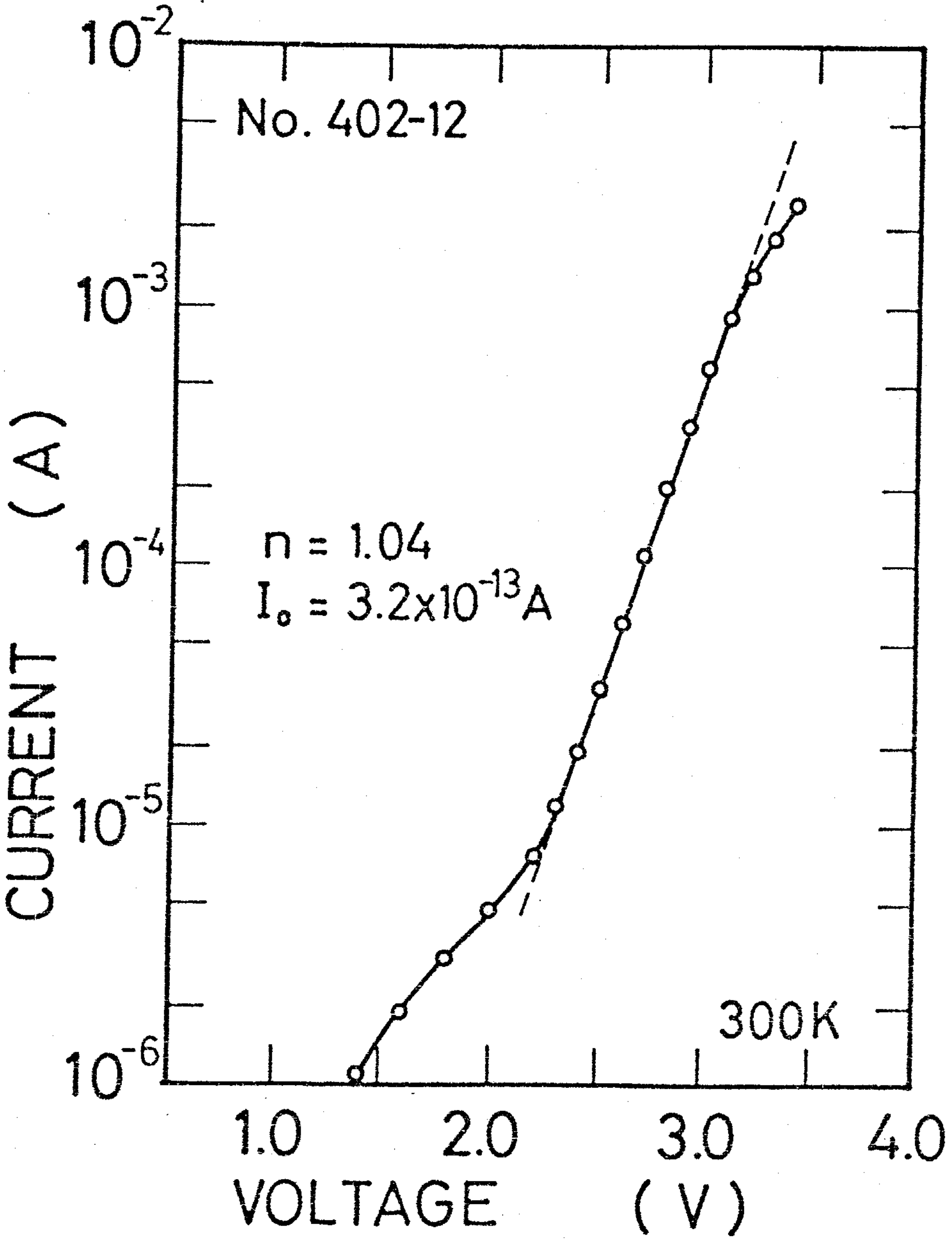

Fig. 11-4.

Dark I-V curve for the Schottky barrier type cell array. The average diode quality factor n is defined in Eq. 11-2.

This SB type solar cell array exhibited an open circuit ltage of 3.0 V for an array consisting of five adjacent cells. e average open circuit voltage per subcell is 0.6 V, which the usual value for GaAs MS solar cells. The fill factor s 0.76, which is one of the highest values reportes for GaAs or MIS solar cells (Yeh, 1977). The dark I-V curve for is cell array is shown in Fig. 11-4. The average diode ality factor n is defined as

$$I = I_0 \exp(qV/mnkT), \tag{11-2}$$

ere m is the number of subcells and the other symbols ve their usual meaning. This cell has n = 1.04, and it is nsidered that a nearly ideal Schottky barrier was achieved this device.

-3. The p-n homojunction type monolithic GaAs solar cell array.

A major problem in the p-n homojunction type solar cell ray is to prevent the interconnecting metal from shorting e junction at the groove wall. An insulating layer such SiO_2 had to be deposited at the edge of the p-type ohmic ntact side of each subcell in order to avoid junction shortage the previous fabrication process (Borden, 1980) as shown in g. 11-5(a). In this work, a new method for the connection each subcell on a single wafer was proposed as shown in g. 11-5(b). The opposite side to the n-type ohmic contact de of the etched groove covered with a p-type GaAs region,

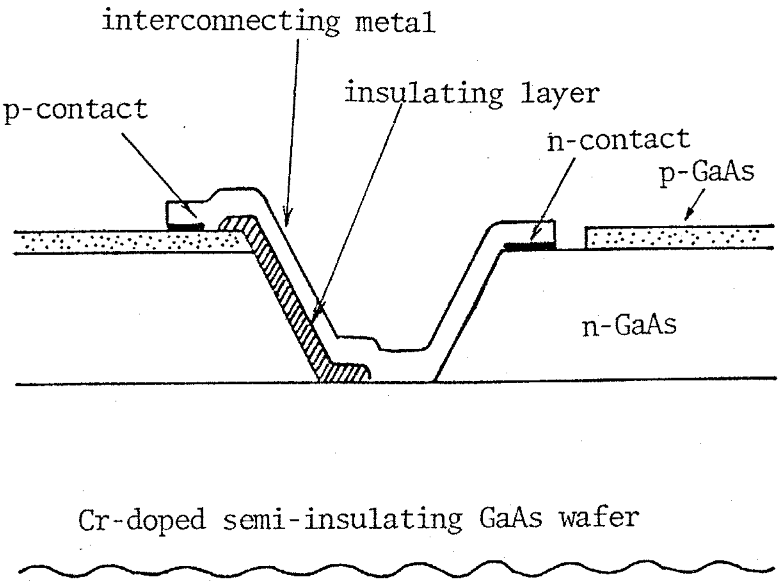

(a) the current type

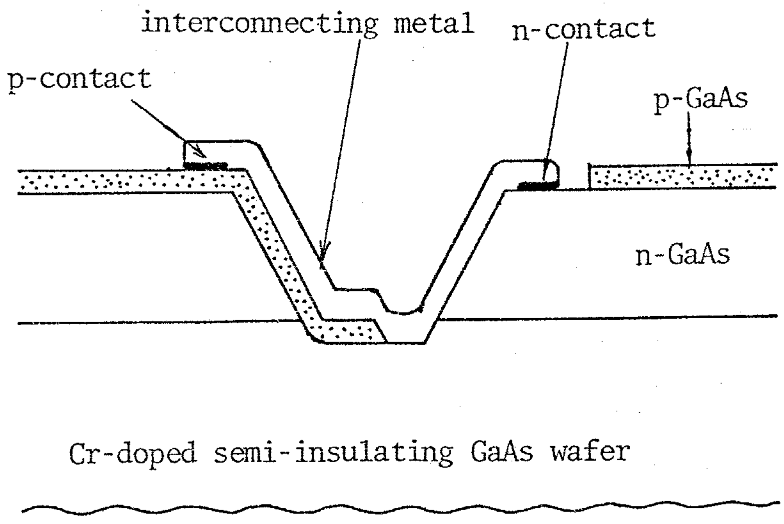

Fig. 11-5.

(b) this work

chematic diagram of two types of p-n homojunction monolithic olar cell arrays.

a) The current type: An insulating layer such as SiO_2 is necessary to prevent the interconnecting metal from shorting the junction at the groove wall of each subcell.

b) This work: The groove wall is covered with a p-GaAs region, so that an insulating layer is not necessary.

so that an insulating layer such as SiO_2 was not necessary to avoid junction shortage. This covering by a p-type GaAs region increases the cell stability because it is not necessary to consider the leakage through the insulating layer, and thus higher stability can be expected under high sunlight concentration operation.

The starting material for p-n homojunction type solar cell array is a (100) Cr-doped semi-insulating GaAs wafer with a 5μm n-GaAs epitaxial layer as for the SB type device. The p-n homojunction was formed by diffusion of Zn using the usual closed-ampoule annealing technique.

The p-n homojunction type cell arrays were fabricated by the following process.

(1) First mesa-etching. (Each subcell of n-GaAs was isolated electrically.)

(2) Zn diffusion to form the p-n junction.

(3) Second mesa-etching. (n-GaAs region revealed on one side of each groove.)

(4) Ohmic contacts formation on the p- and n-GaAs regions. (Ag + Zn for the p-contacts and Au + Ge + Ni for the n-contacts.)

(5) Deposition of the interconnecting metal. (Silver was usually used.)

(6) Deposition of Sb_2O_3 for the AR coating.

The Zn diffusion was carried out at a temperature of 650°C for 20min. The junction depth was about 0.5μm.

The I-V characteristics as measured in the solar simulator are shown in Fig. 11-6. Each curve in this figure

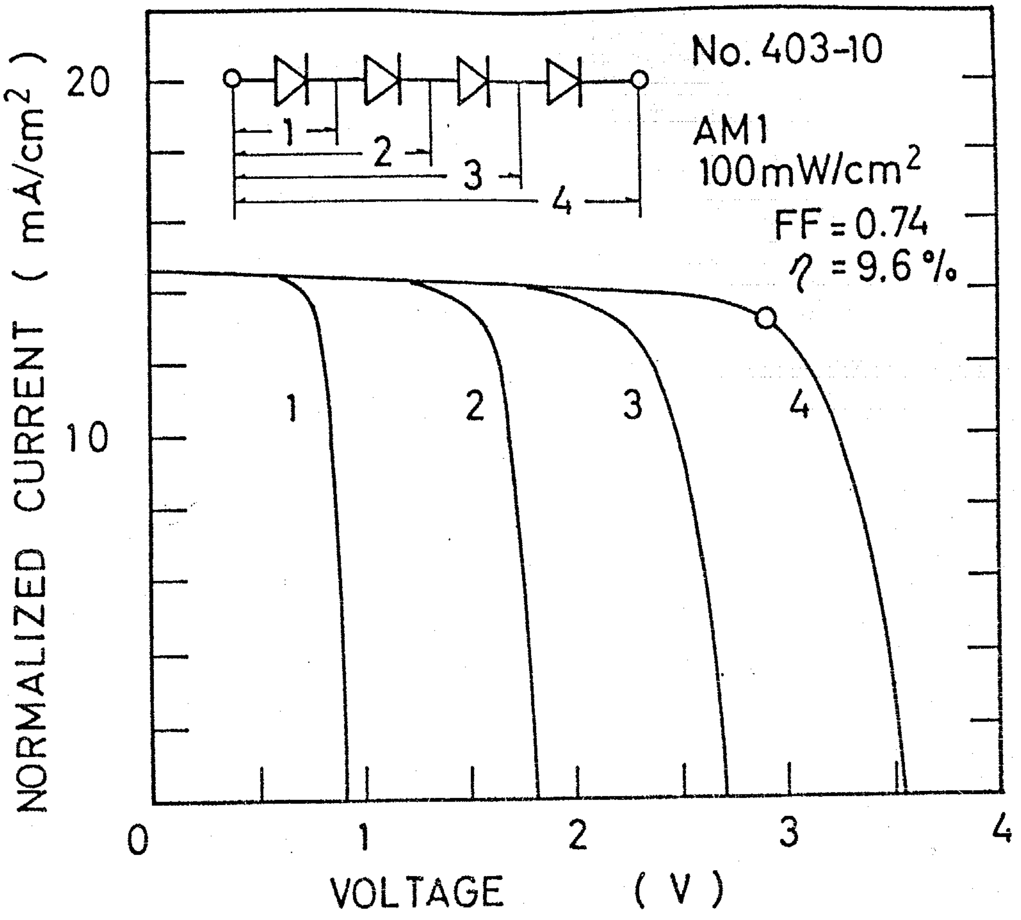

Fig. 11-6.

I-V curves for the p-n homojunction type solar cell array measured in the solar simulator (AM1, 100mWcm^{-2}). Each curve represents the I-V characteristics for the number of subcells indicated i.e., 1, 2, 3, and 4, respectively.

represents the I-V characteristic for the number of subcells indicated (1, 2, 3, and 4, respectively). This cell array consisting of four adjacent subcells. One can see that the total open circuit voltage increases proportionally with the number of subcells. The total open circuit voltage and conversion efficiency under simulated AM1 insolation are 3.55 V and 9.6%, respectively. Detailed cell performance in including data for other p-n homojunciton type solar cell arrays are listed in Table 11-1. The average open circuit voltage of about 0.9 V is a very high values for GaAs p-n homojunction type solar cells. The conversion efficiency is also very high.

Figure 11-7 shows the dark I-V curves for this cell array. Each curve represents the I-V characteristic for the number of subcells indicated, i.e. 1, 2, 3, and 4, respectively. The diode quality factor for each subcell and the average value (see Eq. 7-2) was about 2, which is normal for Zn-diffused type GaAs p-n homojunction solar cells.

The Zn-diffusion process described in this section was also applied in the fabrication of the (GaAl)As/GaAs heterostructure type solar cell array.

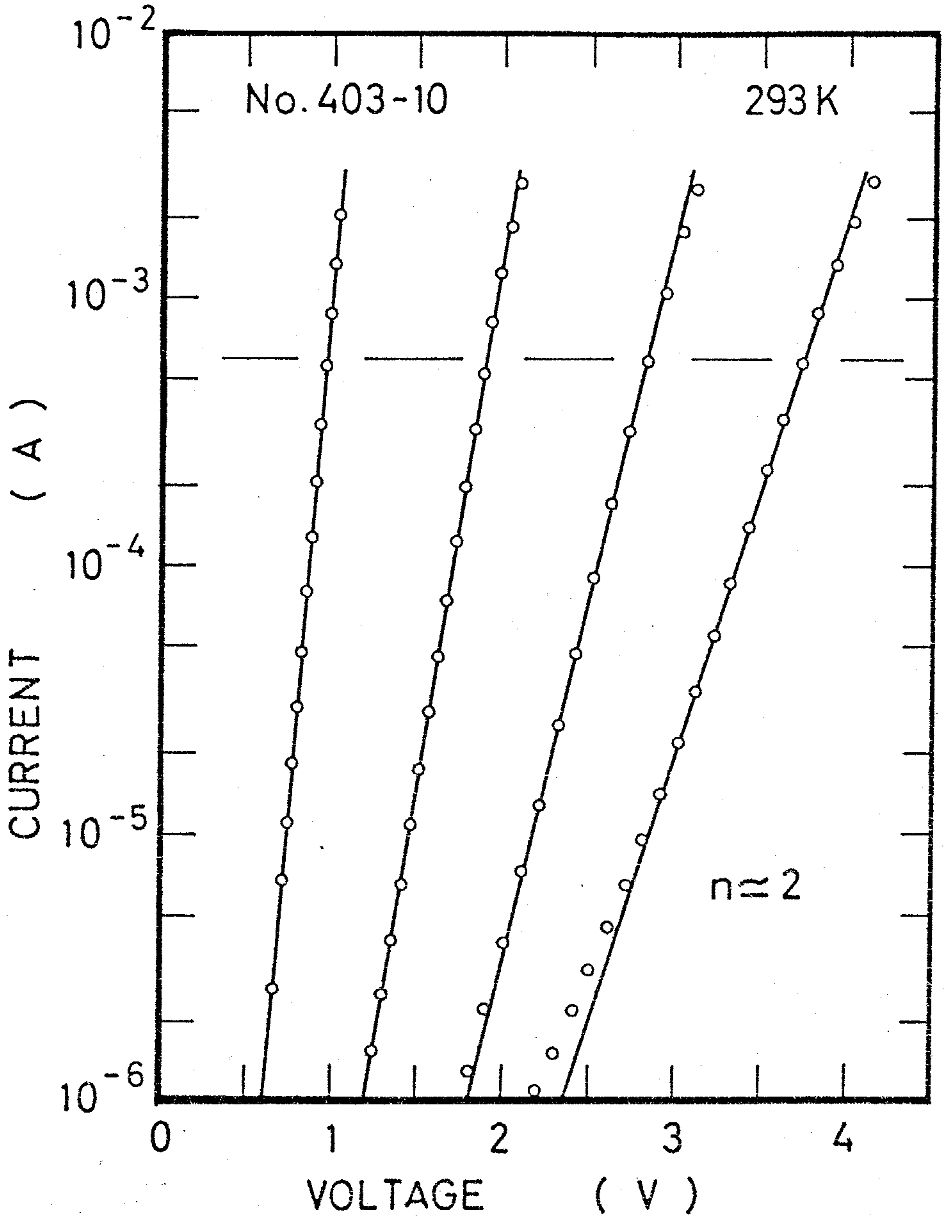

Fig. 11-7

Dark I-V characteristics for the p-n homojunction type solar cell array. The diode quality factor for each curve as defined in Eq. 11-2 is about two.

Table 11-1.

Photovoltaic Characteristics of GaAs Monolithic Solar Cell Arrays

No.	Junction type	m^*	V_{oc} (V)	I_{sc} ($mAcm^{-2}$)	F.F.	η (%)	AM^{**}
402-2	SB	3	1.8	14.8	0.76	6.8	1
402-12	SB	5	3.0	16.3	0.76	7.5	1
401-10	p-n	4	3.20	14.9	0.70	8.4	1
403-10	p-n	4	3.52	14.6	0.74	9.6	1
		4	3.58	12.1	0.77	11.4	2
		5	4.30	12.1	0.74	10.6	2

*) m is the number of subcells.

**) AM1 : 100$mWcm^{-2}$ solar simulator.

AM2 : 73 $mWcm^{-2}$ solar simulator.

11-4. The (GaAl)As/GaAs heterostructure type monolithic solar cell array.

(GaAl)As/GaAs p-p-n heterostructure solar cells have demonstrated high conversion efficiencies of over 20%. Consequently, the (GaAl)As/GaAs p-p-n structure should be used in monolithic solar cell arrays in order to obtain such high conversion efficiencies.

Therefore (GaAl)As/GaAs heterostructure type monolithic solar cell arrays were fabricated by adopting the Zn diffusion process described in the previous section. Figure 11-8 shows a schematic diagram of the (GaAl)As/GaAs heterostructure type cell array. Since the groove wall on the p-type ohmic contact side is covered with the Zn-diffused region, an insulating layer was not necessary in order to avoid junction shortage.

The starting material was (100) Cr-doped semi-insulating wafers with a p-(GaAl)As/p-GaAs/n-GaAs heterostructure. The fundamental fabrication process was the same as that for the p-n homojunction type device described in the previous section.

The GaAs wafer with the heterostructure was prepared by the usual LPE method as described in Chap. 10. The Sn-doped n-GaAs (5-6μm) and Be-doped p-$Ga_{1-x}Al_xAs$ ($x>0.8$, 2μm) layers were grown at a temperature of about 750°C. p-GaAs was formed by the diffusion of Be into the n-GaAs epitaxial layer during the growing process of the Be doped p-(GaAl)As. The junction depth was about 2μm. This is the usual

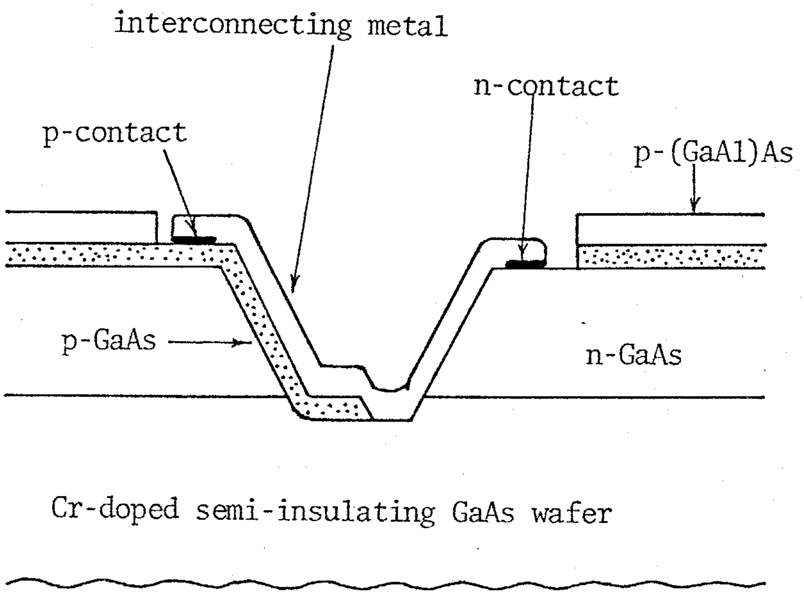

Fig. 11-8.

Schematic diagram of the (GaAl)As/GaAs heterostructure type monolithic solar cell array fabricated with an additional Zn diffusion process in order to avoid junction shortage at the groove wall.

V_{oc} = 3.55 V

I_{sc} = 24.3 $mA \cdot cm^{-3}$

FF = 0.70

η = 15.0 %

- simulated AM1 insolation.
- 4 adjacent cell array.

Table 11-2. The photovoltaic characteristics of a
The photovoltaic characteristics of a (GaAl)As/GaAs heterostructure type monolithic solar cell array.

structure of (GaAl)As/GaAs p-p-n single junction solar cells (as described in Chap. 10) apart from the semi-insulating substrate.

The additional Zn diffusion process was carried out at a temperature of 650°C for 20 min. Zinc does not reach the p-GaAs region, i.e. Zn diffusion is limited to the p-(GaAl)As layer.

The device performance is given in Table 11-2. The cell array, consisting of 4 adjacent subcells, has an open circuit voltage of 3.55V and a conversion efficiency of 15.0% under AM1 insolation. The cell performance is low compared to that of single junction (GaAl)As solar cells. This is attributed to a low fill factor, which probably arises from the non-uniformity of the subcell area (About 7% in this device). The bias point of each subcell is adjusted to compensate for the subcell area variation so that a constant current flows through the cell array.

The cell performance could be enhanced by improvements in the fabrication process.

11-5. Summary and conclusion .

Three types of monolithic GaAs solar cell arrays formed on Cr-doped semi-insulating GaAs wafers were fabricated and tested.

In order to explore the fabrication process, Schottky barrier type and p-n homojunction type solar cell arrays were fabricated as a starting point for monolithic solar cell arrays. The Schottky barrier type solar cell array exhibited V_{oc}=3.0V and η=7.5% (AM1) for a 5 adjacent cell array.

One of the major problems in a monolithic solar cell array is junction shortage at the edge of each subcell, caused by the interconnecting metal. (This problem does not occur in the SB type cell array.) In the p-n homojunction type cell array, this difficulty was overcome by forming a p-GaAs region at the edge of each subcell. The p-n homojunction type cell array, in which the p-n homojunction was formed by diffusion of Zn using the usual closed-ampoule-annealing technique, exhibited V_{oc}=3.52V and η=9.6% (AM1), and η=11.4%(AM2) for a 4 adjacent cell array.

Additional Zn diffusion was proposed in order to solve the problem of junction shortage at the edge of each subcell caused by the interconnecting metal in the (GaAl)As/GaAs p-p-n heterostructure device. Using this method, an insulating layer such as SiO_2 was not necessary in order to avoid junction shortage, since the groove wall on the p-type ohmic contact side was covered with the Zn diffused p-GaAs region. The (GaAl)As/GaAs p-p-n type cell array exhibited

V_{oc}=3.55V and η=15.0% (AM1) for a 4 adjacent cell array. Although the conversion efficiency is low compared to that of single junction (GaAl)As/GaAs solar cells because of a low fill factor, the device performance could be enhanced by improvements in the fabrication process.

PART V

GENERAL CONCLUSIONS

Chapter 12. General conclusions.

CHAPTER 12. GENERAL CONCLUSIONS.

It must be emphasized that investigations of the physical properties relating to III-V compound semiconductor alloys are required in order to obtain high performance electronic devices for the 1980's. This research work was performed with the following primary aims; to investigate the bahaviour of II-column impurities in $Ga_{1-x}Al_xAs$ ternary alloys,to develop new III-V quaternary alloys, and to develop high performance GaAs based solar cells as an application field.

In this chapter, the achievements which were described in detail in PARTs II, III, and IV, are summarized and the main conclusions of this research programme are stated.

BEHAVIOUR OF II-COLUMN IMPURITIES IN $Ga_{1-x}Al_xAs$ TERNARY ALLOYS.

The diffusion of II-column impurities in GaAs during the LPE growth process, which is a technique widely utilized in the formation of p-n structures for the preparation of various electronic devices, was thoroughly investigated for both Be and Zn. From an evaluation of the free-carrier concentration profiles in the Be diffused p-GaAs regions formed by Be diffusion during the LPE growth of Be doped p-$Ga_{0.2}Al_{0.8}As$, it was shown that this diffusion process could be treated as simple diffusion in a semi-infinite medium, if the surface free-carrier concentration was less than $6x10^{18}cm^{-3}$. The diffusion coefficient takes the form $D = D_o(-E_o/kT)$, where $D_o = 0.66cm^2s^{-1}$ and $E_o = 2.43eV$ for Be diffusion in the temperature range from 700°C to 900°C.

The results presented in Chap. 3 have established the treatment of II-column impurity diffusion during LPE growth process.

The Hall mobility, which can be measured simply by the van der Pauw method, is one of the most important indices used in studying, characterizing, and assessing the quality of semiconducting materials. In the previous analyses and experimental studies, an important problem has been left unresolved, i.e., the analytically calculated values for the Hall mobility. In previous investigations, only the calculated drift mobility and the experimentally observed values for Hall mobility were given. A modified two-band transport model was derived which enables the separate calculation of the drift and Hall mobilities. In this model the drift and Hall mobilities are calculated from the sum of various mobility components using Matthiessen's rule, and the Hall coefficient factor can be calculated essentially from the ratio of the heavy to the light hole effective masses. Numerical calculations were performed for p-type $Ga_{1-x}Al_xAs$, taking into account the acoustic and non-polar optical phonon, the polar optical phonon, the ionized impurity, and the alloy scattering. The alloy scattering is an additional scattering mechanism found in ternary and quaternary alloys. The numerical calculation results showed that the room temperature Hall mobility (and also the drift mobility) was influenced according to the magnitude of the alloy scattering potential, and the compositional dependence of the room temperature mobility would be significantly bowed by the existence of alloy scattering with an alloy scattering potential of 0.7eV.

It is noted that the coupled-Boltzmann transport equations must be solved for a strict analysis. However, few studies in which the solutions of the coupled transport equations were used in explaning the experimental Hall mobility data. This is no doubt due to the difficulty of the solutions. Since the modified two-band transport model,which is derived in this thesis, has simpler expressions than those for the strict derivation ,this model will be utilized for the analysis of the Hall mobility data of other III-V ternary and quaternary alloys.

Few systematic studies of the electrical properties of p-type $Ga_{1-x}Al_xAs$ have been reported. Nevertheless the $Ga_{1-x}Al_xAs$ ternary alloy is one of the most commonly used III-V ternary alloys for various electronic devices.

It is shown that the acceptor energy level in $Ga_{1-x}Al_xAs$ increases with increasing Al composition from about 25meV to 70meV, from theoretical considerations using the modified hydrogenic model which takes the valence band structure through the Luttinger's valence band parameters. The acceptor energy level for Zn in $Ga_{1-x}Al_xAs$ increases with increasing Al composition as theoretically predicted. Good agreement between the theoretical values and the experimental values was observed for Al compositions less than 0.5. The acceptor energy level for Zn reaches 140meV at $x = 1.0$ (AlAs), and zinc produces a relatively deep level in $Ga_{1-x}Al_xAs$ with a large Al composition of x > 0.5. On the other hand, beryllium produced a relatively shallow acceptor energy level in $Ga_{0.2}Al_{0.8}As$ of 47meV whereas that for Zn was about 80-90meV. Although it is expected that beryllium as a p-type dopant will produce a shallow acceptor energy level in $Ga_{1-x}Al_xAs$, the doping characteristics have not been reported. It was shown that the free-carrier concentration (from $3x10^{17}$ to $3x10^{18}cm^{-3}$) of $Ga_{0.2}Al_{0.8}As$ can be controlled by the Be concentration in the LPE growth melt, and that the distribution coefficient for $Ga_{0.2}Al_{0.8}As$ is about 0.03. If alloy scattering existed in p-$Ga_{1-x}Al_xAs$, then the room temperature Hall mobility would exhibit a significant bowing. However, the alloy scattering potential has been left as a justifiable parameter in the numerical calculations. Comparing the observed Hall mobility, the compositional variation of Hall mobility can be explained by the existence of alloy scattering, and the scattering potential was found to be 0.7eV for p-$Ga_{1-x}Al_xAs$.

The theoretical and experimental results described in PART II are the most significant achievements of this research programme, and these are arguably the most profound investigations of the physical properties of p-type $Ga_{1-x}Al_xAs$ yet reported.

DEVELOPMENT OF NEW III-III-III-V QUATERANRY SEMICONDUCTORS.

The main material requirement for optical devices in the 1980's is for materials whose energy band gap wavelength is less than 750 nm (for visible region) or greater than 1.0 μm (for the infra-red region). It is also preferable that the direct energy band gap should be in the required wavelength region. The III-III-III-V quaternary alloys such as (AlGaIn)As and (AlGaIn)P are amongst the most attractive materials for opto-electronic devices operating in these wavelength regions. However, phase diagram calculations showed that it was almost impossible to prepare these materials on appropriate substrates using the conventional LPE technique because of the large Al segregation coefficient. On the other hand, the MBE process, in which epitaxial growth occurs by impinging thermal molecular beams on a heated substrate in an ultra-high vacuum environment, can produce these materials on appropriate substrates.

$(Al_xGa_{1-x})_yIn_{1-y}As$ quaternary alloys lattice matched to InP substrates were prepared by the MBE technique. It was shown that these quaternary alloys had direct energy band gaps of 1.0-1.65 μm as predicted, from room temperature transmittance measurements and photoluminescence measurements at 77 K. The undoped films exhibited n-type conduction and p-type films could be prepared using Be as a p-type dopant.

These results, which represent the first preparation of $(Al_xGa_{1-x})_yIn_{1-y}As$ on InP substrates, demonstrate that III-III-III-V materials might be one of the promising materials in the 1980's. This preparation and the demonstration of its properties has profound significance for device and material research.

Previously MBE for III-V semiconductor alloys was mainly utilized for device preparation. However, this work has demonstrated that MBE can equally be used for the production of unknown materials which can not be prepared by LPE. It is also of particularly importance that this work has shown that MBE is a useful technique for material development.

DEVELOPMENT OF HIGH PERFORMANCE GaAs BASED SOLAR CELLS.

Of the various solar cell materials, GaAs is only material which can produce high conversion efficiencies of over 20%. High performance is expected in (GaAl)As/GaAs p-p-n solar cells under solar cencentration conditions, using Be as a p-type dopant (which produces a shallow acceptor energy level). The Be doped (GaAl)As/GaAs p-p-n solar cells were fabricated and tested. These devices exhibited high conversion efficiencies of over 20% (AM 1) and 24.7% (AM 1.3) , comparing well with previous reported efficiencies. When placed in a concentrator assembly, the device produced an output power of 5 Wcm^{-2} at 400 suns and the corresponding conversion efficiency was 15%.

The monolithic solar cell array, in which several solar cells are series-connected on a semi-insulating GaAs wafer, is suitable for a tracking concentrator power system and for consumer use. Three types of GaAs based monolithic solar cell arrays were developed, namely the Schottky barrier type, the p-n homojunction type, and the (GaAl)As/GaAs p-p-n type solar cell arrays. In order to prevent the interconnecting metal from shorting the junction at the groove wall, an additional Zn diffusion process was developed for the (GaAl)As/GaAs p-p-n type device. This process obviates the necessity of an insulating layer which had previously been used to avoid junction shortage at the groove wall. The (GaAl)As/GaAs p-p-n type cell array exhibited a conversion efficiency of 15% for AM 1 solar simulator insolation.

****

A systematic study of p-type $Ga_{1-x}Al_xAs$ ternary alloys and the considerations concerning new semiconductor materials for the 1980's are described in this thesis.

In conclusion, the author would like to reemphasiz that R&D for electronic devices consisting of III-V compound semiconductor alloys must be carried out together with sufficient investigations and analyses of the physical properties of III-V compound semiconductor alloys.

ACKNOWLEDGEMENTS

The author is greatly indebted to Professor K. TAKAHASHI for providing such an interesting theme and for his continuous guidance and encouragement during the author's undergraduate and post-graduate courses.

The author would like to express special gratitude to Associate Professor M. KONAGAI for his extensive advice and encouragement, and personally instructing him in the LPE technique and several other measurements. Without his guidance, few significant experimental results would have been obtained.

The author is grateful to Professors S. YAMANAKA, S. NOMURA, T. HINO and Associate Professors M. NAOE, M. ABE, T. MORIIZUMI, M. MATSUMURA for their guidance and fruitful discussions.

The author would like to thank all members of the TAKAHASHI Lab., especially Messers. M SUGIMOTO (NEC) for his discussions and encouragement, T. MISHIMA for useful discussions concerning MBE, and some graduate and undergraduate students for their technical assistance. The author is also grateful to the members of the YAMANAKA and NAOE Lab., NOMURA and ABE Lab., HINO Lab., YASUDA and MORIIZUMI Lab., SUEMATSU and FURUYA Lab., and MATSUMURA Lab. for providing experimental equipments.

The author would like to express his gratitude to Dr. M. D. Rogers (British Embassy) and his wife Mrs. A. Rogers for their kind discussions regarding the English in this thesis.

Finally, but by no means least the author would like to acknowledge the constant encouragement and support of his parents, Toshio and Kaneko, his sister, Miyako, and particularly his wife, Yuko.

APPENDIX A. PHASE EQUILIBRIA OF III^n-V SYSTEMS.

The phase diagram of III-III-III-V quaternary systems can be analyses by extending the ternary system, which was reported by Ilegems, et al.(1)(2) The following analysis is generally performed for the III^n-V system, and is also easily applied to the III-V^n system (such as Ga-As-P, and In-As-P-Sb). The ternary phase diagram such as Ga-Al-As can be calculated by putting n = 2, and the quaternary such as Ga-In-Al-As by putting n = 3.

Here, the solid solutions are assumed to be represented by $A^1_{X^s_1}A^2_{X^s_2}$--$A^n_{X^s_n}B$, where A^i is the group-III element, B is the group-V element, and X^s_i is the composition of A^iB. The fundamental assumptions for the deviation are as follows:

1. The solid solutions of composition $A^1_{X^s_1}A^2_{X^s_2}$--$A^n_{X^s_n}B$ is treated as a mixture of A^1B, A^2B---, and A^nB, and separate equilibrium conditions are written between A^iB (i=1-n) in the solid and A^i(i=1-n) and B in the liquid.
2. The chemical potentials of the pure binary compounds are related to the chemical potentials of their constituent elements in the binary liquid by means of a relationship derived by Vieland(3).

The following expressions are obtained for systems in which there are liquid solutions of elements A^i(i=1-n) and B and solid solutions of the binary compounds A^iB (i=1-n):

$$\xi_i \cdot X_i^s = \{4\gamma_i\gamma_{n+1}X_i^l X_{n+1}^l/(\gamma_i^{sl}\gamma_{n+1}^{sl})\}\cdot \exp\{\Delta S_F^i(T_F^i - T)/RT\}, \quad (n=1-n) \qquad \text{(A-1)}$$

$$\sum_{i=1}^{n+1} X_i^l = 1, \qquad \text{(A-2)}$$

$$\sum_{i=1}^{n} X_i^s = 1. \qquad \text{(A-3)}$$

where

ξ_i : the activity coefficient of the compound (A^iB, $i=1\sim n$) in the solid.

γ_i : the activity coefficient of the indicated element (A^1, A^2--A^n, and B) in the liquid

X_i^s ($i= 1\sim n$): the mole fraction of A^iB in the solid.

X_i^l ($i=1\sim n+1$): the mole fraction of the indicated element in the liquid.

ΔS_F^i($i= 1\sim n$): the entropy of fusion of the pure binary compound A^iB.

The subscript 'sl' indicates the stoichiometric liquid (liquid A^i-B for i = 1 n in Eq. A-1.)

When the simple solution approximation is extended to III^n-V systems, equations for the activity coefficients are given by the usual expressions.(2)

$$RT\cdot\ln\gamma_i = \sum_{\substack{j=1\\ i\neq j}}^{n+1} \alpha_{ij}X_j^l + \sum_{\substack{k=1\\ k<j\\ j\neq i}}^{n+1} X_k^l X_j^l(\alpha_{ij}+\alpha_{ik}-\alpha_{kj}), \qquad \text{(A-4)}$$

$$\text{and}\quad RT\cdot\ln\xi_i = \sum_{\substack{j=1\\ i\neq j}}^{n} \beta_{ij}X_j^s + \sum_{\substack{k=1\\ k<j\\ j\neq i}}^{n} X_k^s X_j^s(\beta_{ij}+\beta_{ik}-\beta_{kj}). \tag{A-5}$$

where α_{ij} is the interaction coefficient between i and j in the liquid, and is given by

$$\alpha = a - bT \quad \text{for III-V systems.} \tag{A-6}$$

β_{ij} is the interaction coefficient between A^iB and A^jB in the solid. The computer program for the III^n-V plural systems solves the non-linear simultaneous eqations of Eq. A-1~A-5, the input data being α, β, ΔS^F, and T^F. The parameters are listed in Table A-1.

References

(1) M. Ilegems and G. L. Pearson; Proc. of 1968 Symp. on GaAs, The Institute of Physics and The Physical Society, 1968, p. 3.

(2) M. B. Panish and M. Ilegems; Progress in Solid State Chemistry, Vol. 7, (Pergamon, NY, 1969) p.39.

(3) H. C. Casey, Jr. and M. B. Panish; "Heterojunction Lasers" (Academic Press, 1978)

(4) H. Kressel and J. K. Butler; "Semiconductor Lasers and Heterojunction LEDs" (Academic Press, 1977)

(5) T. W. Wu and G. L. Pearson; J. Phys. Chem. Solids, 33 409 (1972).

(6) T. P. Pearsall and R. W. Hopson, Jr.; J. Appl. Phys., 48 4407 (1977).

Table A-1.

Liquidus and solidus interaction parameters for the calculation of the III-V phase diagram.

i-j -	T^F (K)	ΔS^F (cal $mole^{-1}K^{-1}$)	α_{ij}	Ref.
Al-P	2803	15.0	1750-2.0T	(3)
	2803	15.0	2800-4.8T	(2)
Al-As	2043	15.6	-6390-5.5T	(3)
	2013	22.8	9040-9.16T	(1)
	2043	15.6	600-12.0T	(2)
Al-Sb	1333	14.57	12300-10.0T	(3)
Ga-As	1511	16.64	5160-9.16T	(1)
Ga-P	1740	17.3	2120-4.45T	(3)
	1738	16.8	2800-4.8T	(2)
	1813	12.85	14690-13.15T	(4)
Ga-Sb	983	15.80	4700-6.0T	(3)
In-P	1335	15.2	3578-3.54T	(3)
	1343	14.0	4500-4.0T	(2)
	1333	14.76	9030-9.75T	(4)
In-As	1215	14.52	3860-10.0T	(3)
	1210	14.52	4030-10.16T	(5)
In-Sb	798	14.32	3400-12.0T	(3)

(continued to next page)

i-j	α_{ij} (cal)	Ref.	i-j	β_{ij} (cal)	Ref.
Al-Ga	104	(2)	AlP -GaP	0	(2)
			AlAs-GaAs	0	(2)
				400 at 973K -3892+4T(1073-1273K)	(3)
			AlSb-GaSb	0	(2)
Al-In	$=\alpha_{Ga-In}$		AlP -InP	3500	(2)
			AlAs-InAs	2500	(2)
			AlSb-InSb	600	(2)
Ga-In	1060	(2)	GaP -InP	3500	(2)
	1850	(6)	GaAs-InAs	2.83T-1130	(5)
				2100	(6)
			GaSb-InSb	1900	(2)
P -As	1500	(2)	AlP -AlAs	400	(2)
	2000	(4)	GaP -GaAs	400	(2)
			InP -InAs	400	(2)
				1000	(4)
As-Sb	750	(2)	GaAs-GaSb	4500	(2)
			InAs-InSb	2250	(2)

APPENDIX B.

ANALYTICAL METHOD OF (GaAl)As/(GaAl)As p-p-n SOLAR CELLS.

Spectral response and the short circuit current can be calculated using the solution of the usual minority carrier continuity equations. The details of formulae are omitted since they are summarized in literatures.*

For convenience, the parameters used in this research for the numeracal calculations for (GaAl)As/(GaAl)As p-p-n solar cells are listed in Table B-1.

*) for example,

1. A, G. Milnes and D. L. Feucht; "Heterojunction and metal-semiconductor junctions" (Academic press, 1973), chap 5.
2. H. J. Hovel; "Semiconductor and semimetals" Vol.10. Solar cells (Academic press, 1975)
2. "Taiyoko Hatsuden" (ed. K. Takahashi, Y. Hamakawa, and A. Ushirikawa, Morikita Shuppan, 1979) Chap. 3 and Chap. 8.

1. Energy band gap of $Ga_{1-x}Al_xAs$.

$$E_g^{\Gamma}(x) = 1.424 + 1.247x \text{ (eV) for } 0 < x < 0.45$$

$$E_g^{X}(x) = 1.900 + 0.125x + 0.143x^2 \text{ (eV)}$$

2. Absorption coefficients.

For the surface $p\text{-}Ga_{1-x}Al_xAs$ layer $(x > 0.8)$

$\beta = 3.2\times10^4\{h\nu - E_{g1}(x)\}^{1/2}$ (cm^{-1}) --- direct transition.

$\beta = 4.9\times10^3\{h\nu - E_{g1}(x)\}^2$ (cm^{-1}) --- indirect transition.

For the active $p\text{-}Ga_{1-y}Al_yAs$ region $(0 < y < 0.4)$

$\alpha = 3.5\times10^4\{h\nu - E_{g2}(y)\}1/2$ (cm^{-1})

3. The other parameters.

Thickness of the surface $p\text{-}Ga_{1-x}Al_xAs$: 0.1 - 0.5 μm

Thickness of the active $p\text{-}Ga_{1-y}Al_yAs$: variable

Electron diffusion length of the surface layer : 0.7-1.0 μm

Electron diffusion length of the active p-type region : 4-5 μm

Hole diffusion length of the active n-type region: 0.7 μm

Diffusion coefficient of the surface layer : 6 cm^2sec^{-1}

Diffusion coefficient of the active p-type region: 80 cm^2sec^{-1}

Diffusion coefficient of the active n-type region: 6 cm^2sec^{-1}

Surface recombination velocity of the surface layer : 10^6-10^7 $cm\cdot s^{-1}$

Table B-1.

Parameters used in the calculations.

REFERENCES

1. T.Arizumi, T. Nishizawa, and M.Kakehi (1968); Japan.J.Appl. Phys. 7 468.
2. A. Baldereschi and N. O. Lipari (1973); Phys. Rev. B8 2697.
3. S. M. Bedair , J. A. Hutchby, J. Chiang, M. Simson, and J. R. Hauser (1981); Proc. 15th IEEE PVSC, p.21.
4. P. G. Borden (1979); Appl. Phys. Lett. 35 553.
5. P. G. Borden (1980): Proc. 15th IEEE PVSC, p.554.
6. C. O. Bozler, J. C. C. Fan, and R. W. McClelland (1978); Proc. 7th Symp. on GaAs and Related Compounds, p.429.
7. Cappasso (1981); private communication.
8. H. C. Casey, B. I. Miller, and E. Pinkas (1973); J. Appl. Phys. 44 1281.
9. H. C. Casey, Jr. (1973b); "Atomic diffusion in semiconductors" Edited by C. Shaw (Plenum Press, 1973), Chpa. 3.
10. H. C. Casey. Jr., D.D. Sell, and M.B. Panish (1974); Appl. Phys. Lett. 24 63.
11. H. C. Casey, Jr. and M. B. Panish (1978); "Heterostructure Lasers" (Academic Press, 1978).
12. A. Chandra and L. F. Eastman (1980); J. Appl. Phys. 51 2669.
13. S. Charan, M. Konagai, and K. Takahashi (1979); J. Appl. Phys. 50 963.
14. S. S. Chu, T. L. Chu, and H. T. Yang (1978a); Appl. Phys. Lett. 32 557.
15. S. S. Chu, T. L. Chu, and H. T. Yang (1978b); Proc. 13th IEEE PVSC, p.956.
16. S. S. Chu, T. L. Chu, H. T. Yang, and K. H. Hang (1978c); J. Electrochem. Soc. 125 1668.
17. S. S. Chu, T. L. Chu, and M. S. Lan (1979); J. Appl. Phys. 50 5804.
18. M. Costato and L. Roggiani (1973a); Phys. Status Solidi 58 471.
19. M. Costato and L. Reggiani (1973b); Phys. Status Solidi 59 47.
20. M. Costato, G. Galiani, C. Jcoboni, and L. Reggiani (1974); J. Phys. Chem. Solids, 35 1605.
21. P. D. Dapkus, R. D. Dupuis, R. D. Yingling, J. J. Yang, W. I. Simpson, L. A. Moudy, R. E. Johnson, A. G. Cambell, H. H. Manasevit, and R. P. Ruth (1978); Proc. 13th IEEE PVSC, p.960.
22. G. Dresselhaus, A. F. Kip, and C. Kittel (1955); Phys. Rev. 98 368.
23. R. D. Dupuis, P. D. Dapkus, R. D. Yingling, and L. A. Moudy (1977); Appl. Phys. Lett. 31 201.

24. H. Ehrenreich (1957); J. Phys. Chem. Solids 2 131.
25. H. Ehrenreich (1959); J. Phys. Chem. Solids 9 129.
26. M. Ettenberg and C. J. Neuse (1975); J. Appl. Phys. 46 3500.
27. M. Ettenberg and H. Kressel (1976); J. Appl. Phys. 47 1538.
28. J. Ewan, R. C. Knechtli, and G. S. Kamath (1978); Proc. 13th IEEE PVSC, p. 941.
29. J. C. C. Fan and C. O. Bozler (1978a); Proc. 13th IEEE PVSC, p.953.
30. J. C. C. Fan, C. O. Bozler, and R. L. Chapman (1978b); Appl. Phys. Lett. 32 390.
31. J. C. C. Fan, R. L. Chapman, J. P. Donnelly, G. W. Turner, and C. O. Bozler (1979a); Appl. Phys. Lett. 34 780.
32. J. C. C. Fan, A. R. Calawa, R. L. Chapman, and G. W. Turner (1979b); Appl. Phys. Lett. 35 804.
33. J. C. C. Fan, R. L. Chapman, and C. O. Bozler (1980a); Appl. Phys. Lett. 36 53.
34. J. C. C. Fan, C. O. Bozler, and R. W. McClelland (1980); Proc. Symp. on Materials and New Processing Technologies for Photovoltaics (Proc. Vol. 81-3, The Electrochem. Soc. Inc.), p.304.
35. J. C. C. Fan, C. O. Bozler, and R. W. McClelland (1981); Proc. 15th IEEE PVSC, p.666.
36. A.Flat, A. G. Milnes, and D. L. Feucht (1974); Solid State Electron. 20 1024.
37. S. Fujuta, S. M. Bedair, M. A. Littlejohn, and J. R. Hauser (1980); J. Appl. Phys. 51 1980.
38. R. P. Gale, B. Y. Tsaur, J. C. C. Fan, F. M. Davis, and G. W. Turner (1981); Proc. 15th IEEE PVSC, p.1051.
39. A. R. Gobat, M. F. Lamorte, and G. W. McIver (1962); IRE Tran. Military Electr. 60 20.
40. A. R. Goodwin and P. R. Selway (1970); IEEE QE-6 285.
41. P. D. Greene (1971); Solid State Commun. 9 1299.
42. W. H. Hackett, Jr., R. H. Saul, R. W. Dixon, and G. W. Kammolott (1972); J. Appl. Phys. 43 2857.
43. Y. Hamakawa (1981); OYO BUTSURI 50 342. (in Japanese)
44. J. S. Harris and W. L. Snyder (1969); Solid State Electron. 12 337.
45. J. W. Harrison and J. R. Hauser (1976); J. Appl. Phys. 47 292.
46. J. W. Harrison and J. R. Hauser (1976a); Phys. Rev. B13 5347.

47. I. Hayashi, M. B. Panish, P. W. Foy, and S. Sumski (1970); Appl. Phys. Lett. 17 109.
48. D. E. Hill (1970); J. Appl. Phys. 41 1815.
49. S. Hiyamizu, M. Miura, T. Fujii, and K. Nanb (1980); Appl. Phys. Lett. 37 805.
50. H. J. Hovel and J. M. Woodall (1973); J. Electrochem. Soc. 120 1246.
51. H. J. Hovel (1975a);"Semiconductor and Semimetals' Vol. 11.
52. H. J. Hovel and J. M. Woodall (1975b); Appl. Phys. Lett. 27 447.
53. D. J. Howarth and E. H. Sondheimer (1953); Proc. Roy. Soc. A219 53.
54. A. R. Hutson (1957); Phys. Rev. 108 222.
55. S. Iida and K. Ito (1971); J. Electrochem.Soc. 118 768.
56. H. Ijuin and S. Gonda (1976); J. Electrochem. Soc. 123 1109.
57. M. Ilegems and M. B. Panish (1974); J. Phys. Chem. Solids 35 409.
58. S. Isozumi, et al. (1977); J. Cryst. Growth 41 166.
59. L. W. James and R. L. Moon (1975); Proc. 11th IEEE PVSC, p.402.
60. D. A. Jenny, J. J. Loferski, and P. Rappaport (1956); Phys. Rev. 101 1208.
61. W. D. Johnston, Jr. and W. H. Callahan (1976); Proc. 12th IEEE PVSC, p.934.
62. G. S. Kamath, J. Ewan, and R. C. Knechtli (1976); Proc. 12th IEEE PVSC, p.929 & IEEE ED-24 (1977) 473.
63. T. Kamiya and T. Kuriyama (1976); OYO BUTSURI 45 883. (in Japanese)
64. C. S. Kang and P. D. Greene (1968); Proc. Int. Symp. on GaAs, p.92.
65. T. Kawakami (1973); Japan. J. Appl. Phys. 12 151.
66. Y. Kawamura, H. Asahi, M. Ikeda, and H. Okamoto(1981); J. Appl. Phys.,to be published.
67. C. S. Kim and M. Sakata (1979); Japan. J. Appl. Phys. 18 247.
68. M. Konagai and K. Takahashi (1975); J. Appl. Phys. 3542.
69. M. Konagai and K. Takahashi (1976a); Solid State Electron. 19 259.
70. M. Konagai and K. Takahashi (1976b); Proc. Int. Symp. on Solar Energy, p.154.
71. M. Konagai, M. Ogura, and K. Takahashi (1976c); OYO BUTSURI 45 530. (in Japanese)
72. M. Konagai, M. Sugimoto, and K. Takahashi (1978); J. Cryst. Growth 45 277.
73. M. Konagai and K. Takahashi (1981a); Electronics, S.56-10 gatsu-go, p.1170.
74. M. Konagai (1981b); OYO BUTSURI 50 990. (in Japanese)
75. D. Kranzer (1976); J. Phys. C. 6 2967.
76. H. Kressel and J. K. Butler (1977); "Semiconductor Lasers and Heterojunction LED's" (Academic Press).

77. M. F. Lamorte and D. H. Abbott (1980); IEEE ED-27 231.
78. P. Lawaetz (1971); Phys. Rev. B4 3460.
79. C. P. Lee, S. Marfalit, and A. Yariv (1978); Solid State Electron. 21 905.
80. M. A. Littlejohn, J. R. Hauser, T. H. Glisson, D. K. Ferry, and J. W. Harrison (1978); Sold State Electron. 31 107.
81. J. J. Loferski (1956); J. Appl. Phys. 27 777.
82. P. L. Luscher (1977); Solid State Technology, Dec. p.43.
83. P. L. Luscher, W. S. Knodle, and Y. Chai (1980): Electronics/August 28, p.160.
84. J. M. Luttinger (1956); Phys. Rev. 102 1030.
85. L. Makowski and M. Glicksman (1973); J. Phys. Chem Solids 34 487.
86. G. W. Masden and C. E. Backus (1978); Proc. 13th IEEE PVSC, p.853.
87. S. Matsubara, M. Konagai, and K. Takahashi (1979); OYO BUTSURI 48 1050. (in Japanese)
88. T. Matsuzawa (1981); OYO BUTSURI 50 331. (in Japanese)
89. A. L. Mears and R. A. Stradling (1971); J. Phys. C. 4 L22.
90. K. Mitsui, et al. (1981); Presented at Autumn Meeting of the Japan Society of Applied Phys. 8p-F-13.
91. T. Miura, S. Hiyamizu, T. Fujii, and K. Nanb (1980); Japan. J. Appl. Phys. 19 L225.
92. R. L. Moon, L. W. James, H. A. VanderPlas, and N. J. Nelson (1978); Appl. Phys. Lett. 33 196.
93. S.Mukai, Y. Makita, and S. Ginda (1979); J. Appl. Phys. 50 1304.
94. N. J. Nelson, K. K. Johnson, R. L. Moon, H. A. VanderPlas, and L. W. James (1978); Appl. Phys. Lett. 38 26.
95. H. Neumann (1976); "Semiconductor Sources of Electromagnetic Radiation" (ed. M. A. Herman), Warszawa 1976, p.45.
96. H. Neumann and N. V. Nam (1978); Kristall und Teknik 13 211.
97. M. G. Panish and A. Y. Cho (1980); IEEE Spectrum April/1980 18.
98. R. L. Petritz (1958); Phys. Rev. 110 1254.
99. B. G. Russel and D. L. Pulfrey (1976); Proc. 12th IEEE PVSC, p.962.
100. R. Sahai, D. D. Edwall, E. Corny, and J. S. Harris, Jr. (1976); Proc. 12th IEEE PVSC, p.986.
101. R. Sahai, D. D. Edwall, and J. S. Harris, Jr. (1978); Proc. 13th IEEE PVSC, p.946
102. T. Saitoh and T. Tokuyama (1981); OYO BUTSURI 50 398.

103. R. R. Sexena, et al. (1980); J. Appl. Phys. 51 4501.

104. R. Solomon (1968); Proc. 2nd Int. Symp. On GaAs, paper II .

105. A. J. SpringThorpe, F. D. King, and A. Becke (1975); J. Electron. Materials 4 101.

106. R. J. Stirn and Y. C. M. Yeh (1975a); Proc. 11th IEEE PVSC, p.437.

107. R. J. Stirn and Y. C. M. Yeh (1975b); Appl. Phys. Lett. 27 95.

108. R. J. Stirn and Y. C. M. Yeh (1976) ; Proc. 12th IEEE PVSC, p.883.

109. R. J. Stirn and Y. C. M. Yeh (1977a); IEEE ED-24 476.

110. R. J. Stirn (1976b); unpublished.

111. R. J. Stirn (1981) ; Proc. IEEE 15th IEEE PVSC, p. 1045.

112. M. Sugimoto. M. Konagai, and K. Takahashi (1979); Tran. IEE of Japan 99-A 305. (in Japanese).

113. K. Takahashi, Y. Hamakawa, and Ushirokawa (Editors) (1980); "Taiyoko Hatsuden" (Morikita Shuppan, 1980). (in japanese)

114. K. Takahashi (1981); OYO BUTSURI 50 350. (in Japanese)

115. J. J. Tietjen and L. R. Weisberg(1965); Appl. Phys. Lett. 7 261.

116. G. W. Turner, J. C. C. Fan, R. L. Chapman, and R. P. Gale (1981); Proc. 15th IEEE PVSC, p.151.

117. W. T. Tsang (1979); Appl. Phys. Lett. 34 473.

118. H. A. VanderPlas, L. W. James, R. L. Moon, and N. J. Nelson (1978); Proc. 13th IEEE PVSC, p.934.

119. J. A. VanVechten and T. K. Bergstresser (1970); Phys. Rev. B1 3351.

120. J. Vilms and J. P. Garrett (1972); Solid Stae Electron. 15 443

121. E. Y. Wang, I. Hsu, and H. W. Bradhorst, JR. (1977); J. Electrochem Soc. 124 1915.

122. J. D. Wiley and M. DiDomenico (1970); Phys. Rev. B2 427.

123. J. D. Wiley (1970a); Sold State Commun. 8 1865.

124. J. D. Wiley (1971) : Phys. Rev. B4 2485.

125. J. D. Wiley (1975) ; "Semiconductor and Semimetals", Vol. 10. (Academic Press, 1975), Chap.2.

126. J. M. Woodall and H. J. Hovel (1972); Appl. Phys. Lett. 21 379.

127. J. M. Woodall and H. J. Hovel (1975); Appl. Phys. Lett. 30 492.

128. J. J. Yang, W. I. Simpson, and L. A. Moudy (1981); Proc. 1981 Int. Symp. on GaAs and Related Compounds, to be published.

129. J. J. Yang (1981b); private communication.

130. Y. C. M. Yeh, F. P. Ernest, and R. J. Stirn (1978a): Proc. 13th IEEE PVSC, p.966.

131. Y. C. M. Yeh and R. J. Stirn (1978b); Appl. Phys. Lett. 33 401.
132. K. H. Zschauer (1973); Proc. 4th Int. Symp. On GaAs and Related Compounds, Bouldler, 1972.

(Supplementary List)

1. L. R. Weisberg and J. Blank (1963); Phys. Rev. 131 1548.
2. D. W. Yarbrough (1968); Semicond. Prod. 11 28.
3. S. Zukotynski, S. Sumski, M. B. Panish, and H. C. Casey, Jr. (1979); J. Appl. Phys. 50 5795.

* PVSC --- Photovoltaic Specialists Conference

LIST OF PUBLICATIONS

(Full papers)

(1) K. Masu, M. Konagai, and K. Takahashi,
" Acceptor energy level for Zn in $Ga_{1-x}Al_xAs$ "
J. Appl. Phys. 51 (2) (1980) 1060.

(2) K. Masu, M. Konagai, and K. Takahashi,
" (GaAl)As/GaAs solar cells – Dopant study of Zn and Be "
Japan. J. Appl. Phys. 19 Suppl. 19-2 (1980) 191.

(3) K. Masu. Y. S. Quan, M. Konagai, and K. Takahashi,
" A monolithic GaAs solar cell array "
Japan. J. Appl. Phys. 20 Suppl. 20-2 (1981) 95.

(4) K. Masu, S. Nakatsuka, M. Konagai, and K. Takahashi,
" The role of Be in (GaAl)As/GaAs solar cells "
J. Electrochem. Soc. (1981),to be published.

(Letter)

(1) K. Masu, M. Konagai, and K. Takahashi,
" Reproducible diffusion of beryllium into GaAs during liquid phase epitaxy "
Appl. Phys. Lett. 37 (2) (1980) 182.

(International Conferences)

(1) K. Masu, S. Nakatsuka, M. Konagai, and K. Takahashi,
" The role of Be in (GaAl)As/GaAs solar cells "
The Electrochem. Soc., Fall Meeting, Florida, U.S.A.
(Oct., 1980) Abs. No. 285.
Proceeding of the Symposium on Materials and New Processing Technologies for Photovoltaics. (The Electrochem Soc. Inc., NJ), Proceeding Volume 81-3 (1981), p.295.

(2) K. Masu, Y. S. Quan, M. Konagai, and K. Takahashi,
" A monolithic GaAs solar cell array "
The 15th IEEE Photovoltaic Specialists Conference, Florida, U.S.A. (May, 1981) Abs. p.315.
Proceeding of the 15th IEEE Photovoltaic Specialists Conference (1981) p.1337.

(3) K. Masu, S. Hiroi, T. Mishima, M. Konagai, and K. Takahashi, " Preparation of $(Al_xGa_{1-x})_yIn_{1-y}As$ $(0 < x < 0.5, y=0.47)$ lattice matched InP substrate grown by molecular beam epitaxy "
The 1981 International Symposium on GaAs and Related Compounds, Kanagawa, Japan (Sept., 1981).
Proceeding of the 1981 International Symposium on GaAs and Related Compounds. (1981), to be published.

(Domestic conferences)

(1) 応用物理学会

昭和53年 春 27p—S—12.
昭和53年 秋 4a—T—4.
昭和54年 春 30p—Q—5, 30p—Q—13.
昭和54年 秋 30p—K—5.
昭和55年 春 1p—E—9.
昭和55年 秋 19p—B—12.
昭和56年 春 31p—L—9.
昭和56年 秋 7a—F—6, 8p—F—10.

(2) 電子通信学会

昭和52年 半導体部門全国大会 講演予講集 p. 213.

(3) 他

The 1st Photovoltaic Science and Engineering Conference in Japan. (1979) IIIp-3.

The 2nd Photovoltaic Science and Engineering Conference in Japan. (1980) IIa-4.